

SFB 837
Interaction Modeling in
Mechanized Tunneling

Nina Silvia Müthing

On the consolidation behaviour of fine-grained soils
under cyclic loading

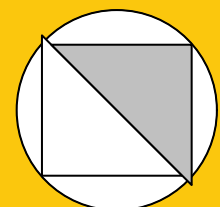
Bochum 2017

Heft 62

Schriftenreihe des Lehrstuhls für
Grundbau, Boden- und Felsmechanik

Herausgeber: Tom Schanz

ISSN 2190-3255



Ruhr-Universität Bochum

Schriftenreihe Grundbau, Boden- und Felsmechanik

Heft 62

Herausgeber:

Prof. Dr. -Ing. habil. Tom Schanz

Ruhr-Universität Bochum

Fakultät für Bau- und Umweltingenieurwissenschaften

Lehrstuhl für Grundbau, Boden- und Felsmechanik

44801 Bochum

Telefon: 0234/ 3226135

Telefax: 0234/ 3214236

Internet: www.gbf.ruhr-uni-bochum.de

ISSN 2190-3255

© 2017 der Herausgeber

On the consolidation behaviour of fine-grained soils under cyclic loading

DISSERTATION

zur Erlangung des akademischen Grades

Doktor-Ingenieur (Dr.-Ing.)

an der

Fakultät für Bau- und Umweltingenieurwissenschaften

der Ruhr-Universität Bochum

vorgelegt von

Nina Silvia Müthing

geboren am 14. Februar 1987 in Essen

Hauptberichter: Univ. Prof. Dr.-Ing. habil. Tom Schanz
Mitberichter: Prof. Dr. Maria Datcheva
Mitberichter: Chancellor's Professor Kenichi Soga, PhD FREng FICE
Mitberichter: Univ. Prof. Dr.-Ing. habil. Theodoros Triantafyllidis

Bochum, November 2017

Vorwort des Herausgebers

Die vorliegende Promotion von Frau Müthing ist im Bereich der Grundlagenforschung in der experimentellen und theoretischen Bodenmechanik angesiedelt. Sie ist thematisch nah am Teilprojekt A5 des aktuellen Bochumer SFB 837 angegliedert, das sich inhaltlich u.a. mit dem Verhalten von strukturierten Tonen unter monotoner und zyklischer Beanspruchung beschäftigt. Die Analyse der Konsolidation vor allem feinkörniger Böden wird oft als die Geburtsstunde der modernen Bodenmechanik bezeichnet. Diese mit den Namen Terzaghi, Fillunger und Biot verbundenen, wegweisenden Forschungen, untersuchen seit den 30er Jahren des vergangenen Jahrhunderts den zeitlichen Verlauf der Setzungen und der Porenwasser(über)-drücke zufolge monotoner Belastung unter eventueller Berücksichtigung von zwischenzeitlichen Entlastungen. Dabei stellt die Kompressionskurve ausschließlich Gleichgewichtszustände dar, d.h. Porenwasser(über)drücke sind vollständig dissipiert. Im Verlauf der vergangenen 80 Jahre wurden umfangreiche Weiterentwicklungen der ursprünglichen Theorie erzielt. So wurde die ursprünglich eindimensionale Theorie auf räumliche Probleme erweitert und auch der weiterhin monotone Verlauf der Belastung um qualitative weitere Belastungsformen erweitert. Hier setzt die Arbeit von Frau Müthing an: schon Mitte der 50er Jahre sind analytische Lösungen für nicht monotone Belastungen erzielt worden. Experimentelle Untersuchungen zur Verifizierung dieser Lösungen existieren nur in zwei bis drei bekannten Fällen. Diese Arbeiten sind in der Variation der Parameter und der Materialien unzureichend. Die vorliegende Arbeit von Frau Müthing liefert eine detaillierte Studie zum Verhalten von feinkörnigen Böden unter zyklischer Beanspruchung, die in dieser Qualität nach meinen Kenntnissen einmalig ist.

Das Materialverhalten von feinkörnigen Böden unter monotoner und zyklischer Beanspruchung steht im Mittelpunkt der Promotion von Frau Müthing. Der experimentelle Teil beinhaltet als ersten exzellenten Beitrag die Entwicklung eines Ödometergeräts, welches neben den üblichen Eigenschaften die Messung der Radialspannung und des Porenwasserüberdrucks ermöglicht. Da die Probe vollkommen abgedichtet ist, kommt es im Vergleich zu herkömmlichen Zellen bei der Messung der Vertikalkraft zu besonderen Herausforderungen. Frau Müthing löst dieses Problem durch die Anordnung jeweils einer Kraftmessdose ober- und unterhalb der Probe. Durch diesen international originären Versuchsauf-

bau ist die quantitative Erfassung des Reibungsverlusts möglich, der in der Fachliteratur fast immer vernachlässigt oder nur grob abgeschätzt wird. Es zeigt sich, dass dieser Verlust bis in die Größenordnung von 15% der nominal aufgetragenen Last gehen kann. Das Gerät wird umfangreich kalibriert und die beobachteten Phänomene präzise diskutiert. An Proben eines aufbereiteten industriellen Tons und eines strukturierten, ungestörten Tons werden sowohl monotone als auch zyklische Belastungspfade (unter Variation der Belastungsamplitude und -frequenz) untersucht. Ausgewertet wird die Entwicklung des Seitendruckbeiwerts und der transienten Dissipation des Porenwasserüberdrucks. Diese Versuche sind hervorragend dokumentiert und werden ohne Zweifel als Referenzversuche ihren Weg in die Fachliteratur finden. In Anbetracht der Vielzahl der originären Beiträge dieses Teils der Promotion möchte ich nur zwei Sachverhalte hervorheben: Die erzielten Ergebnisse zur zeitlichen Entwicklung des Erdruchdruckbeiwertes unter monotoner Belastung in Funktion der Größe der Belastung sind nach meinem Kenntnisstand einzigartig. Die erzielten Ergebnisse zur Dissipation der Porenwasserüberdrücke bei zyklischer Beanspruchung unter- und oberhalb der Fließspannung eines ungestörten Tons sind in der internationalen Fachliteratur ohne Vergleich. Der Vergleich des aufbereiteten Tons mit dem natürlichen Ton zeigt deutlich den Einfluss der unterschiedlichen inhärenten und induzierten Mikrostruktur. Einen weiteren Schwerpunkt der Arbeit bildet der Vergleich der experimentellen Ergebnisse mit einer analytischen Lösung und numerischen Berechnungen mit der FEM. Es zeigt sich klar, dass die Ergebnisse der linearen analytischen Lösung nicht die wesentlichen Aspekte der Beobachtungen nachvollziehen können. Mit der nicht-linearen FEM ist dies zu mindestens qualitativ möglich. Ein besonderer Beitrag an dieser Stelle ist die Analyse des experimentellen Phasenversatzes zwischen der aufgetragenen zyklischen Belastung und der Bodenreaktion, der sich auch zu mindestens qualitativ aus der analytischen Lösung, nicht aber aus der FEM Lösung ergibt. Elegant zeigt Frau Müthing, wie dieser Phasenversatz zur effizienten Bestimmung der Permeabilität benutzt werden kann. Das von ihr vorgeschlagene Verfahren wurde in der Zwischenzeit patentiert. Die Arbeit von Frau Müthing bewegt sich international auf höchstem Niveau der theoretischen, analytischen und experimentellen Bodenmechanik. Die von ihr vorgelegten Untersuchungen zum Konstitutivverhalten von natürlichen und aufbereiteten Tonen unter monotoner und zyklischer Beanspruchung sind in dieser strengen Systematik, dem damit verbundenen Umfang, und in dieser Qualität, nach meinem Wissen einzigartig. Die erzielten Ergebnisse zum Erdruchdruck und der Destrukturierung unter zyklischer Beanspruchung sind international erstmalig dokumentiert. Sie eignen sich in hervorragender Art und Weise zur Verifizierung existierender Konsolidationsmodelle bzw. bestehender Stoffmodelle.

Vorwort des Verfassers

Die vorliegende Arbeit entstand im Rahmen meiner Tätigkeit als wissenschaftliche Mitarbeiterin am Lehrstuhl für Grundbau, Boden- und Felsmechanik der Ruhr-Universität Bochum unter der Leitung von Herrn Univ. Prof. Dr.-Ing. habil. Tom Schanz.

Mein grenzenloser und immerwährender Dank gilt Herrn Professor Tom Schanz, der mir diese Arbeit ermöglicht und mich stets in jeder Hinsicht unterstützt hat. Mit seinem wissenschaftlichen Enthusiasmus hat er meine Begeisterung für die Bodenmechanik und das Thema der zyklischen Konsolidierung im Besonderen entfacht. Seine fachliche Expertise, seine kreativen Ideen und seine kritischen Anmerkungen haben maßgeblich den Erfolg dieser Arbeit bestimmt. Ich bin ihm dankbar für alles, was er mir ermöglicht hat, darunter zahlreiche Reisen und Begegnungen mit Wissenschaftlern aus aller Welt, sowie für die vielen, wertvollen und spannenden Diskussionen mit ihm, die mich sowohl fachlich als auch persönlich geprägt haben. Ich bin unendlich traurig über seinen viel zu frühen Tod.

I would like to thank Prof. Dr. Maria Datcheva, Chancellor's Professor Kenichi Soga and Univ. Prof. Dr.-Ing. habil. Theodoros Triantafyllidis for acting as reviewers of my thesis. Their critical, constructive comments and suggestions significantly improved this work.

Einen Teil meiner Promotionszeit habe ich auch am Lehrstuhl Baugrund-Grundbau der TU Dortmund unter der Leitung von Herrn Univ. Prof. Dr.-Ing. habil. Achim Hettler verbracht. Die Arbeit in Dortmund war für mich eine interessante, lehrreiche und gute Zeit. Für die Eröffnung dieser Möglichkeit und für die entgegengebrachte Unterstützung möchte ich mich herzlich bei Herrn Professor Hettler bedanken.

Experimentelle Arbeiten stellen immer eine besondere Herausforderung dar, die kaum ohne eine helfende Hand zu bewältigen ist. Für die Unterstützung bei der Versuchsdurchführung danke ich dem Team des bodenmechanischen Labors, allen voran Herrn Michael Skubisch, sowie den Studenten Kristin Ader, Wolfgang Lieske, Maximilian Schoen und Jonas Schröder. Herrn Dr.-Ing. Lars Röchter danke ich für die Weitergabe dieses spannenden Forschungsthemas und für die wertvollen Hinweise und Anregungen, die sich aus unseren Gesprächen ergeben haben.

Darüber hinaus möchte ich mich bei all meinen Kollegen am Lehrstuhl für Grundbau, Boden- und Felsmechanik der Ruhr-Universität Bochum sowie am Lehrstuhl für Baugrund-Grundbau der TU Dortmund bedanken. Sie haben die Promotionszeit zu einem unvergesslichen Abschnitt meines Lebens gemacht und sind mir motivierend und ermutigend zur Seite gestanden. Ein besonderer Dank geht dabei an Herrn Thomas Barciaga, auf dessen fachliche und freundschaftliche Unterstützung ich mich immer verlassen konnte.

Zu guter Letzt gebührt mein größter Dank meiner Familie, ohne deren uneingeschränkte und bedingungslose Unterstützung ich dies alles nie geschafft hätte. Ihr widme ich diese Arbeit.

Bochum, November 2017

Nina Müthing

Abstract

Cyclic loading due to earthquake shaking, traffic or wind and wave loading plays an important role in a multitude of geotechnical applications. Particularly for structures, which are of civil importance and involve high investment costs, the consideration of cyclic soil behaviour finds increasing attention. Relevant examples from engineering practice are the dimensioning of on- and offshore foundation systems, the analysis of the subsoil behaviour in mechanised tunnelling or the evaluation of loading history for deep excavation walls or dams. Sophisticated calculation approaches are applied within the design process of these boundary value problems. When fine-grained, low-permeable soils are involved, the dissipation of excess pore water pressure becomes relevant and cyclic consolidation needs to be considered. While analytical solutions are available, experimental studies on the cyclic consolidation process are rare. Therefore, in the present thesis, the consolidation behaviour of fine-grained soils under cyclic loading was experimentally investigated by oedometer tests on Spergau kaolin and Onsøy clay. A new oedometer device was designed and constructed, allowing for the measurement of pore water pressure, radial stress and friction. The influence of material characteristics, loading and boundary conditions on the stress/strain state and the time-dependent development of settlements and pore pressure dissipation was assessed from the experimental testing data. The effect of a phase shift, known from equivalent conduction phenomena, was analysed for the cyclic consolidation process. Based on the experimental evaluation of the measured phase shift between the vertical effective stress and pore pressure, a concept to derive the consolidation coefficient c_v and the hydraulic permeability k , was suggested and registered for German patent approval. Analytical solutions for the cyclic consolidation process were derived. By comparison of the experimental results to the mathematical solutions of the boundary value problem (analytical solutions and numerical modelling), the limitations of the mathematical models incorporating constitutive linearisations were evaluated and the ability of different, constitutive non-linearities to reproduce the experimental results was assessed. Based on the performed investigation a better understanding of the cyclic consolidation process could be derived and suggestions for further studies were made.

Kurzfassung

Zyklische Belastungen infolge von Erdbeben, Verkehrs-, Wind- und Wellenlasten sind für eine Vielzahl von geotechnischen Fragestellungen von Bedeutung. Insbesondere bei der Beurteilung von Bauwerken, die von ziviler Bedeutung sind oder hohe Investitionskosten bedingen, wird daher zunehmend das zyklische Bodenverhalten betrachtet. Relevante Beispiele aus der Ingenieurspraxis sind die Dimensionierung von Windkraftanlagen (on- und offshore), die Analyse des Bodenverhaltens beim maschinellen Tunnelvortrieb oder die Beurteilung von Belastungsvorgängen bei tiefen Baugrubenwänden oder Staudämmen. Für die Bemessung dieser geotechnischen Randwertprobleme finden zunehmend aufwendige Berechnungsansätze Anwendung. Werden hierbei feinkörnige Böden betrachtet, so spielt der zeitverzögerte Abbau der Porenwasserdrücke eine Rolle und zyklische Konsolidationsprozesse müssen berücksichtigt werden. Während in der Literatur analytische Ansätze zur Berechnung der zyklischen Konsolidierung vorliegen, finden sich nur wenige experimentelle Untersuchungen zu diesem Thema. In der vorliegenden Arbeit wurde daher das Konsolidationsverhalten feinkörniger Böden unter zyklischer Last in Oedometerversuchen an Spergau Kaolin und Onsøy Ton experimentell untersucht. Hierzu wurde eine neuartige Oedometerzelle konstruiert, die die Messung von Porenwasserdrücken, Radialspannung und Reibung erlaubt. Anhand der experimentellen Daten wurde der Einfluss von Materialeigenschaften, Belastungs- und Randbedingungen auf das Spannungs-Dehnungsverhalten sowie den zeitlichen Verlauf der Setzungen und des Porenwasserdrucks untersucht. Der aus verwandten Konduktionsphänomenen bekannte Effekt des Phasenversatzes wurde für die Fragestellung der zyklischen Konsolidierung untersucht. Auf Basis der experimentellen Messungen des Phasenversatzes zwischen aufgebrachtter Spannung und Porenwasserdruck, wurde so ein Verfahren zur Bestimmung des Konsolidationskoeffizienten c_v und der hydraulischen Durchlässigkeit k entwickelt, welches bereits zum Patent angemeldet wurde. Mit Hilfe des Vergleichs zwischen mathematischer Modellierung (analytische Lösung und numerische Modellierung) und experimentellen Ergebnissen, konnten die Einschränkungen der linearisierten, mathematischen Ansätze aufgezeigt und die Eignung verschiedener, nicht-linearer Konstitutivansätze bewertet werden. Auf

Grundlage der durchgeführten Studie konnte so ein wesentlich verbessertes Verständnis des zyklischen Konsolidationprozesses erlangt und Vorschläge für weiterführende Untersuchungen erarbeitet werden.

Contents

1	Introduction	1
1.1	Motivation	1
1.2	Objectives	3
1.3	Layout of the thesis	3
2	Compressibility and permeability of fine-grained soils	5
2.1	Soil structure	5
2.1.1	Clay fabric	5
2.1.2	Methods for clay fabric investigation	6
2.1.3	States of clay structure	7
2.2	One-dimensional compression of soils	9
2.2.1	Laboratory determination	10
2.2.2	Primary compression of fine-grained soils	11
2.2.3	Primary compression of natural, structured clay	12
2.2.4	Barotropy and pycnotropy	16
2.2.5	Historiotropy	17
2.2.6	Secondary compression	18
2.2.7	Rate dependency	20
2.2.8	Temperature dependency	22
2.2.9	Development of horizontal stress	22
2.3	Permeability of fine-grained soils	24
2.3.1	Darcy's law	24
2.3.2	Permeability of soils	25
2.3.3	Hydraulic permeability of clays	26
2.3.4	Laboratory measurement	27
2.3.5	Anisotropy	30
2.4	Summary	30

3	Consolidation of fine-grained soils	31
3.1	Introduction	31
3.2	Principle of effective stress	31
3.3	One-dimensional, linear consolidation theory	32
3.3.1	General theory of consolidation - Biot model	32
3.3.2	Hybrid model	34
3.3.3	Terzaghi model	34
3.4	Analytical solution for one-dimensional, linear consolidation	35
3.4.1	Initial and boundary conditions	35
3.4.2	Pore water pressure u	36
3.4.3	Settlement s	38
3.4.4	Degree of consolidation U_m	39
3.4.5	Dimensionless consolidation time T_v	40
3.4.6	Coefficient of consolidation c_v	40
3.5	Multi-dimensional and non-linear consolidation	43
3.5.1	Multi-dimensional consolidation	44
3.5.2	Non-linear constitutive approaches	44
3.5.3	Further enhancements in consolidation theory	45
3.6	Summary	46
4	Consolidation under cyclic loading	47
4.1	Mathematical approaches in literature	47
4.2	Analytical solution for consolidation under cyclic loading of haversine form	48
4.2.1	Pore water pressure u	50
4.2.2	Settlement s	54
4.3	Experimental studies in literature	58
4.4	Summary	61
5	Oedometer device	63
5.1	Introduction	63
5.2	Design and construction	64
5.2.1	General construction	64
5.2.2	Vertical stress and deformation measurement	66
5.2.3	Oedometer ring and radial stress measurement	68
5.2.4	Drainage system and pore pressure measurement	73
5.3	Calibration	77
5.3.1	Calibration with steel	77

5.3.2	Calibration with water	78
5.3.3	Calibration with clay	82
5.4	Summary	83
6	Materials and methods	85
6.1	Materials	85
6.1.1	General	85
6.1.2	Spergau kaolin clay	85
6.1.3	Onsøy clay	95
6.1.4	Summary of material properties of studied clays	101
6.2	Experimental programme	102
6.2.1	Monotonic oedometer tests	102
6.2.2	Cyclic oedometer tests	103
6.3	Sample preparation and testing procedure	108
6.3.1	Soil material preparation	108
6.3.2	Sample installation	109
6.3.3	Installation procedure	110
6.4	Summary	112
7	Experimental study on consolidation under monotonic loading	117
7.1	Deformation behaviour	117
7.1.1	General one-dimensional compression behaviour	117
7.1.2	Friction	120
7.1.3	Consolidation settlements	123
7.1.4	Coefficient of consolidation c_v	126
7.1.5	Development of stiffness and permeability	128
7.1.6	Secondary compression	131
7.2	Pore water pressure dissipation	132
7.3	Comparison to analytical solution	138
7.4	Development of radial stress	140
7.5	Summary	143
8	Experimental study on cyclic consolidation	147
8.1	Introduction	147
8.2	Friction	148
8.3	Cyclic deformation behaviour	149
8.3.1	General	149

8.3.2	Final mean deformation e_{ss}	152
8.3.3	Rate of consolidation	153
8.3.4	Amplitude of deformation Δe	157
8.3.5	Development of equivalent stiffness \bar{E}_s	159
8.3.6	Permeability from cyclic c_v and equivalent stiffness	162
8.3.7	Deformation in the stationary state	162
8.4	Cyclic pore water pressure dissipation	163
8.4.1	Maximum pore water pressure and rate of pore water pressure dissipation	165
8.4.2	Pore pressure amplitude Δu	167
8.5	Cyclic stress-strain behaviour	169
8.6	Comparison to analytical solution	170
8.7	Numerical modelling	175
8.7.1	Verification of the analytical solution by linear-elastic FEA	175
8.7.2	Numerical analysis using hierarchical, constitutive models	176
8.7.3	Conclusions	181
8.8	Development of radial stress	181
8.9	Summary and discussion	182
9	Phase shift in cyclic consolidation	187
9.1	Introduction	187
9.2	Analytical solution from consolidation equation	188
9.3	State of the art - Phase shift in conduction phenomena	189
9.4	Experimental analysis	190
9.4.1	Phase shift of deformation $\bar{\psi}_e$	190
9.4.2	Phase shift of pore water pressure $\bar{\psi}_u$	191
9.4.3	Comparison to analytical solution	193
9.5	Testing concept: from phase shift to material characteristics	195
9.5.1	Motivation	195
9.5.2	Suggested concept and validation strategy	196
9.6	Summary	198
10	Summary and conclusions	199
10.1	Conclusions	199
10.2	Recommendations for further studies	202
	References	202

List of Figures

2.1	Modes of particle association, modified after van Olphen (1977).	7
2.2	Time-dependent compression of a fine-grained soil, modified after Casagrande and Fadum (1940).	10
2.3	Compression curve of a fine-grained soil, after Schofield and Wroth (1968).	12
2.4	Compression curves for structured and destructured clay: (a) experimental curve for Onsøy clay, (b) Scematic illustration of compression of a structures clay, modified after Mitchell and Soga (2005).	13
2.5	Intrinsic compression line (ICL) and sedimentation compression line (SCL) (Burland, 1990).	15
2.6	In situ stress states for different clay types (Chandler et al., 2004).	15
2.7	Definition of the coefficient of secondary compression.	19
2.8	Ageing effect due to secondary compression, modified after Bjerrum (1967).	21
2.9	Rate dependency in CRS tests - typical CRS test data on Batiscan clay (Leroueil et al., 1985).	21
2.10	Strain rate ranges in laboratory tests and in situ (Leroueil, 2006).	21
2.11	Temperature dependency in CRS tests - test data on Lulea clay (Eriksson, 1989).	22
2.12	K_0 versus void ratio for kaolin clay in lower stress / higher void ratio range (Ting et al., 1994).	24
3.1	Definition of oedometric boundary conditions.	36
3.2	Analytical solution: normalised pwp (a) over sample height at different consolidation times, (b) versus T_v at different positions over the sample height.	37
3.3	Influence of (a) Skempton B coefficient and (b) consolidation coefficient on the excess pore water dissipation curves the analytical solution of the consolidation equation.	37

3.4	Influence of (a) Skempton B coefficient and (b) consolidation coefficient on the normalised settlement curves from the analytical solution of the consolidation equation.	39
3.5	Determination of t_{50} , $t_{22.14}$ and $\sqrt{t_{90}}$ according to Casagrande and Fadum (1940), Robinson and Allam (1996) and Taylor (1942).	42
4.1	Boundary value problem with definition of coordinate system for the two analytical solutions by Müthing et al. (2016b) and Verruijt (2014).	51
4.2	Pore water pressure versus time from the analytical solution for linear-elastic, one-dimensional consolidation under haversine and monotonic loading, computed with $\hat{\sigma}_v = \Delta\sigma_v = 100 \text{ kN/m}^2$, $d = 120s$, $h_0 = 20 \text{ mm}$, $c_v = 1 \cdot 10^{-7} \text{ m}^2/\text{s}$	51
4.3	Phase shift between pore water pressure and vertical stress, from the analytical solution for linear-elastic, one-dimensional consolidation under haversine loading, computed with $\hat{\sigma}_v = 100 \text{ kN/m}^2$, $d = 120s$, $h_0 = 20 \text{ mm}$, $c_v = 1 \cdot 10^{-6} \text{ m}^2/\text{s}$	53
4.4	Pore water pressure over sample height in the first cycle and stationary state, from the analytical solution for cyclic loading, computed with $\hat{\sigma}_v = 100 \text{ kN/m}^2$, $d = 120s$, $c_v = 1 \cdot 10^{-7} \text{ m}^2/\text{s}$, $h_0 = 20 \text{ mm}$	53
4.5	Influence of T_0 on the excess pore water dissipation from the analytical solution for consolidation under cyclic loading.	55
4.6	Normalised settlements versus time, from the analytical solution for linear-elastic, one-dimensional consolidation under haversine and monotonic loading, computed with $\hat{\sigma}_v = \sigma'_v = 100 \text{ kN/m}^2$, $d = 120s$, $h_0 = 20 \text{ mm}$, $c_v = 1 \cdot 10^{-7} \text{ m}^2/\text{s}$	56
4.7	Phase shift between normalised settlement and vertical stress from the analytical solution for linear-elastic, one-dimensional consolidation under haversine loading, computed with $\hat{\sigma}_v = 100 \text{ kN/m}^2$, $d = 120s$, $h_0 = 20 \text{ mm}$, $c_v = 1 \cdot 10^{-6} \text{ m}^2/\text{s}$	56
4.8	Influence of T_0 on the normalised settlement amplitude from the analytical solution for consolidation under cyclic loading.	58
4.9	(a) Consolidometer cell and (b) main testing results from repeated loading tests (Elgohary, 1973).	59
4.10	(a) Inter connected consolidation apparatus and (b) main results from (Kono, Ochiai, Omine and Tsukamoto, 1995).	60
5.1	Sketch (left) and photograph (right) of the modified oedometer device.	65

5.2	UTS control stand: photograph with loading frame (centre), central processing unit (right side) and data acquisition (left side).	66
5.3	Bottom part of the oedometer device.	67
5.4	Stainless steel oedometer ring with applied strain gauges - top and front view.	68
5.5	Stress distribution over the sample height for fixed-ring type and floating-ring type, modified after Muhs and Kany (1954).	69
5.6	Drainage system of the oedometer cell (left) with photos of filter plates (top) and drainage slots on oedometer bottom (bottom).	74
5.7	Photograph and sketch of the piezo-resistive pressure transducer (KELLER, 2007).	75
5.8	Implemented ppt in oedometer bottom.	75
5.9	De-airing of filter plates in desiccator.	76
5.10	Volume measuring unit.	76
5.11	Stress-deformation diagram from calibration with steel dummy under repeated loading-unloading.	78
5.12	Vertical stress diagram from calibration with a steel dummy.	79
5.13	Vertical stress and friction from calibration with water.	80
5.14	(a) Frictional stress and (b) radial stress over vertical stress, from calibration with water.	81
5.15	(a) Vertical stress and pore-water pressure versus time, (b) pore water pressure versus vertical stress, from calibration with water.	82
5.16	Pore-water pressure over time, from calibration with clay.	83
5.17	Stress-dependent compression, from calibration with water and clay under repeated loading.	83
6.1	Grain size distribution of Spergau kaolin clay.	87
6.2	Plasticity diagram for Spergau kaolin clay according to DIN:18196 (2006).	88
6.3	Diagrammatic sketch of tetrahedral and octahedral units, modified after Grim (1968): (a) single silica tetrahedron (left), sheet of tetrahedra arranged in a hexagonal network (right), (b) single octahedron (left), dioctahedral sheets (right) (Baille, 2014).	91
6.4	Diagrammatic sketch and charge distribution of kaolinite, modified after Grim (1968): (a) diagrammatic sketch of the kaolinite structure, (b) charge distribution on kaolinite (Baille, 2014).	93

6.5	(a) ESEM microphotographs of Spergau kaolin powder, (b) ESEM microphotographs and (c) cyro-BIB-SEM microphotograph of Spergau kaolin slurry ($w \approx 1.1w_L$).	94
6.6	Onsøy block sample (left) with inhomogeneities (right): (a) sand inclusions and (b) shell fragments, after (Lieske, 2015).	96
6.7	Grain size distribution of Onsøy clay.	97
6.8	Plasticity diagram for Onsøy clay according to DIN:18196 (2006).	98
6.9	Haver-sine loading function.	104
6.10	Approximation of haver-sine loading in the experiment.	105
6.11	Kaolin material preparation: from clay pellets (left) to powder (middle) and slurry (right).	109
6.12	Sample installation for reconstituted samples: (a) equipment, (b) sample installation using spatula, (c) installed sample.	111
6.13	Sample installation for natural samples in three steps.	113
6.14	Stepwise assembling of the oedometer device: step 1-4.	114
6.15	Stepwise assembling of the oedometer device: step 5 and 6.	115
7.1	Compression behaviour of (a) kaolin clay and (b) natural and reconstituted Onsøy clay.	118
7.2	Compression behaviour of natural and reconstituted Onsøy clay - comparison to literature from Lunne et al. (2003).	119
7.3	I_v - σ'_v relationship relative to ICL and SCL for Kaolin and natural and reconstituted Onsøy clay.	120
7.4	Development of friction with respect to (a) vertical stress, (b) deformation and (c) consolidation time in the load step $200 \rightarrow 400 \text{ kN/m}^2$.	121
7.5	Time-dependent deformation during compression (left) and unloading (right) load steps from tests on (a) Spergau kaolin clay, (b) reconstituted and (c) natural Onsøy clay.	125
7.6	(a) Stress- and void-ratio-dependent consolidation coefficient c_v for kaolin clay, and stress-dependent consolidation coefficient c_v for (b) reconstituted and (c) natural Onsøy clay.	126
7.7	Time-dependent deformation of Spergau kaolin clay during compression and unloading for different stress paths.	128
7.8	Effective stress dependent stiffness E_s of (a) kaolin and (b) Onsøy clay.	129
7.9	Void ratio dependent permeability of (a) kaolin, (b) reconstituted and natural Onsøy clay.	130

7.10	(a) Coefficient of secondary compression and (b) C_α/C_C over vertical effective stress for kaolin and Onsøy clay.	131
7.11	Pore water dissipation during (a) compression and (b) unloading load steps from tests Spergau kaolin clay.	132
7.12	Pore water dissipation during compression and unloading load steps from tests on (a) reconstituted and (b) natural Onsøy clay.	133
7.13	(a) Maximum pore pressure versus c_v and (b) time delay versus c_v , from tests on kaolin clay.	134
7.14	Development of pore water pressure with dimensionless consolidation time and increasing degree of consolidation.	135
7.15	Pore water pressure dissipation with varying saturation for a kaolin clay sample (scenario 1: $p_0 = 10 \text{ kN/m}^2$ $k = 1 \cdot 10^{-8} \text{ m/s}$, $E_s = 100 \text{ kN/m}^2$, $h = 0.02 \text{ m}$; scenario 2: $p_0 = 400 \text{ kN/m}^2$ $k = 5 \cdot 10^{-9} \text{ m/s}$, $E_s = 5000 \text{ kN/m}^2$, $h = 0.015 \text{ m}$).	138
7.16	(a) Degree of consolidation and (b) pore water pressure dissipation - comparison between experimental data (test MK04) and analytical solution using the hybrid model.	139
7.17	Development of radial stress from consolidation of kaolin clay: (a) Radial stress versus consolidation time in a single load-step $100 \rightarrow 200 \text{ kN/m}^2$, (b) radial stress versus effective stress (c) radial stress versus consolidation time - comparison to Gareau et al. (2006).	142
7.18	Radial effective stress versus vertical effective stress with respect to K_0 for (a) kaolin clay and (b) Onsøy clay.	143
8.1	Development of friction in the cyclic oedometer tests: (a) vertical stress versus time, (b) friction versus number of loading cycle. (test CK08: $d = 120 \text{ s}$, $\hat{\sigma}_v = 100 \text{ kN/m}^2$)	148
8.2	Deformation behaviour of kaolin clay under haversine loading: (a) void ratio versus time, (b) void ratio amplitude versus time. (test CK08: $d = 120 \text{ s}$, $\hat{\sigma}_v = 100 \text{ kN/m}^2$)	150
8.3	Deformation behaviour of kaolin clay under haversine loading: (a) influence of load period d , (b) influence of load amplitude $\hat{\sigma}_v$ (tests CK13,19,11,14).	151
8.4	Compression behaviour of (a) kaolin clay and (b) natural and reconstituted Onsøy clay under cyclic loading ($d = 120 \text{ s}$).	153
8.5	Influence of load period on the compression of kaolin under cyclic loading, tested at $\hat{\sigma}_v = 100 \text{ kN/m}^2$	154

8.6	Normalised time-dependent settlements in the first loading cycle of kaolin clay ($\hat{\sigma}_v=100 \text{ kN/m}^2$).	154
8.7	Normalised time-dependent settlements versus time - comparison to monotonic loading tests for varying (a) load period and (b) load amplitude from cyclic loading tests on kaolin clay.	154
8.8	Normalised time-dependent settlements of (a) natural and (b) reconstituted Onsøy clay under cyclic loading with varying load amplitude $\hat{\sigma}_v$	155
8.9	c_v versus (a) load period, tested at $\hat{\sigma}_v=100 \text{ kN/m}^2$, and (b) load amplitude, tested at $d=120 \text{ s}$, from cyclic consolidation tests on kaolin clay and (c) on Onsøy clay.	156
8.10	Dependency of final void ratio amplitude Δe_{ss} on (a) load period ($\hat{\sigma}_v=100 \text{ kN/m}^2$) and (b) load amplitude ($d=120 \text{ s}$) from cyclic consolidation tests on kaolin clay and (c) Onsøy clay.	158
8.11	Dependency of η_e on (a) load period, tested at $\hat{\sigma}_v=100 \text{ kN/m}^2$, and (b) load amplitude, tested $d=120 \text{ s}$, from cyclic consolidation tests on kaolin clay and (c) Onsøy clay.	159
8.12	(a) Development ε_v over time during cyclic consolidation of kaolin clay, (b) development of $\bar{E}_{s,n}$ over number of loading cycles n (test CK08: $d = 120 \text{ s}$, $\hat{\sigma}_v = 100 \text{ kN/m}^2$).	160
8.13	Equivalent stiffness \bar{E}_s versus (a) load period, tested at $\hat{\sigma}_v=100 \text{ kN/m}^2$, (b) load amplitude, tested at $d=120 \text{ s}$, from cyclic consolidation tests on kaolin clay and (c) Onsøy clay.	161
8.14	Void-ratio dependent permeability k computed from cyclic consolidation tests for kaolin and Onsøy clay.	162
8.15	\bar{C}_α from cyclic loading tests on kaolin and Onsøy clay - dependency on (a) load period (b) load amplitude.	163
8.16	Pore water dissipation of kaolin clay under haversine loading: (a) normalised excess pore water pressure versus time, (b) normalised pore water pressure amplitude versus time (test CK08: $d = 120 \text{ s}$, $\hat{\sigma}_v = 100 \text{ kN/m}^2$).	164
8.17	Pore water pressure dissipation of kaolin clay under haversine loading: (a) influence of load period d , (b) influence of load amplitude $\hat{\sigma}_v$ (tests CK13,19,11,14).	165
8.18	Pore water dissipation curves from monotonic and cyclic oedometer test.	166
8.19	Maximum pore water pressure versus loading characteristics.	166
8.20	Pore water dissipation of natural and reconstituted Onsøy clay under cyclic loading with an amplitude of $\hat{\sigma}_v = 50 \text{ kN/m}^2 \leq \sigma'_y$	167

8.21	Pore water pressure amplitude Δu versus (a) load period, tested at $\hat{\sigma}_v=100 \text{ kN/m}^2$ and (b) load amplitude, tested at $d=120 \text{ s}$ from cyclic consolidation tests on kaolin clay and (c) Onsøy clay.	168
8.22	Dissipation factor η_u versus (a) load period, tested at $\hat{\sigma}_v=100 \text{ kN/m}^2$ and (b) load amplitude, tested at $d=120 \text{ s}$ from cyclic consolidation tests on kaolin clay and (c) Onsøy clay.	168
8.23	(a) Total stress, (b) pore water pressure and (c) effective stress versus strain diagram for cyclic consolidation of kaolin clay (test CK08: $d = 120 \text{ s}$, $\hat{\sigma}_v = 100 \text{ kN/m}^2$).	169
8.24	Consolidation deformation of kaolin clay under cyclic loading - comparison between experiment and analytical solution.	171
8.25	Pore water pressure dissipation of kaolin clay during consolidation under cyclic loading - comparison between experiment and analytical solution. . .	172
8.26	Development of pore water pressure amplitude Δu - comparison between results from (a) analytical solution and (b),(c) experiment.	173
8.27	Development of deformation amplitude Δe - comparison between results from (a) analytical solution and (b),(c) experiment.	173
8.28	Development of (a) pore water pressure and (b) deformation amplitude with increasing T_0 - comparison between experiment and analytical solution. 174	
8.29	Pore water pressure over sample height for different loading cycles (at time of maximum loading) from the numerical simulation and analytical solution, according to (Müthing et al., 2016b).	176
8.30	Development of the normalised excess pore-water pressure over the number of loading cycles from the numerical simulation of oedometer tests under cyclic loading on natural Onsøy clay ($\hat{\sigma}_v = 200 \text{ kN/m}^2$, $d = 120 \text{ s}$) - using different constitutive models: (a) MCC, (b) SANICLAY, (c) SANICLAY D, (d) SANICLAY BSP+D Barciaga et al. (2017).	179
8.31	Development of the normalised settlement over the number of loading cycles from the numerical simulation of oedometer tests under cyclic loading on natural Onsøy clay using different constitutive models ($\hat{\sigma}_v = 200 \text{ kN/m}^2$, $d=120 \text{ s}$) (Barciaga et al., 2017).	180
8.32	Development of (a) pore water pressure amplitude and (b) deformation amplitude over the number of loading cycles from the numerical simulation of oedometer tests under cyclic loading on natural Onsøy clay using different constitutive models ($\hat{\sigma}_v = 200 \text{ kN/m}^2$, $d=120 \text{ s}$).	180

8.33	Development of (a) radial stress σ_{rad} and (b) normalised radial stress $\sigma_{\text{rad}}/\sigma_v$ during cyclic consolidation. (test CK08: $d = 120$ s, $\hat{\sigma}_v = 100$ kN/m ²) . . .	181
9.1	Phase shift between applied vertical stress σ and the pore water pressure u in stationary state, $\psi_{u,\text{ss}}$, versus dimensionless loading time T_0	189
9.2	Deformation behaviour of kaolin clay under haversine loading: (a) void ratio versus time, (b) void ratio amplitude versus time. (test CK08: $d = 120$ s, $\hat{\sigma}_v = 100$ kN/m ²)	191
9.3	Deformation phase shift in stationary state $\bar{\psi}_{e,\text{ss}}$ versus (a) load period, tested at $\hat{\sigma}_v=100$ kN/m ² , (b) load amplitude, tested at $d=120$ s, (c) normalised loading time T_0 , from cyclic consolidation tests on kaolin clay.	192
9.4	Deformation behaviour of kaolin clay under haversine loading: (a) void ratio over time, (b) void ratio amplitude over time	193
9.5	Pore water pressure phase shift in stationary state $\bar{\psi}_{u,\text{ss}}$ versus (a) load period, tested at $\hat{\sigma}_v=100$ kN/m ² , (b) load amplitude, tested at $d=120$ s, (c) normalised loading time T_0 , from cyclic consolidation tests on kaolin clay.	193
9.6	Pore water pressure phase shift - comparison between (a) experimental results $\bar{\psi}_{u,\text{ss}}$ and (b) analytical solution $\psi_{u,\text{ss}}$	194
9.7	Concept of deriving consolidation parameters from the of phase shift between applied vertical stress σ and the pore water pressure u in stationary state of cyclic consolidation by semi-analytical fit.	196
9.8	Concept of deriving consolidation parameters from the of phase shift between applied vertical stress σ and the pore water pressure u in stationary state of cyclic consolidation by semi-analytical fit.	197
10.1	Prospect facilities for measuring the pore water pressure distribution over the sample height: (a) large scale oedometer tests, (b) adaption of the existing oedometer cell according to Schudy (2015).	203

List of Tables

2.1	Classification of clay sensitivity.	15
2.2	$K_0(\varphi')$ equations with resulting values for Kaolin, cf. Ting et al. (1994). . .	23
6.1	Comparison of Atterberg limits and activities of Spergau kaolin with the range for relevant kaolinites from literature (Mitchell and Soga, 2005). . .	88
6.2	Quantitative mineralogical composition of Spergau kaolin clay after Baille (2014).	90
6.3	Chemical composition of Spergau kaolin clay after Baille (2014).	90
6.4	Specific surface area of Spergau kaolin clay after Baille (2014).	92
6.5	Exchangeable cations and CEC of Spergau kaolin clay after Baille (2014).	92
6.6	Onsøy block sample - natural state characteristics.	96
6.7	Mineralogical composition of Onsøy clay according to Kaufhold et al. (2016).	99
6.8	Chemical composition of Onsøy clay according to Kaufhold et al. (2016).	99
6.9	Exchangeable cations and CEC of Onsøy clay after Lieske (2015) and Kaufhold et al. (2016).	100
6.10	Summary of the main material characteristics of the clays studied.	101
6.11	Experimental programme: Monotonic oedometer tests.	103
6.12	Experimental programme: Cyclic oedometer tests on kaolin clay.	106
6.12	Experimental programme: Cyclic oedometer tests on kaolin clay.	107
6.13	Experimental programme: Cyclic oedometer tests on Onsøy clay.	108
7.1	Comparison of compression and recompression indices of Spergau kaolin and Onsøy clay from experimental results and literature.	119
7.2	Parameters for computing of monotonic consolidation with analytical solution using the hybrid model.	140
8.1	Computing parameters and consolidation characteristics derived from the analytical solution for consolidation under haversine cyclic loading.	170
8.2	Constitutive parameters for natural Onsøy clay (Barciaga et al., 2017).	178

1 Introduction

1.1 Motivation

Cyclic soil behaviour plays an important role in a multitude of geotechnical and geoenvironmental applications as cyclic loading occurs frequently caused by earthquake shaking, traffic or wind and wave loading. The consideration of cyclic loading effects finds increasing attention nowadays. This particularly holds true for structures, which are of civil importance and involve high investment costs. Relevant examples from engineering practice are the dimensioning of on- and offshore foundation systems, the analysis of the soil behaviour in mechanised tunnelling processes as well as the evaluation of loading histories related to deep excavation walls or the filling and discharging of dams. Sophisticated calculation approaches are applied within the design process of these boundary value problems, as e.g. the high-cycle accumulation model (HCA) proposed by Niemunis et al. (2005).

Soils under drained and undrained cyclic loading have been studied intensively in the last decades. Thereby, the stress-strain behaviour of granular material under cyclic and dynamic loading, strain-accumulation as well as liquefaction phenomena were in the focus of experimental research. To name just a few, relevant studies can be found in (Brown et al., 1975; Castro, 1975; Mohamad and Dobry, 1987; Robertson and Wride, 1998; Bouckovalas et al., 2003; Wichtmann, 2005; Wichtmann and Triantafyllidis, 2016*a,b*). A recent, very detailed study on the general soil behaviour under cyclic loading can be found in Wichtmann (2016). However, most of these studies and calculation models analyse undrained stress paths, where cyclic loading leads to a continuous generation of excess pore water pressure, or completely drained stress paths, neglecting the occurrence of pore water pressure. Neither of these assumption is realistic when fine-grained, low-permeable soils under low-frequency loading are involved. In these cases, the dissipation of excess pore water pressure becomes relevant and the cyclic consolidation of the soil needs to be considered.

The theory of consolidation was originated by Terzaghi (1923) and is often denoted as the cornerstone of modern soil mechanics. As the compressibility and the time-dependent development of deformations are of significant importance for the dimensioning of the majority of geotechnical structures, the consolidation behaviour of soils was studied intensively ever since then. Within this research also numerous studies analysing consolidation under non-constant loading can be found. In the 50s to 70s of the past century non-constant loading was introduced to Terzaghi's one-dimensional consolidation theory for the first time (Schiffman, 1958; Wilson and Elgohary, 1974; Olson, 1977). Since then the development of consolidation theory under cyclic loading followed mainly three enhancements. These are the implementation of constitutive non-linearities, the implementation of different loading types and of various initial and boundary conditions. As Terzaghi's fundamental theory is based on a series of linearisations and simplifying assumptions, a multitude of research studies has been performed to prove whether or not these linearisations are acceptable. Due to the more complex stress-strain-paths, this aspect of consolidation theory is of particular importance for the consideration of non-constant loading tests. Therefore, mathematical work has been performed to introduce enhancements and non-linearities to better fit the processes in reality (Baligh and Levandoux, 1978; Favaretti and Soranzo, 1995; Zhuang and Xie, 2005; Conte and Troncone, 2006; Xie et al., 2006; Geng et al., 2006; Cai et al., 2007; Toufigh and Ouria, 2008; Xie et al., 2008; Zimmerer, 2011; Xie et al., 2014). Moreover, substantial contributions have been made to introduce different loading types to the consolidation theory (Zhuang and Xie, 2005; Geng et al., 2006; Cai et al., 2007; Yazdani and Toufigh, 2012) and to account for different boundary conditions, as e.g. multi-layer approaches, partial saturation and simultaneous hydraulic-mechanical loading (Miao et al., 2010; Hsu and Liu, 2013; Ni et al., 2013; Qin et al., 2008).

However, besides this broad range of mathematical studies, only a limited number of experimental studies on consolidation under cyclic loading is available worldwide (Elgohary, 1973; Fujiwara et al., 1985; Kono, Ochiai, Omine and Tsukamoto, 1995; Rahal and Vuez, 1998; Vuez et al., 2000; Conte and Troncone, 2006; Toufigh and Ouria, 2009; Porhoseini et al., 2014; Abbaspour, 2014). These studies are partly difficult to access and to some extent contradictory. Moreover, non of them comprises a holistic analysis of the cyclic consolidation process analysing systematically the influence of loading conditions and material characteristics on the cyclic consolidation behaviour. To fill this gap and to gain a better, holistic understanding of the cyclic consolidation process, is the motivation of the present study.

1.2 Objectives

The main objective of the present study is to analyse the behaviour of fine-grained soils during consolidation under cyclic loading. Hereunto, the influence of material characteristics, loading and boundary conditions on the state of deformation and stresses in the soil and their time-dependent development is to be analysed. The second objective, is to evaluate available mathematical models for the cyclic consolidation process based on experimental findings. The fine-grained soils used as exemplary soil material within this study are Spergau kaolin and marine Onsøy clay. To achieve these objectives, the following tasks are accomplished:

- Design, construction and validation of a new oedometer cell for testing soft clay under cyclic loading, which enables the measurement of pore water pressure and radial stress.
- Experimental analysis of the consolidation behaviour under monotonic loading.
- Experimental analysis of the consolidation behaviour under cyclic loading.
- Assessment of the influence of material characteristics, loading and boundary conditions on the state of stresses and deformation during the cyclic consolidation process.
- Analysis of the differences between available mathematical models (analytical solutions, numerical models) and the experimental results.
- Analysis of the effect of phase shift between applied stress and pore water pressure in the cyclic consolidation process. Assessment of its usability for the determination of soil characteristics.

1.3 Layout of the thesis

The present thesis is composed of ten chapters.

The **first chapter** gives an introduction to the present study. It illustrates the motivation for this research and states the objectives and outline of this particular study.

In the **second chapter** the state of the art on compressibility and permeability is summarised.

The **third chapter** focuses on the consolidation under monotonic loading. The consolidation theories of Terzaghi and Biot are introduced and the analytical solution for the consolidation problem is derived.

Chapter four deals with the consolidation under cyclic loading. Mathematical and experimental approaches in literature are reviewed and an analytical solution for the consolidation process under cyclic loading of haversine form is derived and evaluated.

Chapter five introduces the new oedometer cell, which was designed and constructed to perform the experimental consolidation study. The calibration tests performed for the validation of the testing equipment are demonstrated.

Chapter six is divided into three sections. In the first section the clay materials used in the experimental study are characterised regarding their basic properties. The second section gives details on the experimental programme comprising oedometer tests under monotonic as well as cyclic loading. The last section of this chapter deals with the details of sample preparation and testing procedure.

Chapter seven presents the results derived from monotonic oedometer tests and compares them to the analytical solution. The compression behaviour, time dependent settlements and pore water pressure dissipation are evaluated together with the analysis of consolidation characteristics, i.e. stiffness and hydraulic permeability as well as the development of radial stress.

Chapter eight comprises the experimental study and analysis of the cyclic oedometer tests. Firstly, the consolidation behaviour is characterised by determination of time-dependent deformation and pore water pressure. Based on these findings, the influence of material characteristics, loading and boundary conditions on the cyclic consolidation behaviour is analysed and compared to the analytical solution and numerical modelling approaches.

Chapter nine deals with the special effect of phase shift in cyclic consolidation, comprising an analytical as well as experimental analysis. A testing concept to derive consolidation parameters from the phase shift measurement is suggested.

The last chapter (**Chapter ten**) summarizes the findings of the present study by presenting the conclusions drawn based on the obtained results. Suggestions and recommendations for further research in this field concludes this thesis.

2 Compressibility and permeability of fine-grained soils

The structure, compressibility and permeability are three of the key characteristics identifying a soil's volume change and conduction behaviour. This chapter summarises the state of the art on these soil characteristics. Thereby, the basic knowledge on clay structure, one-dimensional compression behaviour and hydraulic permeability of fine-grained soils is covered.

2.1 Soil structure

Although soil is a multi-phase material consisting of discrete soil particles, in geotechnical engineering it is usually analysed as a continuum. However, the size and shape of the soil particles as well as their arrangement and interaction forces on the microscopic level strongly influence their macroscopic behaviour. Therefore, a distinct analysis of the soil structure and its change during compression helps to understand the ongoing processes. When referring to clay, the term *soil structure* following Mitchell and Soga (2005) combines *fabric* and *bonding* of the soil particles. Thereby, the term *fabric* describes the arrangement of soil particles, particle groups and the distribution of the pore space. The term *bonding* on the other hand refers to the acting interparticle forces connecting the particles forming the soil skeleton, which are not of frictional kind.

2.1.1 Clay fabric

Clays minerals consist of clay layers (two-sheet or three-sheet layers) stacking to form a clay particle. While the clay particle's surface (face) is generally charged negatively, the edges can be positively or negatively charged. Several particles together form an aggregate (Bergaya and Lagaly, 2013). The arrangement of these particles and/or aggregated is

defined as the clay fabric. According to van Olphen (1977) the following modes of particle association are defined:

1. Dispersed
No face-to-face particle association is present.
2. Aggregated
The particles form aggregates in a face-to-face particle association.
3. Flocculated
Either an edge-to-edge (EE) or an edge-to-face (EF) association between aggregates is formed.
4. Deflocculated
No association between single particles or aggregates is present.

Figure 2.1 illustrates the different possible combinations of particle association.

2.1.2 Methods for clay fabric investigation

For the investigation of fabric nowadays direct as well as indirect measurement techniques are available. Among the direct methods, microscopy and mercury intrusion porosimetry (MIP) are the most common techniques, while wave propagation and electrical as well as thermal conductivity measurement have to be mentioned as indirect methods.

With ongoing precision and computational advance, microscopy techniques allow for a precise optical study of particles, particle arrangement and pore space distribution. Among them scanning electron microscopy (SEM), by the use of an electron beam scanning the soil surface, provides a resolution with which clay particles can be analysed. While a standard SEM has the drawback, that samples can only be tested under dry conditions, the environmental scanning electron microscopy (ESEM) allows for detection of signals within a gaseous environment in the sample chamber and thus enables the analysis of humid samples. This has the advantage that probable structure changes due to the drying process during sample preparation can be minimized. A novel technique to avoid this problem, is the cryo-BIB-SEM method. By this technique the samples are rapidly frozen by liquid nitrogen to avoid the crystallisation of water during a slower freezing process. Afterwards the sample is cut and its surface is polished by the use of Broad Ion Beam (BIB) before analysed in the SEM (Desbois et al., 2014; Schmatz, Urai, Desbois, Berg and Ott, 2015; Schmatz, Berg, Urai and Ott, 2015).

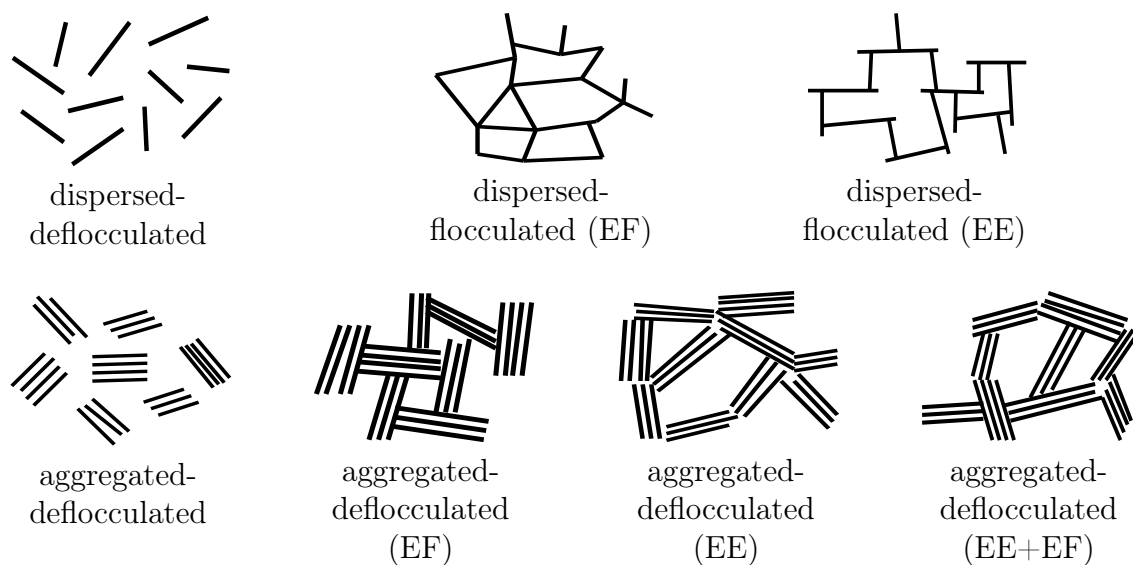


Figure 2.1: Modes of particle association, modified after van Olphen (1977).

The mercury intrusion porosimetry allows for the determination of the pore size distribution. Hereunto, mercury as a non-wetting fluid is intruded into the pore space of a dried specimen by stepwise pressure increase. By the measurement of injected mercury volume and the relation between intrusion pressure u_p and the pore entrance radius given in the Washburn's equation, a pore size distribution can be approximated. Details on this method can be found in Diamond (1970) and Sridharan (1971). Furthermore, a comparative study of fabric investigation methods also accounting for the methods' limitations is given in Baille (2014) and Klaver et al. (2015).

2.1.3 States of clay structure

The initial, in situ structure of a clay is influenced by various factors. The most significant ones can be divided into compositional factors (mineralogy, particle size and shape, chemistry / salinity of the pore water) and environmental factors (pressure, temperature, time and rate of deposition / compression) acting during the formation of the clay.

Modification of the initial clay structure may occur due to postformational factors, which may be chemical processes (leaching, precipitation, cementation, weathering, mineralogical transformation and effects of pressure, temperature and time) and/or physical processes (loading/unloading, shearing, consolidation, shrinking/swelling, drying/wetting, freezing/thawing, seepage and effects of pressure, temperature and time) (Mitchell and Soga, 2005).

In soil mechanics the current state of the clay structure and the presence of a specific fabric and bonding has a significant influence for instance on the permeability and the compression behaviour. One specific combination found mainly in clays deposited under marine conditions is the so-called *cardhouse structure*, which is an edge-to-face arrangement forming an open fabric. Soils exhibiting a similar structure in their natural state are often referred to as *structured soils*.

According to Leroueil et al. (1985), soils can be present in the following four structure states:

1. intact state:

The intact state characterises the original state of a soil formed by geological processes as e.g. deposition environment, consolidation, erosion, thixo-tropic hardening, leaching, weathering etc. - referred to as *natural state* in the following.

2. destructured state:

The destructured state characterises the state of a former intact soil subjected to volumetric or shear deformation of such magnitude that the original clay structure is broken.

3. remoulded state:

The remoulded state describes the state of soil in which it has experienced sufficient mechanical energy, e.g. through mixing, to reduce its strength to a minimum.

4. resedimented state:

The resedimented state a soil reaches after remoulding, mixing to a slurry, depositing and self-weight consolidation.

However, in the present study only two soil states are considered: the natural, structured soil state and the soil state, where the initial structure has been destroyed. To differentiate between these two, the concept and terminology following Burland (1990) is used. While the intact soil state encountered in field is referred to as *natural*, the properties of the fully *reconstituted* material are referred to as *intrinsic* soil properties. A reconstituted clay is defined as a clay, which has been mixed at a water content equal to or greater than liquid limit ($w \geq w_L$) without prior air or oven drying, usually with $w_L \leq w \leq 1.5 w_L$. The term intrinsic is chosen to account for the fact, that these properties are inherent to the soil and independent of its natural state.

2.2 One-dimensional compression of soils

The compression behaviour of soils plays a significant role in all field of geotechnical and geoenvironmental engineering and was hence studied extensively within modern soil mechanics.

In general, a soil consists of three phases: solid particle, water and air phase. However, for the sake of simplicity within the present study only saturated soils are considered. That implicates, that the soil system reduces to a two-phase system comprising the soil particle and pore water phase. The presence of air in the soil system is only considered in terms of very small air bubbles occluded in the water phase reducing its stiffness. The presence of a continuous air phase is neglected within this study.

The compression of a saturated two-phase soil volume due to changes in its stress state is caused by three different processes:

- compression of the phases, i.e. compression of the soil particles and/or water
- expulsion of pore water
- compaction of the soil skeleton caused by relocation of the soil particles and out-flow of intra-particle water

In practical, geotechnical engineering settlements resulting from changes in the stress state are usually categorised according to these three phenomenological approaches:

1. initial settlement (initial compression):
Compression of the soil volume, which occurs almost immediately after load application, caused by elastic deformation of the two phases.
2. consolidation settlement (primary compression):
Time-dependent compression of the soil volume caused by the time-delayed expulsion of water from the pore space.
3. creep settlement (secondary compression):
Time-dependent compression of the soil skeleton due to "sliding at interparticle contacts, expulsion of water from microfabric elements, and rearrangement of adsorbed water molecules and cations into different positions" (Mitchell and Soga, 2005).

Figure 2.2 shows a typical time-settlement curve for a fine-grained soil with the apportionment of settlements into initial, consolidation and creep settlement with respect to time according to Casagrande and Fadum (1940). Although, the apportionment of settlements seems reasonable and is widely accepted in geotechnical engineering, of cause, this

categorisation is only a simplification of what happens in reality. In fact, all physical processes occur simultaneously and thus, influence each other so that a strict time-dependent categorisation of settlements is not realistic.

2.2.1 Laboratory determination

The one-dimensional compression behaviour of soils is usually measured in the way that stress is applied to the soil in axial direction, while strain in the horizontal is prevented. Drainage of the cylindrical sample is usually allowed in axial direction, through top and bottom of the sample. This type of test is referred to as *oedometer test*, one-dimensional compression test, confined compression test or consolidation test. Details on the experimental device are given in Chapter 5, while Chapter 6 provides more insights on the testing procedure.

Another method to analyse the compression behaviour is by strain-controlled tests. Within these tests a sample also under confined conditions is subjected to a controlled rate of strain in vertical direction. This test configuration is referred to as *constant rate of strain (CRS)* and *controlled gradient test (CG)* test (Hamilton and Crawford, 1960; Smith and Wahls, 1969; Lowe et al., 1969; Wissa et al., 1971; Muir Wood, 2016).

In CRS tests the specimen is compressed by a constant rate of strain. Thereby, the strain rate is chosen in a way that pore water pressures, measured at the bottom of the sample, are sufficiently small so that the effective stress in the sample is assumed to equal the

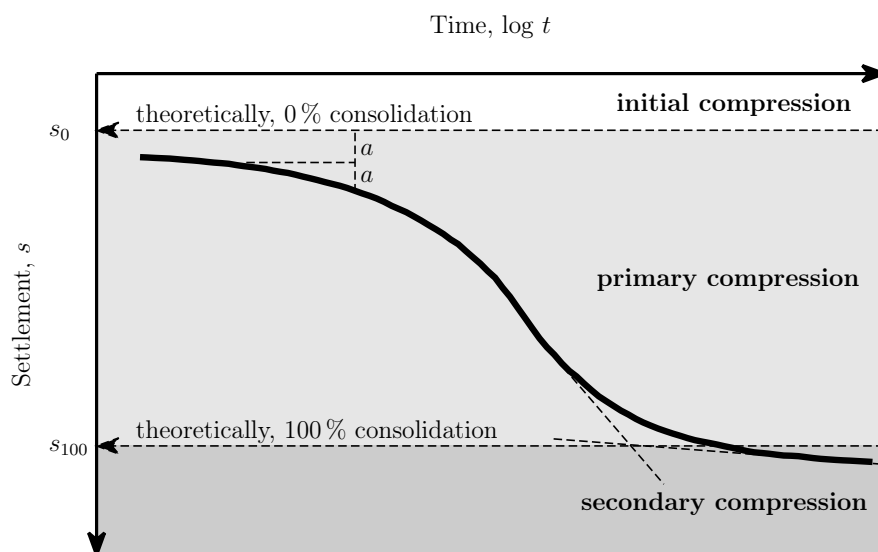


Figure 2.2: Time-dependent compression of a fine-grained soil, modified after Casagrande and Fadum (1940).

applied total stress. In CG tests the specimen is likewise compressed by a constant rate of strain. Though in a way, that the pore water pressure at the base stays constant. Thus, a constant hydraulic gradient is established. Both, CRS and CG tests have the advantage that a continuous stress-strain curve is derived, which allows for a precise determination of the preconsolidation stress. One drawback of these methods though is the dependency of e.g. the stiffness on the applied strain rate (see discussion in Section 2.2.7).

2.2.2 Primary compression of fine-grained soils

To describe the one-dimensional compression behaviour of a soil usually the deformation after expulsion of the water from the pore space is analysed in terms of vertical, effective stress σ'_v dependent void ratio e . Figure 2.3 (a) displays a typical $e - \sigma'_v$ -curve. The curve connecting all stress points for which the soil is in its loosest possible state is often referred to as *virgin compression line* (Schofield and Wroth, 1968). Plotted in semi-logarithmic scale (see Fig. 2.3b) the virgin compression line becomes a straight line, which can mathematically be described by the following function:

$$e = e_0 - C_c \cdot \log \frac{\sigma'_v}{\sigma'_{v,0}} \quad (2.1)$$

The slope of this curve defines the compressibility of the soil and is called compression index C_c

$$C_c = -\frac{de}{d \log \sigma'_v} \quad (2.2)$$

When a soil in its loose state experiences loading, the deformation occurring is caused by two mechanisms: elastic deformation of the soil skeleton and additional changes in soil structure or particle assembly. In the process of particle reassembling mechanical energy is dissipated. Thus, it is irreversible and referred to as plastic deformation. During unloading of the soil the plastic deformation cannot be removed. Thus, the soil shows less deformation in the reverse stress path. It consequently acts stiffer in unloading and reloading than in virgin compression. The slope of the recompression curve is called swelling index or recompression index C_{ur} :

$$C_{ur} = -\frac{de}{d \log \sigma'_v} \quad (2.3)$$

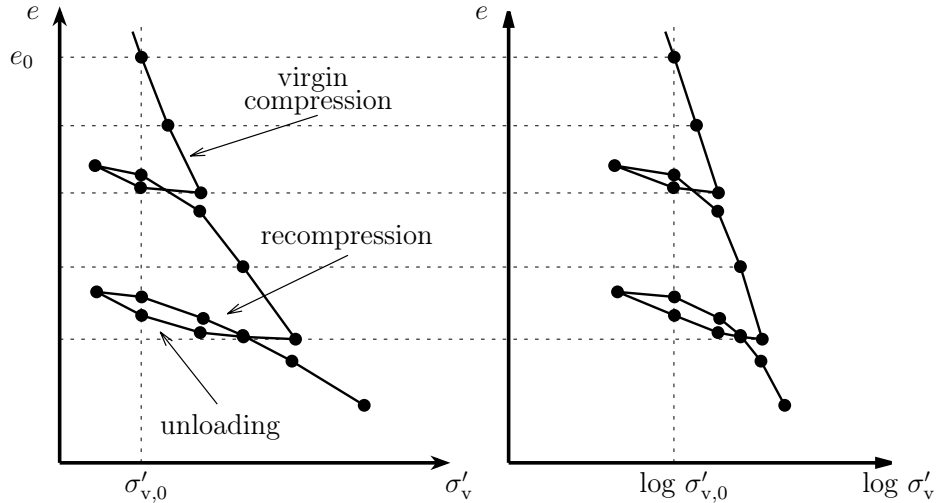


Figure 2.3: Compression curve of a fine-grained soil, after Schofield and Wroth (1968).

C_c and C_{ur} are defined based on logarithmic plots on base 10. However, often compression curves are also plotted in natural logarithmic scale. In this case the compression index is referred to as λ and the recompression index as κ . They can be easily calculated from C_c and C_{ur} by division by $\ln(10)$:

$$\lambda = \frac{C_c}{\ln(10)} \quad (2.4)$$

$$\kappa = \frac{C_{ur}}{\ln(10)} \quad (2.5)$$

2.2.3 Primary compression of natural, structured clay

Structured clays in their undisturbed, natural state exhibit a compression behaviour, which significantly differs from that of the same, but reconstituted material. This is caused by the present structure including a flocculated fabric and bonding, e.g. by cementation, of the particles.

Fig 2.4a illustrates the typical compression behaviour of a structured clay from experimental data on a marine clay. According to Mitchell and Soga (2005) this typical $e - \sigma'_v$ -curve can be abstracted to the representation given in Fig. 2.4b. The compression behaviour can then be characterised with respect to the inherent structure, i.e. fabric and bonding, of the clay, as follows: The natural clay deposited from its initial state (0) to its

natural void ratio by a stress σ'_a (a), shows a very stiff behaviour when loaded additionally to σ'_b (a-b), which is due to the bonding of particles. When loaded beyond σ'_b the bonding is gradually destroyed, which causes a soft behaviour of the clay up to σ'_f (f). This process is referred to as *destruction*, occurring after reaching σ'_b , which is defined as the *yield stress* σ'_y of the clay. At yield stress the difference in void ratio between the structured soil (b) and a completely destructured soil (d) can be attributed to fabric (c-d) and bonding (b-c).

The lower curve in Fig 2.4 displays the compression of a reconstituted soil, in which exhibits no structure. It is unique for every soil. However, the curves for different clays may be normalised using the *void index* I_v introduced by Burland (1990).

$$I_v = \frac{e - e_{100}^*}{e_{100}^* - e_{1000}^*} = \frac{e - e_{100}^*}{C_c^*} \quad (2.6)$$

in which e_{100}^* is the intrinsic void ratio under a vertical effective stress of 100 kN/m², e_{1000}^* is the intrinsic void ratio under a vertical effective stress of 1000 kN/m² and C_c^* is the intrinsic compression index.

Normalised to the void index I_v the intrinsic compression curves of all clays form the *intrinsic compression line (ICL)*, which may be approximated with sufficient accuracy by

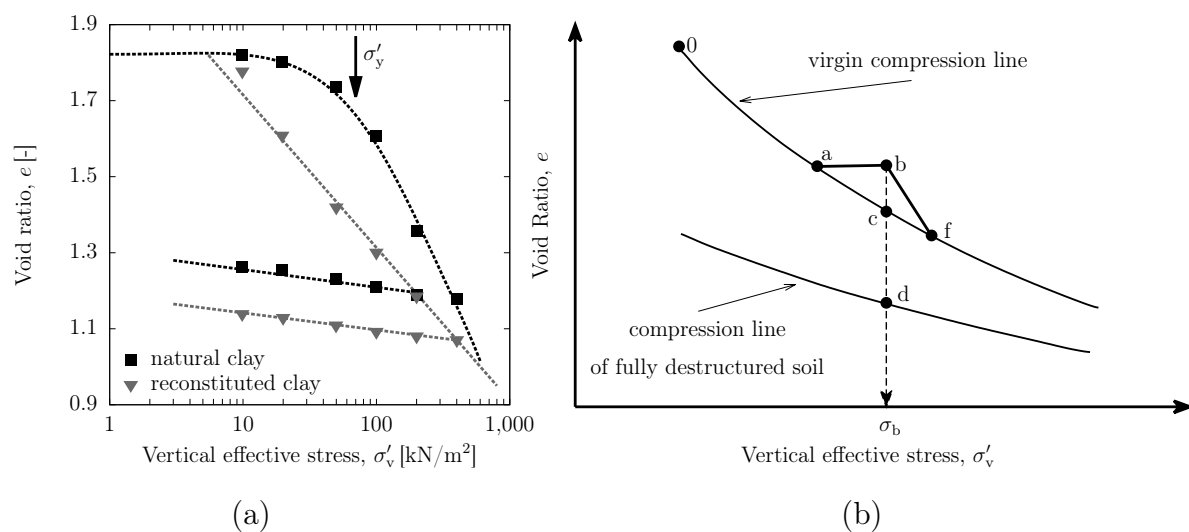


Figure 2.4: Compression curves for structured and destructured clay: (a) experimental curve for Onsøy clay, (b) Schematic illustration of compression of a structures clay, modified after Mitchell and Soga (2005).

the following function (Burland, 1990):

$$I_v(\sigma'_v) = 2.45 - 1.285 (\log \sigma'_v) + 0.015 (\log \sigma'_v)^3 \quad (2.7)$$

Another method to calculate I_v for a given soil, is by use of empirical correlation between e_{100}^* and C_c^* with the void ratio at liquid limit e_L , also given in Burland (1990):

$$e_{100}^* = 0.109 + 0.679 e_L - 0.089 e_L^2 + 0.016 e_L^3 \quad (2.8)$$

$$C_c^* = 0.256 e_L - 0.04 \quad (2.9)$$

Moreover, the void index may be used as a measure of the intrinsic compactness of a clay. As $I_v(e = e_{100}^*) = 0$ the clay is loose for $I_v \leq 0$ and compact for $I_v \geq 0$.

The normalised compression curves of data from various sedimentation compression curves of naturally sedimented clays reported by Skempton (1969) can also be summarized to a unique curve, the so-called *sedimentation compression line (SCL)*. Both lines together are plotted in Fig. 2.5. For $100 \text{ kN/m}^2 \leq \sigma'_v \leq 1000 \text{ kN/m}^2$ the ICL and SCL are approximately parallel. In this stress range the effective stress which is carried by the natural, sedimented clay is approximately five times that which is carried by the equivalent, but reconstituted clay. At higher pressures the ICL and SCL converge, as in higher stress ranges the natural structure vanishes. With reference to the two lines the natural state of clays can be classified according to Chandler et al. (2004) as shown in Fig. 2.6.

A characteristic typically used to describe structured soils is their *sensitivity*, defined by Terzaghi (1944) as the ratio between undisturbed S_{up} and remoulded strength S_{ur} determined by unconfined compression test:

$$S_t = \frac{S_{\text{up}}}{S_{\text{ur}}} \quad (2.10)$$

In literature different classifications regarding the sensitivity can be found. One of them by Skempton (1944) is given in Table 2.1. Clays exhibiting a high sensitivity do so not due to a higher strength in the undisturbed state, but due to a very low remoulded strength. Consequently, so-called *quick clays* in their remoulded state are almost liquid, which results from leaching of the marine clays deposited under saline conditions. Further details would be beyond the scope of this work, but can be found in e.g. Rosenqvist (1953) and Bjerrum (1954). Generally, for the determination of the sensitivity unconfined

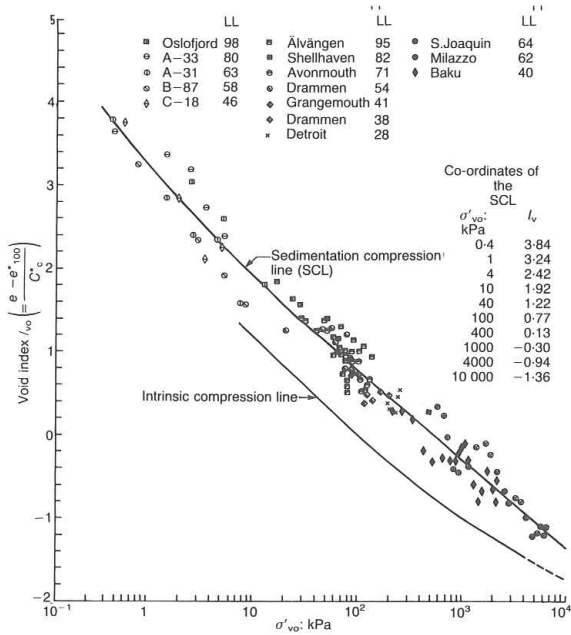


Figure 2.5: Intrinsic compression line (ICL) and sedimentation compression line (SCL) (Burland, 1990).

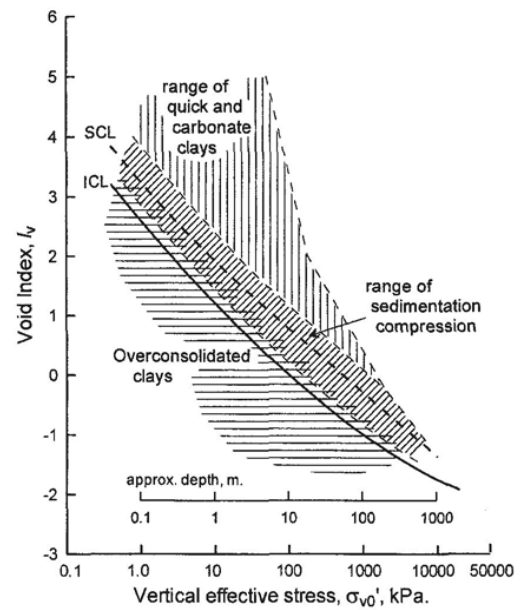


Figure 2.6: In situ stress states for different clay types (Chandler et al., 2004).

compression tests or an other measure of the soil strength is required. However, sensitivity can also be identified using the concept of stress sensitivity, introduced by Chandler and Cotecchia (2000). Here, the stress sensitivity S_σ is defined as the ratio between yield stress σ'_y and vertical effective stress on the ICL at equivalent void ratio $\sigma'_{e^*}_y$:

$$S_\sigma = \frac{\sigma'_y}{\sigma'_{e^*}_y} \tag{2.11}$$

Table 2.1: Classification of clay sensitivity.

Sensitivity classification	S_t
insensitive clay	1
clays of low sensitivity	1 to 2
clays of medium sensitivity	2 to 4
sensitive clays	4 to 8
extra-sensitive clays	> 8
quick - clays	> 16

2.2.4 Barotropy and pycnotropy

The compression and recompression indices characterise the soil's compressibility as material characteristics. However, the oedometric stiffness E_s as the tangent modulus of the stress-strain curve describes the compressibility or extensibility in each state depending on the current soil state and stress path.

$$E_s = \frac{d\sigma'_v}{d\varepsilon_v} \quad (2.12)$$

$$(2.13)$$

In the following the stiffness during virgin compression is denoted as E_s , while the stiffness in unloading and reloading paths is denoted as E_{ur} .

To describe the mechanical behaviour of a material in mathematical form, constitutive equations relate the applied stress state to the deformation of a system. These equations imply a mathematical description of the stiffness. In the most simple form, the stiffness is assumed to be constant, as assumed in the general Terzaghi theory, using Hooke's law:

$$E_s = E \cdot \frac{1 - \nu}{(1 + \nu) \cdot (1 - 2\nu)} \quad (2.14)$$

with a constant elasticity modulus E and Poisson's ratio ν .

However, it is generally known and can be clearly seen from Fig.2.3 that the soil stiffness is not a material constant but dependent on the stress state (mean stress, p) as well as the soil density (void ratio, e). Empirical approaches expressing the stiffness depending on stress and density state are given in Hardin and Black (1969) and Bard (1993). Still, a more common approach to introduce the non-linearity of stiffness in constitutive models, is to consider only the stress dependency. As described in Zimmerer (2011) different mathematical formulations are commonly used.

Ohde's approach

The approach first described by Ohde (1939) allows for a non-linear stress-strain relationship. Details can be found in Ohde (1939), Janbu (1963) and Schanz (1998).

$$E_s = K_{\text{Ohde}} \cdot \sigma^{\text{ref}} \cdot \left(\frac{\sigma}{\sigma^{\text{ref}}} \right)^m \quad (2.15)$$

where σ^{ref} is the reference stress and K_{Ohde} , m are constants. For $m = 0$ the stiffness becomes constant, while with $m = 1$ the equation equals the following logarithmic approach.

Logarithmic approach

The logarithmic approach was introduced by Terzaghi (1925) and is commonly used to account for the stress dependency in the stiffness of clays.

$$E_s = \sigma \frac{(1 + e)}{\alpha} \quad (2.16)$$

Exponential approach

The exponential approach is applied when dealing with extremely soft soils and suspensions. According to Roma (1976) in these cases the deformation behaviour is described most adequately by an exponential relation between void ratio e and applied stress σ of the following type:

$$e = A \cdot \sigma^{-B} \quad (2.17)$$

2.2.5 Historiotropy

To adequately describe the compression behaviour of a fine-grained soil it is important not only to consider the barotropy (dependency on stress state) and pycnotropy (dependency on density state) of the material, but also to account for the historiotropy.

The term historiotropy describes the dependency of the material behaviour on its history in terms of static and/or cyclic preloading and ageing effects. It may result from deposition processes (in situ) or installation procedures (experiment) as well as loading history. Details on ageing effects can be found in Section 2.2.7.

A very elementary term to characterise the historiotropy of a fine-grained soil is the *over consolidation ratio (OCR)* or *yield stress ratio (YSR)*. The OCR is defined as the ratio between present overburden effective stress $\sigma'_{v,0}$ and preconsolidation pressure, which is the maximum past overburden effective stress $\sigma'_{v,max}$. The YSR is used for structured clays and thus is defined as the ratio between present effective stress $\sigma'_{v,0}$ and the yield stress σ'_y :

$$OCR = \frac{\sigma'_{v,max}}{\sigma'_{v,0}} \quad (2.18)$$

$$\text{YSR} = \frac{\sigma'_y}{\sigma'_{v,0}} \quad (2.19)$$

With respect to the OCR, Mitchell and Soga (2005) define three possible soil states:

1. $\sigma'_{v,0} > \sigma'_{v,\max}$ (OCR<1) - underconsolidated

The term underconsolidated describes the soil state, when the present effective stress is larger than the maximum effective stress reached in the past, which means that the soil is still in the process of consolidation and has not yet reached equilibrium state under the applied pressure. In situ this state for instance occurs in situations where deposition rate is faster than the consolidation, as e.g. when caused by a fast drop in the ground water table.

2. $\sigma'_{v,0} = \sigma'_{v,\max}$ (OCR=1) - normally consolidated

The term normally consolidated described the soil state when the present effective stress is equal to the equilibrium effective stress reached before.

3. $\sigma'_{v,0} < \sigma'_{v,\max}$ (OCR>1) - overconsolidated

The term overconsolidated describes all states where the soil has prior reached equilibrium under larger than the present effective stress. As overconsolidation cannot only be caused by mechanical loading, but also by desiccation, creep and physico-chemical processes most soils in field are at least slightly overconsolidated (Mitchell and Soga, 2005). In case of natural, structured soil bonding of the soil particles may result in an effect similar to a mechanical overconsolidation. Details are discussed in the Section 2.2.3.

2.2.6 Secondary compression

For most engineering purposes the stress-strain relationship is plotted using the deformation reached at the end of consolidation (primary compression). However, as shown in Fig. 2.2 clays continue to compress after this state. This compression is referred to as *secondary compression* or *creep*. It is commonly assumed that during secondary compression deformation is caused by a change in the soil fabric driven by particle rearrangement tending towards an energetically more stable configuration. Consequently, the amount and rate of secondary compression are controlled by the ability of the structure to rearrange or the viscosity of the soil, while in contrast the consolidation rate is controlled by the ability of pore water to escape under a specific hydraulic gradient, described by

Darcy's law. Therefore, secondary compression is characterized by this creep rate referred to as *coefficient of secondary compression* C_α , described in terms of strain $C_{\alpha\varepsilon}$ or void ratio change $C_{\alpha e}$:

$$C_{\alpha e} = -\frac{de}{d(\log t)} \quad , \quad C_{\alpha\varepsilon} = -\frac{d\varepsilon}{d(\log t)} \quad (2.20)$$

It is generally assumed that C_α is constant during the process of secondary compression. Although of course, changes in nature occurring during this long-term process may accelerate or retard this process. Ladd et al. (1977) showed that C_α is strongly dependent on the applied effective stress. Therefore, Mesri and Godlewski (1977) related $C_{\alpha e}/C_c$ and found this ratio be a constant for a given soil. $C_{\alpha e}/C_c$ is usually equal to 0.04 for inorganic clays. Further ratios for other types of soils can be found e.g. in Mesri and Castro (1987). However, Graham et al. (1983) and Leroueil et al. (1985) showed that this is not universally valid, particularly not for soft, sensitive clays.

The question about the assumption of a constant $C_{\alpha e}/C_c$ ratio comes together with the following two questions, which are continuously discussed: (a) whether the void ratio at the end of consolidation for a given effective stress is unique or dependent on the applied load increment and deformation ratio and (b) whether secondary compression starts after completed consolidation or if both processes occur simultaneously. Some approaches regarding these questions are illustrated in the following section 2.2.7 on the rate dependency of soft soil compression.

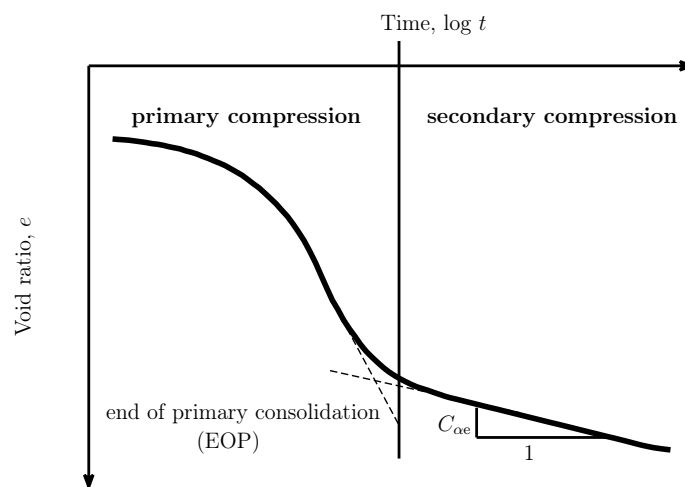


Figure 2.7: Definition of the coefficient of secondary compression.

2.2.7 Rate dependency

The question whether consolidation processes are rate independent or whether and how the load increment has to be considered, is a question of excessive discussion in geotechnical engineering. Particularly when considering the compression behaviour of soft and structured clays, rate effects may play an important role (Soga and Mitchell, 1996; Mitchell et al., 1997). An overview on available rheological models, which can be defined to study the compression behaviour of clays, can be found in Leroueil et al. (1985) and Leroueil (2006) and is summarised in the following.

The very basic rheological models, as used e.g. the original Terzaghi consolidation theory (Terzaghi, 1925), assume the effective stress-void ratio relationship of a soil to be unique and independent of time and strain rate. However, already Buisman (1936) recognized, that time has an effect on the compression behaviour. Thus, models were developed accounting for the observed time-effect. Relevant examples of this type of models can be found in Koppejan (1948) and Bjerrum (1967). The main limitations of these models are the necessity of a defined initial time t_0 and the treatment of time-dependent loading. Therefore, Suklje (1957) introduced a rheological model, in which the void ratio change depends on the effective stress and the rate of void ratio change. In this concept the function $e(\sigma')$ can be plotted using isotaches.

Accounting for time effects in compression of clay, Bjerrum (1967) introduced the ageing effect in the framework of the seventh Rankine lecture. Figure 2.8 illustrates this concept. A clay stratum, which is loaded up to a specific stress on virgin compression line by the overburden pressure (Point A), after consolidation experiences further deformation due to secondary compression. Normally, the amount of deformation due to secondary compression is small compared to the deformation caused by consolidation. However, when the clay is loaded for thousands of years, secondary compression may reach a considerable amount (Point B). According to Bjerrum (1967) in this state the clay structure has reached a more stable configuration and thus can carry additional loading in excess of the effective overburden pressure without any significant change in void ratio. The clay will act similarly to an overconsolidated clay until reaching the critical stress (Point C) and afterwards again follow the virgin compression line. This type of rheological model describes the rate of change in void ratio as a function of effective stress, void ratio and the rate of change in effective stress and was first used by Taylor and Merchant (1940).

The rate dependency of deformation is of particular importance for the interpretation of constant rate of strain (CRS) tests. Figure 2.9 shows the compression behaviour of

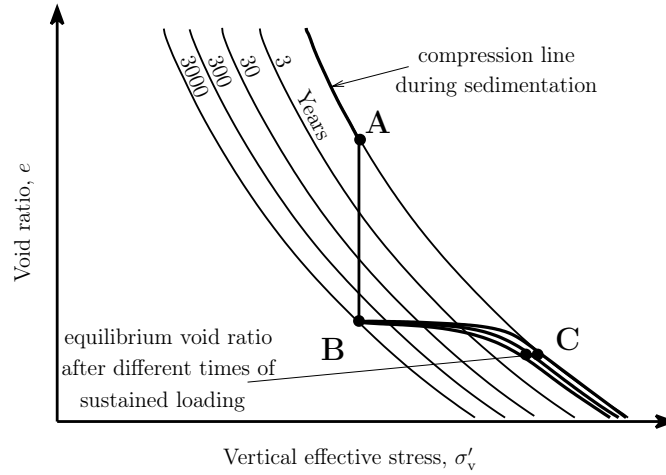


Figure 2.8: Ageing effect due to secondary compression, modified after Bjerrum (1967).

Batiscan clay under different loading rates. The viscous resistance of the soil structure becomes obvious, as for higher strain rates the preconsolidation or yield stress becomes larger. However, as shown by Leroueil (2006) strain rates in laboratory tests are usually much higher compared to the strain rates occurring in situ (see Fig. 2.10). Therefore, for the interpretation of CRS test results a correction regarding the strain rate has to be considered (see e.g. Watabe et al. (2012)).

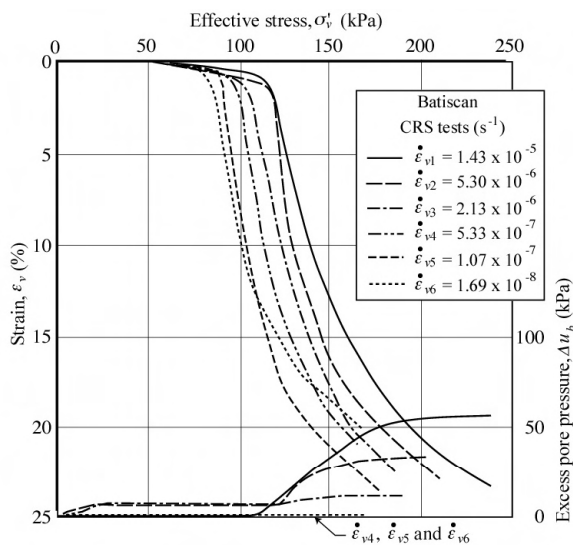


Figure 2.9: Rate dependency in CRS tests - typical CRS test data on Batiscan clay (Leroueil et al., 1985).

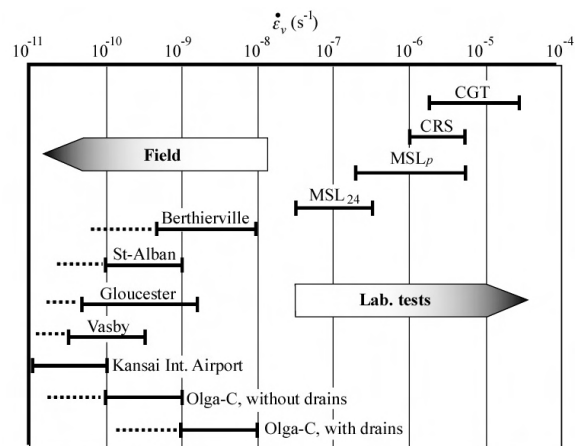


Figure 2.10: Strain rate ranges in laboratory tests and in situ (Leroueil, 2006).

2.2.8 Temperature dependency

The compression behaviour of clays in addition to the strain rate is also susceptible to changes in temperature. Various studies investigating the temperature effect on clays can be found in literature (Eriksson, 1989; Drnevich et al., 1989; Boudali, 1995; Graham et al., 2001; Marques et al., 2004). Figure 2.11 displays oedometer test results on Lulea clay at various temperatures (Eriksson, 1989). It can be seen, that with increasing temperature the soil becomes softer and the preconsolidation pressure decreases. This effect is of particular importance for temperatures less than 35 °C. However, as temperature can be controlled in experimental analyses, temperature effects are not considered in this study.

2.2.9 Development of horizontal stress

In one-dimensional compression the vertical effective stress is increased causing deformation in vertical direction, while the lateral deformation is constrained. However, of course the lateral / horizontal stress σ'_h changes with changing vertical stress state σ'_v . The ratio between horizontal and vertical effective stress in the case of one-dimensional compression with no lateral deformation is referred to as *coefficient of earth pressure at rest* K_0 .

$$K_0 = \frac{\sigma'_h}{\sigma'_v} \quad (2.21)$$

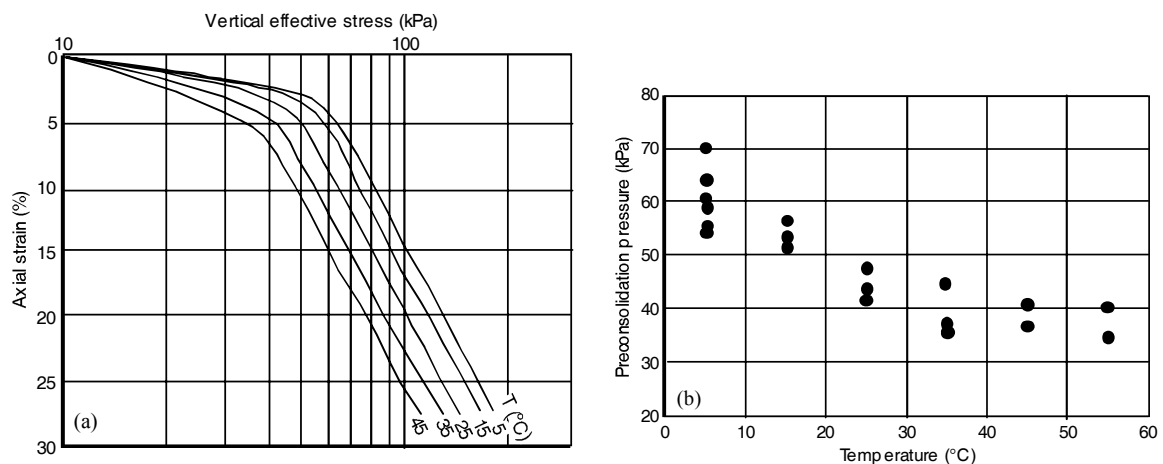


Figure 2.11: Temperature dependency in CRS tests - test data on Lulea clay (Eriksson, 1989).

According to Jaky (1944, 1948), K_0 of a normally consolidated soil can be estimated using the friction angle φ' by

$$K_0 = 1 - \sin \varphi' \quad (2.22)$$

For normally consolidated clays, K_0 consequently ranges between 0.3 to 0.75. Since Jaky (1944), many studies have been performed suggesting empirical or semi-empirical approaches for the calculation of K_0 . A selection is given in Table 2.2.

Following Ting et al. (1994) the values given in Table 2.2 are values for soft soils under higher effective stress. In lower stress ranges, i.e. higher void ratio range, soft soils coming from slurry state may show even smaller K_0 values. Figure 2.12 displays the void ratio - K_0 relationship, where K_0 lies between two lines mathematically described by

$$K_0 = -0.22 e + 0.9 \quad (2.23)$$

$$K_0 = -0.25 e + 0.87 \quad (2.24)$$

K_0 as a state parameter is dependent on the soil composition and structure as well as on the stress state and history (Mitchell and Soga, 2005). That means, that after compression and unloading a part of the vertical stress stays imprinted in the horizontal stress, i.e. K_0 increases with increasing OCR of a clay. The coefficient of earth pressure at rest for overconsolidated soils can thus be derived based on K_0^{NC} and a function of the

Table 2.2: $K_0(\varphi')$ equations with resulting values for Kaolin, cf. Ting et al. (1994).

K_0 approach	Reference	K_0 ($\varphi' = 22^\circ$)
$K_0 = (1 - \sin \varphi') \cdot \frac{(1+2/3 \sin \varphi')}{(1+\sin \varphi')}$	Jaky (1944)	0.56
$K_0 = 1 - \sin \varphi'$	Jaky (1948)	0.63
$K_0 = \tan^2 \left(45^\circ - \frac{1.15(\varphi' - 9^\circ)}{2} \right)$	Rowe (1957)	0.59
$K_0 = 0.95 - \sin \varphi'$	Abdelhamid and Krizek (1976) Brooker and Ireland (1965)	0.58

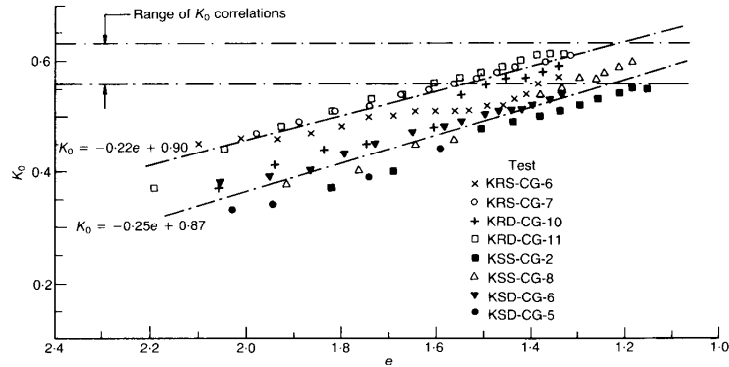


Figure 2.12: K_0 versus void ratio for kaolin clay in lower stress / higher void ratio range (Ting et al., 1994).

overconsolidation ratio $f(\text{OCR})$.

$$K_0 = K_0^{\text{NC}} \cdot f(\text{OCR}) \quad (2.25)$$

An approach commonly used to account for the OCR-dependency of K_0 is the one introduced by Kulhawy and Mayne (1990).

$$K_0 = (1 - \sin \varphi') \cdot \text{OCR}^{\sin \varphi'} \quad (2.26)$$

However, other approaches can be found in Schmidt (1966); Alpan (1967); Bellotti et al. (1975); Schmidt (1983). A detailed study on the development of K_0 for structured soils can be found in Leroueil and Vaughan (1990).

Whether or not K_0 is also dependent on time is the subject of ongoing discussion. Contributions can be found by Schmertmann (1983); Kavazanjian, E. and Mitchell (1984); Holtz and Jamiolkowski (1985).

2.3 Permeability of fine-grained soils

2.3.1 Darcy's law

The consolidation process is mainly influenced by two components: the compressibility of the soil structure and the ability of the soil to dewater and thus by its permeability or hydraulic conductivity. Steady-state as well as transient flow processes in soil mechanics

are analysed based on Darcy's law (Darcy, 1856), which states that the flow rate Q through the cross-section area A and thus the apparent water flow velocity q are directly proportional to the hydraulic gradient i , described by the following equations:

$$Q = k \cdot i \cdot A \quad (2.27)$$

$$q = k \cdot i \quad (2.28)$$

where k is the proportionality factor referred to as the *hydraulic conductivity* k of saturated media.

2.3.2 Permeability of soils

The hydraulic conductivity k is a material factor accounting for the properties of permeated solid and permeating fluid. In general, the hydraulic conductivity of soils is defined by the Kozeny-Carman equation (Kozeny, 1927; Carman, 1956) as

$$k = \left(\frac{\gamma_p}{\nu_p} \right) \cdot \left(\frac{1}{k_0 T^2 S_0^2} \cdot \frac{e^3}{1+e} \right) \quad (2.29)$$

$$= \left(\frac{\gamma_p}{\nu_p} \right) \cdot \bar{K} \quad (2.30)$$

where γ_p and ν_p are the unit weight and viscosity of the permeating fluid, \bar{K} is the absolute or intrinsic permeability of the soil, e is the void ratio, k_0 is the pore shape factor, T is the tortuosity factor and S_0 is the wetted surface area per unit volume of particles.

The hydraulic conductivity has units of a velocity, in SI units [m/s], while the absolute permeability has units of area [m²]. Under the assumption that only water is considered as permeating fluid within the present study and for the seek of simplicity, the hydraulic conductivity is referred to as *hydraulic permeability* and abbreviated as *permeability* k [m/s] in the following.

The dependency of the permeability on temperature is mainly influenced by the viscosity of the permeating fluid. Therefore, Eq. 2.31 gives the relation for the permeability at different temperatures t_1 and t_2 .

$$k_{t_1} = k_{t_2} \cdot \frac{\nu_{t_2}}{\nu_{t_1}} \quad (2.31)$$

2.3.3 Hydraulic permeability of clays

Mesri and Olson (1971) showed that the hydraulic permeability of clays depends upon mechanical as well as physico-chemical characteristics of the clay-water system. The most significant mechanical variables are the size, shape, and the geometrical arrangement of the clay particles, namely the fabric. The physico-chemical characteristics apply to the clay's tendency to disperse.

The Kozeny-Carman equation given in Eqn. 2.30 accounts well for granular material like sands. However, in its general form it is not that suitable for clays. Following Mitchell and Soga (2005) this may be attributed to two main factors. First of all, clays due to their fabric mostly do not exhibit a uniform pore size. Beyond that, changes in pore fluid type often affect the clay fabric and then may not only be attributed by changing the factor $\left(\frac{\gamma_p}{\nu_p}\right)$.

Therefore, Olsen (1962) introduced the so-called *cluster model*, which accounts for the non-uniform void ratio distribution in clays. In this model, it is assumed that the clay aggregates or clusters formed by the clay particles, can be differentiated into two void systems: inter-cluster voids and intra-cluster voids. The ratio of small voids as well as the cluster size are considered as factors influencing the global permeability, described as

$$k = \left(N^{2/3} \cdot \frac{(1 - \frac{e_c}{e_t})^2}{(1 + e_c)^{4/3}} \right) \cdot \underbrace{\left(\frac{\gamma_p}{\nu_p} \right) \cdot \left(\frac{1}{k_0 T^2 S_0^2} \cdot \frac{e^3}{1 + e} \right)}_{k \text{ from Kozeny-Carman Eq. 2.30}} \quad (2.32)$$

where N is the number of particles per cluster, e_c is the intra-cluster void ratio and e_t is the total void ratio.

Haase and Schanz (2016) showed, that the cluster-model is suitable for the description of void ratio dependent permeability of different clays, among them Spergau kaolin. Further enhancement of the cluster-model using the DDL theory can be found in Achari et al. (1999).

Equations 2.30 and 2.32 demonstrate the dominating influence of void ratio changes on the permeability. This is the reason why in literature, many empirical and semi-empirical relations can be found describing the permeability as a function of the void ratio accounting for its change with ongoing compression. In the following, exemplarily some approaches of different mathematical type are summarized.

Logarithmic approach

Taylor (1948) first introduced a logarithmic approach to describe the hydraulic permeability k as a function of the void ratio e in the following form:

$$\log k = \log k_0 - \frac{e_0 - e}{C_k} \quad (2.33)$$

where k_0 is the known hydraulic permeability at void ratio e_0 and C_k is the hydraulic conductivity change index, which may be assumed to be approximately $0.5 e_0$ for void ratios $e_0 \leq 2.5$.

The application of similar equations can be found in Lambe and Whitman (1969), Narasimhan and Witherspoon (1977) and Mesri and Godlewski (1977), also in the form

$$\log k = A' \cdot \log e + B' \quad (2.34)$$

Exponential approach

Exponential approaches for instance in the form

$$k = C \cdot \left(\frac{e^n}{1 + e} \right) \quad (2.35)$$

can be found in Keshian et al. (1977), Samarasinghe et al. (1982) and Wissa et al. (1983).

2.3.4 Laboratory measurement

The permeability of soils can be measured either in field or in laboratory tests. Field measurements, as e.g. pumping tests, have the disadvantage that they are expensive in time and costs. On the other hand, laboratory tests face the difficulty of getting representative samples in terms of in situ structure and variability. This particularly holds true for structured soils, where the in situ fabric may have a significant influence on the permeability. In the present study the focus is set on laboratory determination of material parameters. Therefore, in the following the main methods for permeability measurement in laboratory tests are discussed.

Three methods are generally used to determine the permeability in laboratory tests:

1. Constant head permeameter

2. Falling or variable head test
3. Indirect measurement via oedometer testing

Further direct methods, as e.g. *constant rate of flow tests*, are described in ASTM D 5084-00 (2002), while indirect methods, e.g. using empirical relations between pore size distribution and permeability, can be found in Kulhawy and Mayne (1990).

In the constant head permeameter and falling head test, a hydraulic gradient is applied to the soil specimen. By measurement of the permeating fluid volume per time and the known gradient and cross-area, the hydraulic permeability can be back-calculated according to Darcy's law. Details on the methodology of these tests can be found in Head (1998) and German standard code DIN EN ISO 18130-1 (1989).

A critical parameter in the performance of direct permeability tests for clays is the choice of an adequate hydraulic gradient. When possible, of course the hydraulic gradient in the experiment should reproduce the flow situation in situ. As in situ often hydraulic gradients $i \leq 5$ are encountered, this could lead to a very long testing time. On the other hand, too large gradients must be avoided, as high flow pressures could lead to the erosion of fine particles and the validity of Darcy's law has to be guaranteed. Therefore, ASTM D 5084-00 (2002) suggests a maximum hydraulic gradient $i_{\max} = 30$ for media with a low hydraulic permeability ($k < 10^{-9}$ [m/s]), $i_{\max} = 20$ for $10^{-9} < k < 10^{-8}$ [m/s] and $i_{\max} = 10$ for $10^{-8} < k < 10^{-7}$ [m/s]. According to Shackelford et al. (2000) these hydraulic gradients may be increased for thinner samples with reference to the effective stress difference acting on the sample. Following Tavenas et al. (1983) in natural soft clays Darcy's law is valid for gradients ranging between 0.1 and 50.

An alternative approach to derive the permeability from laboratory test, is by interpretation of the consolidation rate from oedometer, CG or CRS tests.

Permeability from oedometer tests

Following Terzaghi's theory the hydraulic permeability k can be back-calculated from the coefficient of consolidation c_v , the stiffness E_s and the unit weight of water γ_w according to

$$k = \frac{c_v \cdot \gamma_w}{E_s} \quad (2.36)$$

In a stepwise oedometer test, for each loading step c_v can be determined according to Casagrande and Fadum (1940) or Taylor and Merchant (1940) (details see Section 3.4.6),

with E_s by Eqn. 2.12. With respective void ratio in each loading step, a $k(e)$ relationship can be calculated.

Permeability from CG tests

In controlled gradient tests, the pore pressure at the bottom of the specimen is kept constant, while the pore pressure distribution over sample height can be assumed as parabolic. By measurement of the deformation rate dh/dt and constant pore water pressure at the bottom u_b with knowledge of the initial height h , the hydraulic permeability k can be calculated with reference to Tavenas et al. (1983) as

$$k = \frac{dh}{dt} \cdot \frac{h\gamma_w}{2u_b} \quad (2.37)$$

With the corresponding void ratio a $k(e)$ relationship can be directly derived.

Permeability from CRS tests

In contrast, in CRS tests the deformation rate is imposed and constant, why the pore pressure u_b is measured. However, for the common assumption of constant void ratio over depth, the same equation for k depending on deformation rate and pore water pressure as for the CG tests can be derived. Thus, Eq. 2.37 can be used to calculate k based on the measurement of u_b for the given strain rate. The $k(e)$ relationship can be derived accordingly.

A detailed comparison assessing the different direct and indirect methods described above, can be found in Tavenas et al. (1983). There, it is clearly shown that direct measurement of the permeability is much more accurate than the indirect methods. This can be explained by the fact, that all indirect methods use Terzaghi's theory to back calculate the hydraulic permeability, which implies a series of assumptions that do not properly fit the actual behaviour of natural clays. Among them, the assumption of constant k , E_s may be seen as the most critical one. According to Tavenas et al. (1983) the falling head test in an oedometer apparatus is the best practical method to determine the hydraulic permeability of natural clays. However, in the absence of direct permeability measurement due to time or effort reasons, an approximate assessment of the hydraulic permeability by the consolidation behaviour may be a reasonable estimation.

2.3.5 Anisotropy

Due to preferred orientation of elongated or platy clay particles and the stratification of soil deposits, the hydraulic permeability may vary significantly in vertical and horizontal direction. Anisotropy ratios of horizontal-to- vertical hydraulic conductivity from less than 1 to over 7 are reported by Mitchell (1956).

2.4 Summary

The state of the art on the structure, one-dimensional compression behaviour and permeability of fine-grained soils was summarised in this chapter. Herein, the definition of soil structure comprising fabric and bonding was given. The different modes of particle association were studied, together with methods to investigate clay fabric and possible changes in clay structure. Moreover, the basic knowledge on one-dimensional compression behaviour was introduced, covering the definition and characteristics of the different compression phases. Thereby, particular focus was set on the primary compression of clays. To do so the stress, history, rate and temperature dependency of the compression of fine-grained soils was introduced, and the effect of an inherent soil structure on the compressibility was discussed, introducing the concept of Burland (1990). Besides the one-dimensional compression behaviour also the development of horizontal stresses was illustrated. In the last section, the state of art on the hydraulic permeability of fine-grained soils and its laboratory determination was presented.

3 Consolidation of fine-grained soils

3.1 Introduction

Consolidation describes the time-dependent compression of a soil volume experiencing loading, caused by the delayed outflow of water from the pore system. This process was first noted by Terzaghi (1923). His one-dimensional consolidation theory based on physical principals was published in Terzaghi (1925) and is often referred to as the beginning of modern soil mechanics. This one-dimensional theory was later extended by Biot (1941) to a coupled, three-dimensional theory and since then studied in multitudinous research works. As the delayed outflow of water from the pore system is mainly inherent to low-permeable materials, consolidation is of particular importance for the compression behaviour of fine-grained soils.

3.2 Principle of effective stress

The principal of effective stress was introduced by Terzaghi (1923, 1925). It states that in a saturated soil the applied total stress σ is transferred to the effective stress σ' and the pore water pressure u . The effective stress σ' is understood as the portion of stress which is carried by the solid material phase. It controls the soil's volume change.

$$\sigma = \sigma' + u \tag{3.1}$$

Eq. 3.1 suits well for soft soils. However, for porous material in which the compressibility of the grains is smaller compared to the matrix compressibility, the stress distribution has to be considered differently. A detailed study on different approaches to account for this, can be found in Lade and De Boer (1997). One comprehensive approach following Biot and Willis (1957) suggest to write the effective stress more adequately in the following

form

$$\sigma = \sigma' + \alpha \cdot u \quad (3.2)$$

where α is the so-called Biot's coefficient defined as

$$\alpha = 1 - \frac{C_s}{C_m} \quad (3.3)$$

with C_s compressibility of the solid (soil grain) and C_m compressibility of the soil matrix. For soft soils α equals 1 and thus Eq. 3.2 yields Eq. 3.1.

3.3 One-dimensional, linear consolidation theory

3.3.1 General theory of consolidation - Biot model

The one-dimensional deformation of a homogeneous, porous material with reference to Biot (1941) is, following the *principle of conservation of mass*, given by the storage equation as follows

$$\frac{\partial \varepsilon_v}{\partial t} = \underbrace{-C_f \cdot n \cdot \frac{\partial u}{\partial t}}_{\text{compression of fluid}} - \underbrace{C_s \cdot \left(\frac{\partial \sigma_v}{\partial t} - n \cdot \frac{\partial u}{\partial t} \right)}_{\text{compression of solid}} - \underbrace{\frac{\partial q_v}{\partial z}}_{\text{outflow}} \quad (3.4)$$

where z : coordinate of vertical direction (indicated by index v) which is the direction of compression and outflow, [m]

ε_v : vertical strain, [-]

σ_v : total, vertical stress, [kN/m²]

u : pore water pressure, [kN/m²] or [kPa]

q_v : specific discharge / outflow, [m/s]

t : time, [s]

C_m : compressibility of the soil matrix, [m²/kN]

C_f : compressibility of the fluid, [m²/kN]

C_s : compressibility of the solid, [m²/kN]

n : porosity, defined as $n = \frac{e}{(1+e)}$, [-]

In simple words, it can be said that, the vertical strain is equal to the sum of compression of the fluid, compression of the solid and outflow of water.

As one-dimensional compression is assumed, the vertical strain can be related to the vertical effective stress σ' , assuming linear elasticity, as follows

$$\frac{\partial \varepsilon_v}{\partial t} = -C_m \cdot \frac{\partial \sigma'_v}{\partial t} = -C_m \cdot \left(\frac{\partial \sigma_v}{\partial t} - \alpha \frac{\partial u}{\partial t} \right) \quad (3.5)$$

According to Darcy's law (Darcy, 1856), the outflow is proportional to the hydraulic gradient by the hydraulic conductivity given in Eq. 2.28. In case of consolidation, the hydraulic gradient is caused by the acting pore pressure. Therefore, the pressure head is defined as

$$h = \frac{u}{\gamma_w} \quad (3.6)$$

assuming the influence of the hydrostatic pressure to be small enough to be neglected. Consequently, the hydraulic gradient yields

$$i = \frac{\partial h}{\partial z} = \frac{1}{\gamma_w} \cdot \frac{\partial u}{\partial z} \quad (3.7)$$

The one-dimensional discharge thus can be written as

$$\frac{\partial q_v}{\partial z} = \frac{k}{\gamma_w} \cdot \frac{\partial^2 u}{\partial z^2} \quad (3.8)$$

Combining Eqs. 3.4, 3.5 and 3.8 gives

$$\frac{\partial u}{\partial t} = \underbrace{\frac{1}{1 + n \cdot \frac{C_f - C_s}{C_m - C_s}}}_{\text{Skempton B coefficient}} \cdot \frac{\partial \sigma_v}{\partial t} + \underbrace{\frac{k}{\gamma_w \cdot (C_m - C_s) \cdot \left(1 + n \cdot \frac{C_f - C_s}{C_m - C_s}\right)}}_{\text{coefficient of consolidation } c_v} \cdot \frac{\partial^2 u}{\partial z^2} \quad (3.9)$$

Equation 3.9 is the general differential equation describing one-dimensional consolidation under the assumption of a linear elastic material behaviour. It is commonly referred to as Biot's theory (Biot, 1941). It can be also written as

$$\frac{\partial u}{\partial t} = B \cdot \frac{\partial \sigma_v}{\partial t} + c_v \cdot \frac{\partial^2 u}{\partial z^2} \quad (3.10)$$

with

$$B = \frac{1}{1 + n \cdot \frac{C_f - C_s}{C_m - C_s}} \quad (3.11)$$

and

$$c_v = \frac{k}{\gamma_w \cdot (C_m - C_s) \cdot \left(1 + n \cdot \frac{C_f - C_s}{C_m - C_s}\right)} \quad (3.12)$$

The parameter B is referred to as the *Skempton B coefficient* introduced as a pore pressure coefficient by Skempton (1954). It accounts for the compressibility of the fluid and solid. In case both, solid and fluid, are assumed as incompressible B equals 1.

The parameter c_v is referred to as the *coefficient of consolidation*. It is a material parameter, which incorporates the permeability and stiffness of the material and accounts for the material's ability to consolidate. More details on c_v are given in Section 3.4.6.

For a constant load, Eq. 3.10 can be further simplified to

$$\frac{\partial u}{\partial t} = c_v \cdot \frac{\partial^2 u}{\partial z^2} \quad (3.13)$$

3.3.2 Hybrid model

Equation 3.9 describes the general case of consolidation. However, to describe the consolidation behaviour of soils, the simplification of this general concept regarding the compressibility of the phases is common. A common assumption is, that the compressibility of the solid is much smaller compared to the compressibility of the soil matrix, i.e. $C_s = 0$ is assumed. The model incorporating this assumption is often called *hybrid model* (Pollmann and Steeb, 2014). Introducing $C_s = 0$ Eq. 3.9 yields

$$\frac{\partial u}{\partial t} = \underbrace{\frac{1}{1 + n \cdot \frac{C_f}{C_m}}}_B \cdot \frac{\partial \sigma_v}{\partial t} + \underbrace{\frac{k}{\gamma_w \cdot C_m \cdot \left(1 + n \cdot \frac{C_f}{C_m}\right)}}_{c_v} \cdot \frac{\partial^2 u}{\partial z^2} \quad (3.14)$$

3.3.3 Terzaghi model

The original Terzaghi theory is based on the following assumptions:

- The soil volume is homogeneous.
- The relationship between void ratio and effective stress is linear, i.e. strains are relatively small.
- Flow and deformation occur in one direction only.
- All pores are completely filled with water, $S_r = 1$.
- Darcy's law is valid.
- The material properties of the soil do not change during consolidation:
 $k = \text{const.}, C_m = \text{const.}$
- The soil grains and water phase are incompressible: $C_s = C_f = 0$.

Under these assumptions (introducing $C_s = C_f = 0$) Eq. 3.9 yields

$$\frac{\partial u}{\partial t} = \frac{\partial \sigma_v}{\partial t} + \underbrace{\frac{k}{\gamma_w \cdot C_m}}_{c_v} \cdot \frac{\partial^2 u}{\partial z^2} \quad (3.15)$$

and for constant loading can be simplified to

$$\frac{\partial u}{\partial t} = \frac{k}{\gamma_w \cdot C_m} \cdot \frac{\partial^2 u}{\partial z^2} \quad (3.16)$$

which is Terzaghi's basic equation for one-dimensional consolidation under constant total stress.

3.4 Analytical solution for one-dimensional, linear consolidation

3.4.1 Initial and boundary conditions

To derive an analytical solution for Eq. 3.9 for the oedometric case, the following initial and boundary conditions according to Terzaghi (1943) are introduced. Fig. 3.1 illustrates the definition of these boundary conditions.

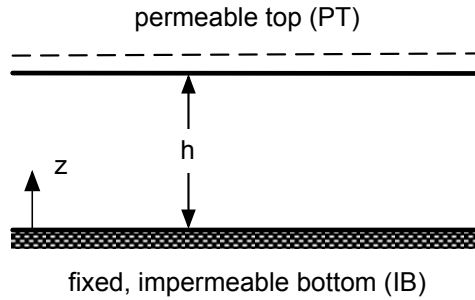


Figure 3.1: Definition of oedometric boundary conditions.

1. At the moment of loading, there has not been any fluid loss from the sample:

$$t = 0 \quad : \quad u = u_0 = \frac{1}{1 + n \cdot \frac{C_f - C_s}{C_m - C_s}} \cdot \sigma_v \quad (3.17)$$

2. The outflow occurs through the top of the sample ($z = 0$). Therefore, at the top the pore water pressure equals 0 all the time:

$$t > 0, \quad z = h \quad : \quad u = 0 \quad (3.18)$$

3. The bottom of the sample with a height h is fixed in place:

$$t > 0, \quad z = 0 \quad : \quad \frac{\partial u}{\partial z} = 0 \quad (3.19)$$

To solve the differential equation in Eq. 3.13 under these initial and boundary conditions, different mathematical approaches, e.g. Fourier or Laplace transformation, can be used, see e.g. Carslaw and Jaeger (1959).

3.4.2 Pore water pressure u

The following solution for the pore water pressure using Laplace transform is given in Verruijt (2014) for constant loading σ_{tot} .

$$\frac{u}{u_0}(z, t) = \frac{4}{\pi} \sum_{j=1}^{\infty} \left\{ \frac{(-1)^{j-1}}{2j-1} \cos \left[(2j-1) \cdot \frac{\pi}{2} \cdot \frac{z}{h} \right] \exp \left[-(2j-1)^2 \cdot \frac{\pi^2}{4} \cdot \frac{c_v t}{h^2} \right] \right\} \quad (3.20)$$

Figure 3.2 illustrates the evolution of pore water pressure over sample height with increasing time.

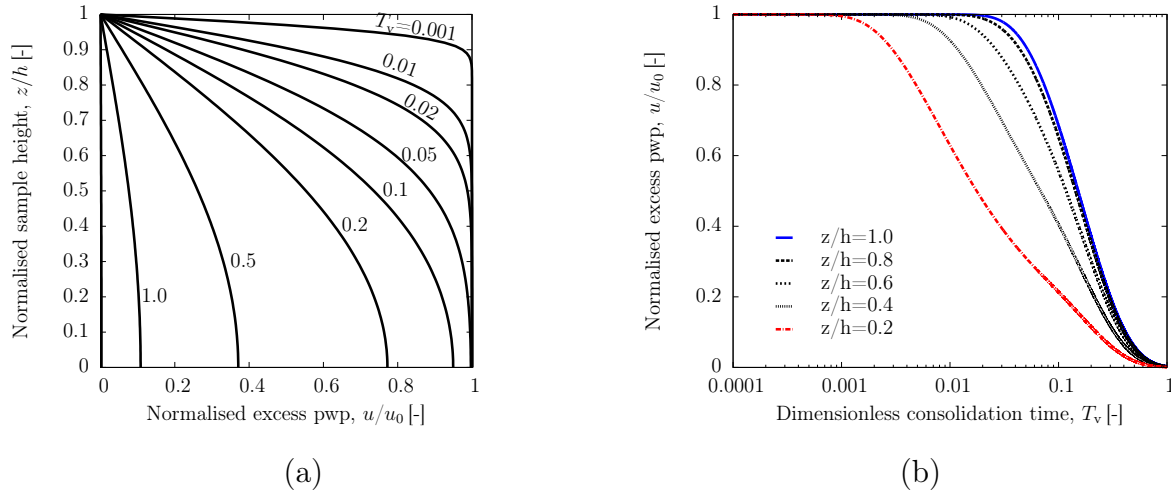


Figure 3.2: Analytical solution: normalised pwp (a) over sample height at different consolidation times, (b) versus T_v at different positions over the sample height.

For normalised time $t_{\text{norm}} = t/d$ and location $z_{\text{norm}} = z/h$, the pore water pressure depends only on the material parameters c_v and B as well as on the magnitude of the applied vertical loading σ_v influencing u_0 . The influence of variation in B and c_v is illustrated in Fig. 3.3. With decreasing B value, the initial pore water pressure decreases and the end of primary consolidation is reached later. With increasing consolidation coefficient c_v consolidation occurs earlier as the rate of consolidation increases. The normalised pore water pressure versus time diagram with increasing c_v is shifted parallelly to the left. The inclination of the curve is not effected by c_v .

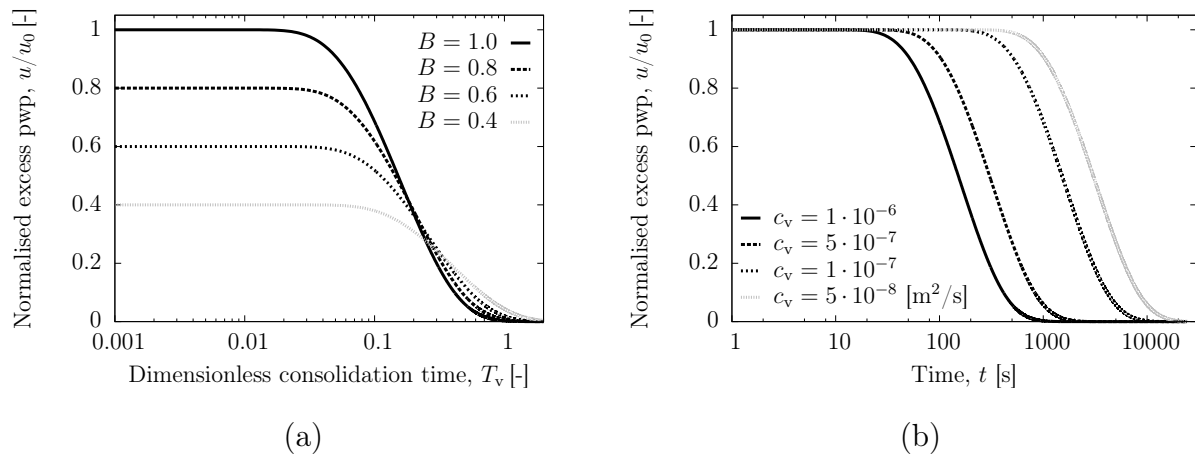


Figure 3.3: Influence of (a) Skempton B coefficient and (b) consolidation coefficient on the excess pore water dissipation curves the analytical solution of the consolidation equation.

3.4.3 Settlement s

The according settlement can be calculated by integration of the vertical strain ε_v over the sample height as

$$\begin{aligned}
 s &= - \int_0^h \varepsilon_v dz = C_m \cdot h \cdot \sigma_v - C_m \cdot \alpha \cdot \int_0^h u dz \\
 &= \frac{1}{E_s} \left[h \cdot \sigma_v - B \cdot \sigma_v \cdot \alpha \cdot \frac{4}{\pi} \sum_{j=1}^{\infty} \left\{ \frac{(-1)^{j-1}}{(2j-1)^2} \cdot \frac{2h}{\pi} \cdot \sin \left[(2j-1) \cdot \frac{\pi}{2} \cdot \frac{z}{h} \right] \right. \right. \\
 &\quad \left. \left. \cdot \exp \left(-(2j-1)^2 \cdot \frac{\pi^2}{4} \cdot \frac{c_v t}{h^2} \right) \right\} \right] \quad (3.21)
 \end{aligned}$$

At infinite time, when all pore pressure has dissipated, the settlement is given by

$$s_{\text{fin}} = \frac{1}{E_s} \cdot h \cdot \sigma_v \quad (3.22)$$

The initial settlement for the given pore pressure at time $t = 0$ according to Eq. 3.17 is

$$s_0 = \frac{h \cdot \sigma_v}{E_s} \cdot \frac{\frac{C_s}{C_f} + \frac{C_f - C_s}{C_m - C_s}}{1 + n \cdot \frac{C_f - C_s}{C_m - C_s}} \quad (3.23)$$

which equals 0 for the Terzaghi case $C_s = C_f = 0$.

The influence of variation in B and c_v on the normalised settlement behaviour is illustrated in Fig. 3.4. For $B \geq 0$, an initial settlement arises, which is larger for larger B . Moreover, as known from the influence of B on the dissipation of pore water pressure, the end of primary consolidation (EOP) is reached later. With increasing consolidation coefficient c_v , settlements occur earlier as the rate of consolidation increases. The normalised settlement versus time diagram with increasing c_v is shifted parallelly to the left.

The deformation in terms of changing void ratio e can be calculated from the settlements s by employment of the initial void ratio e_0 as

$$e(s) = e_0 - A \cdot s \cdot \frac{\rho_s}{m_d} \quad (3.24)$$

where A is the area, ρ_s the grain density and m_d the dry mass of the soil sample.

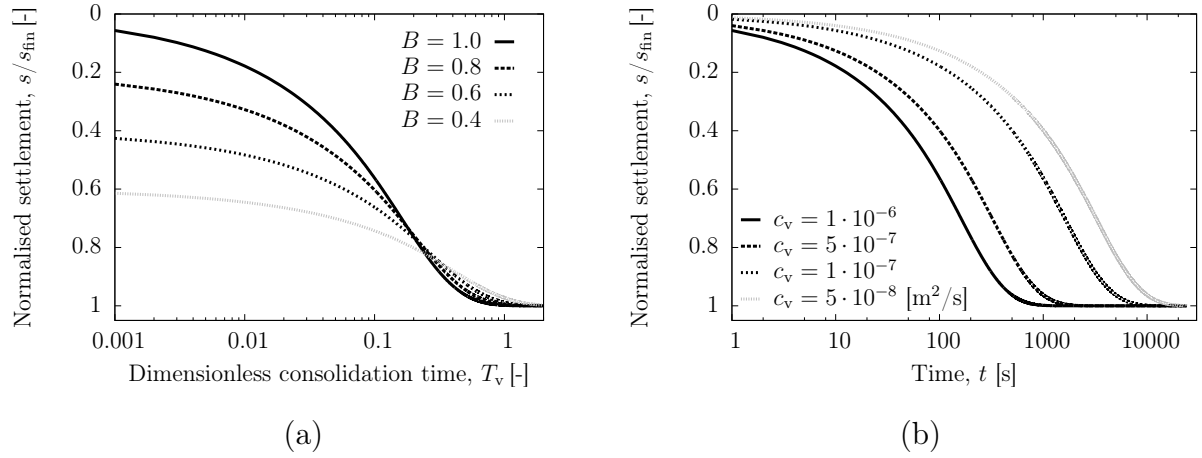


Figure 3.4: Influence of (a) Skempton B coefficient and (b) consolidation coefficient on the normalised settlement curves from the analytical solution of the consolidation equation.

3.4.4 Degree of consolidation U_m

Typically, the settlement is described in terms of the non-dimensional quantity, which is referred to as the *degree of consolidation* U . The degree of consolidation is usually given as a mean value over the sample height, U_m . It can be expressed in terms of settlements or pore water pressure. In terms of settlements it is computed as

$$U_m = \frac{s - s_0}{s_{fin} - s_0} \quad (3.25)$$

In terms of pore pressure, hence, U_m can be written as

$$U_m = \frac{1}{h} \int_0^h \frac{u_0 - u}{u_0} dz \quad (3.26)$$

$$= 1 - \frac{8}{\pi^2} \sum_{j=1}^{\infty} \left\{ \frac{1}{(2j-1)^2} \exp \left[-(2j-1)^2 \cdot \frac{\pi^2}{4} \cdot T_v \right] \right\} \quad (3.27)$$

where

$$T_v = \frac{c_v \cdot t}{h^2} \quad (3.28)$$

is the *dimensionless consolidation time* T_v .

The degree of consolidation varies between 0 (at time $t = T_v = 0$) and 1 (at time $t = T_v \rightarrow \infty$, when the consolidation process is completed).

3.4.5 Dimensionless consolidation time T_v

According to Taylor (1948) the function $T_v(U)$ may be approximated with high precision by

$$\text{For } U < 0.6 : T_v = \frac{\pi}{4} \cdot U^2 \quad (3.29)$$

$$\text{For } U > 0.6 : T_v = -0.9332 \log(1 - U) - 0.0851 \quad (3.30)$$

Other approximations are available, e.g. in Sivaram and Swamee (1977). Theoretically, for $T_v \rightarrow \infty$, U equals 1. However, for practical purposes it is commonly assumed that for $T_v = 2$, $U \approx 99.6\%$.

Moreover, the dimensionless consolidation time T_v is a very useful parameter illustrating the influence of material and geometry on the consolidation process. For instance, when c_v increases by the factor 2 due to change in stiffness or permeability by factor 2, the consolidation time doubles. Whereas, when the drainage length h doubles, the consolidation time is increased by the factor 4.

This relationship can be used to compute the consolidation time in-situ (prototype) from the consolidation time in the small-scale experiment (model) by

$$\frac{t_P}{t_M} = \left(\frac{h_P}{h_M} \right)^2 \quad (3.31)$$

where t_P and h_P are the time and minimal drainage length in the prototype and t_M and h_M are the time and minimal drainage length in the model.

3.4.6 Coefficient of consolidation c_v

In consolidation theory the material's ability to consolidate and thus the consolidation rate are characterised by the consolidation coefficient c_v . Equation 3.12 describes c_v as a function of k , n , C_m , C_f and C_s . For the Terzaghi model, Eq. 3.12 reduces according to Eq. 3.15 or can be expressed in terms of permeability k , stiffness E_s and unit weight of

water γ_w as

$$c_v = \frac{k \cdot E_s}{\gamma_w} \quad (3.32)$$

As c_v is a material parameter characterising the soil's consolidation behaviour, it is commonly determined from oedometer tests (1) as a consolidation characteristic of the material or (2) for the back-calculation of the permeability (see Section 2.3.4). Generally, c_v is assumed to be a constant, which does not change within the consolidation process. In experimental reality, this does not hold true for most soils and testing conditions. Details on approaches introducing a non-constant c_v are described in more detail in Chapter 3.5.2.

For the determination of c_v from consolidation curves various methods exist. However, the most common ones are the *logarithm-of-time method* according to Casagrande and Fadum (1940) and the *square-root-of-time method* proposed by Taylor (1942). A rather new approach is the *early-stage-log-t method* introduced by Robinson and Allam (1996). This method is of interest for the present study as it reduces the influence of secondary compression on the c_v value significantly. A comparison of different methods in Robinson and Allam (1996) shows that, c_v is always larger when derived from Taylor's method compared with the value computed from the Casagrande method. The largest value is derived from the early-stage-log-t method. This can be explained by the fact, that in the analyses different parts of the settlement curve are used, where secondary compression has more or less influence. As Taylor's method uses an earlier part of the compression curve, which is less affected by secondary compression, c_v values become larger. The same reason accounts for the early-stage-log-t method, which uses the very early part of the compression curve for computing. Various other methods to approximate c_v from experimental data can be found in literature (Sridharan and Prakash, 1985, 1993; Pandian et al., 1992; Das, 2010; Mckinley and Sivakumar, 2009; Lovisa et al., 2012; Al-Zoubi, 2015). However, most of these methods are rarely used. According to Olson (1986) the main reason for this is, that many of these approaches require trial solutions and are more complex than the standard approaches without improving the precision of the result.

Logarithm-of-time method

In the logarithm-of-time method suggested by Casagrande and Fadum (1940) t_{50} , the time at which 50 % of the settlement is reached ($U_m = 0.5$), is used to back-calculate c_v from the T_v - c_v relationship. From Eq. 3.30 for $U_m = 0.5$ the corresponding dimensionless time

$T_v = 0.197$ can be calculated. With Eq. 3.28 it follows

$$c_{v,Cas} = \frac{T_v(U_m = 0.5) \cdot h^2}{t(U_m = 0.5)} = \frac{0.197 \cdot h^2}{t_{50}} \quad (3.33)$$

The time t_{50} is determined graphically from the logarithmic time-settlement curve as illustrated in Fig. 3.5a. The intersection point (A) of primary and secondary consolidation part defines the settlement at the end of primary consolidation s_{100} . The difference in settlement from Point (B) in the early settlement part to a Point (C), at time $t_C = 4 \cdot t_B$, defines the initial settlement s_0 . The time t_{50} is defined as the time, where 50 % of the settlement ($s_{50} = (s_{100} + s_0)/2$) is reached.

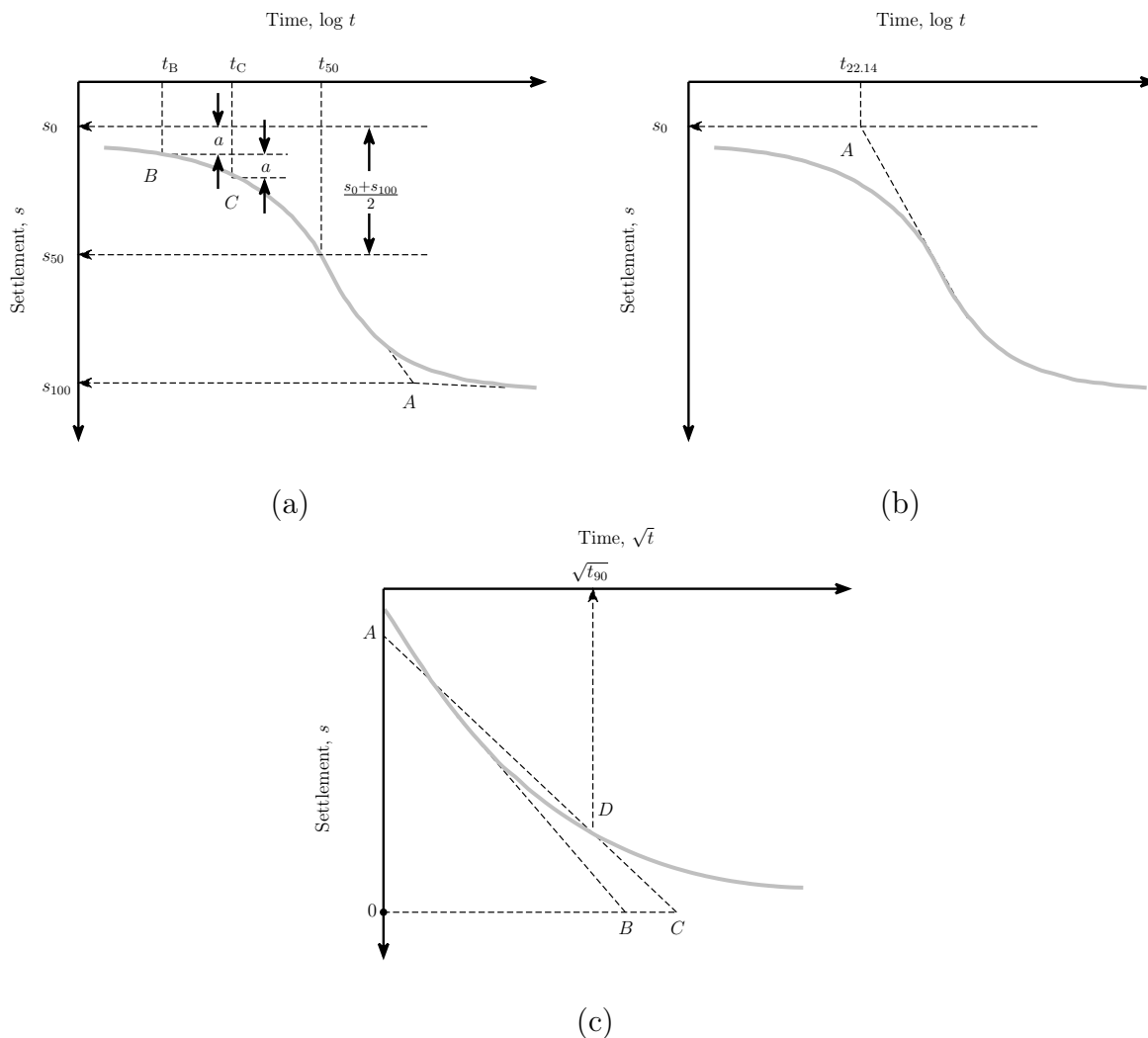


Figure 3.5: Determination of t_{50} , $t_{22.14}$ and $\sqrt{t_{90}}$ according to Casagrande and Fadum (1940), Robinson and Allam (1996) and Taylor (1942).

Early-stage-log-t method

The early-stage-log-t method introduced by Robinson and Allam (1996) is an extension of the logarithm-of-time method using the early part of the logarithmic-time-settlement plot to determine c_v . By that, the influence of secondary compression on the determination of c_v is neglected. This method is particularly suitable for soils exhibiting a significant creep behaviour. For $U_m = 0.2214$ at $T_v = 0.0385$, c_v can be calculated as

$$c_{v,RA} = \frac{T_v(U_m = 0.2214) \cdot h^2}{t(U_m = 0.2214)} = \frac{0.0385 \cdot h^2}{t_{22.14}} \quad (3.34)$$

The time $t_{22.14}$ is determined graphically from the logarithmic time-settlement curve as illustrated in Fig.3.5b. The intersection point (A) of the primary consolidation part with the s_0 -line (determined according to Fig.3.5a) defines the time $t_{22.14}$, where 22.14 % of the settlement is reached.

Square-root-of-time method

The square-root-of-time method according to Taylor (1942) uses the square-root-of-time-settlement plot in order to determine t_{90} . For $U_m = 0.9$ at $T_v = 0.848$, c_v is calculated by

$$c_{v,Tay} = \frac{T_v(U_m = 0.9) \cdot h^2}{t(U_m = 0.9)} = \frac{0.848 \cdot h^2}{t_{90}} \quad (3.35)$$

The time t_{90} is determined graphically from the square-root-of-time-settlement curve as illustrated in Fig.3.5c. The intersection point (D) of the line \overline{AC} with the consolidation curve defines the time and settlement at which $U_m = 0.9$. The line \overline{AC} is constructed in the way that $\overline{0C} = 1.15 \overline{0B}$ where \overline{AB} is a line through the early part of the consolidation curve.

3.5 Multi-dimensional and non-linear consolidation

Terzaghi's consolidation theory and the description of the principle of effective stress are commonly seen as the starting point of modern soil mechanics. Introduced in 1923 they initiated further studies on coupled problems in geotechnical engineering. Since then a multitude of studies has been performed dealing with consolidation problems. As Terzaghi's fundamental theory is based on a series of linearisations and simplifying assumptions, experimental research has been performed to prove whether or not these linearisa-

tions are adequate. Additionally, mathematical work has been performed to introduce enhancements and non-linearities to better fit the processes in reality. The following section summarizes the main fields, in which consolidation research was evolved. It tries to illuminate the historical development in consolidation theory and name some of the most significant research works performed in this field. However, consolidation is one of the central subjects in soil mechanics and a complete survey of literature on consolidation within the last 94 years would be far beyond of the scope of this work. Additional information and an interesting summary of the historical background can also be found in de Boer et al. (1996) and de Boer (2000, 2005).

3.5.1 Multi-dimensional consolidation

Parallel to Terzaghi Fillunger (1935) published a coupled consolidation theory. However, due to the severe personal discord of Terzaghi and Fillunger concluding with Fillunger's suicide, this theory at that time did not attract much interest. Fillunger's theory was further developed by Heinrich (1938) and evolved to a three-dimensional consolidation theory based on the later used mixture theory, published by Heinrich and Desoyer (1961). Based on Terzaghi's one-dimensional theory Biot (1941) introduced a three-dimensional consolidation theory accounting for flow and deformation in all three axial directions. Later, Biot (1955) and Biot (1956) expanded Terzaghi's theory for anisotropy. In the second half of the 20th century various studies on multi-dimensional consolidation were performed. Effects occurring in three-dimensional consolidation like as e.g. Mandel-Cryer and Noordbergum effect were studied by Mandel (1953); Cryer (1963); Gibson et al. (1963); Verruijt (1969) and find attention till today (Abousleiman et al., 1996; Zhang and Briaud, 2006; Lee, 2008). Consolidation theories accounting for cylindrical samples and radial consolidation were introduced (Paria, 1958; De Leeuw, 1964, 1965; De Josselin de Jong and Verruijt, 1965; Kumamoto and Yoshikuni, 1982). And, solutions for three-dimensional consolidation for different boundary value problems were analysed (Gibson et al., 1963, 1970; Davis and Poulos, 1972; Gibson and Sills, 1975).

3.5.2 Non-linear constitutive approaches

Commonly, c_v is assumed as a material constant, which according to the assumption in Terzaghi's theory does not change in the given stress-strain interval. However, it is well known, that the permeability and stiffness change with changing in effective stress state. c_v as the product of the two would only be constant, if both parameters change inverse

proportionally as stated in Davis and Raymond (1965). However, studies have shown that this is not the case. First approaches to introduce non-linearity with respect to stiffness and permeability can be found in Barden (1965); Mikasa (1965); Gibson et al. (1967); Gibson (1989). Some of these approaches also account for large strain. More phenomenological studies arose later. The change of c_v with changing void ratio, effective stress and mineralogy is illustrated in Robinson and Allam (1998) and Karunaratne et al. (2001). There it is shown, that depending on whether the soil is governed by its mechanical or physico-chemical properties, the c_v value increases or decreases with increasing σ'_v (Karunaratne et al., 2001). Kaolinite, illite and quartz for instance shows an increase in c_v with increasing σ'_v , while montmorillonite show a decrease. This observation is in good accordance with the analysis of other clay characteristics, as e.g. the liquid limit or shrinkage limit, presented in Sridharan (2002). According to this study, the opposite behaviour of kaolinite and montmorillonite can be explained by the fact that diffuse double layer repulsion dominates the behaviour of montmorillonite, while kaolinite is mainly controlled by the electrical attractive forces as well as its fabric. The influence of the consideration of changing c_v with increasing σ'_v on the modelling of consolidation processes is for instance demonstrated in Abuel-Naga and Pender (2012), Schiffman (1958), Zimmerer (2011) and Muir Wood (2016) and various other studies on cyclic consolidation, which will be discussed later in this thesis (see Chapter 4).

3.5.3 Further enhancements in consolidation theory

Of course, beyond dimensional and constitutive non-linearity there is a multitude of other studies dealing with consolidation under different boundary conditions. Just to name a few, the analysis of multi-layer problems can be found in Abbott (1960); Xie et al. (1999); Morris (2002). Consolidation for unsaturated soils is treated in Barden (1965); Fredlund and Hasan (1979); Rahardjo and Fredlund (1995); Conte (2004); Qin et al. (2008); Ausilio and Conte (2005) and self-weight consolidation finds attention in Been and Sills (1981); Toorman (1999); Major (2000); Sridharan and Prakash (2003). In addition, of course many publications can be found on the numerical approximation of the differential equations describing the consolidation process and the implementation of consolidation theory for Finite Element Simulations (Davis and Poulos, 1972; Seneviratne et al., 1996; Yao et al., 2002).

3.6 Summary

In this chapter the basics of the theory for linear elastic one-dimensional consolidation under monotonic loading was introduced. Following the description of the effective stress concept, the general theory of consolidation according to Biot (1941) was introduced. By simplification of the consolidation equations according to Biot (1941), the Hybrid model and the consolidation model according to Terzaghi (1925) were extracted. Based on the definition of the boundary and initial conditions, the analytical solution for the consolidation equation was derived. Thereby, the analytical solution for the pore water pressure and settlements in the consolidation process were presented. Moreover, important consolidation characteristics as the degree of consolidation U , the dimensionless consolidation time T_v and the consolidation coefficient c_v were introduced. Special focus was set on different methods to compute c_v from the consolidation curves, as these methods will be used in the experimental analysis. Finally, a literature review on different enhancements, introducing multi-dimensionality or non-linear constitutive approaches, to the linear, one-dimensional consolidation theory were presented shortly.

4 Consolidation under cyclic loading

The following chapter covers the state of the art on consolidation under cyclic loading and introduces the analytical solution for the boundary value problem of consolidation under cyclic loading of haversine form. First of all, a brief survey on available mathematical approaches analysing consolidation under non-constant loading is presented. In the main part of this chapter, the analytical solution for consolidation under haversine loading is derived. Herein, the equations for the cyclic pore water pressure and deformation are given. The chapter is concluded by a literature review on experimental studies dealing with consolidation under cyclic loading, leading over to the laboratory study presented in the next chapters.

4.1 Mathematical approaches in literature

Schiffman (1958) and Olson (1977) were the first to consider non-constant loading in the frame of the one-dimensional consolidation theory. Also, in 1974, Wilson and Elgohary (1974) started to analyse consolidation under cyclic square loading, i.e. load-on-load-off cycles. Since then, three major enhancements were followed within the development of consolidation under cyclic loading: (1) the implementation of constitutive non-linearities (with respect to c_v , k , C_m), (2) the implementation of different variable loading types (cyclic square, trapezoidal, harmonic) and (3) the implementation of various other initial and boundary conditions (multi-layer approaches, partial saturation, simultaneous hydraulic and mechanical loading).

Research implementing constitutive non-linearities of different type can be found in various studies (Baligh and Levandoux, 1978; Favaretti and Soranzo, 1995; Zhuang and Xie, 2005; Conte and Troncone, 2006; Xie et al., 2006; Geng et al., 2006; Cai et al., 2007; Toufigh and Ouria, 2008; Xie et al., 2008; Zimmerer, 2011; Xie et al., 2014). As one of the first, Baligh and Levandoux (1978) derived an analytical solution for a cyclic square load, i.e. load-on-load-off cycles, introducing a different c_v for normally consolidated and

overconsolidated stress states, namely $c_v(OCR)$. A similar approach was followed later by Toufigh and Ouria (2008, 2009) using different solution strategies and validating the approach by comparison with experimental data. A comparison to experimental large scale tests, can be also found in Conte and Troncone (2006).

Analytical and semi-analytical approaches introducing non-constant, but anti-proportional permeability and stiffness ($c_v \neq \text{const.}$), as suggested in the theory by Davis and Raymond (1965), can be found in Favaretti and Soranzo (1995) and Xie et al. (2006, 2008, 2014). While Favaretti and Soranzo (1995) derived an analytical solution for rectangular cyclic loading, Xie et al. (2006) focused on trapezoidal loading form. Xie et al. (2008) expanded their solution accounting for rheological characteristics. In 2014 they additionally analysed the consolidation behaviour under simultaneous mechanical and hydraulic loading. Consolidation caused by cyclic hydraulic loading, as it is may result from wave loading, is also studied in Barends (1992); Xiao-Yun et al. (1995); Chen (2002); Barends (2006, 2011).

Zhuang and Xie (2005), Geng et al. (2006) and Cai et al. (2007) present semi-analytical solutions for different loading types, namely cyclic square, trapezoidal and triangular loading. The stiffness and permeability are thereby updated depending on the effective stress or void ratio respectively. A similar study can be found in Zimmerer (2011), comparing different constitutive approaches. Introducing $e - \sigma'_v$ and $k - \sigma'_v$ relationships Yazdani and Toufigh (2012) derived an analytical solution for rectangular, cyclic loading.

Consolidation analyses for high frequency, cyclic loading and partially drained conditions are presented in Yasuhara et al. (1991); Xu et al. (2002); Sakai et al. (2003); Paul et al. (2010); Paul and Sahu (2012). The influence of depth and time dependent loading is analysed by Liu and Griffiths (2015). Miao et al. (2010) study multi-layer situations. Radial consolidation under cyclic loading is addressed in Hsu and Liu (2013); Ni et al. (2013). The problem of cyclic consolidation for unsaturated soils is discussed in Qin et al. (2008).

4.2 Analytical solution for consolidation under cyclic loading of haversine form

For the present study, consolidation under harmonic, cyclic loading of haversine form is analysed. Analytical solutions for this type of loading form are presented in Verruijt (2010b, 2014) using Laplace transform method and in Razouki and Schanz (2011); Razouki

et al. (2013); Müthing et al. (2016b) using Fourier transformation to solve the PDE. Other solutions for harmonic loading are given in Verruijt (2010a) (general harmonic loading), Barends (1992) (cosine lading) and Geng et al. (2006) (sinusoidal loading).

The haversine loading function in the present study was chosen with reference to Barksdale (1971) and Huang (1993). Among other authors, they suggest this type of loading function as particularly suitable for geotechnical applications. This is the case, as the haversine loading function accounts for the fact, that in geotechnical applications mostly compression loading is considered. Details on the loading function used in the present experimental study are given in Section 6.2.2.

The vertical loading is thus expressed as

$$\sigma_v = \hat{\sigma}_v \sin^2 \frac{\pi t}{d} \quad (4.1)$$

where σ_v is the total vertical stress applied over time t , $\hat{\sigma}_v$ is the load amplitude and d is the load period.

By substitution of Eq. 4.1 into Terzaghi's one-dimensional consolidation equation (compare Eq. 3.15), the governing differential equation for the consolidation problem under cyclic loading can be written as

$$\frac{\partial u}{\partial t} = \frac{\hat{\sigma}_v \cdot \pi}{d} \sin \frac{2\pi t}{d} + \frac{k \cdot E_s}{\gamma_w} \cdot \frac{\partial^2 u}{\partial z^2} \quad (4.2)$$

expressed in terms of stiffness $E_s = 1/C_m$ instead of compressibility C_m .

Analogue to the monotonic loading case, oedometric boundary conditions as illustrated in Fig. 3.1 are considered:

$$t > 0 : u(h, t) = 0, \quad \frac{\partial u(0, t)}{\partial z} = 0 \quad (4.3)$$

The initial condition is assumed as

$$t = 0 : u(z, 0) = 0 \quad (4.4)$$

4.2.1 Pore water pressure u

Various approaches to solve non-homogeneous partial differential equations as Eq. 4.2 are available in literature, see e.g. Carslaw and Jaeger (1959).

Using Fourier transformation the following solution for the pore water pressure can be derived.

$$u(z, t) = 16 \hat{\sigma}_v \sum_{j=0}^{\infty} \frac{(1+2j)T_0}{64 + (1+2j)^4 \pi^2 T_0^2} \cdot \sin \frac{(1+2j)\pi z}{2H} \cdot \left\{ \sin \frac{2\pi t}{d} - \frac{8}{(1+2j)^2 \pi T_0} \left[\cos \frac{2\pi t}{d} - \exp \left(-(1+2j)^2 \frac{\pi^2 T_v}{4} \right) \right] \right\} \quad (4.5)$$

where $T_v = \frac{c_v \cdot t}{h^2}$ and $T_0 = \frac{c_v \cdot d}{h^2}$.

The detailed derivation of this solution is presented in Müthing et al. (2016b).

Another method to derive a solution for Eq. 4.2 is by Laplace transform method. Verruijt (2014) states the complete solution derived by this method as follows

$$\begin{aligned} \frac{u(z, t)}{\hat{\sigma}_v} = & -\frac{1}{2} \Im \left\{ \frac{\cosh[az(1+i)]}{\cosh[ah(1+i)]} - 1 \right\} \cdot \sin \left(\frac{2\pi t}{d} \right) \\ & + \frac{1}{2} \Re \left\{ \frac{\cosh[az(1+i)]}{\cosh[ah(1+i)]} - 1 \right\} \cdot \cos \left(\frac{2\pi t}{d} \right) \\ & + \frac{2}{\pi} \sum_{j=0}^{\infty} \frac{(-1)^j}{1+2j} \cdot \frac{\cos[(1+2j)\frac{\pi z}{2h}]}{1+(1+2j)^4 \frac{\pi^2 T_0^2}{64}} \cdot \exp \left[-(1+2j)^2 \frac{\pi^2 T_v}{4} \right] \end{aligned} \quad (4.6)$$

with $a^2 = \frac{\pi}{c_v \cdot d}$.

Both ways of derivation are common methods for engineering purposes and give the same result for cyclic pore water pressure. The only difference lies in the definition of the coordinate system. As illustrated in Fig. 4.1 in the solution given by Müthing et al. (2016b), $z = 0$ defines the drained boundary, while in the solution given by Verruijt (2014) the boundary conditions are as defined above. Apart from that, the two solutions may be used analogue to each other.

Figure 4.2 shows the development of pore water pressure under cyclic loading in comparison to the pore water pressure dissipation under monotonic loading predicted by the analytical solution for identical material conditions in terms of c_v and sample height h ,

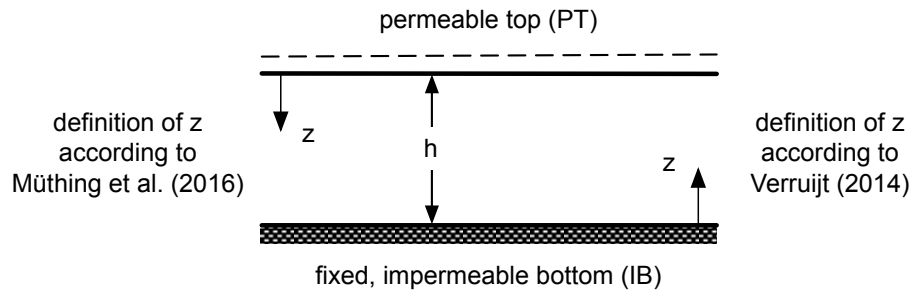


Figure 4.1: Boundary value problem with definition of coordinate system for the two analytical solutions by Müthing et al. (2016b) and Verruijt (2014).

as well as identical loading magnitude. The pore water pressure curve derived from the analytical solution under cyclic loading consists of the transient mean pore water pressure u_{mean} , which is superposed by a cyclic pore water pressure fluctuation of amplitude Δu . After a finite time, a stationary state is reached, in which the mean pore water pressure equals zero and the pore water amplitude in compression and unloading is of the same magnitude. For identical c_v , the end of primary compression (EOP) in the analytical solution for monotonic loading is reached at the same time as the stationary state (SS) under cyclic loading.

Generally, the pore water pressure dissipation under cyclic loading at the undrained boundary can be identified by three characteristics: (1) the mean pore water pressure in the first loading cycles $u_{\text{mean,1st}}$, (2) the rate of pore water pressure dissipation, characterized by t_{ss} (time at beginning of SS) or n_{ss} (number of cycles to reach SS) and (3) the pore water pressure amplitude Δu . In the stationary state, the pore water pressure

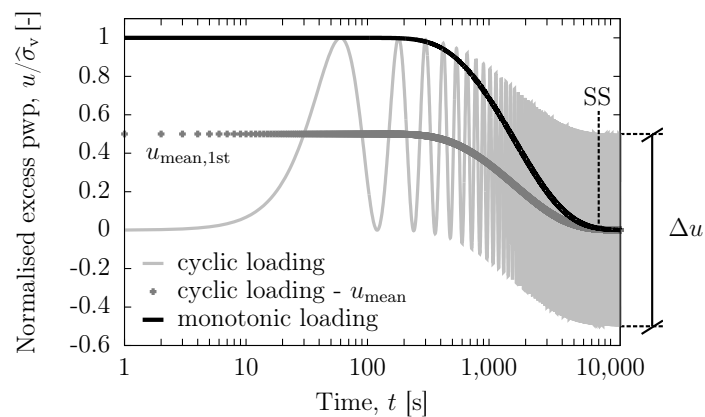


Figure 4.2: Pore water pressure versus time from the analytical solution for linear-elastic, one-dimensional consolidation under haversine and monotonic loading, computed with $\hat{\sigma}_v = \Delta\sigma_v = 100 \text{ kN/m}^2$, $d = 120 \text{ s}$, $h_0 = 20 \text{ mm}$, $c_v = 1 \cdot 10^{-7} \text{ m}^2/\text{s}$.

is shifted with respect to the applied loading by a phase shift ψ_u , which depends on the material and loading characteristics (see Fig. 4.3).

The development of pore water pressure over sample height in the first cycle and in the stationary state is demonstrated in Fig. 4.4. In the first cycle, with increasing load application the pore water pressure shows the typical form of pore pressure isochrones from monotonic consolidation testing. During unloading drainage in the upper layers occurs faster due to the vicinity of drainage boundary causing negative pore water pressures. In the lower part of the sample pore water pressures remain positive. In the stationary state the consolidation boundary has progressed to the lower part of the sample, so that negative pore water pressures also reach the lower bound of the sample. The distribution of pore water pressure within one loading cycle becomes symmetric.

Equation 4.6 allows for a mathematical subdivision of pore water pressure into (1) transient mean pore water pressure u_{mean} and (2) pore water pressure in the stationary state u_{ss} . By normalisation of time $t_{\text{norm}} = t/d$, which is the number of loading cycles n , and location $z_{\text{norm}} = z/h$, the total pore water pressure can then be written as

$$u_{\text{norm}} = \frac{u(z_{\text{norm}}, t_{\text{norm}})}{\hat{\sigma}_v} = \underbrace{\frac{\Delta u}{2} \cdot \sin(2\pi \cdot t_{\text{norm}} + \psi)}_{\text{pwp in stationary state, } u_{\text{ss}}} + \underbrace{\frac{2}{\pi} \sum_{j=0}^{\infty} \frac{(-1)^j}{1+2j} \cdot \frac{\cos[(1+2j)\frac{\pi}{2} \cdot z_{\text{norm}}]}{1 + (1+2j)^4 \frac{\pi^2 T_0^2}{64}} \cdot \exp\left[-(1+2j)^2 \frac{\pi^2 T_0}{4} \cdot t_{\text{norm}}\right]}_{\text{transient mean pwp, } u_{\text{mean}}} \quad (4.7)$$

In this Equation the pore pressure amplitude in stationary state Δu and the phase angle of the pore pressure variation ψ are given by

$$\frac{\Delta u}{2} = \sqrt{f^2 + g^2} \quad (4.8)$$

$$\psi = \arctan\left(\frac{g}{f}\right) \quad (4.9)$$

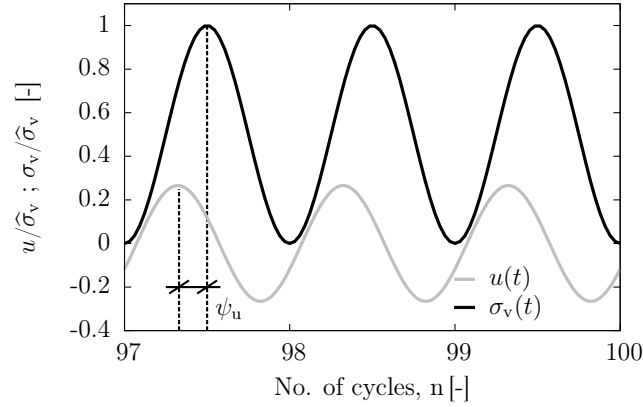


Figure 4.3: Phase shift between pore water pressure and vertical stress, from the analytical solution for linear-elastic, one-dimensional consolidation under haversine loading, computed with $\hat{\sigma}_v = 100 \text{ kN/m}^2$, $d = 120 \text{ s}$, $h_0 = 20 \text{ mm}$, $c_v = 1 \cdot 10^{-6} \text{ m}^2/\text{s}$.

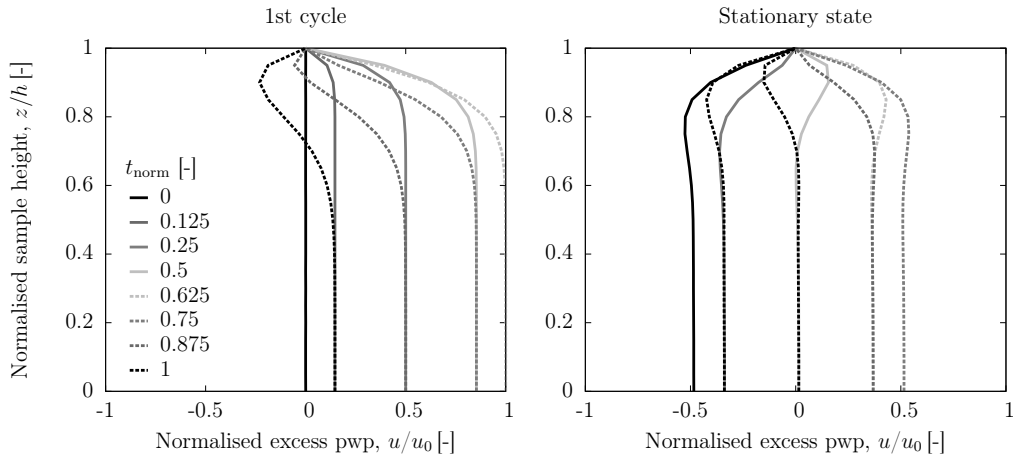


Figure 4.4: Pore water pressure over sample height in the first cycle and stationary state, from the analytical solution for cyclic loading, computed with $\hat{\sigma}_v = 100 \text{ kN/m}^2$, $d = 120 \text{ s}$, $c_v = 1 \cdot 10^{-7} \text{ m}^2/\text{s}$, $h_0 = 20 \text{ mm}$.

with

$$\frac{f}{\hat{\sigma}_v} = -\frac{1}{2} \Im \left\{ \frac{\cosh[\sqrt{\pi/T_0} \cdot z_{\text{norm}} \cdot (1+i)]}{\cosh[\sqrt{\pi/T_0} \cdot (1+i)]} - 1 \right\} \quad (4.10)$$

$$\frac{g}{\hat{\sigma}_v} = +\frac{1}{2} \Re \left\{ \frac{\cosh[\sqrt{\pi/T_0} \cdot z_{\text{norm}} \cdot (1+i)]}{\cosh[\sqrt{\pi/T_0} \cdot (1+i)]} - 1 \right\} \quad (4.11)$$

where $T_0 = \frac{c_v \cdot d}{h^2} = \frac{E_s \cdot k \cdot d}{\gamma_w \cdot h^2}$ [-] introduces the dependency on material and loading characteristics.

The mean pore water pressure in the first cycle $u_{\text{mean,1st}}$ can be written as

$$\frac{u_{\text{mean,1st}}}{\hat{\sigma}_v} = \frac{u_{\text{mean}}(\frac{z}{h} = 0, t = 0)}{\hat{\sigma}_v} = \frac{2}{\pi} \sum_{j=0}^{\infty} \frac{(-1)^j}{1+2j} \cdot \frac{1}{1+(1+2j)^4 \frac{\pi^2 T_0^2}{64}} \quad (4.12)$$

From Eqs. 4.7 - 4.12 it can be seen, that the pore water pressure dissipation under cyclic loading for normalised time and location depends only on the material and loading characteristics T_0 and $\hat{\sigma}_v$. The influence of variation in T_0 on the normalised pore water dissipation under cyclic loading is illustrated in Fig. 4.5.

As illustrated in Fig. 4.5a and Fig. 4.5b, the rate of consolidation depends only on the ratio c_v/h^2 . With increasing T_0 , t_{EOP} and n_{EOP} decrease. Figure 4.5c shows, the development of mean pore water pressure in the first cycle $\sigma_{\text{mean,1st}}$ and pore pressure amplitude Δu with T_0 . Both characteristics evolve congruently. For $T_0 \leq 0.1$ the pore pressure amplitude equals the applied load amplitude, with $\sigma_{\text{mean,1st}} = 0.5\Delta u$. For values $0.1 \leq T_0 \leq 1.8$ the pore pressure exceeds the load amplitude $\hat{\sigma}_v$ reaching a maximum of $\Delta u/\hat{\sigma}_v \approx 1.15$ at $T_0 \approx 1.8$. For $T_0 \geq 1.8$ the pore water pressure decreases with increasing T_0 .

4.2.2 Settlement s

The settlements from the analytical solution for cyclic loading can be calculated as

$$\begin{aligned} s &= \frac{1}{E_s} \int_0^z \sigma'_v dz - \frac{1}{E_s} \int_0^z (\sigma_v - u) dz = \frac{1}{E_s} \left[\int_0^z \hat{\sigma}_v \sin^2 \frac{\pi t}{d} dz - \int_0^z u(z) dz \right] \\ &= \frac{\hat{\sigma}_v}{E_s} \left[\sin^2 \frac{\pi t}{d} \cdot z + \frac{1}{2} \Im \left\{ \frac{\sinh[az(1+i)]}{a(1+i) \cosh[ah(1+i)]} - z \right\} \cdot \sin \left(\frac{2\pi t}{d} \right) \right. \\ &\quad \left. - \frac{1}{2} \Re \left\{ \frac{\sinh[az(1+i)]}{a(1+i) \cosh[ah(1+i)]} - z \right\} \cdot \cos \left(\frac{2\pi t}{d} \right) \right. \\ &\quad \left. - \frac{2}{\pi} \sum_{j=0}^{\infty} \frac{(-1)^j}{(1+2j)^2} \cdot \frac{\frac{2h}{\pi} \cdot \sin[(1+2j)\frac{\pi z}{2h}]}{1+(1+2j)^4 \frac{\pi^2 T_0^2}{64}} \cdot \exp \left(-(1+2j)^2 \frac{\pi^2 T_v}{4} \right) \right] \end{aligned} \quad (4.13)$$

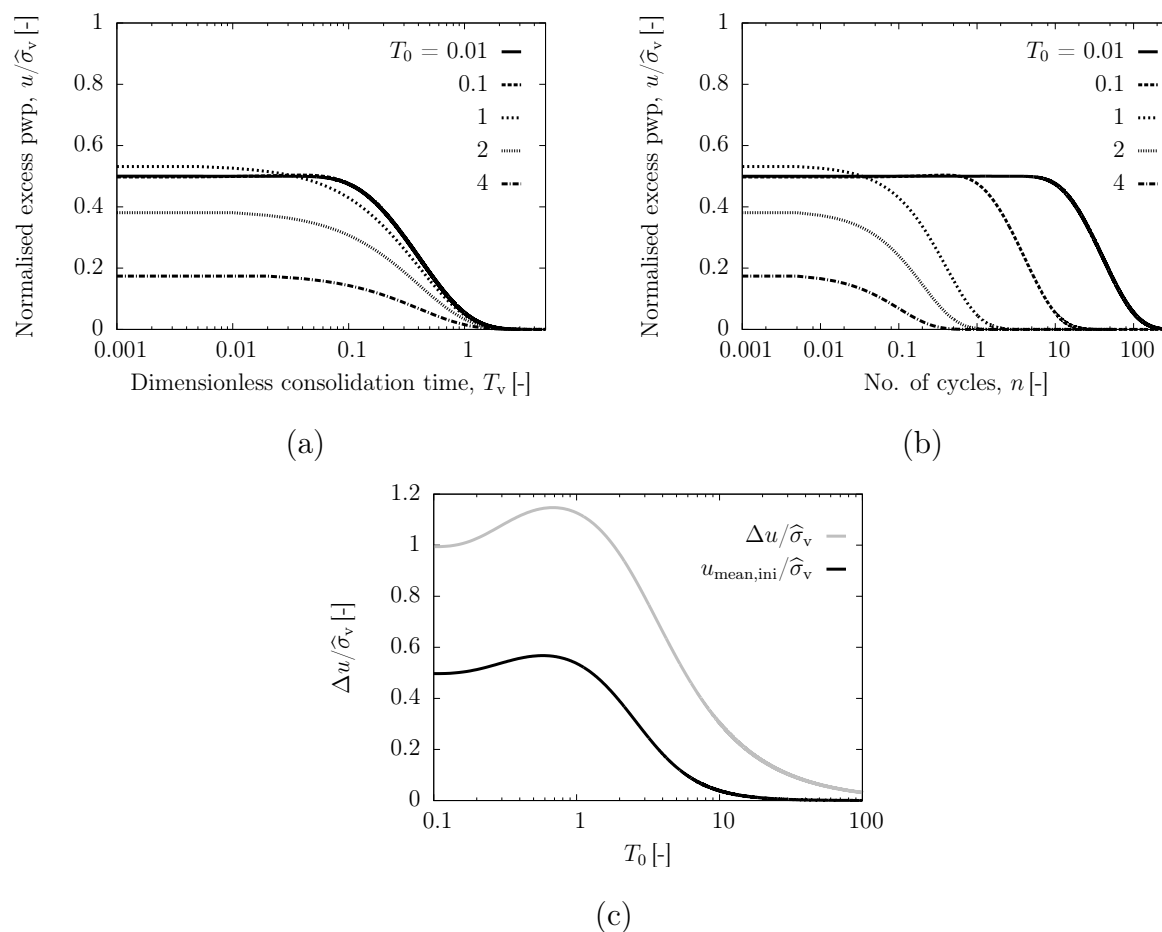


Figure 4.5: Influence of T_0 on the excess pore water dissipation from the analytical solution for consolidation under cyclic loading.

Figure 4.6 shows the development of settlements with time from Eq. 4.13 in comparison with the settlements under monotonic loading predicted by the analytical solution for identical material conditions in terms of c_v and sample height h as well as identical loading magnitude.

The cyclic settlements consist of the mean settlement s_m , which equals in its course the settlement curve under equivalent, monotonic loading. It is superposed by a cyclic settlement fluctuation of amplitude Δs . As known from the comparison of the pore water dissipation curves, for identical c_v the end of primary compression in the analytical solution is reached at the same time for cyclic and monotonic loading. The final mean settlement, assuming the same sample height and stiffness at equal loading magnitude, is only half the magnitude in cyclic compared to monotonic loading (compare Eqs. 3.22 and 4.19).

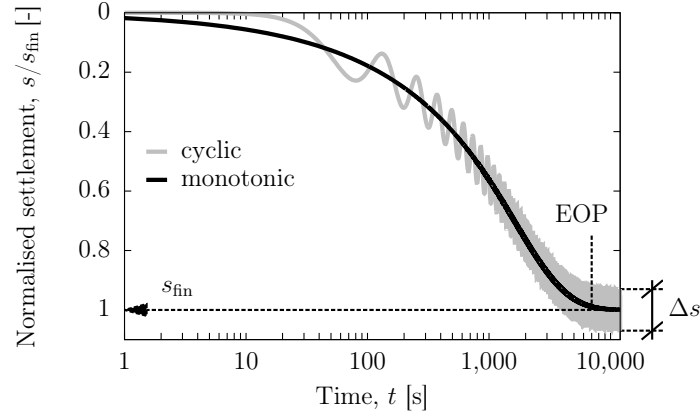


Figure 4.6: Normalised settlements versus time, from the analytical solution for linear-elastic, one-dimensional consolidation under haversine and monotonic loading, computed with $\hat{\sigma}_v = \sigma'_v = 100 \text{ kN/m}^2$, $d = 120 \text{ s}$, $h_0 = 20 \text{ mm}$, $c_v = 1 \cdot 10^{-7} \text{ m}^2/\text{s}$.

Analogue to the pore water dissipation, the settlements under cyclic loading can be identified by three characteristics: (1) the final mean deformation $s_{\text{fin}} = s_{\text{ss}}$, (2) the rate of mean deformation characterized by the consolidation coefficient, c_v , and (3) the deformation amplitude Δs and its development.

Like as the pore water pressure, the deformation s is shifted with respect to the applied loading by a phase shift ψ_s , which depends on the material and loading characteristics (see Fig. 4.7).

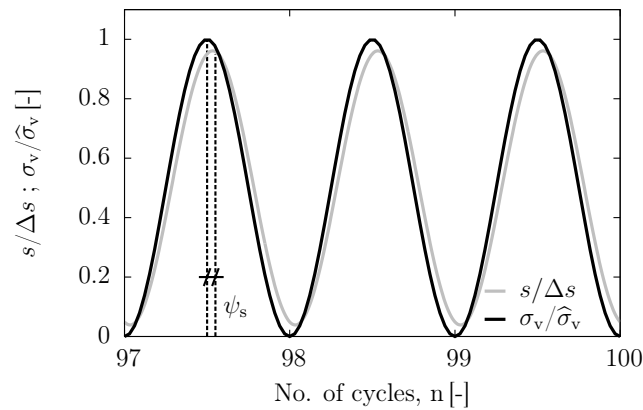


Figure 4.7: Phase shift between normalised settlement and vertical stress from the analytical solution for linear-elastic, one-dimensional consolidation under haversine loading, computed with $\hat{\sigma}_v = 100 \text{ kN/m}^2$, $d = 120 \text{ s}$, $h_0 = 20 \text{ mm}$, $c_v = 1 \cdot 10^{-6} \text{ m}^2/\text{s}$.

The displacement at the top s_{top} ($z=h$) can be written as

$$s_{\text{top}} = \frac{\hat{\sigma}_v}{E_s} \left[\frac{h}{2} - \frac{\Delta s_{\text{norm}} \cdot h}{2} \sin \left(\frac{2\pi t}{d} + \psi \right) - \frac{2}{\pi} \sum_{j=0}^{\infty} \frac{(-1)^j}{(1+2j)^2} \cdot \frac{\frac{2h}{\pi} \cdot \sin[(1+2j)\frac{\pi}{2}]}{1 + (1+2j)^4 \frac{\pi^2 T_0^2}{64}} \cdot \exp \left(-(1+2j)^2 \frac{\pi^2 T_v}{4} \right) \right] \quad (4.14)$$

with

$$\frac{\Delta s_{\text{norm}}}{2} = \sqrt{f^2 + g^2} \quad (4.15)$$

$$\psi = \arctan \left(\frac{g}{f} \right) \quad (4.16)$$

with

$$f = -\frac{1}{2} \Im \left\{ \frac{\sinh[\sqrt{\pi/T_0}(1+i)]}{\sqrt{\pi/T_0}(1+i) \cosh[\sqrt{\pi/T_0}(1+i)]} - 1 \right\} \quad (4.17)$$

$$g = \frac{1}{2} \Re \left\{ \frac{\sinh[\sqrt{\pi/T_0}(1+i)]}{\sqrt{\pi/T_0}(1+i) \cosh[\sqrt{\pi/T_0}(1+i)]} - 1 \right\} + \frac{1}{2} \quad (4.18)$$

where $T_0 = \frac{c_v \cdot d}{h^2} = \frac{E_s \cdot k \cdot d}{\gamma_w \cdot h^2}$ [-] introduces the dependency on material and loading characteristics.

The final settlement s_{fin} , can then be written as

$$s_{\text{fin}} = \frac{h \cdot \hat{\sigma}_v}{2E_s} \quad (4.19)$$

and the settlement amplitude in the stationary state as

$$\Delta s = 2\sqrt{f^2 + g^2} \cdot \frac{h \cdot \hat{\sigma}_v}{E_s} = \Delta s_{\text{norm}} \cdot \frac{h \cdot \hat{\sigma}_v}{E_s} \quad (4.20)$$

With Eq. 4.20 and Eq. 3.22 the deformation amplitude can therefore be approximated by

$$\Delta s = \Delta s_{\text{norm}} \cdot s_{\text{fin,monotonic}} \quad (4.21)$$

and

$$\Delta e = \Delta s_{\text{norm}} \cdot \Delta e_{\text{fin,monotonic}} \quad (4.22)$$

It can be seen, that s_{fin} depending on sample height, stiffness and load amplitude is independent of the load period d . However, Δs depends on T_0 , h and E_s . In contrast to the pore water pressure amplitude, the settlement amplitude cannot be described by T_0 solely.

Figure 4.8 demonstrates the development of Δs_{norm} with T_0 . For increasing T_0 , Δs_{norm} increases from 0 to 1.

4.3 Experimental studies in literature

In literature only a limited number of experimental studies on the consolidation behaviour under cyclic loading are available worldwide. Elgohary (1973) was one of the first to perform cyclic consolidation tests under oedometric conditions. In a high consolidometer (see Fig. 4.9a) he performed repeated loading tests on Kaolin samples and compared the outcome of the experimental results in terms of pore water pressure and settlement (see Fig. 4.9b) to an analytical solution presented in Wilson and Elgohary (1974) and tests under constant loading. His main conclusion was that the soil under repeated loading does not reach full consolidation $U_m = 1$ and occurs slower than in monotonic loading test.

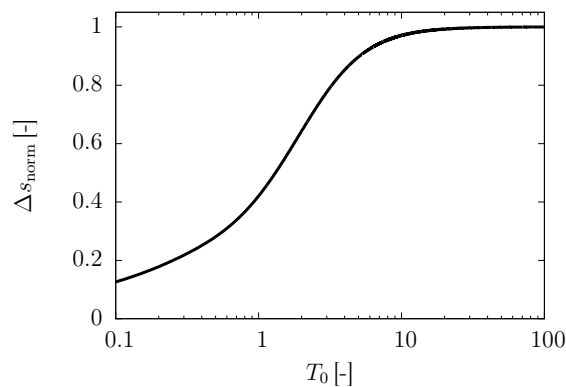


Figure 4.8: Influence of T_0 on the normalised settlement amplitude from the analytical solution for consolidation under cyclic loading.

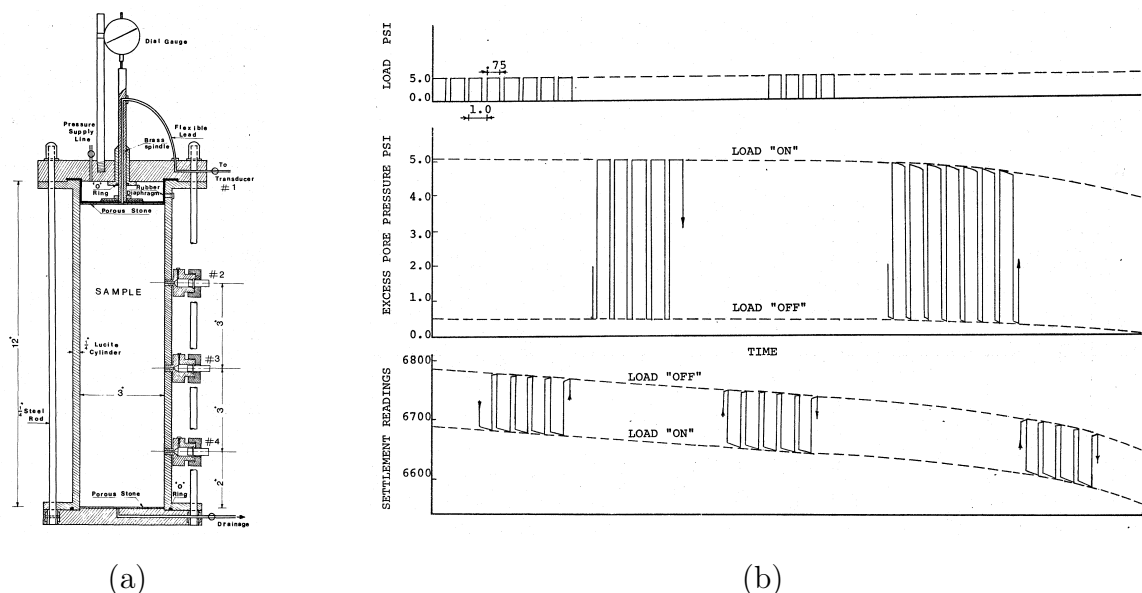


Figure 4.9: (a) Consolidometer cell and (b) main testing results from repeated loading tests (Elgohary, 1973).

In 1985, at Kyushu University, Japan repeated loading tests were performed on alluvial clay, comparing the settlement behaviour under repeated and static loading (Fujiiwara et al., 1985). Following this work, in the mid 1990s an inter-connected consolidation apparatus (see Fig. 4.10a) was developed (Kono, Ochiai and Yasufuku, 1995) to study remoulded clay material behaviour under cyclic loading (Kono, Ochiai, Omine and Tsukamoto, 1995; Kono, Ochiai, Yasufuku and Umezaki, 1995). The pore pressure and settlement at the maximum of each cycle were studied. It was found, that after a certain time a stationary-state condition is reached, where the pore water pressure approaches a constant value and change in the void ratio decreases linearly with the logarithm of time (see Fig. 4.10b). Moreover, the pore pressure maximum reached in the first cycle was shown to be about twice the value of the pore pressure in the stationary-state. The degree of consolidation was found to be the same under static and cyclic loading.

Another experimental study on cyclic consolidation is described in Rahal and Vuez (1998), showing in-situ measurements on cyclic silo filling. Expanding this study, Vuez et al. (2000) compared an analytical solution accounting for fluid compressibility to oedometer tests on a silt-bentonite mixture (load amplitude: $\hat{\sigma}_v = 25 \text{ kN/m}^2$, load period: 60 s- 20 h). To the knowledge of the author, it is the only study, where in the experiments pore pressure amplitude (attenuation) as well as the phase shift between pore water pressure and applied sinusoidal loading are measured experimentally. Unfortunately, a detailed analysis of the phase shift and its dependency on soil and loading characteristics are not

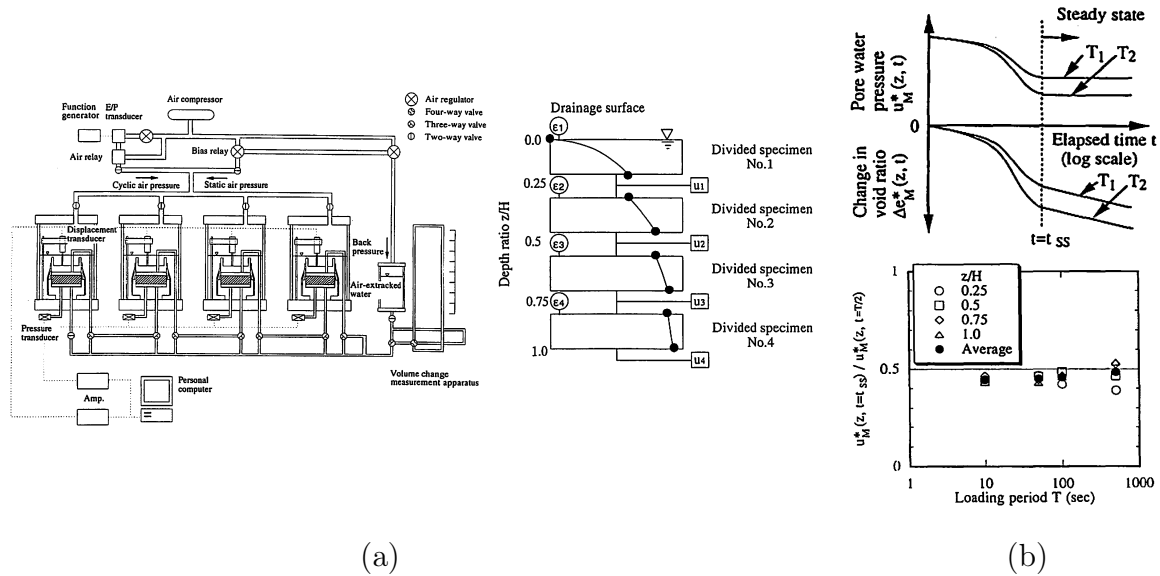


Figure 4.10: (a) Inter connected consolidation apparatus and (b) main results from (Kono, Ochiai, Omine and Tsukamoto, 1995).

given in this publication. The main conclusions given are, that the compressibility of the fluid (back-calculated from measurement data and analytical solution) reaches the compressibility of the pore fluid and that pore pressure exceeds loading about 15 % depending on load frequency, thickness of the soil layer and consolidation coefficient.

Further experimental studies on time-dependent loading in consolidation tests are described in Conte and Troncone (2006) and Toufigh and Ouria (2009). Conte and Troncone (2006) compared the deformation in step-wise loading tests on sandy silt with clay and clayey, silty sand in the oedometer as well as in situ measurements from an embankment construction to their analytical solution. Toufigh and Ouria (2009) compared their analytical solution to deformation measurement from repeated loading tests on clay from Kerman, Iran.

A recent study at Yazd University, Iran, analysed the consolidation behaviour of a silt from Meybod ($w_L = 28\%$ $I_P = 8\%$) under triangular, cyclic loading (Porhoseini et al., 2014; Abbaspour, 2014). A comparison of settlement and pore water pressure measurement with a linear and non-linear analytical solution is drawn. It states, that settlement in the experiment is up to twice as large as in the analytical model.

4.4 Summary

This chapter summarised the state of the art on consolidation under cyclic loading and introduced the analytical solution for the consolidation of a soil sample under cyclic loading of haversine form. In a literature review available research studies on consolidation under non-constant loading was studied. The three main enhancement paths followed in literature, i.e. the implementation of constitutive non-linearities, of different loading types and of various initial and boundary conditions to the consolidation theory of non-constant loading, were demonstrated. Based on the definition of initial and boundary conditions, the analytical solution for consolidation under cyclic loading of haversine form was derived in terms of pore water pressure and settlements. A survey on the limited number of experimental studies in literature was presented.

5 Oedometer device

In the following chapter the oedometer device designed and constructed to perform the experimental consolidation study at Ruhr-Universität Bochum is introduced. The analysis of the consolidation behaviour of soft soils causes special demands for the design of the oedometer cell. These requirements are illustrated in the following together with details of the construction used in the design of the modified device based on recommendation from literature. To prove the functionality and accurate measuring of the system, calibration tests were performed. The main results of these tests are presented in the last part of this chapter.

5.1 Introduction

In a conventional one-dimensional compression test the soil sample, which is constrained in lateral direction, experiences an axial deformation due to a stepwise, constant axial loading. The outflow of water during the consolidation process is allowed through drainage facilities at the top and bottom of the sample. Standard measurement comprises the vertical deformation of the soil sample with ongoing time.

However, the comprehensive experimental analysis of the transient consolidation behaviour of soft soils under oedometric conditions necessitates the use of a non-standard oedometer device, where the pore water pressure, the volume flow of water and the stresses in vertical and lateral direction as well as the friction can be measured. To fulfil these requirements a modified oedometer cell was designed and constructed at Ruhr-Universität Bochum, in which additional to the standard facilities these measurements are made possible.

5.2 Design and construction

5.2.1 General construction

According to German standard code DIN:18135 (2012), a conventional one-dimensional compression cell consists of a cylindrical ring, in which the soil sample is installed, a base and top plate with filter plates allowing the drainage from the sample and a fixation of the ring in radial direction. The general construction of the modified oedometer cell introduced here follows this basic concept.

Figure 5.1 shows the modified oedometer cell. The soil sample is embraced by a thin oedometer ring, placed between two filter plates. The oedometer ring is fixed in vertical position by three ring fixtures. Strain gauges applied to this thin ring allow the measurement of radial stresses.

The filter plates, on which the sample is placed, are located completely inside the oedometer ring. Drainage is allowed through these filter plates and drainage piping at the top and bottom or top or bottom only. In order to perform tests on very soft soil materials and slurries, it is necessary to seal the soil sample in a way that squeezing out of the soft material during loading is prevented. Therefore, O-rings are placed between top as well as bottom part of the oedometer device and the ring. A pore pressure transducer is installed in the bottom part of the device. It allows the measurement of pore water pressure dissipation during testing.

While the bottom part of the device is fixed in position by anchorage on the experimenting table, the top part is connected to the piston of the loading frame, which is responsible for the actual load application. A load cell at the top (included in the loading frame) and bottom part of the device allows the measurement of vertical force above and below the sample and facilitates the evaluation of the friction.

Sample size

Muhs and Kany (1954) and Berre and Iversen (1972) studied the influence of the specimen size on the consolidation behaviour. They showed that the length of the drainage path and friction between the sample and the oedometer ring have a significant influence on the compression rate and pore water pressure measurement. Therefore, the choice of an adequate drainage path length and consequently of the sample size in terms of diameter-

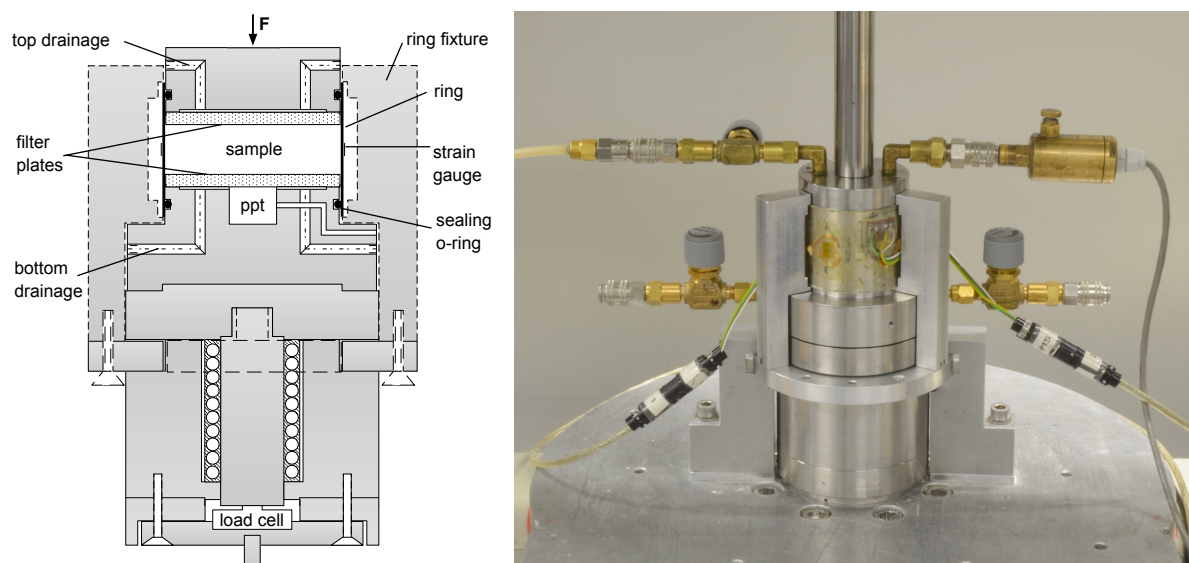


Figure 5.1: Sketch (left) and photograph (right) of the modified oedometer device.

to-height-ratio is an important issue within the construction of a modified oedometer cell.

In general, the specimen size is preferred to be as large as possible in order to be most representative of the soil structure itself and to compensate possible sample disturbances and inhomogeneities (Sivrikaya and Togrol, 2006). Additionally, with larger sample height, the measurement inaccuracy of the deformation measurement decreases. This particularly accounts for soft soils, which experience large deformation during the consolidation process.

On the other hand, large sample heights have the disadvantage of significant friction due to friction between the sample material and the oedometer ring. The effect of friction in oedometer cells has been studied by Taylor (1942); Burland and Roscoe (1969); Sivrikaya and Togrol (2006); Lovisa and Sivakugan (2015) and others. Some more details regarding these studies and their consequences for vertical stress measurement are given in Chapter 7.1.2.

Following these research studies, DIN:18135 (2012) specifies the diameter-to-height-ratio of the sample to be larger than 3 for fixed and larger than 2.5 for floating rings, with a diameter larger than 36 mm and height larger than 12 mm and five-times the maximum grain size for non-uniform soils or ten-times the maximum grain size for uniform soils. Usual diameter-to-height-ratios range between 3 and 5.

With respect to this, the dimensions for the oedometer device were chosen to be 70 mm in diameter and 20 mm in height, resulting in a diameter-to-height-ratio of 3.5. The influence of side friction between sample and ring was studied for this oedometer by different calibration tests. Results are demonstrated in 5.3.

5.2.2 Vertical stress and deformation measurement

Loading frame - load application and deformation transducer

The load application is provided by the UTS loading frame shown in Fig. 5.2. The loading frame allows testing under quasi-static load as well as displacement controlled loading and unloading. A load cell measuring the applied pressure at the top of the oedometer cell as well as a displacement transducer measuring the deformation are attached to the loading frame.

Load cell at the oedometer bottom

As illustrated above, the oedometer cell is designed and equipped for testing soft clays by the application of an O-ring sealing at outer edge of top and bottom plate of the device. Preventing the outflow of water or the squeezing out of fine soil material, this sealing has the disadvantage of causing additional friction during load application. The friction due to this constructional design has to be considered supplementary to the friction caused by friction between sample and oedometer ring.



Figure 5.2: UTS control stand: photograph with loading frame (centre), central processing unit (right side) and data acquisition (left side).

To account for this type of friction, the knowledge of the amount of friction is essential. Hence, additional to the load measurement above the oedometer cell, a load cell is installed in the bottom part of the oedometer device. This load cell enables an evaluation of friction and its development during load application. The detailed study of this issue is described in Chapter 5.3.

For the present study a load cell with a maximum capacity of 5 kN (type designation: K-13, manufacturer: Lorenz Messtechnik GmbH) was integrated into the bottom construction of the oedometer device. However, the load cell can be replaced effortlessly through the underside of the device so that an adaptation of the measurement range to the applied loading can be performed easily.

Figure 5.3 shows the special construction used for the bottom part of the oedometer device. The oedometer base including filter plate is placed on a load plate with a piston. This piston is guided with the help of ball bearing directly towards the load cell, which is positioned at the very bottom of the oedometer device. The ball bearing guarantees a load transfer from the bottom of the sample to the load cell with a minimum of friction within the load transmission facility. The bottom part of the oedometer device is screwed on the experimental table in order to fix it in position and avoid an uplift of the cell in the case of short periods of tensile forces acting on the device.

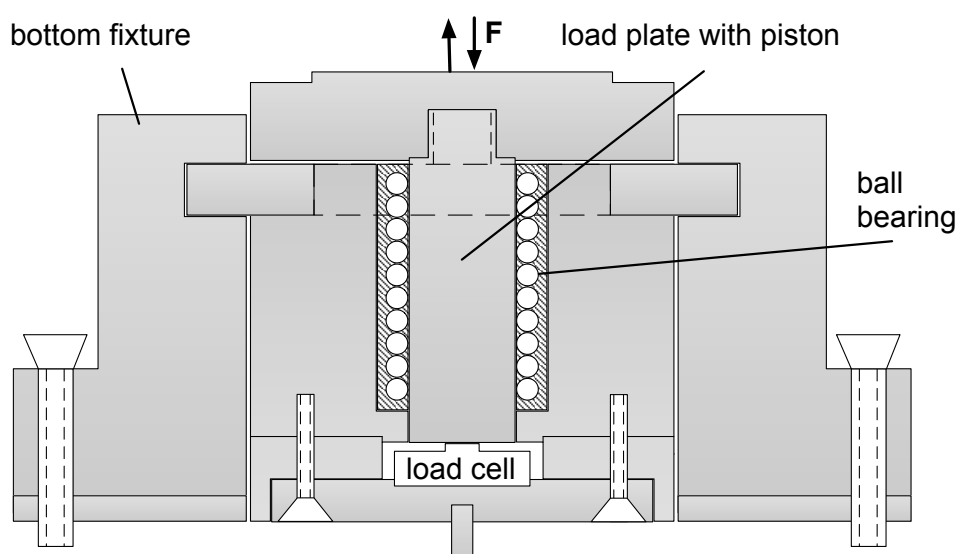


Figure 5.3: Bottom part of the oedometer device.

5.2.3 Oedometer ring and radial stress measurement

Ring dimensions and material

Figure 5.4 shows a front and top view of the oedometer ring used within the present study. It has an inner diameter of 70 mm and a height of 54 mm. The height results from the sample height and the additional length necessary for the sealing by o-rings attached to the top and bottom plate of the oedometer. The thickness of the ring results from calculations for the strain measurement to 0.75 mm, which is described later in this section.

The material of the ring likewise plays an important role regarding the friction, as this is strongly influenced by the friction coefficient of the utilised material. Olson (1986) in an experimental study evaluated the dependency of friction on the material used for the fabrication of the oedometer ring. Comparing fixed-type rings made out of cadmium-coated steel and ungreased / greased plastic respectively, they showed that in the stress range of up to 400 kPa the material may cause a severe friction of up to 20 % for tests on clay of low plasticity.

Following this study, particular care was taken to fabricate the ring in a manner to obtain a maximum sleek ring. Thus, the ring was lathed from solid, stainless steel material (austenitic chrome-nickel steel, material number 1.4301, with an E-modulus of approx. 200 GPa) polished from the inside. The stainless steel material was chosen in order to attain a rust-proof ring. The lathing guarantees a ring without any pre-set positions of failure or inhomogeneity in stress distribution along the circumference.

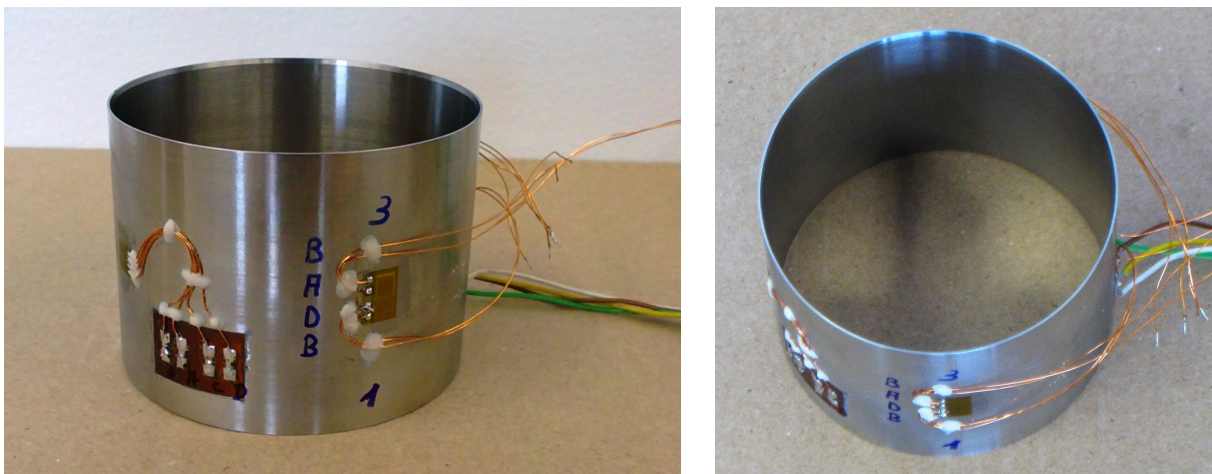


Figure 5.4: Stainless steel oedometer ring with applied strain gauges - top and front view.

Additionally, to reduce the amount of friction around the attached O-rings, spray grease was used within the experimental setup.

Ring type

Regarding the vertical fixation of the ring, in general two manners of construction are possible and conventionally in use. The ring may be fixed in vertical position (fixed-ring type) or may move freely during ongoing compression of the sample (floating-ring type).

The ring type influences the distribution and thus the amount of frictional stress occurring between oedometer ring and material. Muhs and Kany (1954) studied the influence of the chosen ring-type on the friction during consolidation. They analytically determined the friction distribution over the sample height for the two ring-types: fixed and floating ring (see Fig. 5.5). They report that for monotonic oedometer tests of usual height-to-diameter ratio on silt the amount of friction is slightly smaller using an oedometer ring of floating-ring type. However, Bauer (1992) investigated the effect of a floating-ring type for cyclic oedometer tests with loading and unloading conditions. By a comparison of the stress distribution for a floating-ring type, he showed that this ring-type shows smaller discrepancies from the in-situ homogeneous stress distribution and thus is to be preferred.

However, pre-studies with a floating-ring type implemented in the presented oedometer device revealed, that the floating ring was displaced during the cyclic deformation. This displacement can be explained by the high deformation of the soft soil sample due to

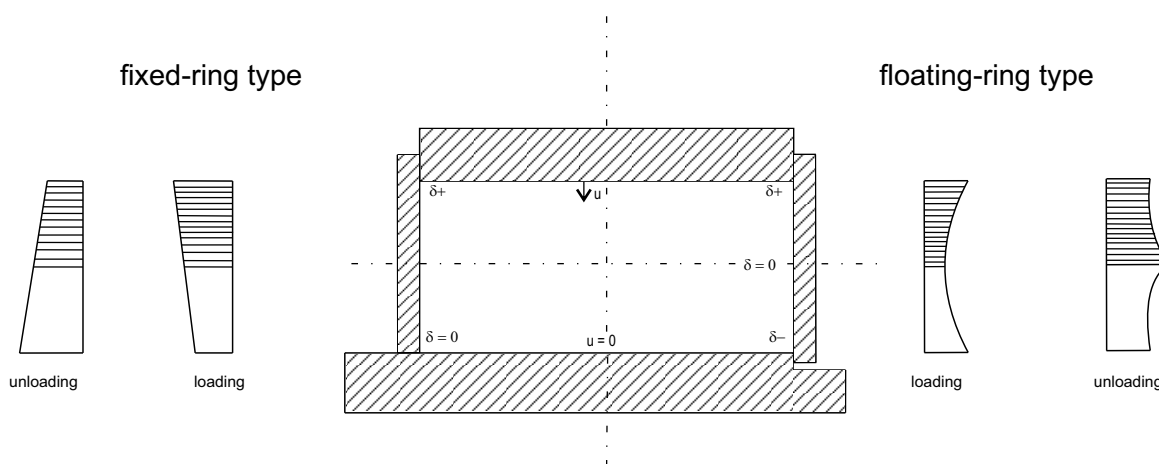


Figure 5.5: Stress distribution over the sample height for fixed-ring type and floating-ring type, modified after Muhs and Kany (1954).

its low stiffness and high compressibility. The resulting large relative movement of the oedometer top within the oedometer ring and the friction between sealing O-ring and oedometer top thus forced a movement of the ring. However, this ring displacement during the test was to be avoided strictly as due to this the friction distribution changes erratically. Additionally, for the measurement of radial stresses it is important to keep the ring in position during testing in order to measure the radial stress at a fixed position and under constant confining conditions.

Consequently, the general construction of this newly designed oedometer cell follows the basic design principle of a fixed-ring type. The fixation in vertical direction is realized by three ring fixtures embracing the ring at radial position of 0° , 120° and 240° . The ring fixtures themselves are screwed to the outer part of the oedometer bottom (see Fig. 5.1), so that frictional forces transmitted through the ring are directly transferred to the experimental table and not to the load cell included in the oedometer bottom part.

Radial stress measurement by applied strain gauges

In order to allow the analysis of the full stress state and to study e.g. the anisotropic behaviour of deposited natural clays, the measurement of radial stress and its development during the consolidation process was to be enabled within the construction of the modified oedometer device. Based on the demand for constrained radial deformation, the measurement of radial stresses in conventional oedometer devices is rather difficult.

In literature, different methods to measure the radial stress under oedometric conditions can be found. Hendron (1963) and Brooker and Ireland (1965) gave an overview of older measurement systems. Newer systems basically use the therein described concepts and improve them with the help of modern measuring and control technology (Bauer, 1992). In general two basic approaches can be distinguished: systems with and without deformation compensation. In the so-called compensation method a deformation of the oedometer ring due to loading is compensated by load application in the counter-direction. Devices using both techniques are illustrated in Bauer (1992):

The K_0 -triaxial cell developed by Bishop et al. (1965) is a double-cell triaxial apparatus, in which the integral deformation of the sample is measured and compensated by the water surrounding the sample. The stress-meter by Sherif et al. (1974) uses a stiff plate for stress-controlled compensation of the radial deformations. The high pressure chamber by Hendron (1963) as well as the enhancement developed by Gareau et al. (2006) are further variations of the compensation method. Within these methods, the radial strain

is first measured by strain gauges applied to the inner oedometer ring and consequently compensated by application of oil pressure.

The second type of systems works without deformation compensation, but with an oedometer ring allowing for very small radial deformations, from which the stress state can be calculated. General examples for this type of devices can also be found in Bauer (1992): the large cell construction by Kjellman and Jakobsen (1955), the K_0 -oedometer by Dyvik et al. (1985) as well as the oedometer by Komoronik and Zeiteln (1965). In addition to these, studies on oedometer constructions exist using strain gauges applied to the oedometer ring to measure the radial stress from the ring deformation itself. Here, particularly the studies on oedometer constructions by Kolymbas and Bauer (1993) and Senneset (1989) were used as archetypes for the design of the oedometer device conceived for the present study.

An evaluative comparison of the two methods for radial stress measurement under oedometric conditions by Bauer (1992) reveals the following:

- In the compensation method, the compensation application is influenced by several factors, difficult to control.
- The deviation from the K_0 condition in the method without deformation compensation can be calculated before the testing and kept sufficiently small by the choice of an adequate ring thickness.
- The ring construction without deformation compensation is much more straightforward and therefore represents a cost efficient way of construction.

Following this evaluation, in the present oedometer design, the measuring technique for radial stresses without deformation compensation was chosen. The method of choice in this case is the application of strain gauges on a thin oedometer ring. As described by Bauer (1992) non-contact displacement measurement by, e.g. by wave transit time measurement, could be an alternative for the deformation analysis, but are very expensive regarding installation and cost.

As described above, one key point in the design of the oedometer ring for radial stress measurement by strain gauges is the ring deformability or ductility. The deformability is dependent on the ring material and the ring thickness or the ratio between ring thickness and diameter respectively. As the material was chosen to be an austenitic chrome-nickel steel (material number 1.4301, with an E-modulus of approx. 200 GPa) and the diameter was preset to be 7 mm, the ring thickness had to be calculated achieving a compromise between the two following antithetic requirements:

- The ring should experience small deformation in order not to deviate to far from the oedometric condition of constrained lateral deformation.
- The ring should allow for enough deformation to guarantee a high resolution of the measurement value.

For the calculation of tangential ring deformation, Barlow's formula was used:

$$P = \frac{2 \cdot \sigma_t \cdot t}{D} \quad (5.1)$$

where P is the applied pressure, σ_t is the tangential stress, t is the ring thickness and D is the ring diameter.

Under the assumption that deformation is to be in the linear range only, Hooke's law is valid. Consequently,

$$\sigma_t = E \cdot \varepsilon_t \quad (5.2)$$

To fulfil the two antithetic requirements listed above, the radial strain is limited to $\varepsilon = 0.01\%$. With this assumption, the ring thickness for vertical loading of the oedometer cell can be calculated to be

$$t = \frac{P \cdot D}{2 \cdot E \cdot \varepsilon_t} = \frac{400 \text{ kPa} \cdot 0.7 \text{ mm}}{2 \cdot 200 \text{ GPa} \cdot 0.01\%} = 0.7 \text{ mm} \quad (5.3)$$

For the strain measurement two different strain gauge systems were applied. First of all, two t-rosette strain gauges placed oppositely on the ring were connected to one measuring system. Additionally, a Wheatstone full bridge strain gauge measuring system was applied at 90° position to the t-rosettes. All strain gauges have a nominal resistance of 350Ω and were applied using M-Bond 200 cyanoacrylate strain gauge adhesive. Additionally, M-Bond 610, a two-component, solvent-thinned, epoxy-phenolic adhesive, was used to coat the strain gauges. Care was taken to align them fully horizontally in order to prevent disturbances due to the lateral strain sensitivity of the strain gauges. Particular considerations regarding temperature influences on the strain gauge measurement could be neglected as all tests are performed within a climate-controlled laboratory with a variation in temperature of $\pm 1^\circ \text{C}$.

5.2.4 Drainage system and pore pressure measurement

Drainage facilities and filter plates

The modified oedometer device possesses in total four drainage facilities, as in each of the top and bottom plate two drainage pipings are included (see Fig. 5.6). This facilitates

- a. the application of different drainage scenarios during oedometer testing (drainage through top and bottom or top or bottom only).
- b. the individual flushing of top and bottom part of the device in order to purge potentially included air bubbles in the piping system.
- c. water flow from bottom to top of the sample as required for e.g. permeability tests and sample saturation in an oedometer cell.

The sample itself is embraced by two filter plates made of sinter material (see Fig. 5.6). The filter plates are cut-outs from larger plates of GKN sinter metal. The sinter material was chosen regarding its coarseness and permeability in the way that the filter plates do not hinder or retard the pore water in flowing out of the sample. As air inclusions in the filter plates were to be avoided. The filter plates had to be carefully de-aired before each testing. This de-airing was carried out using a desiccator (see Fig. 5.9).

The filter plates are placed on the bottom part and screwed to the top part of the oedometer device respectively. A milled ridge at the edge of filter plate and top and bottom part guarantees the facile centering of the filter plates. On the surface of the top and bottom plate milled slots allow the distribution of water underneath the filter plates (compare Fig. 5.6 -bottom and Fig. 5.8). This guarantees a rapid drain of water from the sample towards the outflow or pore pressure transducer.

Pore pressure measurement

Pore pressure measurement in cyclic oedometer tests causes many challenges. For monotonic loading tests it was found that the pore pressure measured at the bottom of an oedometer specimen does not completely coincide with the excess pressure predicted by Terzaghi's consolidation theory. Usually, the measured maximum value of pore water pressure is detected not immediately after the application of an additional pressure increment but retarded, i.e. after a finite time-span. Furthermore, the maximum value is usually smaller than the applied pressure increment. These effects can be related to the stiffness of the measuring system, which is influenced by inclusion of air-bubbles and

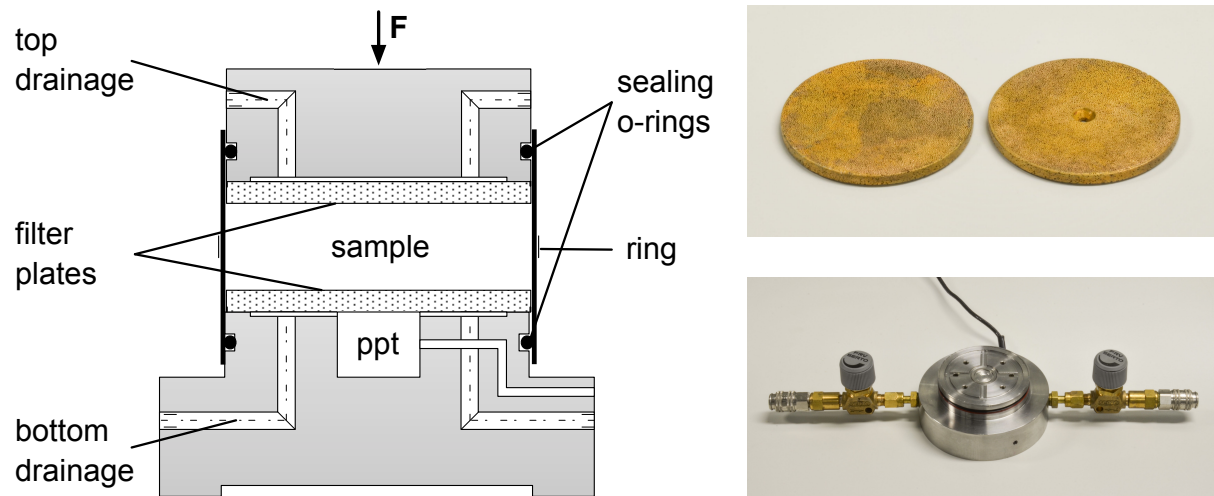


Figure 5.6: Drainage system of the oedometer cell (left) with photos of filter plates (top) and drainage slots on oedometer bottom (bottom).

geometry as well as material used for the system, and its relationship to the stiffness of the soil skeleton.

A multitude of studies can be found in literature dealing with the measurement of pore water pressure in soil-mechanical experiments and the influence of the measuring system stiffness, e.g. see Whitman and Richardson (1961); Gibson (1963); Perloff et al. (1965); Northey and Thomas (1965); Burland and Roscoe (1969); Robinson (1999).

Gibson (1963) studied the influence of the system flexibility on the pore pressure measurement, namely the maximum pore water pressure and its retardation in time. He described, that the system flexibility can arise from two effects: from compressibility of the fluid itself by included air-bubbles in the water volume, which can be compressed and therefore increase the compressibility, and from the volume expansion of the measurement system. Additionally, Burland and Roscoe (1969) stated that

"The most important requirement of a pore water pressure probe is that it should be as 'stiff' as possible (i.e. the volume of water passing through unit area of the porous surface of the probe during unit change in pore water pressure should be extremely small). It is also important that the volume of 'dead water' between the porous tip and the pressure sensing device should be as small as possible."

Consequently, two basic principles have to be considered in the construction of a pore pressure measurement system:

1. Minimisation of air inclusions in the water volume inside the measuring system, i.e. apply measures to avoid or remove occluded air-bubbles
2. Maximisation of the measuring system stiffness, i.e. minimisation of water volume in the measuring system

Hence, for the general application of pore pressure measurement frequently miniature pore pressure probes are used, which are embedded in the soil and therefore involve a very small volume of water. However, this technique requires the penetration of the recording device into the soil and might cause disturbances in the sample, which is a problem for sample volumes as small as the present one. Moreover, in the present study the pore water pressure is not to be measured locally, as achieved by miniature pore pressure probes, but as an integral value over the bottom of the sample in order to avoid measurement of geometrical effects as for instance the Mandel-Cryer effect (Mandel, 1953; Cryer, 1963; Gibson et al., 1963).

Therefore, in the present oedometer design, a compromise had to be found permitting an accurate, global measurement of pore water pressure. As described above the sample is embraced by filter plates covering the complete top and bottom surface of the sample. Underneath the filter plate, a drainage loop is milled into the bottom plate, which is filled with de-aired water and distributes the water volume underneath the sample and water pressure respectively. In the centre of the bottom plate a piezo-resistive pore pressure transducer (ppt) with a diameter of 19 mm fabricated by KELLER is implemented (see Fig. 5.7). It is capable of measuring positive water pressures up to 1000 kPa and negative water pressures up to -100 kPa, as required during unloading load-steps.

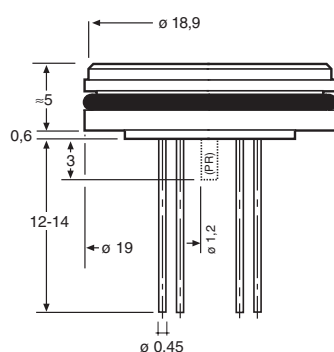


Figure 5.7: Photograph and sketch of the piezo-resistive pressure transducer (KELLER, 2007).

Figure 5.8: Implemented ppt in oedometer bottom.

The pore pressure measuring system can be flushed through the both-sided bottom drainage piping, in order to remove possible air-inclusions in the measuring system. Additionally, the water volume in the system is kept minimal. Both, in order to accommodate the two construction requirements listed above and to guarantee a high stiffness of the measuring system. The feasibility of these measures has been proven by calibration testing (see Chapter 5.3) and comparison of the measurements to the data presented in literature (see Chapter 7.2).

Outflow measurement

The volume of water squeezed out from the sample during consolidation testing is measured by a volume measuring unit. Hence, one of the top drainage pipes is connected to the volume measuring system (see Fig. 5.10), where the expelled water flows into a stand pipe. By a differential pressure gauge the water level rise in the stand pipe can be determined in comparison to a reference pipe. For details of the construction see e.g. Wichtmann (2005). From the water level rise and the known diameter of the tube, the expelled water volume can be calculated. Under the assumption of full saturation of the sample an equivalent settlement can be assessed additionally.

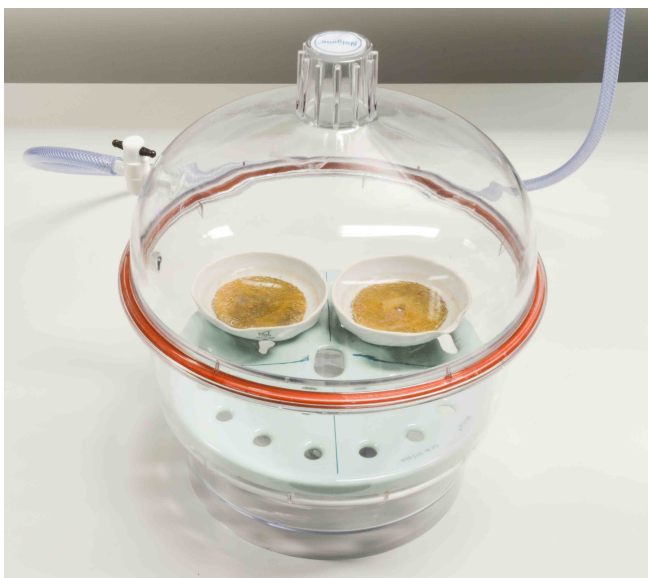


Figure 5.9: De-airing of filter plates in desiccator. Figure 5.10: Volume measuring unit.

5.3 Calibration

In order to prove the functionality and the correctness of the oedometer measurement, calibration tests were performed on a steel dummy as well as on water and clay under undrained conditions. The results of these calibration tests are presented in the following section analysing the plausibility of the different measurements, the self-deformation of the system, friction due to the sealing O-rings and typical Skempton B-values reached for the kaolin clay slurry.

5.3.1 Calibration with steel

In a first calibration test a stainless steel dummy was tested in the oedometer cell. The steel dummy was fabricated from V2A steel material with an elastic modulus of approximately 200 GPa. With a diameter of 69.5 mm and a height of 20 mm the size of the dummy approximates the size of the later soil sample. The steel dummy was inserted and tested in the closed oedometer cell. Due to the slightly reduced diameter no force bound between oedometer ring and dummy was persisting.

System deformation

Due to the high elastic modulus of the dummy material and the comparatively small applied maximum load of 400 kN/m^2 , the deformations resulting from the steel dummy can be neglected. All deformations occurring thus can be assigned to the self-deformation of the system.

Figure 5.11 shows the deformation curve under repeated loading-unloading of the steel dummy itself up to a maximum load of 400 kN/m^2 . Two main characteristics can be observed: First of all, it can be seen, that the self-deformation is non-linear. Secondly, in the first loading a deformation of approx. 0.07 mm is imprinted. Both characteristics could be reproduced in several calibration tests of the same type. They can be explained by the non-linear deformation of the filter plates consisting of porous sinter material and an arranging deformation of the system caused by screwed and loosely applied connections. However, these plastic deformations are small enough to be neglected compared to the later testing deformations in the consolidation analysis.

The self-deformation of the system amounts to approximately 0.26 mm at 400 kN/m^2 and can be well approximated with the following root function, which is used to purge

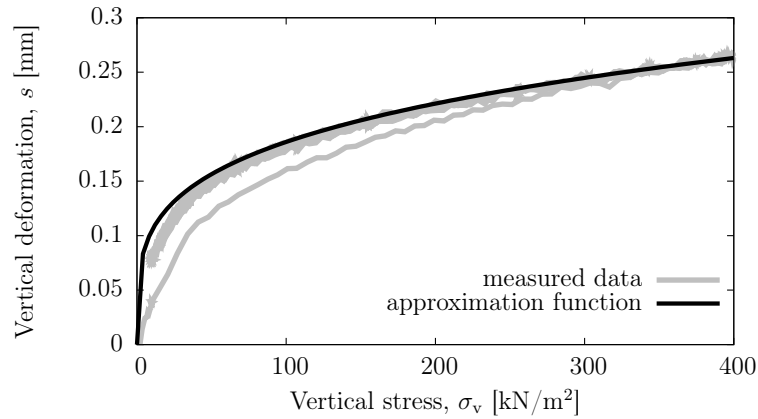


Figure 5.11: Stress-deformation diagram from calibration with steel dummy under repeated loading-unloading.

the deformations measured in the consolidation analysis from the self-deformation of the system:

$$s_{\text{self}} [\text{mm}] = \frac{\sqrt[4]{\sigma_v [\text{kN/m}^2]}}{17} \quad (5.4)$$

Later shown experimental data was corrected by this function accounting for the self-deformation of the system. The relatively high self-deformation of the system can be explained by the rather high compressibility of the sinter material of the filter plates and the rather long load piston of the UTS loading frame.

Vertical stress

Figure 5.12 shows the vertical stress measured at the bottom of the device depending on the vertical stress applied at the top for the calibration tests on a steel dummy. It can be observed, that for small deformations in the range of the self-deformation of the system almost no frictional loss is occurring.

5.3.2 Calibration with water

In a second calibration test the oedometer cell was filled with water up to a height of 20 mm, equalling the later sample height. The system was fully flushed to remove possible air-inclusion. Than all drainage was closed and a vertical loading of different type (see

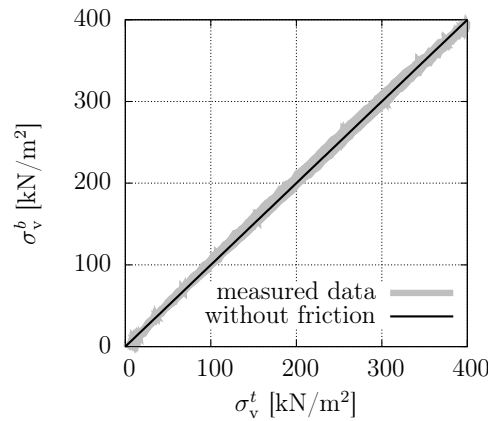


Figure 5.12: Vertical stress diagram from calibration with a steel dummy.

Fig. 5.13) was applied to the undrained system. From this calibration test the vertical and radial stress as well as the pore pressure measurement can be validated.

Vertical stress and friction

Figure 5.13 illustrates the applied and measured vertical stress as well as the friction in the undrained calibration test on water. Thereby, the friction is calculated as the difference between the vertical stress at the top σ_v^t and the vertical stress at the bottom σ_v^b of the sample.

$$F = \sigma_v^t - \sigma_v^b \quad (5.5)$$

The following observations regarding friction can be made

- The friction amounts up to a total stress of approx. $+15 \text{ kN/m}^2$ at the maximum loading of 400 kN/m^2 and to approx. -5 kN/m^2 after complete unloading.
- Thus, maximum $+3.75\%$ of the applied loading is transferred to friction during loading and -5% during unloading.
- The friction caused during unloading is in total larger than during loading.
- Hence, after loading and unloading an imprinted frictional stress remains, which abates by time to 0.

In general, it can be assumed that the total friction can be subdivided into sticking and sliding friction parts. From the observations and the fact that deformations are small

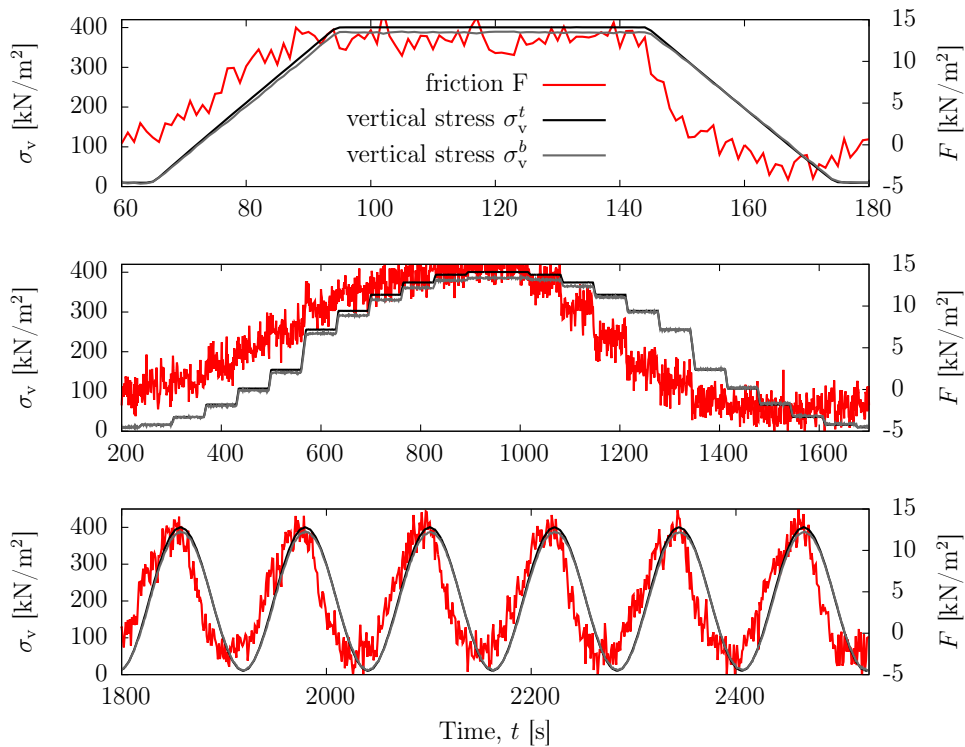


Figure 5.13: Vertical stress and friction from calibration with water.

within this calibration test, it can be concluded that mostly sticking friction is responsible for the friction measured here. As there is no force bound between water and oedometer ring, the frictional stress measured here can be assigned completely to the friction of the cell sealing system, namely the friction between O-rings and oedometer ring.

Figure 5.14a shows the evolution of friction depending on the applied vertical load. It can be seen that the friction during loading is almost linear, while the loss during unloading is non-linear, reducing more pronouncedly in the higher stress ranges. It can be concluded, that the friction is (a) dependent on the applied load, but also (b) dependent on the loading direction and magnitude. Therefore, the plotted relation cannot be used to purge the later stress measurement in the consolidation analysis. Still, this calibration test gives an idea of the amount of sealing friction compared to the sample friction, which is analysed in more detail in Chapter 7.1.2.

Radial stress

The radial stress is measured by means of two strain gauge systems (SG1 and SG2), as illustrated above. Figure 5.14b shows the measurement of these two compared with the

theoretical graph for water. The theoretical graph for water follows the assumption of an isotropic water pressure neglecting effects of air-inclusion in the fluid and the existence of an additional hydrostatic water pressure caused by the filling height of the "water sample" of 20 mm.

It can be seen that SG 1 is almost perfectly parallel to the theoretical graph, while SG 2 is slightly inclined and thus for smaller stresses underestimates and for larger stresses overestimates the radial stress. As the same trend was found from calibration tests on clay and although this effect could be accommodated by the application of calibration factors, in the following consolidation study SG 1 is primarily used for the analysis of radial stress evolution.

Pore pressure measurement and system saturation

From the calibration test with water also the pore-water pressure measurement as well as the system saturation can be calibrated. Hence, Fig. 5.15 displays the measurement of the pore-water pressures. It shows that the applied vertical load is entirely captured by the pore pressure transducer and that there is no significant time delay in the measurement, which validates the stiffness of the measuring system itself as elucidated above. A more detailed analysis of this issue is presented in Chapter 7.2.

From the amount of compression during the undrained loading of water up to 400 kPa conclusions regarding the compressibility of the system can be drawn. Figure 5.17 shows the compression of water during load application in the calibration test with water. A

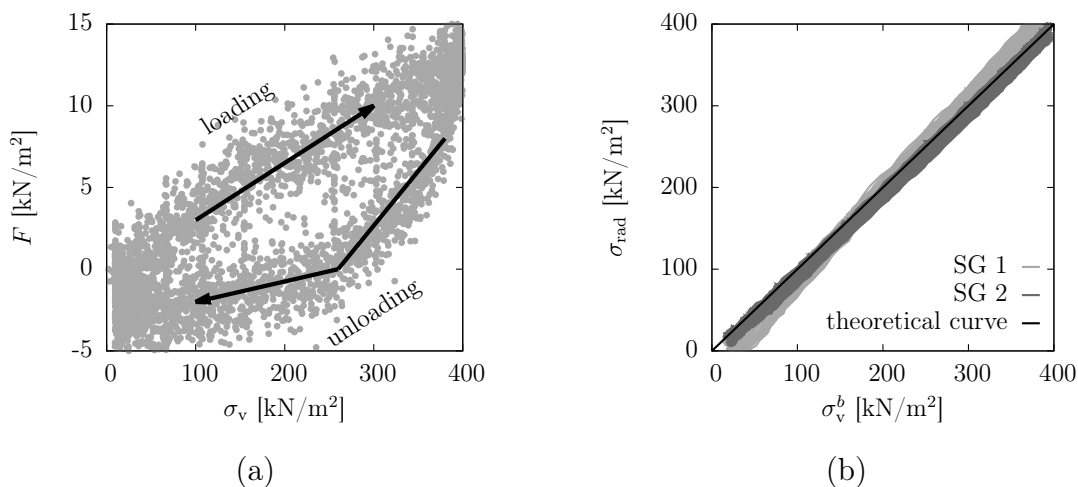


Figure 5.14: (a) Frictional stress and (b) radial stress over vertical stress, from calibration with water.

maximum, vertical compression of approx. 0.6 mm is detected, which corresponds to a maximum of 3% of the height of the water volume.

5.3.3 Calibration with clay

In a third calibration test a kaolin clay sample equivalent to the samples in the later consolidation analysis, with a water content of $w = 59\%$ and a height of 20 mm, was installed in the oedometer test. Like in the consolidation experiments, the system was flushed to remove possible air-inclusion. Then the drainage system was closed and a vertical loading of the same type as in the calibration with water was applied to the undrained system. This calibration test enables the validation of the retardation in pore-water pressure measurement and degree of saturation of a typical clay sample, which is illustrated in the following. As all other results from this calibration are equivalent to the calibration with water, they are not discussed here any further.

Pore pressure measurement

Figure 5.16 displays the pore-water pressure measurement in the calibration test on an undrained clay sample. Only a negligible retardation in the build-up of the pore-water pressure can be observed, which lies within the range of measurement accuracy.

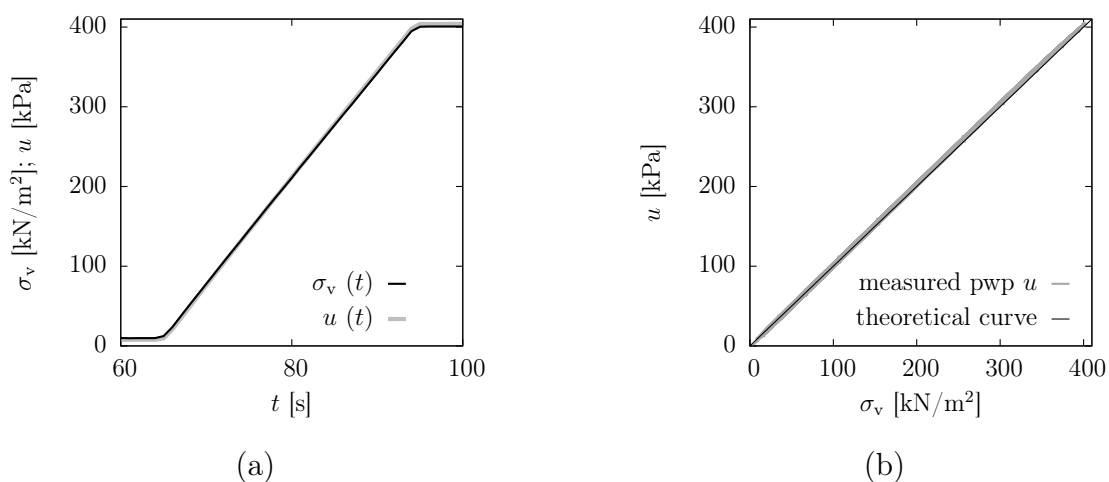


Figure 5.15: (a) Vertical stress and pore-water pressure versus time, (b) pore water pressure versus vertical stress, from calibration with water.

Sample saturation

From the comparison of compression due to loading in the calibration tests with water and clay (see Fig. 5.17) it can be seen that the maximum, vertical compression of 0.6 mm is detected in both tests. Thus, it can be concluded that the saturation of the system is only to an insignificant amount influenced by a possible non-saturation of the sample.

5.4 Summary

To perform the experimental study on the cyclic consolidation behaviour of slurry-type fine-grained clays, a modified oedometer cell was designed and constructed at Ruhr-Universität Bochum. The design comprising vertical stress and deformation measurement, oedometer

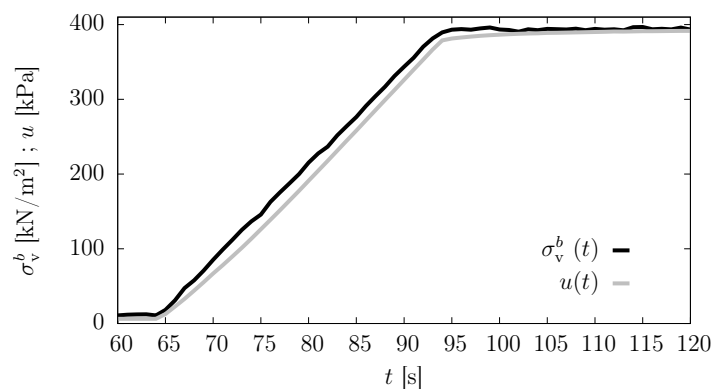


Figure 5.16: Pore-water pressure over time, from calibration with clay.

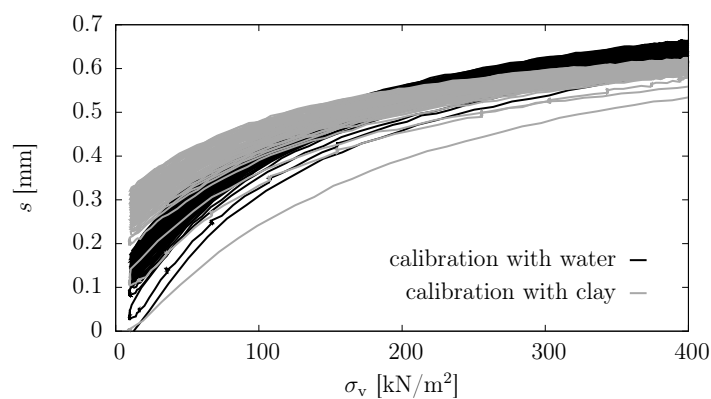


Figure 5.17: Stress-dependent compression, from calibration with water and clay under repeated loading.

ring and radial stress measurement as well as drainage system and pore water pressure measurement was introduced in this chapter. Herein, the particular features of the device defining the difference to a conventional oedometer device were illustrated. The general construction of the designed oedometer device is that of a fixed-ring type oedometer cell with typical diameter-to-height dimensions of 70-20 mm. The vertical stress measurement at the top and bottom of the sample allows for the calculation of friction in the sealed system. The thin-walled oedometer ring, equipped with two strain gauge systems, enables the measurement of radial stress. A two way drainage systems makes different drainage configurations possible, of which the top-drained-bottom-undrained configuration with pore pressure measurement at the bottom of the sample was selected for the present study. The presented calibration with steel, water and clay provides the validation of the device regarding the system deformation, stress, friction and pore water pressure measurement as well as the system and sample saturation.

6 Materials and methods

Chapter 6 illustrates the soil materials and experimental protocols used within the present study. First of all, the two soils - Spergau kaolin clay and Onsøy clay - are characterised regarding their basic material properties and mineralogy. The second part of this chapter deals with the performed oedometer study. The experimental programme is introduced regarding the applied loading functions and material variation. Moreover, the sample preparation techniques used for reconstituted and natural soil samples are described and the installation process for the experimental programme comprising monotonic and cyclic consolidation tests is illustrated.

6.1 Materials

6.1.1 General

The following section characterises the two soil materials used in the present study: Spergau kaolin clay and Onsøy clay. This characterisation covers the main basic material properties such as specific gravity, grain size distribution, Atterberg limits and permeability. Moreover, the mineralogy of the clays is characterised by chemical composition, specific surface area and cation exchange capacity. Results are compared to relevant literature on the two materials.

6.1.2 Spergau kaolin clay

The kaolin clay used for the present study is a reconstituted clay material originating from Spergau, Germany. The sample material was prepared from milled clay pellets. Details are describe in Chapter 6.3.1. Numerous, completed as well as on-going studies executed at *RUB Soil Laboratory* were performed using this kaolin clay (see e.g. Baille, 2014; Haase and Schanz, 2016). The following characterisation is based on these works.

Specific gravity and grain size distribution

The specific gravity ρ_s of kaolin clay was determined according to ASTM D854-14 (2014) by pycnometer method using kerosene as recommended by Head (1998) to be $\rho_s = 2.63 \text{ g/cm}^3$. The grain size distribution for Spergau kaolin clay was determined by Baille (2014) using sedimentation technique according to DIN:18123 (1996) and by laser diffraction method. Figure 6.1 presents the comparative results.

The difference in the grain size distribution curves for the two methods can be explained by the different dispersing agents used during the sample preparation: Trinonylphenylphosphite (TNPP) for laser diffraction method and Tetrasodium pyrophosphate (TSPP) for sedimentation analysis (Baille, 2014). However, also in general the two methods are not expected to give the exactly same result. This can be explained first of all by the inherent variability of the tested material and secondly by the different assumptions underlying the two methods. In the sedimentation technique the sedimentation velocity is measured. By the use of Stoke's law, the particle diameter can be calculated from the velocity and particle density, idealising the particle to be of spherical shape with an equivalent particle diameter. The laser diffraction method uses the detected deflection of a laser beam directed to the particle. From the detection of the laser deflection and calibration data the particle size is back calculated. Therefore, in both methods the individual shape of the particle is not taken into account.

Atterberg limits and plasticity

The liquid limit w_L and plastic limit w_P were determined according to ASTM D4318-10e1 (2010), using the Casagrande method for the determination of w_L . The plasticity index I_P was calculated as

$$I_P = w_L - w_P \quad (6.1)$$

and is a measure of how the soil behaviour reacts to changes in water content.

According to DIN:18196 (2006) the liquid limit and plasticity index together describe the plasticity of a soil. Using these two characteristics, the soil can be classified using the empirical A-Line, developed by Arthur Casagrande, in the plasticity diagram. The plasticity diagram for kaolin clay can be found in Fig. 6.2. With a liquid limit of $w_L = 51\%$ and a plasticity index of $I_P = 18.7\%$ Spergau kaolin lies slightly below the A-line in the

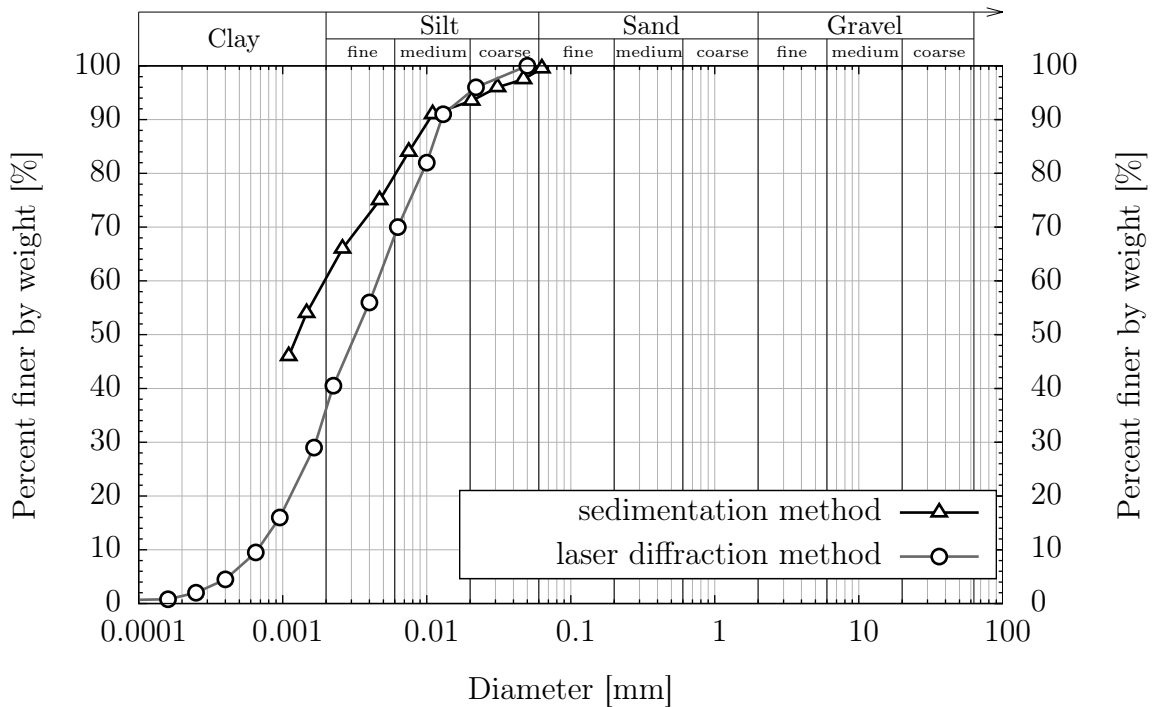


Figure 6.1: Grain size distribution of Spergau kaolin clay.

highly plastic range. It can therefore be characterised as a silt of high plasticity.

The shrinkage limit was determined according to ASTM D4943-08 (2008) using the fluid displacement method for volume measurement with kerosene as recommended by Peron et al. (2007).

The activity according to Skempton (1953) is defined as

$$I_A = \frac{I_P}{M_{\%,\text{fines}}} \quad (6.2)$$

where I_A is the activity, I_P is the plasticity index and $M_{\%,\text{fines}}$ is the clay size fraction (given in terms of percentage finer by weight for particles finer than 0.002 mm).

It is a measure of how much the material behaviour is influenced by the clay fraction. The higher the activity, the higher the influence of the clay fraction on the material behaviour. With an activity of $I_A = 0.5 < 0.75$ the Spergau kaolin can be characterised as inactive.

Table 6.1 compares the Atterberg limits and activity found for the studied Spergau kaolin clay with data for kaolin clay given in literature (Mitchell and Soga, 2005). It reveals, that the material lies well within the range of equivalent kaolinites.

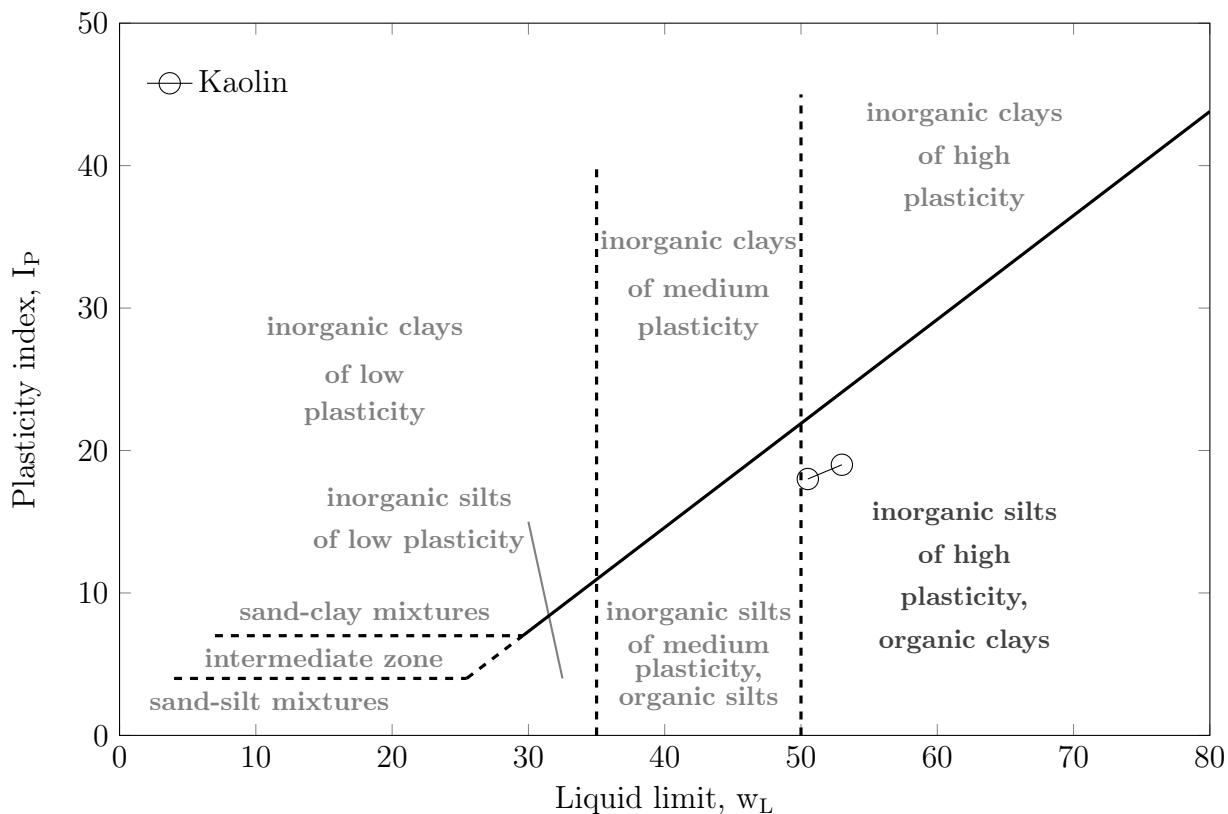


Figure 6.2: Plasticity diagram for Spergau kaolin clay according to DIN:18196 (2006).

Table 6.1: Comparison of Atterberg limits and activities of Spergau kaolin with the range for relevant kaolinites from literature (Mitchell and Soga, 2005).

	Spergau kaolin	Kaolinite
Liquid limit, w_L [%]	51.0	30-110
Plastic limit, w_P [%]	32.3	25-40
Plasticity index, I_P [%]	18.7	
Shrinkage limit, w_S [%]	29.6	25-29
Activity, I_A [-]	0.5	0.5

Hydraulic permeability and compressibility

According to Baille (2014) Spergau kaolin clay exhibits a distinct linear void ratio-permeability relationship for initially saturated samples. The hydraulic permeability given in Baille (2014) ranges between $k=2 \cdot 10^{-11}$ m/s at a void ratio of $e = 0.6$ and

$k=1 \cdot 10^{-9}$ m/s at a void ratio of $e = 1.2$. In Haase and Schanz (2016) slightly higher hydraulic permeabilities for Spergau kaolin clay ranging from $k=1 \cdot 10^{-9}$ m/s for $e = 0.8$ to $k=8 \cdot 10^{-9}$ m/s for $e = 1.5$ are given. In both studies the permeabilities were computed based on oedometer results. The compressibility of Spergau kaolin clay is analysed in detail in Chapter 7.

Mineralogy and chemical composition

Baille (2014) used X-ray diffraction (XRD) and infrared spectroscopy to study the mineralogy of Spergau kaolin clay and determined the amount of minerals according to Kaufhold et al. (2002). The mineralogical composition is given in Table 6.2. Table 6.3 gives the chemical composition of Spergau kaolin determined by means of X-ray fluorescence (XRF) (Baille, 2014).

From this data it can be seen that the Spergau kaolin clay used within the present study mainly consists of Kaolinite ($\text{Al}_2[\text{Si}_2\text{O}_5(\text{OH})_4]$). Kaolinite is a two-sheet layer clay mineral, i.e. each layer is formed by one tetrahedral silica sheet and one dioctahedral gibbsite sheet (see Fig. 6.3). Figure 6.4 illustrates the microscopic structure of kaolinite.

To optically study the microstructure of Spergau kaolin, microphotographs using ESEM and cyro-BIB-SEM were evaluated. The ESEM microphotographs were taken at Ruhr-Universität Bochum, while the cyro-BIB-SEM microphotographs were accomplished in cooperation with Dr. Joyce Schmatz, MaP - Microstructure and Pores GmbH, Aachen. Both types of microphotographs are shown in Figure 6.5.

Table 6.2: Quantitative mineralogical composition of Spergau kaolin clay after Baille (2014).

	Kaolinite	Illite	Quartz
Spergau kaolin	76 %	16 %	8 %

Table 6.3: Chemical composition of Spergau kaolin clay after Baille (2014).

Element	Content [%]
SiO ₂	51.56
Al ₂ O ₃	32.66
Fe ₂ O ₃	0.86
CaO	0.19
MgO	0.35
Na ₂ O	0.05
K ₂ O	1.37
SO ₃	0.03
P ₂ O ₅	0.12
TiO ₂	0.58
MnO	0.01
Loss of ignition	11.96
Sum	99.71

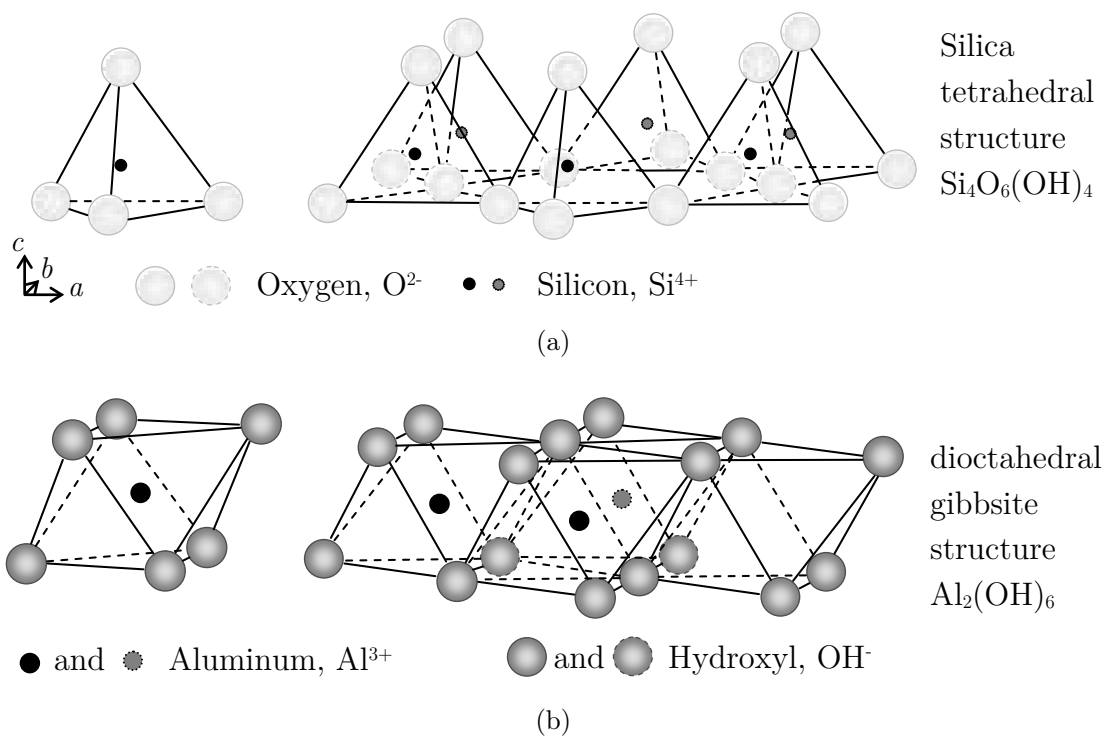


Figure 6.3: Diagrammatic sketch of tetrahedral and octahedral units, modified after Grim (1968): (a) single silica tetrahedron (left), sheet of tetrahedra arranged in a hexagonal network (right), (b) single octahedron (left), di-octahedral sheets (right) (Baille, 2014).

Cation exchange capacity and specific surface area

The specific surface area A_s usually given in $[\text{m}^2/\text{g}]$ is defined as the surface area of clay per soil mass. In Baille (2014) two methods are used to determine the specific surface area of Spergau kaolin: the Brunauer-Emmett-Teller method (BET) to determine the external surface area and the EGME method, which is said to determine the external as well as interlayer surface area. Results for both methods are given in Table 6.4.

Due to the negative charge of clay mineral particles, cations are attracted towards clay mineral particles to preserve electrical neutrality and reach equilibrium state. These cations are held where possible between the clay layer as well as on the surface and edges of the particles. The cation exchange capacity (CEC), typically given in $[\text{meq}/100\text{g}]$, describes the type and amount of exchangeable cations, i.e. cations which may be replaced by cations of another type (Baille, 2014) . Table 6.5 gives the CEC for Spergau kaolin clay determined by Cu-Triethylenetramine method according to Meier and Kahr (1999).

Table 6.4: Specific surface area of Spergau kaolin clay after Baille (2014).

	A_s $[\text{m}^2/\text{g}]$	
	by BET	by EGME
Spergau kaolin	14	28

Table 6.5: Exchangeable cations and CEC of Spergau kaolin clay after Baille (2014).

Exchangeable cation	CEC $[\text{meq}/100\text{g}]$
Na^+	0
K^+	0
Mg_2^+	1
Ca_2^+	5
S value	6
T value	7
S-T	-1
T value (VIS)	-
CEC ¹	7

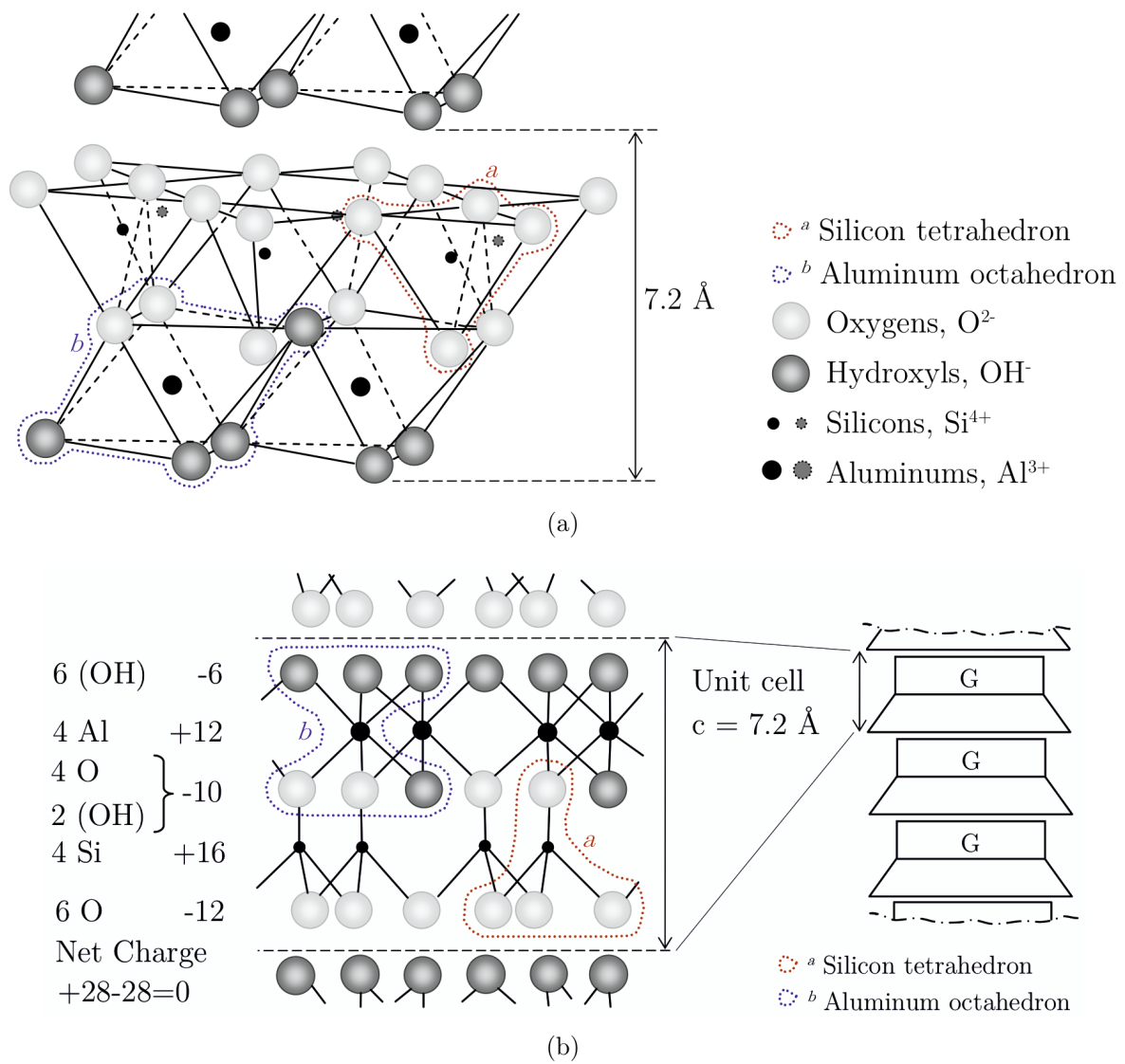


Figure 6.4: Diagrammatic sketch and charge distribution of kaolinite, modified after Grim (1968): (a) diagrammatic sketch of the kaolinite structure, (b) charge distribution on kaolinite (Baille, 2014).

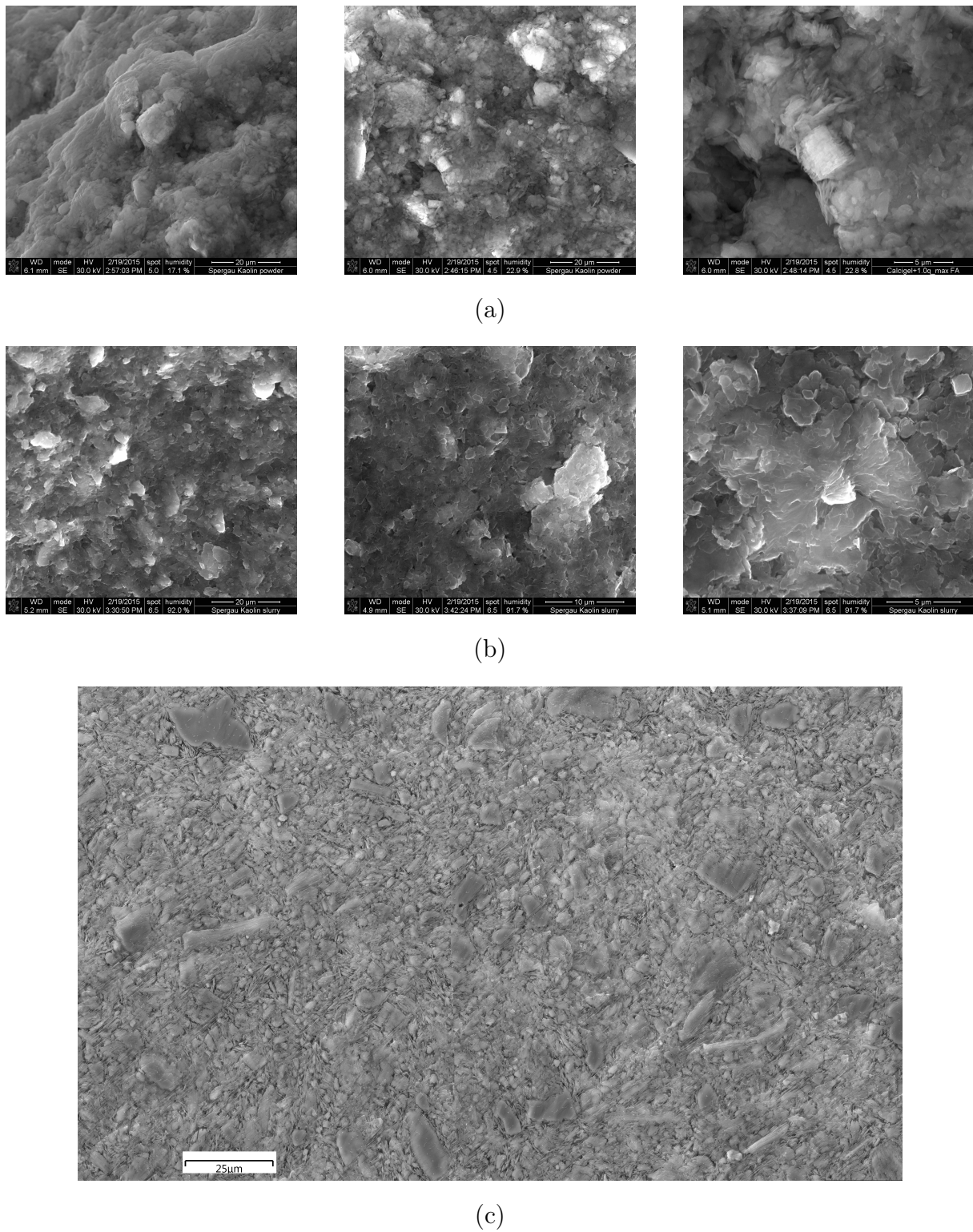


Figure 6.5: (a) ESEM microphotographs of Spergau kaolin powder, (b) ESEM microphotographs and (c) cryo-BIB-SEM microphotograph of Spergau kaolin slurry ($w \approx 1.1w_L$).

6.1.3 Onsøy clay

The consolidation behaviour of natural and reconstituted Onsøy clay was studied within the framework of a master's thesis prepared by Wolfgang Lieske, M.Sc. supervised by the author. The following characterisation was mainly performed within the framework of this work. Details can be found in Lieske (2015). Moreover, the clay material properties from the Onsøy site have been characterized in detail by Lunne et al. (2003) and Lunne et al. (2007) and other studies at *Norwegian Institute of Technology (NGI)*. A comparison of the presented results with the data from literature is drawn.

Soil origin and natural state

The tested Onsøy clay is a marine natural clay from a site approximately 100 km south-east of Oslo, Norway, in the vicinity of Fredikstad. The deposit was formed during the glaciation and early post glaciation (Holocene). During the isostatic uplift, caused by the following de-glaciation, the depositional environment changed from marine to estuarine (Lunne et al., 2003). The block sample (Block No. 3) used in the present study (see Fig. 6.6) was obtained from a depth 9.90-10.30 m below ground using a Sherbrooke sampler to prevent disturbance of the sensitive sample material during sampling (for details see DIN EN ISO 22475-1 (2007) and Lefebvre and Poulin (1979)). The individual samples for the oedometer testing were cut from the sample block as described in Chapter 6.3.1.

The natural water content of the block material was determined to vary between $w_{\text{nat}} = 64\text{--}66\%$ with a mean void ration of approximately $e_{\text{nat}} = 1.77$. These values coincide with the range of approximately $w_{\text{nat}} = 60\text{--}69\%$ given by Lunne et al. (2003) for samples from this depth. The pH value was determined by pH probe to be $pH = 7.31$. With respect to tests by Wichtmann et al. (2013) on similar sample material from a different sampling depth the salt concentration was assumed to be 32.5 g/l, which is in well accordance with Lunne et al. (2003), suggesting an average value of 30 g/l for samples from depths larger than 7 m. Table 6.6 summarizes the most important parameters describing the natural state determined to the block sample used within the present study.

Specific gravity and grain size distribution

The specific gravity ρ_s of Onsøy clay was determined according to ASTM D854-14 (2014) by pycnometer method to be $\rho_s = 2.77\text{ g/cm}^3$. This value lies in the upper range of $\rho_s = 2.6\text{--}2.8\text{ g/cm}^3$, with an average value of $\rho_{s,\text{avg.}} = 2.71\text{ g/cm}^3$ given by Lunne et al. (2003).

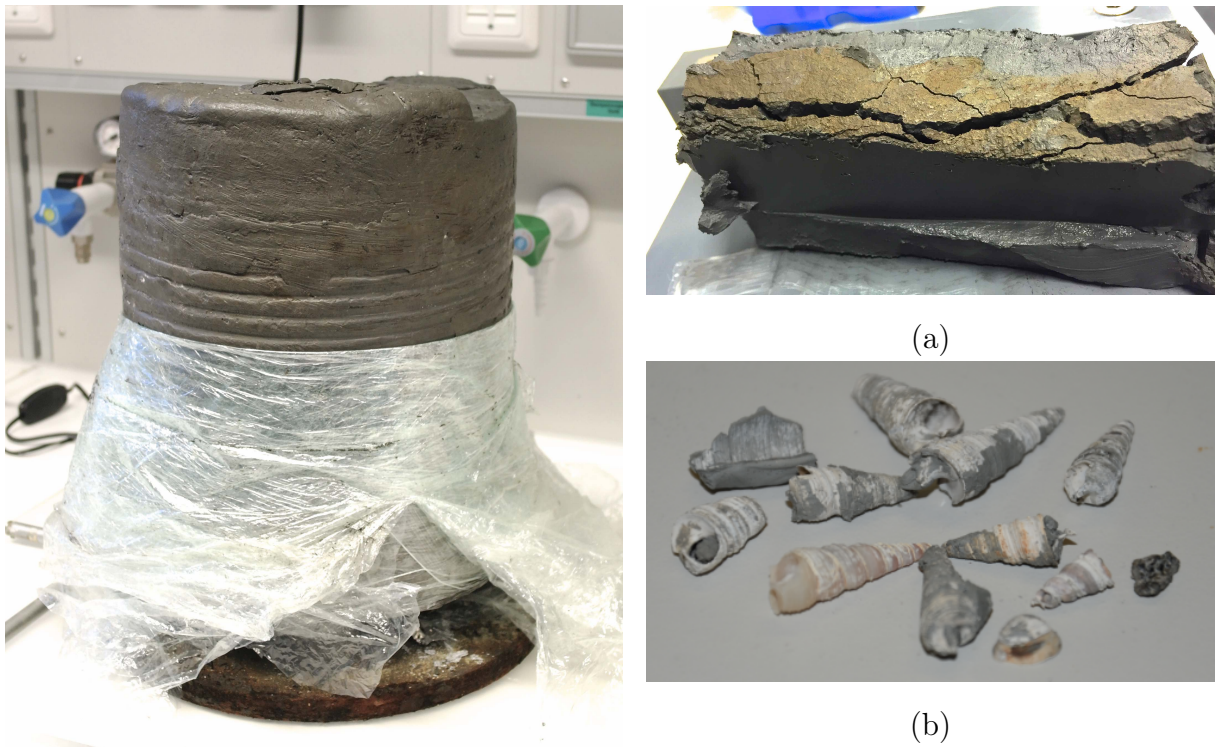


Figure 6.6: Onsoy block sample (left) with inhomogeneities (right): (a) sand inclusions and (b) shell fragments, after (Lieske, 2015).

Table 6.6: Onsoy block sample - natural state characteristics.

	Onsoy clay
Natural water content, w_{nat} [%]	64-66
Natural degree of saturation, S_r [%]	96-100
Mean natural void ratio, e_{nat} [-]	1.77
pH value, pH [-]	7.31
Salt concentration in pore water, Ψ_{Salt} [g/l]	25-29

The grain size distribution was determined using sedimentation technique according to DIN:18123 (1996) and laser diffraction method. Figure 6.7 shows the determined grain size distribution curves. On this basis, Onsoy clay can be characterised as a dark grey clayey silt, with a clay content of 40 %. Within the block sample shell fragments shown in Figure 6.6 were encountered. According to Lunne et al. (2003), the clay matrix in general consists of clay minerals together with finely ground rock flour in a relatively dense, flocculated arrangement and the organic content can be approximated to be 0.6 %.

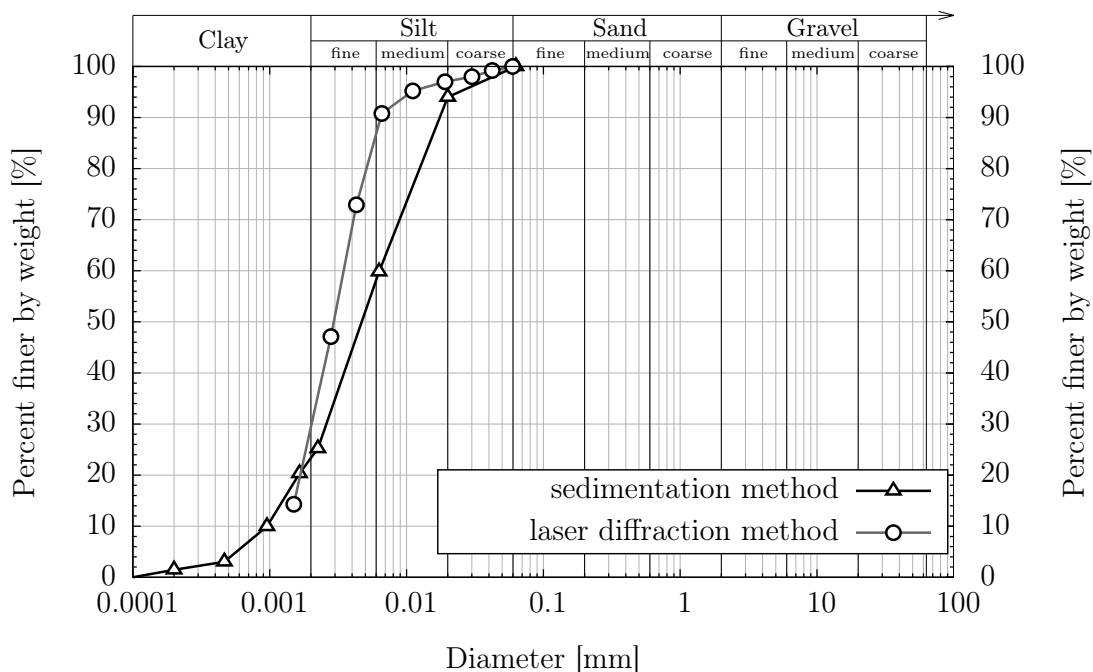


Figure 6.7: Grain size distribution of Onsøy clay.

Atterberg limits and plasticity

The liquid limit w_L was determined according to DIN:18122-1 (1997), using the Casagrande method, and additionally according to DIN ISO/TS 17892-6 (Vornorm) (2005) using fall cone method. The value of $w_{L,Cas} = 67.4\%$ determined by Casagrande method is insignificantly smaller than the value of $w_{L,FC} = 67.6\%$ resulting from fall cone testing. The plastic limit was determined according to DIN:18122-2 (2000) to be $w_P = 29.6\%$ giving a plasticity index of $I_P = 37.8\%$. The shrinkage limit was determined according to DIN:18122-2 (2000) to be $w_S = 28.8\%$. With reference to the plasticity diagram after Arthur Casagrande, the Onsøy clay tested in the present study lies slightly above the A-Line and therefore can be describes as a pronounced plastic clay (see Fig. 6.8). The activity I_A can be calculated to $I_A = 1.9[-]$.

Hydraulic permeability and compressibility

According to Lunne et al. (2003) the hydraulic permeability of Onsøy clay determined based on oedometer test data and in-situ testing data was found to range from $k=5 \cdot 10^{-9}$ m/s at ground level to $k=5 \cdot 10^{-10}$ m/s in a depth of 25 m. The compressibility of Onsøy clay is analysed in detail in Chapter 7.

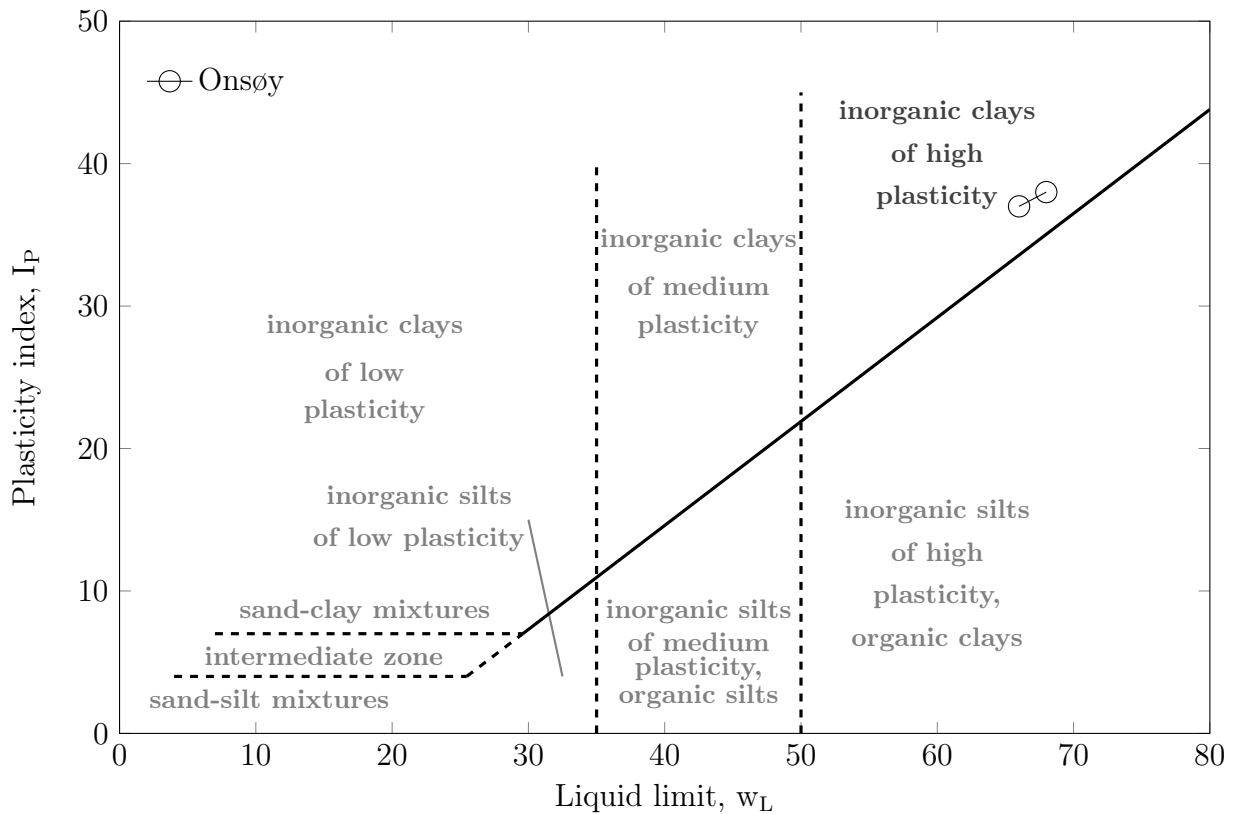


Figure 6.8: Plasticity diagram for Onsøy clay according to DIN:18196 (2006).

Mineralogy and chemical composition

The mineralogical and chemical composition of Onsøy clay was determined by Kaufhold et al. (2016) at Bundesanstalt für Geowissenschaften und Rohstoffe (BGR) in Hannover. The XRD patterns were recorded using a PANalytical X'Pert PRO MPD Θ - Θ diffractometer (Co-K α radiation generated at 40 kV and 40 mA). The diffractometer is equipped with a variable divergence slit, primary and secondary soller, diffracted beam monochromator, point detector, and a sample changer. The samples were investigated from 1deg to 75deg 2Θ with a step size of 0.03deg 2Θ at a measuring time of 12 sec per step. For the preparation of the specimen the back loading technique was used. For quantification the Rietveld program BGMN was used (Bergmann, 2005). The results are summarised in Table.6.7 and 6.8.

Table 6.7: Mineralogical composition of Onsøy clay according to Kaufhold et al. (2016).

Mineral	Content [%]
Muskovite	37
Albite	19
Quartz	18
Chlorite	11
Hornblende	7
Orthoclase	5
Halite	1
Calcite	1
Organics	1
Sum	99.64

Table 6.8: Chemical composition of Onsøy clay according to Kaufhold et al. (2016).

Element	Content [%]
SiO ₂	52.6
Al ₂ O ₃	18.0
Fe ₂ O ₃	8.5
K ₂ O	4.5
MgO	3.5
Na ₂ O	2.4
CaO	1.2
TiO ₂	0.8
P ₂ O ₅	0.2
SO ₃	0.2
MnO	0.01
Loss of ignition	7.7
Sum	99.64

Cation exchange capacity and specific surface area

The cation exchange capacity was determined using ICP-EOS (inductively coupled plasma optical emission spectrometry) at the *Institute for geography (RUB)*. Two different methods were conducted: using BaCl_2 according to DIN EN ISO 11260 (2011) and $\text{Cl}_3\text{CoH}_{18}\text{N}_6$ according to DIN EN ISO 23470 (2011). The results were similar, so that the mean value is given in Table 6.9. It is noticeable that in comparison to other clays, the amount of exchangeable sodium cations is dominating. This can be explained by the saline environment persisting during sedimentation. The CEC value according to Kaufhold et al. (2016) is $CEC = 10 \text{ meq}/100\text{g}$ measured excluding the effect of salt water. The specific surface area was determined using EGME method introduced in Chapter 6.1.2 to be $A_{s,EGME} = 44 \text{ m}^2/\text{g}$. By BET method, performed by Kaufhold et al. (2016) the specific surface area was determined to be $A_{s,BET} = 37 \text{ m}^2/\text{g}$. Both, cec and ssa values are in good agreement with data for Onsøy clay examined by Lunne et al. (2003).

Table 6.9: Exchangeable cations and CEC of Onsøy clay after Lieske (2015) and Kaufhold et al. (2016).

Exchangeable cation	CEC [$\text{meq}/100\text{g}$]
Na^+	20.0
K^+	1.5
Mg_2^+	6
Ca_2^+	9
CEC ¹	10

¹ excluding the effect of salt water

6.1.4 Summary of material properties of studied clays

Table 6.10 summarises the main material characteristics for the two clays studied within the present study.

Table 6.10: Summary of the main material characteristics of the clays studied.

	Spergau kaolin clay	Onsøy clay
Classification (USCS)	MH	CH
Natural water content, w_{nat} [%]	-	64-66
Natural degree of saturation, S_r [%]	-	96-100
Mean natural void ratio, e_{nat} [-]	-	1.77
pH value, pH [-]	-	7.31
Salt concentration in pore water, Ψ_{Salt} [g/l]	-	25-29
Liquid limit, w_L [%]	51.0	67.4
Plastic limit, w_P [%]	32.3	29.6
Plasticity index, I_P [%]	18.7	37.8
Shrinkage limit, w_S [%]	29.6	28.8
Activity, I_A [-]	0.5	1.9
Cation exchange capacity, CEC [meq/100g]	7	10
Specific surface area, A_s [m^2/g]	28	44

6.2 Experimental programme

Within the present experimental study monotonic as well as cyclic oedometer tests were performed on the chosen clays. The following section illustrates the load application method as well as the individual specifications of the conducted tests.

6.2.1 Monotonic oedometer tests

Load application

Three types of monotonic oedometer tests with the following vertical stress application were performed within the present study:

1. **Direct loading-unloading tests (LUD):**
10-110-10 [kN/m²]
2. **Step-wise loading-unloading tests (LUS):**
10-20-50-100-200-400-200-100-50-10 [kN/m²]
3. **Step-wise loading-unloading-reloading tests (LUR):**
10-20-50-20-10-20-50-100-200-100-50-20-10-20-50-100-200-400-200-100-50-20-10 [kN/m²]

While the step-wise loading-unloading-reloading tests are to study the general material behaviour of the tested soil materials, the direct loading tests were performed to better understand the material behaviour in the cyclic consolidation tests, where the load is applied more rapidly compared with a monotonic step-wise tests.

In a series of pre-testing the necessary time for full consolidation was determined. For the kaolin clay a consolidation time of $t = 4$ hours was determined to be sufficient for the full consolidation in each load step. In order to keep the influence of possible creep deformation small, thus, all load steps were applied for 4 hours.

Monotonic testing programme

Table 6.11 contains the initial conditions and test configurations for the conducted monotonic oedometer tests.

Table 6.11: Experimental programme: Monotonic oedometer tests.

Test No. ^a	Initial material conditions			Monotonic Testing Procedure
	Sample height h_0 [mm]	Void ratio e_0 [-]	Water content w_0 [%]	
MK01	20.1	1.68	62	LUD
MK02	19.9	1.60	62	LUD
MK03	19.8	1.58	62	LUD
MK04	19.2	1.45	59	LUS
MK05	19.4	1.67	68	LUS
MK06	20.0	1.53	58	LUR
MK07	19.6	1.48	58	LUR
MOr01	20.3	1.82	64	LUS
MOn01	20.3	1.82	64	LUS

^aNomenclature:

M: monotonic; K: kaolin, On: natural Onsøy, Or: reconstituted Onsøy clay

6.2.2 Cyclic oedometer tests

Loading function

The cyclic loading used within the experimental study should - regarding its type, frequency and amplitude - adequately model the loading occurring during geotechnical application situations in field. To comply with this requirement, for the present study a cyclic loading function of sinusoidal form was chosen.

With reference to Razouki and Schanz (2011); Razouki et al. (2013); Müthing et al. (2016b) the following haversine loading function was selected:

$$\sigma_v(t) = \hat{\sigma}_v \sin^2 \frac{\pi t}{d} \quad (6.3)$$

where $\sigma_v(t)$ is the loading as a function of time, $\hat{\sigma}_v$ is the load amplitude, t is the time and d is the load period.

Fig. 6.9 shows the haversine loading function for normalized loading time and amplitude.

The loading function accounts for the fact that in geotechnical applications mostly compression is considered. Therefore, various authors recommend the use of the haversine

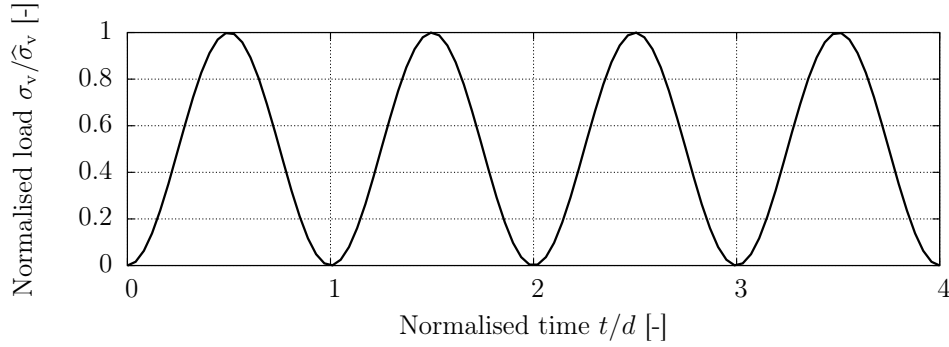


Figure 6.9: Haver-sine loading function.

loading function to model cyclic, geomechanical processes (see Barksdale, 1971; Huang, 1993, and others).

Test were performed under variation of the two load characteristics amplitude $\hat{\sigma}_v$ and period d . The load amplitude $\hat{\sigma}_v$ was varied between $d = 50 \text{ kN/m}^2$ and $d = 350 \text{ kN/m}^2$ accounting for the soft soil behaviour and the short time range of load application. Limitations regarding the load amplitude were defined by the loading frame in terms of the precision of the load application at high loading rates. Generally, tests with the following load amplitudes were performed:

$$\hat{\sigma}_v = 50, 70, 100, 150, 200, 250, 300, 350 \text{ [kPa]} \quad (6.4)$$

The load period was chosen with reference to the time $t(T_0 = 1)$ a sample under equivalent monotonic loading needs for completion of consolidation process. It was than set according to the dimensionless periods e.g. $T_0 = 0.15, 0.30$ or 0.6 . These dimensionless periods originate a load period, which is independent of sample height and the material-dependent consolidation coefficient c_v :

$$T_0 = \frac{c_v \cdot d}{h^2} \rightarrow d = \frac{T_0 \cdot h^2}{c_v} \quad (6.5)$$

where T_0 is the chosen dimensionless period, c_v is the material-dependent coefficient of consolidation, d is the load period and h is the sample height.

For a period of e.g. $T_0 = 0.15$ the period of one loading cycle d can therefore be calculated to be

$$d = \frac{T_0 \cdot h^2}{c_v} = \frac{0.15 \cdot (0.02 \text{ m})^2}{5 \cdot 10^{-7} \text{ m}^2/\text{s}} = 120 \text{ s} \quad (6.6)$$

assuming a constant value of $c_v = 5 \cdot 10^{-7} \text{ m}^2/\text{s}$ determined as a mean value from monotonic consolidation tests on the kaolin clay. Generally, tests with the following load periods were performed:

$$d = 30, 60, 120, 180, 240, 360, 480, 600, 1200 \text{ [s]} \quad (6.7)$$

These load periods correspond to a frequency of

$$f = 3.3 \cdot 10^{-2} - 8.3 \cdot 10^{-4} \text{ [Hz]} \quad (6.8)$$

Load application in experiment

In order to simplify the load application procedure the haversine loading function in the experiment was linearly approximated. Thereby, one loading cycle was approximated by 24 linear loading sections as demonstrated in Fig. 6.10. This linear approximation deviates from the original function in any value by maximum $\pm 0.4\%$. Due to the symmetry of the function, the total applied work is the same for the original function and its approximation.

Pre-consolidation phase

Before each cyclic consolidation phase the sample was pre-consolidated by a seating load of 10 kPa. The seating load in the present study was chosen to be as high as 10 kPa to account for the high percentage of frictional loss between loaded oedometer top and ring in the low stress range. This preloading ought to fulfil two purposes:

1. guarantee full contact between specimen and loading plate,
2. generate a comparable initial stress and contact state for all cyclic tests.

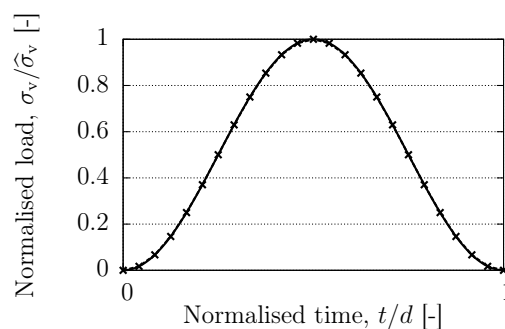


Figure 6.10: Approximation of haversine loading in the experiment.

Cyclic testing programme

Within the experimental study the influence of different boundary conditions on the cyclic consolidation behaviour was to be studied. Namely, the following influencing parameters were analysed:

1. Material characteristics: initial material condition: initial water content / void ratio; inherent structure
2. Applied loading: load amplitude, load period

Thus, tests with variation in initial water content, load amplitude and load period were performed on both testing material - Spergau kaolin clay as well as natural and reconstituted Onsøy clay. Tables 6.12 and 6.13 contain the initial conditions and test configurations for the conducted cyclic oedometer tests.

Table 6.12: Experimental programme: Cyclic oedometer tests on kaolin clay.

Test No. ^a	Initial material conditions			Loading Parameters		
	Sample height h_0 [mm]	Void ratio e_0 [-]	Water content w_0 [%]	Amplitude $\hat{\sigma}_v$ [kN/m ²]	Period d [s]	No. of cyc. n [-]
CK01	20.0	1.52	58	100	60	330
CK02	20.0	1.53	58	100	120	100
CK03	20.1	1.56	59	100	120	87
CK04	20.0	1.54	58	100	60	350
CK05	20.2	1.56	59	100	60	170
CK06	19.8	1.54	61	100	120	100
CK07	20.2	1.56	59	100	120	150
CK08	20.7	1.52	59	100	120	150
CK09	20.2	1.59	60	200	120	100
CK10	20.0	1.56	60	200	120	100
CK11	20.0	1.55	59	50	120	100
CK12	20.0	1.52	58	70	120	100
CK13	20.1	1.56	59	100	30	330
CK14	20.1	1.52	57	350	120	100
CK15	20.4	1.58	59	100	180	150
CK16	20.2	1.56	59	100	240	100
CK17	20.3	1.57	59	100	240	60
CK18	20.1	1.81	68	100	120	100

Table 6.12: Experimental programme: Cyclic oedometer tests on kaolin clay.

Test No. ^a	Initial material conditions			Loading Parameters		
	Sample height h_0 [mm]	Void ratio e_0 [-]	Water content w_0 [%]	Amplitude $\hat{\sigma}_v$ [kN/m ²]	Period d [s]	No. of cyc. n [-]
CK19	20.2	1.55	58	100	1200	30
CK20	19.9	1.70	65	100	120	100
CK21	20.7	1.58	57	100	120	100
CK22	20.0	1.73	65	100	120	100
CK23	20.5	1.32	48	100	120	100
CK24	20.0	1.49	57	100	120	100
CK25	20.5	1.46	53	100	120	100
CK26	20.6	1.41	51	100	120	100
CK27	20.6	1.75	63	150	120	100
CK28	20.3	1.69	63	250	120	100
CK29	20.4	1.72	64	300	120	100
CK30	20.0	1.68	64	50	120	100
CK31	20.6	1.36	48	200	120	100
CK32	20.4	1.34	48	300	120	100
CK33	20.7	1.27	45	50	120	100
CK34	20.2	1.59	59	100	360	35
CK35	20.3	1.55	58	100	480	25
CK36	20.5	1.62	59	100	360	35
CK37	20.16	1.51	55	100	600	25
CK38	20.3	1.72	63	200	120	100
CK39	20.2	1.59	59	100	480	25
CK40	20.2	1.59	59	100	600	20
CK41	20.2	1.59	59	100	360	33

^aNomenclature:

C: cyclic; K: Spergau kaolin

Table 6.13: Experimental programme: Cyclic oedometer tests on Onsøy clay.

Test No. ^a	Initial material conditions			Loading Parameters		
	Sample height	Void ratio	Water content	Amplitude	Period	No. of cyc,
	h_0 [mm]	e_0 [-]	w_0 [%]	$\hat{\sigma}_v$ [kN/m ²]	d [s]	n [-]
COn01	20.7	1.86	63	50	120	250
COn02	20.6	1.91	65	100	120	500
COn03	20.5	1.89	63	200	120	500
COr01	20.8	1.84	63	50	120	250
COr02	20.9	1.81	61	100	120	400
COr03	20.8	1.90	65	200	120	500

^aNomenclature:

C: cyclic; On: natural Onsøy clay, Or: reconstituted Onsøy clay

6.3 Sample preparation and testing procedure

6.3.1 Soil material preparation

Kaolin clay

Figure 6.11 shows the slurry preparation steps for the kaolin clay sample. The sample material was prepared manually by milling the clay pellets (a) and mixing the powdered material (b) with de-aired, de-ionised water to a slurry material (c). The amount of water added to the powder defines the initial water content of the sample material. Within the preparation of the sample material, care was taken to reach the same degree of grinding for all sample material. Moreover, enough time (several days) was given for a full homogenisation of the soil after adding water.

Reconstituted Onsøy clay

The reconstituted sample material was obtained by mixing the natural sample material at the natural water content of $w_{L,nat} = 65\%$, without air or oven drying. According to the definition of Burland (1990) intrinsic clay properties can be derived from the 'reconstituted' soil state. The term 'reconstituted' here refers to a soil mixed at a water content

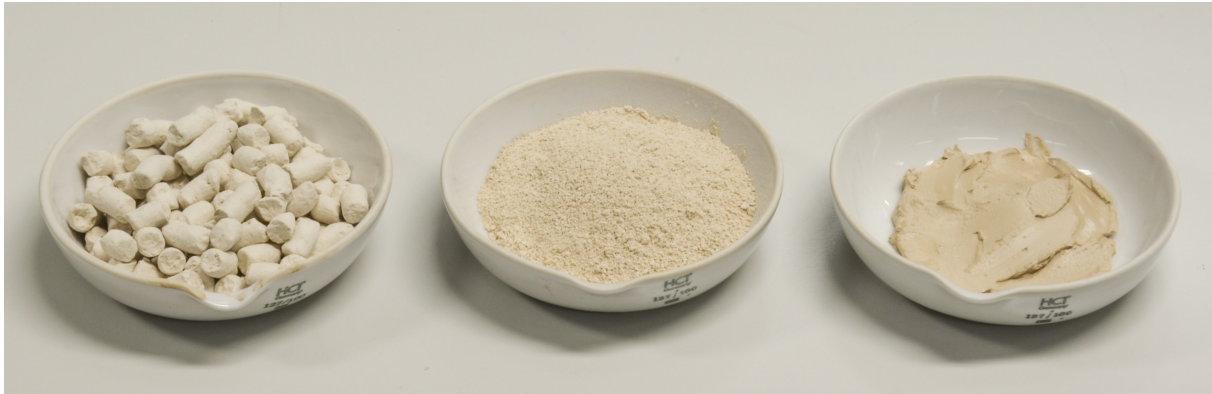


Figure 6.11: Kaolin material preparation: from clay pellets (left) to powder (middle) and slurry (right).

of between w_L and $1.5 w_L$ (details see Chapter 2.2.3) without air or oven drying. As the sample material in the present study was mixed at natural water content, which is only about 1% below w_L and thus within the measurement accuracy, it can be approximately assumed that the sample material may be stated as reconstituted. The mechanical distortion during mixing is presumed to cause a complete destruction of the existing structure in the natural material state.

6.3.2 Sample installation

The sample installation process requires particular elaborateness and precision, as the test is very sensitive to variations in initial and boundary conditions, i.e. the initial material and saturation state of the sample. Throughout the whole installation process, special caution was taken to avoid inclusion of air bubbles in the sample material and to ensure the full saturation of the testing system.

Sample installation for reconstituted clay samples

Figure 6.12 illustrates the sample installation process. In order to guarantee the sample height of 20 mm, the oedometer ring with a spacing dummy was reversely placed on scales. The reconstituted clay material was then placed in the oedometer ring using a spatula. Particular caution was taken to avoid the inclusion of air bubbles during the insertion of sample material into the ring. Filter paper pre-moistured with de-aired, de-ionised water was placed below and above the soil sample, separating the sample material from the filter

plates and by that preventing finest material particles to be flushed out of the sample into the filter plate, clogging its pores.

Sample installation for natural clay samples

Samples were cut from the block sample avoiding inclusion of shell fragments, sand inclusions and disturbed boundary area of the block. The procedure of cutting the sample with the thin-walled oedometer ring was subdivided into three steps illustrated in Fig. 6.13:

step 1: cutting of a pre sample slice of approx. 3 cm height from the block sample.

step 2: cutting the pre sample with a string saw in a self-constructed workaround, so that top and bottom side of the pre sample are plan-parallel areas.

step 3: trepanning of the final sample by pushing the thin-walled oedometer ring into the pre-cut sample.

This sample preparation technique was chosen to guarantee the least disturbance of the sensitive natural material, good contact between sample and oedometer ring for measurement of horizontal stresses and plain, plan-parallel top and bottom surface areas for contact between sample and top and bottom plate of the oedometer cell.

6.3.3 Installation procedure

De-airing of filter plates and drainage system

It is known, that test results particularly regarding the pore pressure measurement are very sensitive to inclusion of air bubbles in the measuring system. Therefore, before each testing the drainage system of the cell as well as both filter plates were carefully de-aired. The de-airing of the filter plates was carried out using an desiccator (see Fig. 5.9). Sufficient time and a vacuum of 1 mBar was given to the filter plates placed in water basin in the desiccator to fully de-air. The status of de-airing was controlled optically by checking of no further occurrence of air bubbles on the filter plates. The drainage system of the oedometer cell was flushed before each testing with de-aired, de-ionised water. The flushing was repeated before and after the sample installation in order to remove possible air inclusions, which might occur during the installation process.

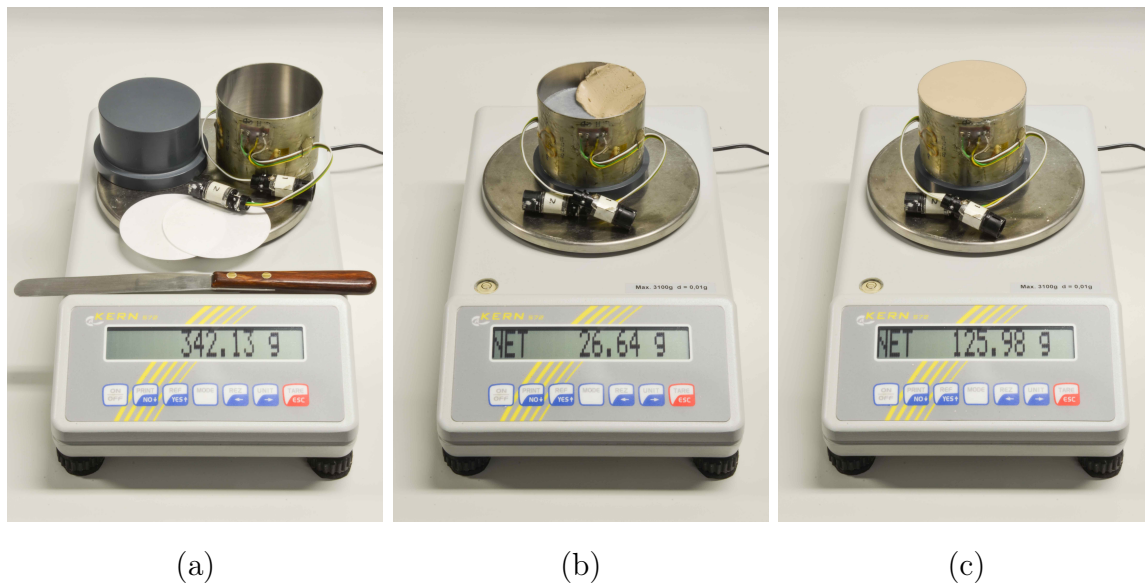


Figure 6.12: Sample installation for reconstituted samples: (a) equipment, (b) sample installation using spatula, (c) installed sample.

Assembling of oedometer device

Figure 6.14 and 6.15 illustrate the procedure of the assembling the oedometer device in the following five steps:

Step 1: Equipment preparation

In a first step all equipment was prepared. The de-aired filter plates were taken out of the desiccator. All parts were cleaned and allocated.

Step 2-4: Installation of the oedometer bottom and filter plates

The bottom part of the oedometer device was assembled by inserting the bottom load piston (Step 2) and placing the oedometer bottom plate on its top (Step 3). Afterwards the oedometer bottom plate was flushed with de-aired water to avoid air inclusions in the drainage pipings. The o-rings at top and bottom of the device were lubricated with sealing grease to reach a better sealing of the ring. As soon as the sample material was installed in the oedometer ring, filter plates were placed on the top and bottom part of the sample (Step 4), in order to keep the time of filter plates exposed to air as short as possible.

Step 5: Placement of the oedometer ring

The oedometer ring was placed on the bottom filter plate. The ring was carefully pushed to be put over the bottom part of the device. Shims placed on the bottom part guarantee

the correct vertical positioning of the oedometer ring. The strain gauges were connected to the measurement system.

Step 6: Closure of the oedometer device

The top part of the oedometer device was lowered until it penetrated the oedometer ring and force bound was reached. The shims were removed and the ring fixities are mounted. The top drain was connected to the outflow measuring system and top and bottom part of the device were flushed again with de-aired water to drive out possible air bubbles included during the installation procedure.

Initialisation of testing

After assembling the oedometer device the measuring system was started taking measurement values with a frequency of 1 Hertz.

Removal of sample and post testing procedure

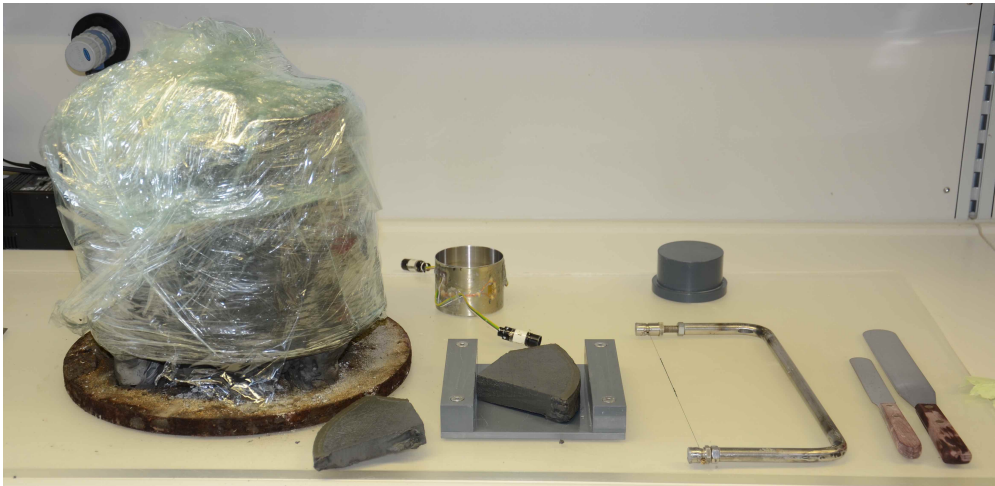
After testing the sample was removed from the device by carefully pushing out the sample of the oedometer ring. Water content probes were taken at four locations of the sample (top boundary, top centre, bottom boundary, bottom centre) in order to get information on the homogeneity of consolidation state.

6.4 Summary

In the first part of this chapter, the two clay materials used within the present study were characterised regarding their main material properties. Table 6.10 summarises the main results from this characteristics for the Spergau kaolin and Onsøy clay. In the second part of the chapter, the experimental programme of this study was introduced, comprising stepwise, monotonic as well as cyclic oedometer tests. The load application method and testing programme were presented. Moreover, the sample preparation method and testing procedure were illustrated.



Step 1



Step 2



Step 3

Figure 6.13: Sample installation for natural samples in three steps.

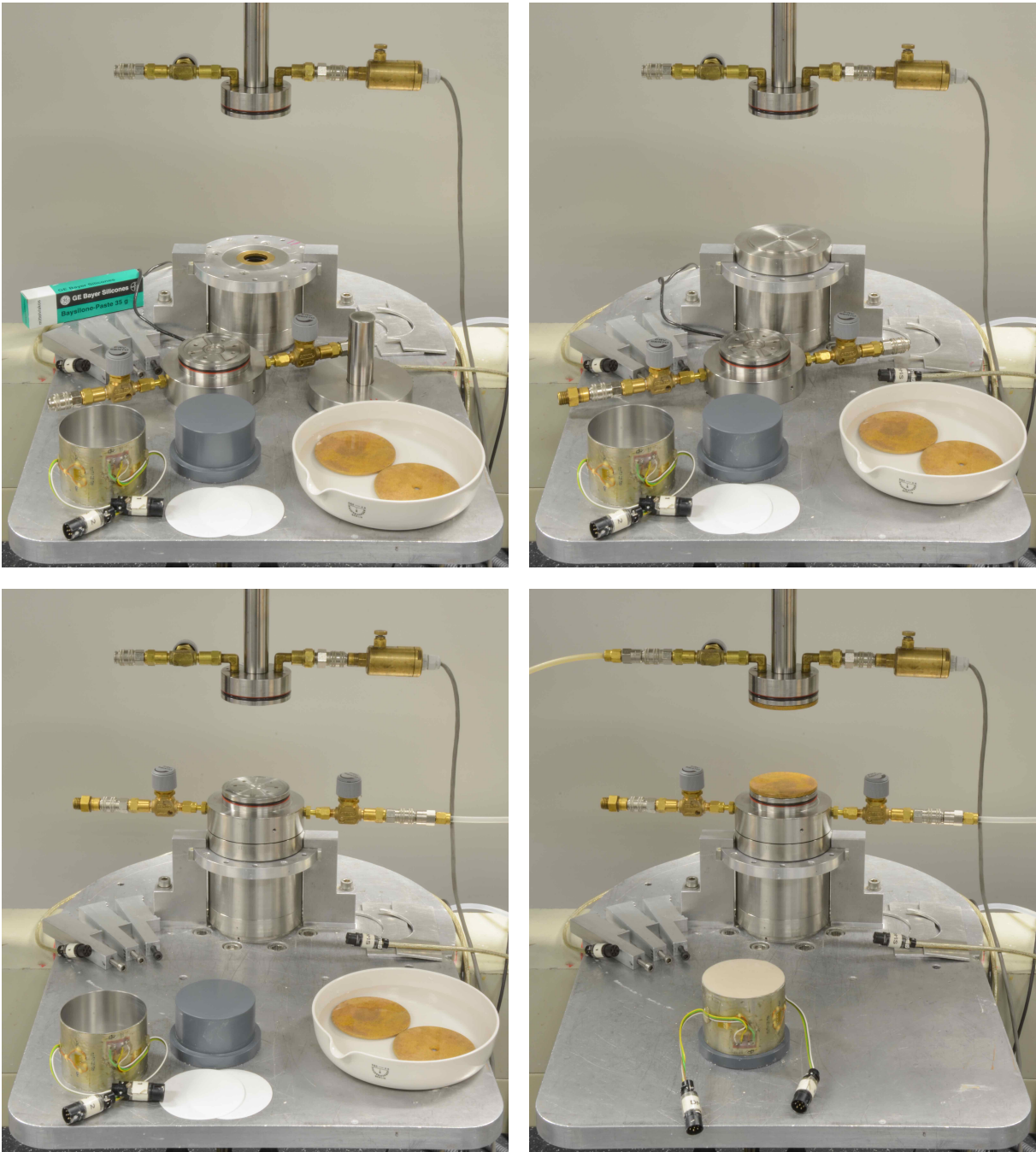


Figure 6.14: Stepwise assembling of the oedometer device: step 1-4.

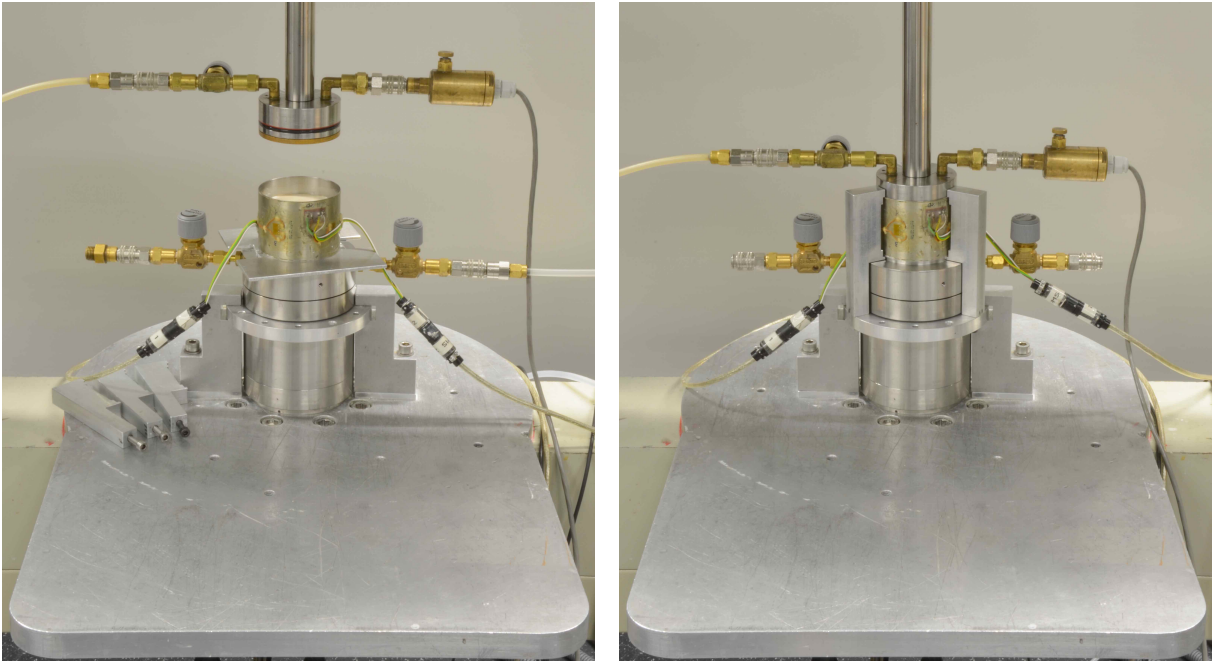


Figure 6.15: Stepwise assembling of the oedometer device: step 5 and 6.

7 Experimental study on consolidation under monotonic loading

To analyse and interpret the consolidation of soils under cyclic loading one needs to understand the consolidation under monotonic loading first. Therefore, Chapter 7 deals with the analysis of the consolidation of Spergau kaolin and Onsøy clay under monotonic loading. Besides the general compression behaviour, time-dependent settlements and pore water dissipation are considered. By a comparison between reconstituted and natural material the special characteristics of the compression behaviour of structured clay are illuminated. Moreover, the evolution of radial stresses during oedometric compression is analysed. In Terzaghi's consolidation theory, the consolidation coefficient c_v , assumed to be a constant value, characterises the consolidation process of a material. Thus, an analysis of this value as a function of material state is given at the end of this chapter.

7.1 Deformation behaviour

7.1.1 General one-dimensional compression behaviour

Figure 7.1a illustrates the compression of Kaolin clay under monotonic oedometer loading derived from six step-wise oedometer tests. By linearisation of the $e - \log \sigma'_v$ plot, the compression and recompression indices can be determined to be $C_c = 0.30$ and $C_{ur} = 0.066$ according to Eq. 2.2 and Eq. 2.3. While the compression index C_c is slightly larger than the range of 0.19 to 0.28 given for kaolinite by Mitchell and Soga (2005), the recompression index lies within the range of 0.05 to 0.15 given by Lambe and Whitman (1969).

Figure 7.1b shows the compression behaviour of natural and reconstituted Onsøy clay from the conducted oedometer tests MOn01 and MOr01. The compression behaviour can

be characterised as typical for a natural, marine clay. The natural clay initially acts very stiff and shows a pronounced destructuration after exceeding the yield stress. Under the applied maximum load of 400 kN/m^2 , the two materials still show a difference in axial strain or void ratio respectively. However, from tests in a high stress oedometer cell (see Lieske (2015)) it is known that the compression curves for natural and reconstituted clay converge when subjected to a stress of about 1000 kN/m^2 .

The yield stress σ'_y marks the stress at the transition point, where the compression of natural soil changes from elastic to elasto-plastic. From the test data it is determined to be $\sigma'_y \approx 70 \text{ kN/m}^2$, which is in accordance with data from literature (Lunne et al., 2003). The elasto-plastic compression index C_c can be calculated from the linearised testing data to be $C_c = 0.40$ for the reconstituted and $C_c = 0.58$ for the natural material after reaching the yield stress. The elastic recompression index C_{ur} is determined to be $C_{ur} = 0.045$.

Figure 7.2 shows a comparison between the present test data to test data given in Lunne et al. (2003) for samples from 6.10 m and 6.23 m depth. In general, the present results are in good agreement with the data from literature. The slightly larger yield stress corresponds to the higher sampling depth of the clay tested within the present study.

With a yield stress of $\sigma'_y = 70 \text{ kN/m}^2$ according to Chandler and Cotecchia (2000) the stress sensitivity of natural Onsøy clay can be determined to be $S_\sigma = \sigma'_y / \sigma'_{e^*_y} \approx 70/15 \approx 4.7$ which is in accordance with the sensitivity given in Lunne et al. (2003).

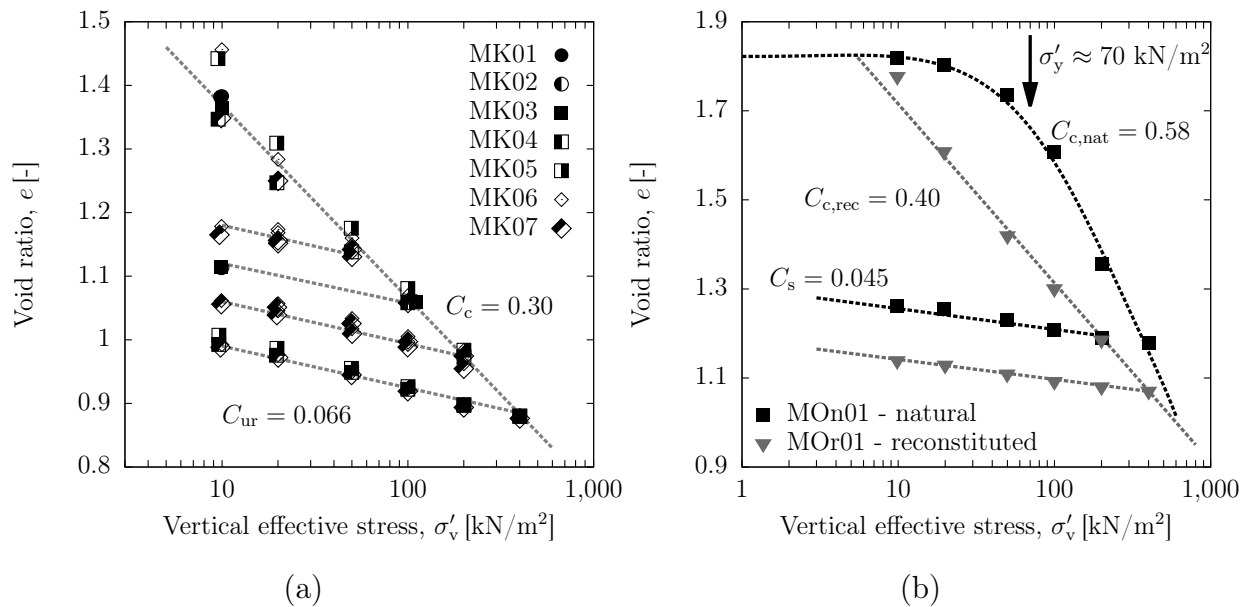


Figure 7.1: Compression behaviour of (a) kaolin clay and (b) natural and reconstituted Onsøy clay.

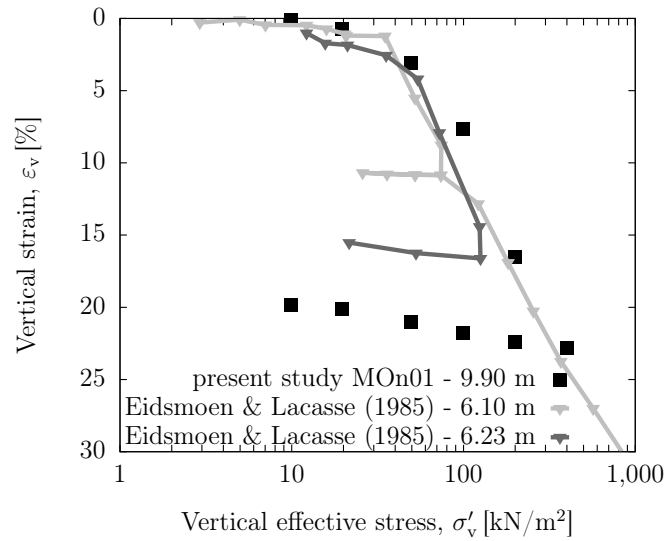


Figure 7.2: Compression behaviour of natural and reconstituted Onsøy clay - comparison to literature from Lunne et al. (2003).

Table 7.1 compares the derived compression and recompression indices from the present oedometer testing to values calculated based on relationships with plasticity index, I_P (according to Kulhawy and Mayne, 1990), and liquid limit, w_L (according to Skempton, 1944). The experimental results derived from the $e - \log \sigma'_v$ plot are in accordance with Skempton's approach. C_c computed based on I_P gives smaller values for kaolin clay and higher values for Onsøy clay.

Table 7.1: Comparison of compression and recompression indices of Spergau kaolin and Onsøy clay from experimental results and literature.

	Spergau kaolin		Onsøy	
	C_c	C_{ur}	C_c	C_{ur}
$e - \log \sigma'_v$ plot	0.30	0.067	0.40 ^a /0.58 ^b	0.045
Skempton (1944): $C_c = 0.007(w_L - 7\%)^a$	0.31	-	0.42	-
Skempton (1944): $C_c = 0.009(w_L - 10\%)^b$	-	-	0.52	-
Kulhawy and Mayne (1990): $C_c = I_P/74$, $C_{ur} = I_P/370$	0.26	0.051	0.51	0.102

^a for reconstituted soils, ^b for natural/undisturbed soils

Following the void index concept by Burland (1990), Fig.7.3 shows the position of compression curves for the tested Kaolin and Onsøy clay with respect to ICL and SCL. The void index was calculated according to Eq.2.6 with $e_{100}^* = 1.08/1.28$ and $C_c^* = 0.30/0.40$ (for Kaolin / Onsøy clay). From this plot, it can be seen that natural Onsøy clay lies slightly below the SCL. According to Chandler et al. (2004) it lies well within the range of sediments (compare Fig. 2.6). Moreover, the position of the compression curve with respect to the SCL is in accordance with data presented by Lunne et al. (2003).

7.1.2 Friction

During load application in the oedometer a difference between applied, vertical load at the top of the system σ_v^t and measured vertical load beneath the sample σ_v^b can be observed. The difference increases with increasing load and deformation as well as ongoing consolidation time (see Fig.7.4). Generally, the friction can be attributed to the following effects: (1) friction in the sealed oedometer system, (2) friction due to frictional contact between sample and oedometer ring, (3) possible arching effects. In the following, the three aspects will be addressed in some more detail.

The vertical stress reduction caused by friction in the oedometer system is to be assigned to the cell's sealing system, namely the friction between O-rings and oedometer ring. To be able to test slurry materials and prevent soft sample material from being squeezed out during relatively fast loading, O-rings have been attached to the cell top and bottom (see

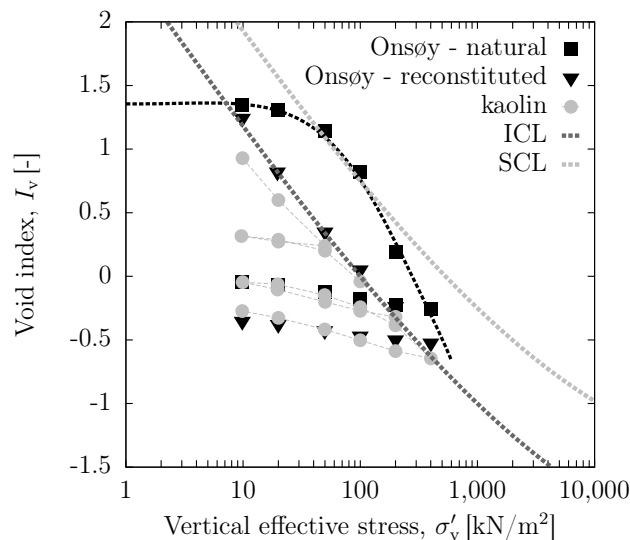


Figure 7.3: I_v - σ'_v relationship relative to ICL and SCL for Kaolin and natural and reconstituted Onsøy clay.

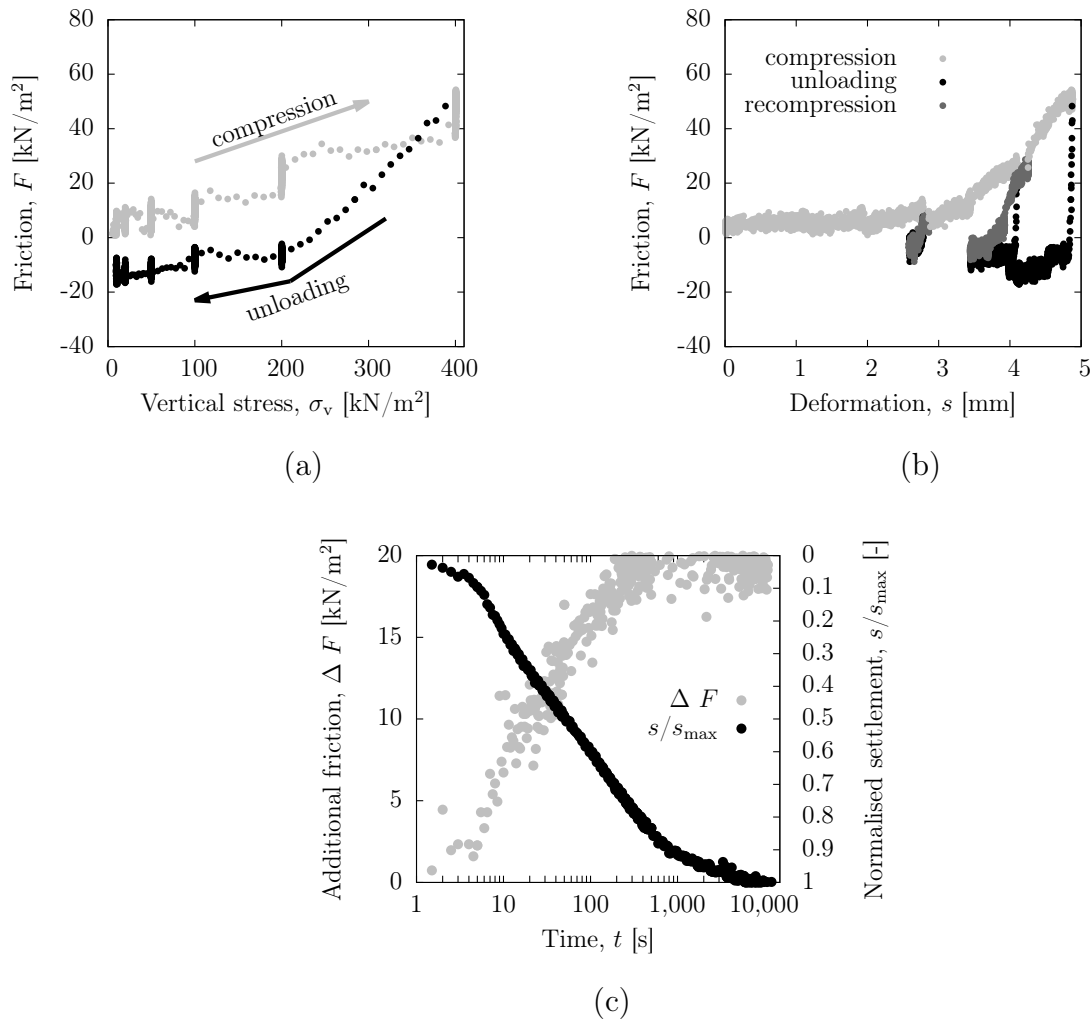


Figure 7.4: Development of friction with respect to (a) vertical stress, (b) deformation and (c) consolidation time in the load step 200 \rightarrow 400 kN/m².

Chapter 5.2.2). During load application these O-rings slide along the inner oedometer ring, which causes friction. A detailed analysis of this part of friction was performed in the calibration of the device and is described in Chapter 5.3.2.

The friction caused by contact between soil sample and oedometer ring was studied by different authors in literature. One of the first to study this problem was Taylor (1942). In an experimental study within the framework of *M.I.T. consolidation research*, he analysed the appearance of friction due to the applied loading in a consolidation experiment. He showed that during the consolidation process an increasing side friction is transferred from the sample to the oedometer ring. With reference to Taylor (1942) the friction between

oedometer ring and sample can be calculated by (Olson, 1986):

$$F = \sigma \cdot \bar{\mu} = \sigma_v \cdot \frac{R/H}{2K_0\mu} \left[1 - \exp\left(-\frac{2K_0\mu}{R/H}\right) \right] \quad (7.1)$$

where F is the average frictional stress, σ_v is the applied load, R/H is the radius-to-height ratio of the sample, μ is the friction coefficient between ring and sample and K_0 is the soil's coefficient of earth pressure at rest. Approximating $K_0 = (1 - \sin \varphi)$ and $\mu = 0.9 \cdot \sin \phi$ (assumption: angle of wall friction δ equals 90% of φ) for the fixed ring type oedometer ($R=35\text{mm}$, $H=20\text{mm}$) used within the present study, the frictional stress by that formula, equals

$$F = \bar{\mu} \cdot \sigma_v = 0.10 \sim 0.12 \cdot \sigma_v \quad (7.2)$$

Although the formula is rather approximate, it shows that friction might be reduced significantly by (a) reduction of the wall friction, e.g. by coating or smearing of the inner ring, and by (b) increasing the R/H ratio or employment of a floating ring type.

The calculated friction of 10-12% for the used device is in accordance with experimental data in literature. Experiments on remoulded Boston Blue clay showed a friction up to 6-11%, according to Taylor (1942) an "appreciable magnitude", but "not large enough to be of major practical importance". Leonards and Girault (1961) analysed the influence of ring material and showed that for steel rings the friction may reach 18%, 12% for rings lined with tetrafluoroethylene and 7% for tetrafluoroethylene coated with molybdenum disulfide grease. Moreover, Olson (1986) reports on unpublished theses at M.I.T. and the university of Illinois, showing friction in the same order of magnitude. Burland and Roscoe (1969) studied the increasing magnitude of side wall friction for higher oedometer rings. They showed, that for $R/H > 2.5$ friction approaches zero and confirmed the positive effect of silicone grease. Based on these studies, suggestions for the height-to-diameter-ratio for oedometer construction were integrated into the relevant standard design codes (see Chapter 5.2.1).

Figure 7.4 shows the emerging friction in the stepwise oedometer tests, performed within the present study. Here, the *friction* F is calculated as

$$|F| = \sigma_v^t - \sigma_v^b \quad (7.3)$$

The friction increases with applied vertical stress and deformation. For a maximum vertical effective stress of 400 kN/m^2 a maximum friction of $15\% \sim 17\%$ is measured. From the calibration tests with water 4% friction for $\sigma'_v = 400 \text{ kN/m}^2$ is measured. Therefore, an additional friction of $11\% \sim 13\%$ must be noticed, which equals the friction calculated by Eq. 7.1 and lies in the range given in literature. During unloading an even higher friction is detected. The relative amount of friction approaches 20% (unloading from 400 to 200 kN/m^2). This is also in agreement with literature (Burland and Roscoe, 1969).

For the present measurement it is difficult to distinguish between friction caused by oedometer cell - ring and sample -ring contact, as both types of friction increase with increasing deformation and thus with increasing stress level. The increase in friction with ongoing consolidation is exemplarily for one load step displayed in Fig. 7.4c. It can be observed that friction increases during consolidation, while in the secondary consolidation no further growth in friction is monitored. This indicates, that some part of the measured friction is due to the O-ring - ring contact rather than due to sample - ring contact. Otherwise, structural changes in the soil material during secondary compression should lead to a further increase in friction.

7.1.3 Consolidation settlements

The time-dependent deformation behaviour and consolidation rate in each load step and their dependency on stress-state and void ratio are of significant importance for the present study. Thus, in this section the time-dependent deformation behaviour for compression and unloading paths from the step-wise monotonic oedometer tests is examined.

The rate of consolidation is mainly influenced by two material properties: permeability and stiffness. With larger permeability and larger stiffness the soil consolidates faster. As illustrated in Chapter 2.2.4 and 2.3 both properties depend on the state parameters void ratio e and effective stress σ'_v . However, it is commonly assumed, that the stiffness is mainly controlled by the acting effective stress and the permeability mainly by the void ratio. While in Terzaghi's theory the rate of consolidation, expressed as c_v , is assumed to be constant, in reality, it may increase or decrease with increasing σ'_v depending on whether the soil is governed by mechanical or physico-chemical processes, as described in Karunaratne et al. (2001) and illustrated in detail in Chapter 3.4.6. Simplified it can be stated, that a soil, which is controlled by mechanical processes, depends more on changes in stiffness and effective stress than changes in void ratio and permeability.

Fig. 7.5a shows the normalised settlement versus time plots from step-wise tests on Kaolin clay. Due to the very small deformations during unloading, a lower measurement resolution is to be observed within this plot. The figure illustrates, that Kaolin is governed by its mechanical rather than physico-chemical processes. With increasing vertical stress, the compression consolidation settlements occur faster. With higher vertical stress, the rate of consolidation increases. During unloading the opposite effect occurs. With loading stiffness increases due to increasing vertical effective stress, while the permeability decreases due to a decrease in void ratio. The two mechanisms are counter-acting with reference to the consolidation rate. For kaolinite, the mechanical behaviour controls the consolidation process (Robinson and Allam, 1998). Therefore, the increase in stiffness and thus the change in effective stress is more dominant, so that for higher effective stress the consolidation occurs faster and c_v increases.

To analyse the development of consolidation rate for structured soils, Fig. 7.5 also compares the time-settlement curves from tests on reconstituted and natural Onsøy clay. Figure 7.5b shows, that reconstituted Onsøy clay like the tested kaolin clay, is governed by mechanical instead of physico-chemical processes as with increasing effective stress and stiffness the consolidation is accelerated. Figure 7.5c displays the normalised time-dependent settlements of natural Onsøy clay. Here it can be recognised, that in the first three load steps, from 10-20 kN/m² and from 20-50 kN/m², settlements occur fast compared to the later load steps. In the first three load steps the natural soil is still structured. The high permeability resulting from high void ratio together with a high stiffness due to the intact bonding affects a high c_v and causes a fast consolidation. After exceeding the yield stress, the stiffness suddenly drops due to the destructuration of the soil, while the void ratio and permeability experience a slower change. This significantly retards the consolidation process or, in terms of c_v , causes a decrease in c_v . In the higher load steps the soil matrix is compressed. The decrease in void ratio causes a decrease in permeability. However, the increase in stiffness is more dominant, so that for higher effective stress the consolidation occurs faster. From comparison of the unloading curves, it can be observed, that due to the experienced destructuration and elastic unloading stress path, both clay states show an equivalent unloading behaviour. Caused by the higher stiffness, the swelling deformation occurs faster in the higher than in the lower stress range. As the change in stress-dependent stiffness is congruent for reconstituted and natural sample (reflected in almost identical inclination of the recompression branch, C_{ur}), the swelling rate in the particular load steps likewise is the same.

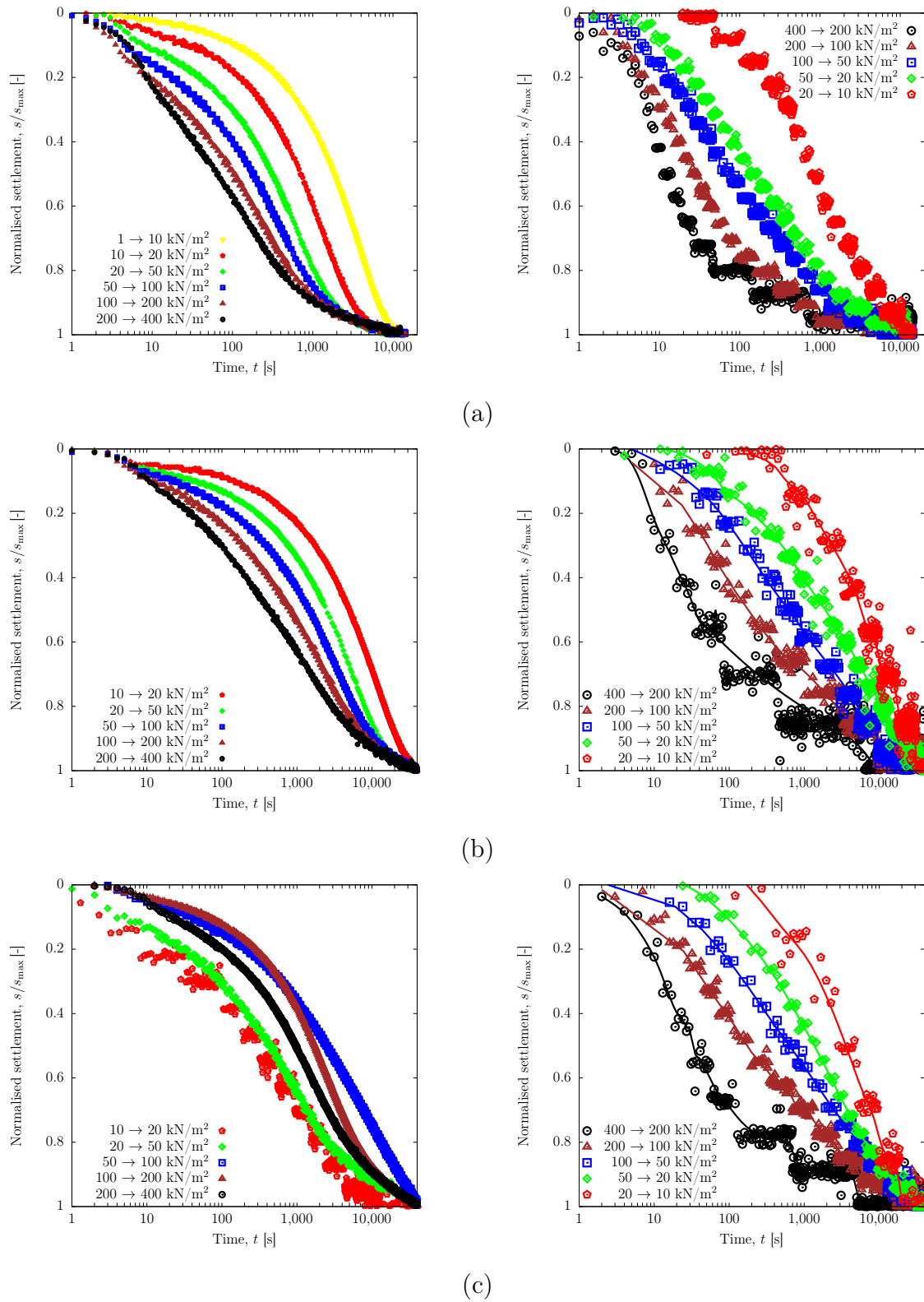


Figure 7.5: Time-dependent deformation during compression (left) and unloading (right) load steps from tests on (a) Spergau kaolin clay, (b) reconstituted and (c) natural Onsøy clay.

7.1.4 Coefficient of consolidation c_v

In Terzaghi's consolidation theory the consolidation rate is mathematically described by the coefficient of consolidation c_v . From oedometer test results c_v can be determined graphically as described in detail in Chapter 3.4.6. As c_v is a good measure to characterise the consolidation behaviour regarding its rate, Fig. 7.6 gives the c_v values calculated from present test data for kaolin and Onsøy clay.

The graph confirms the conclusions from the time-dependent settlement curves and theoretical assumptions:

- c_v increases with increasing effective stress and decreasing void ratio. Thus, both materials, kaolin as well as Onsøy clay can be classified as governed by their mechanical rather than their physico-chemical behaviour.

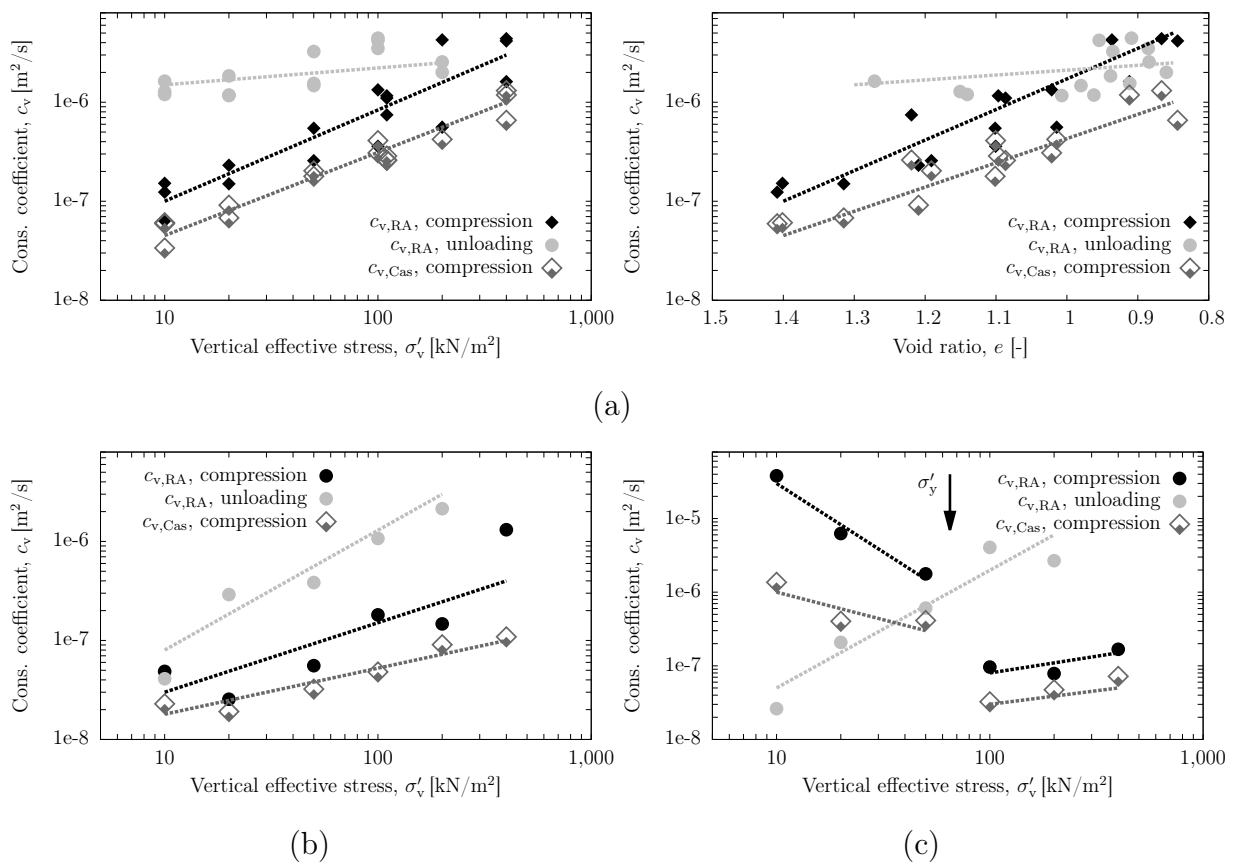


Figure 7.6: (a) Stress- and void-ratio-dependent consolidation coefficient c_v for kaolin clay, and stress-dependent consolidation coefficient c_v for (b) reconstituted and (c) natural Onsøy clay.

- The consolidation coefficient determined using the Casagrande method ($c_{v,Cas}$) is always smaller than the consolidation coefficient $c_{v,RA}$ determined from the early-stage-log-t method according to Robinson and Allam (1996). This is due to the fact, that creep settlements are almost completely neglected in this method. This finding is in accordance with observations in literature (Das, 2010).
- During unloading stress paths, c_v is always much higher at the same reference stress. This is due to the fact, that the stiffness is much higher in unloading stress paths due to plastic deformation in the virgin compression.
- Natural Onsøy clay exhibits a distinct destructuration behaviour which is reflected in c_v . Before reaching the yield stress the structured clay shows a stiff behaviour expressed in a high c_v value. After exceeding the yield stress c_v drops suddenly. For higher effective stress a subsequent increase in c_v can be observed.

To analyse in more detail whether and how the consolidation rate depends not only on the vertical, effective stress, but also on void ratio changes, time-settlement curves from unloading-reloading oedometer tests are illustrated in Fig. 7.7.

Figure 7.7a demonstrates the dependency of the consolidation rate on stiffness and vertical, effective stress. The direct loading test exhibits a similar consolidation rate as the step-wise test reaching equivalent final effective stress and thus a similar material stiffness. It can be concluded that the consolidation rate is most significantly influenced by the stiffness resulting from the applied vertical, effective stress.

Moreover, Fig. 7.7b demonstrates the dependency of the consolidation rate on the loading direction, as for the same mean effective stress $\sigma'_{mean} = 300 \text{ kN/m}^2$ the consolidation rate is significantly different in compression and unloading. During unloading the soil matrix exhibits a much stiffer behaviour ($C_{ur} \gg C_c$), resulting in a faster consolidation progress.

Figure 7.7c compares the time-dependent settlements from four load steps reaching to the same final effective stress $\sigma'_{mean} = 100 \text{ kN/m}^2$ with different final void ratios. The primary loading path exhibits a slower time-settlement behaviour compared to the unloading-reloading curve. This shows, that the consolidation rate is not only dependent on the final effective stress, but also on the final void ratio and loading direction. The two unloading phases ($200 \rightarrow 100 \text{ kN/m}^2$) with assumed equivalent stiffness C_{ur} show almost identical, fast time-settlement paths. The reloading path ($50 \rightarrow 100 \text{ kN/m}^2$) exhibits slightly slower time-dependent settlements than the unloading path. This confirms the strong stiffness dependency of the consolidation rate for the tested kaolin clay, as in reality a reloading path may have a slightly smaller stiffness than the equivalent unloading path.

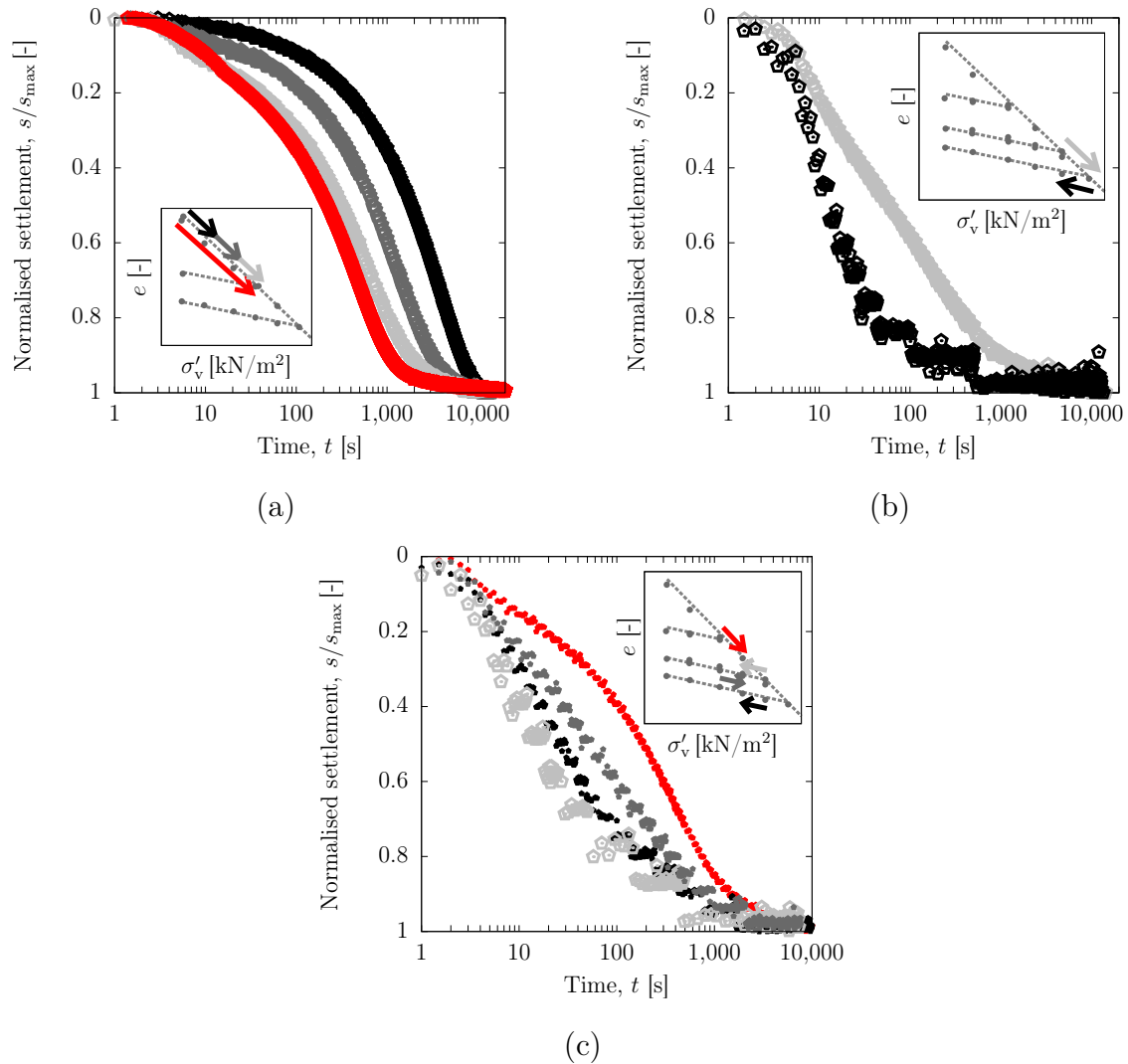


Figure 7.7: Time-dependent deformation of Spergau kaolin clay during compression and unloading for different stress paths.

7.1.5 Development of stiffness and permeability

As illustrated in Chapter 2.2.4 and 2.3 stiffness and permeability change with increasing compression. In a stepwise oedometer test, the stiffness in each loading step can be calculated as the secant modulus

$$E_s = \frac{\Delta\sigma'_v}{\Delta\varepsilon_v} \quad (7.4)$$

Figure 7.8 shows the stiffness-vertical effective stress relationship for loading and unloading stress paths of kaolin and Onsøy clay. The stiffness of the reconstituted clays is similar

and can be approximated properly by Ohde's approach

$$E_s(\sigma'_v) = E^{\text{ref}}(\sigma'_{v,\text{ref}}) \cdot \frac{\sigma'_v}{\sigma'_{v,\text{ref}}} \quad (7.5)$$

with $\sigma'_{v,\text{ref}}=100 \text{ kN/m}^2$ to be $E^{\text{ref}}=1.6/30 \text{ MPa}$ (loading/unloading) for kaolin and $E^{\text{ref}}=1.15/60 \text{ MPa}$ (loading/unloading) for reconstituted Onsøy clay.

Natural Onsøy clay as expected exhibits a different stiffness behaviour. Approaching the yield stress, the stiffness decreases and after exceeding the yield stress increases again.

As demonstrated above, both clays are governed by their mechanical behaviour. A back-calculation of the permeability k from c_v hence is possible. The permeability may therefore be calculated based on the stiffness E_s and the consolidation coefficient c_v in each loading step by

$$k = \frac{c_v \cdot \gamma_w}{E_s} \quad (7.6)$$

Figure 7.9 gives the void-ratio dependent permeabilities for kaolin and Onsøy clay calculated based on the stiffness given in Fig. 7.8 and consolidation coefficient given in Fig. 7.6.

Kaolin clay generally exhibits an approximately 5-times higher permeability than the reconstituted Onsøy clay. Natural clay material at higher void ratio $e > e(\sigma'_y)$ due to

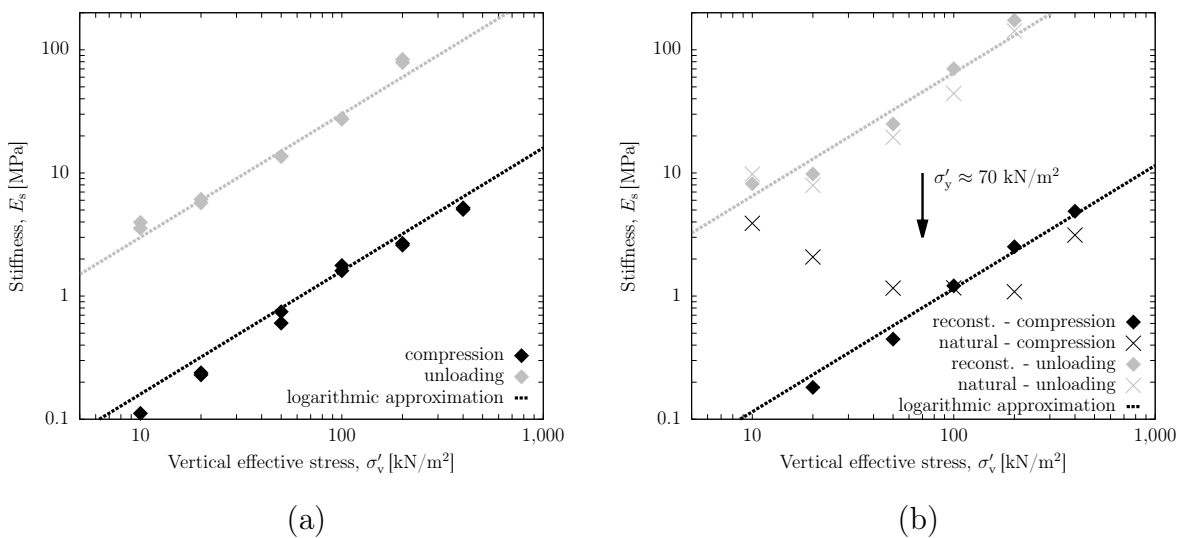


Figure 7.8: Effective stress dependent stiffness E_s of (a) kaolin and (b) Onsøy clay.

its present structure and fabric, shows a 10-20 times higher permeability compared to the reconstituted material. However, after destructureation both materials show a unique permeability-void ratio relationship. For both clays the permeabilities calculated from unloading paths are much smaller than calculated from loading paths.

With the exponential approximation, the permeability-void ratio relationship written as

$$k = k^{\text{ref}} \cdot \left(\frac{e}{e^{\text{ref}}} \right)^n \quad (7.7)$$

can be captured well for the loading path, assuming $k^{\text{ref}}(e^{\text{ref}} = 1) = 4 \cdot 10^{-9}/4 \cdot 10^{-10}$ for kaolin/ Onsøy clay. For the unloading path the Olson cluster model (see Eq. 2.32) given by

$$k = \left(N^{2/3} \cdot \frac{(1 - \frac{e_c}{e_t})^2}{(1 + e_c)^{4/3}} \right) \cdot \underbrace{\left(\frac{\gamma_p}{\nu_p} \right) \cdot \left(\frac{1}{k_0 T^2 S_0^2} \cdot \frac{e^3}{1 + e} \right)}_{k_{\text{KC}}, \text{ see Eq. 2.30}} \quad (7.8)$$

assuming $N = 40$, $e_c = 0.8/0.85$ and $k_{\text{KC}} = \frac{2 \cdot 10^{-7}}{8 \cdot 10^{-9}} \cdot \frac{e^3}{(1+e)}$ for kaolin/ Onsøy clay, provides a much better fit.

For the kaolin as well as Onsøy clay, the derived permeabilities are in good agreement with permeability data from literature (compare Baille (2014); Haase and Schanz (2016) for Spergau kaolin and Lunne et al. (2003) for Onsøy).

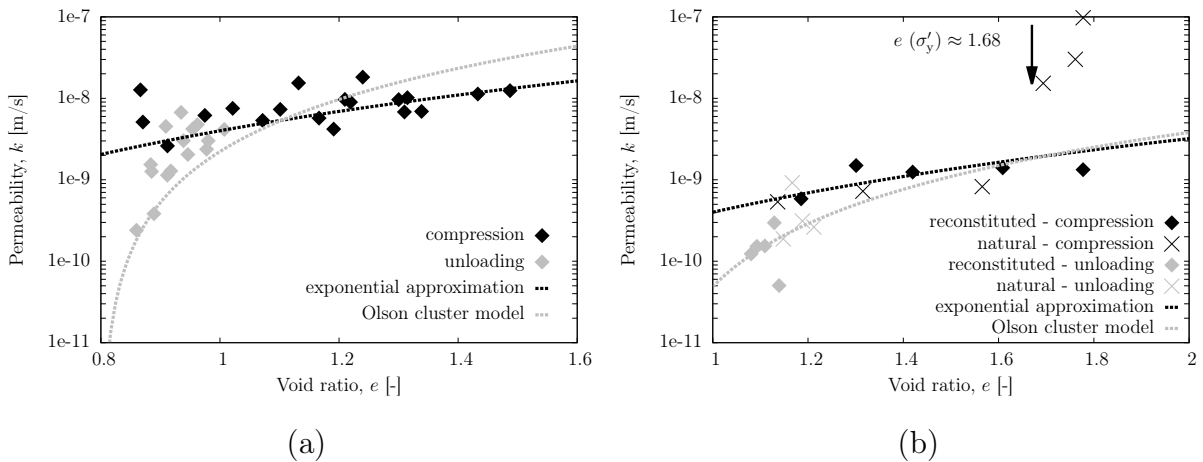


Figure 7.9: Void ratio dependent permeability of (a) kaolin, (b) reconstituted and natural Onsøy clay.

7.1.6 Secondary compression

The coefficient of secondary compression C_α was determined from all tests according to Eq. 2.20. The results are given in Fig. 7.10 in terms of $C_{\alpha,e}$, computed based on the void ratio change.

The kaolin clay shows no significant creep behaviour. With values of C_α lower than 0.01, almost no creep occurs after the end of primary consolidation. With increasing effective stress a slight increase in the secondary compression can be recognized. The values of C_α computed for Onsøy clay exhibit a more pronounced creep behaviour. While for the reconstituted material values of C_α range between 0.01 and 0.02, the values found for the natural material vary strongly with respect to the yield stress. Before reaching the yield stress, C_α is very small, increasing strongly around yield stress. After yielding C_α lies within the same range as C_α for the reconstituted material.

Moreover, Fig. 7.10b gives the C_α/C_C ratio. Generally, the values are in agreement with C_α/C_C ratios given in Mesri and Godlewski (1977). However, it can be observed, that the C_α/C_C ratio of kaolin is not constant at all, but increases with increasing vertical effective stress.

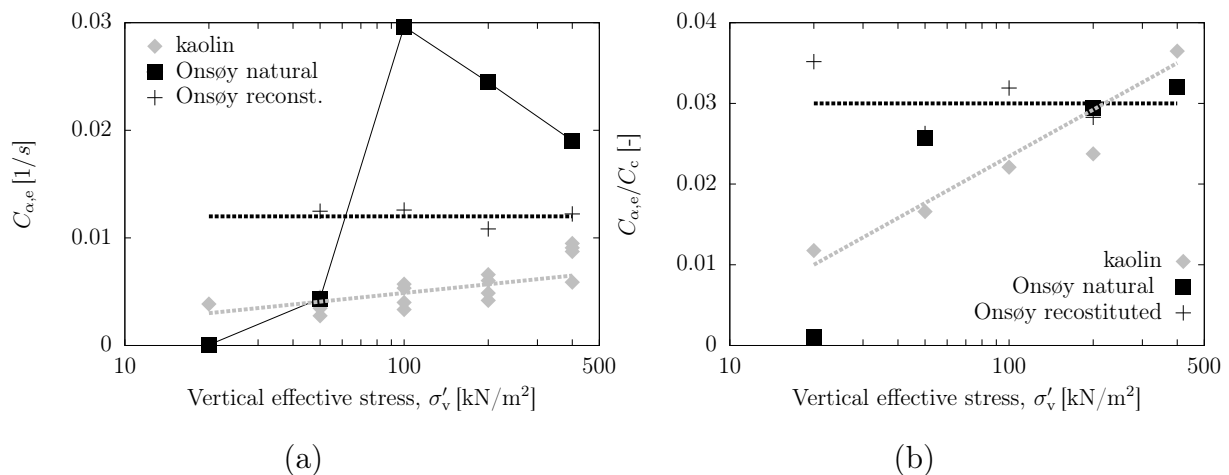


Figure 7.10: (a) Coefficient of secondary compression and (b) C_α/C_C over vertical effective stress for kaolin and Onsøy clay.

7.2 Pore water pressure dissipation

Besides the development of settlements with time, the dissipation of pore water pressure is the second indicator of the consolidation progress. Thus, a detailed study of the stress dependent pore pressure dissipation is necessary for the holistic analysis of consolidation under monotonic loading.

Figure 7.11 shows the typical evolution of pore water pressure over time from the stepwise consolidation of kaolin clay. The curves differ from the theoretical solution of Terzaghi's one-dimensional consolidation theory in two main points: (1) The normalized pore pressure at the beginning of the load step does not equal 1, but increases gradually. It reaches its maximum with a retardation of 20-200 s. (2) The maximum of the normalised pore water pressure does not equal 1, but ranges from 0.95 to approximately 0.6.

Figure 7.12 demonstrates the evolution of pore water pressure over time from the stepwise consolidation of reconstituted and natural Onsøy clay. It can be seen, that the curves for kaolin and reconstituted Onsøy clay evolve similarly, while the stiffer material behaviour of natural Onsøy clay prior to yielding can be observed in the dissimilarity of these curves. In the unloading phases the maximum pore water pressures are much smaller and the retardation is even higher compared to the loading phase. This corresponds to the stiffer behaviour and faster consolidation rate in unloading.

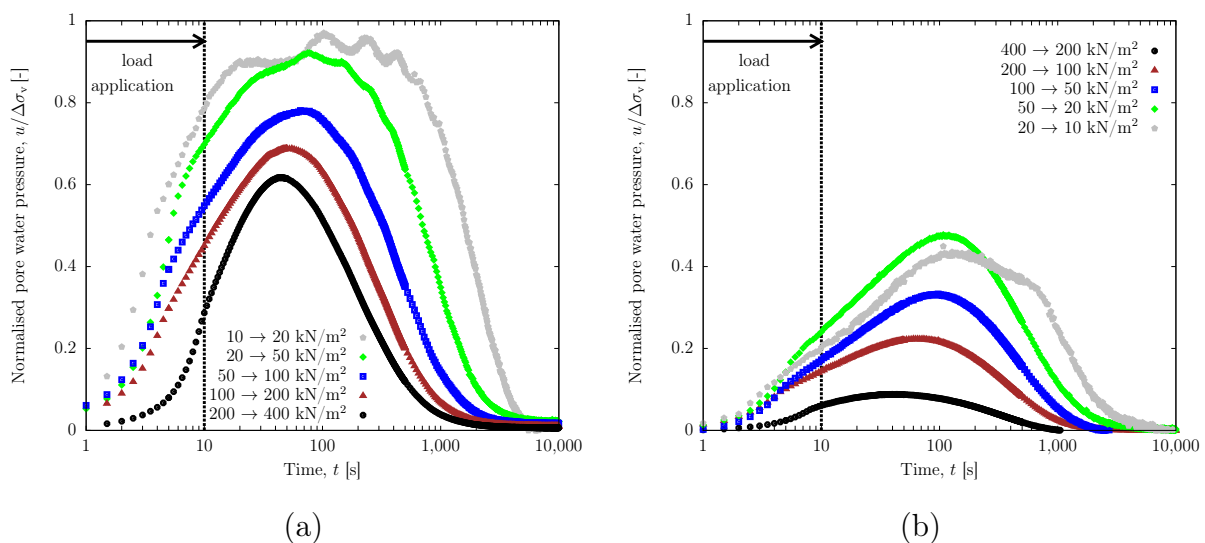


Figure 7.11: Pore water dissipation during (a) compression and (b) unloading load steps from tests Spergau kaolin clay.

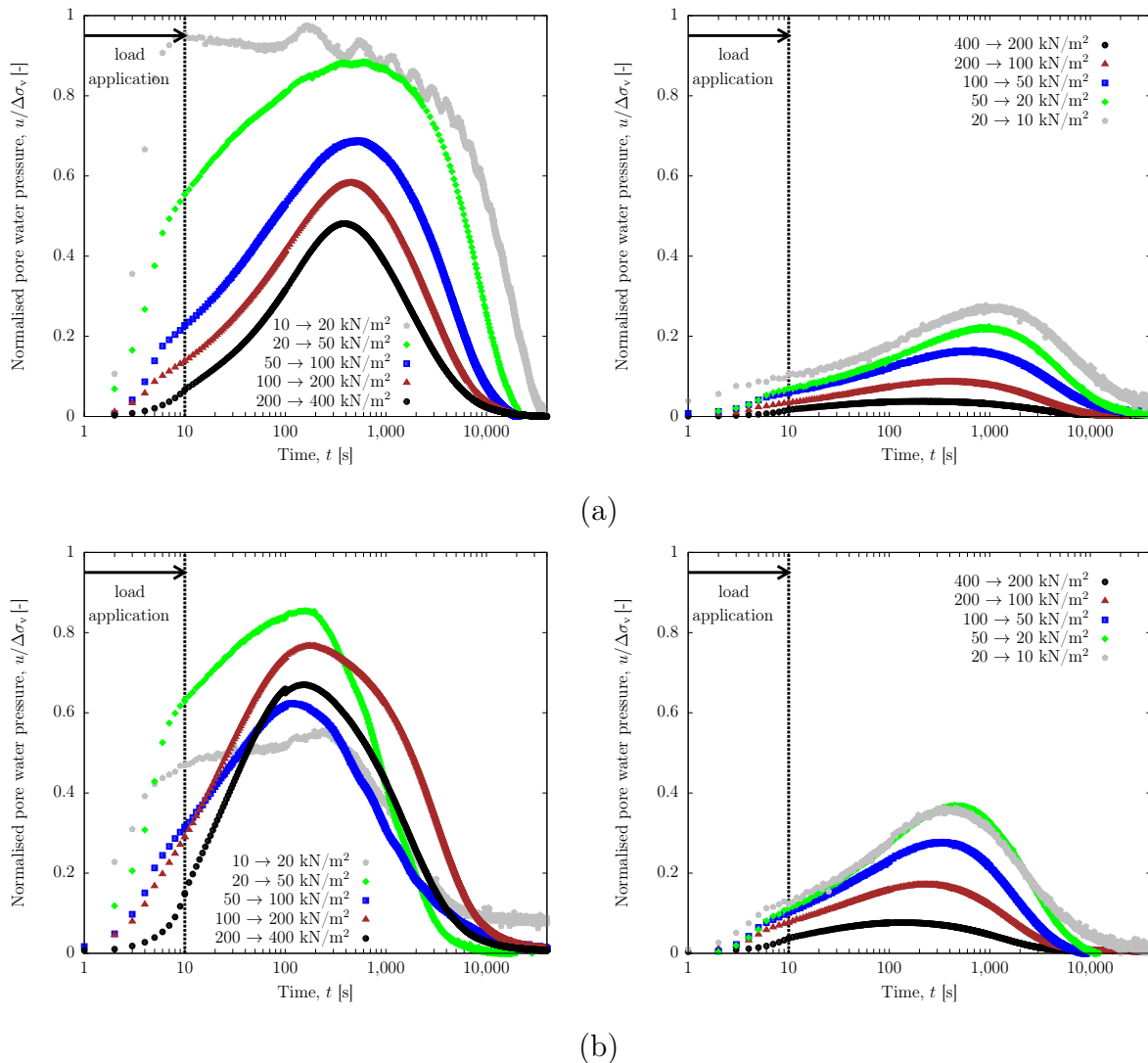


Figure 7.12: Pore water dissipation during compression and unloading load steps from tests on (a) reconstituted and (b) natural Onsøy clay.

Both effects, reduction and delay of u_{\max} , are related to the consolidation rate, expressed in terms of consolidation coefficient c_v . Figure 7.13 illustrate this dependency for the loading paths. The relative, maximum pore pressure reached decreases with increasing c_v (see Fig.7.13a). This effect is directly connected to the retardation of pore water pressure peak, which is reached at the dimensionless consolidation time T_v . With increasing c_v the time to reach u_{\max} increases as well (see Fig.7.13b).

Various research studies in the past were concerned with the measurement of pore water pressure during consolidation (Whitman and Richardson, 1961; Gibson, 1963; Northey and Thomas, 1965; Perloff et al., 1965; Rowe and Barden, 1966; Burland and Roscoe, 1969; Sonpal and Katti, 1973; Soumaya and Kempfert, 2010; Robinson, 1999; Gao et al., 2017).

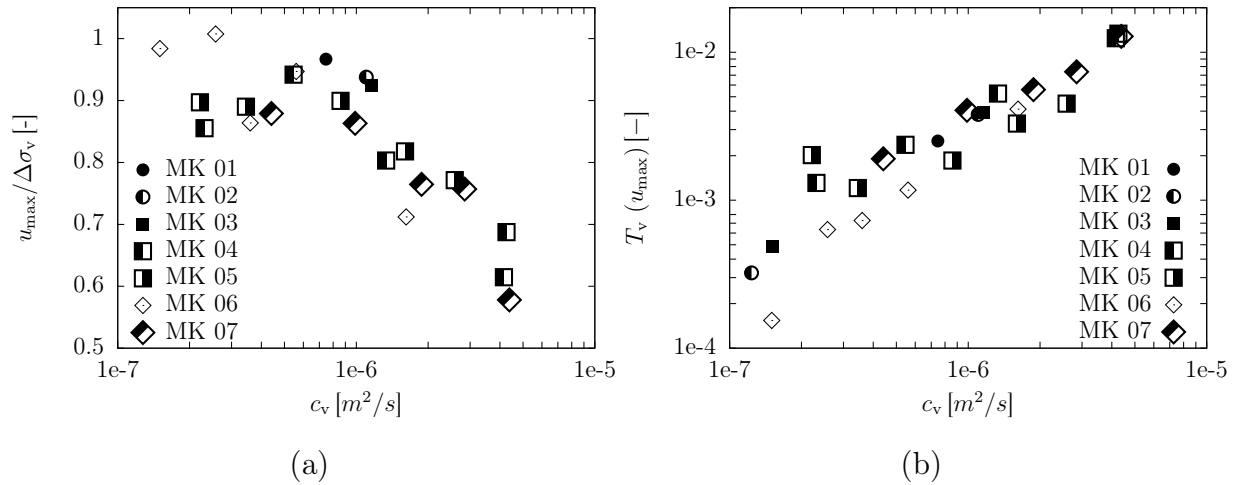


Figure 7.13: (a) Maximum pore pressure versus c_v and (b) time delay versus c_v , from tests on kaolin clay.

Similar curves to the ones in Fig. 7.11 are presented within these studies. The reason for differences between Terzaghi's linear analytical solution and the experimental results lies within the deviation of reality from the assumptions, the consolidation theory is based on. Generally, the described effect of the retarded pore pressure accumulation may be attributed to the following three reasons or deviations from the theoretical assumptions.

1. Gradual load application

In Terzaghi's basic theory an instantaneous loading is assumed. However, in the demonstrated experiments, the load application is performed within a finite time depending on the load application rate. For the monotonic oedometer experiments, the loading rate is chosen such that the additional load in each loading step is applied within approximately 10 to 15 s. The loading function during load application is that of a ramp function. Consolidation behaviour under this type of loading has been studied analytically as well as experimentally by several researches (Olson, 1977; Zhu and Yin, 1998; Hsu and Lu, 2006; Conte and Troncone, 2006; Hanna et al., 2013; Sivakugan et al., 2014). Within these studies it is shown that consolidation occurs during the loading process. Consequently, excess pore water pressures are reduced and the pore water pressure at the peak is decreased.

Figure 7.14 shows for an exemplary load step, that within the load application phase consolidation already progresses. This is indicated by an increasing degree of consolidation. Here, the degree of consolidation is computed based on settlements, according to Eq. 3.25. For a constant load application time with increasing c_v , consolidation occurs faster and the degree of consolidation reached within load application increases.

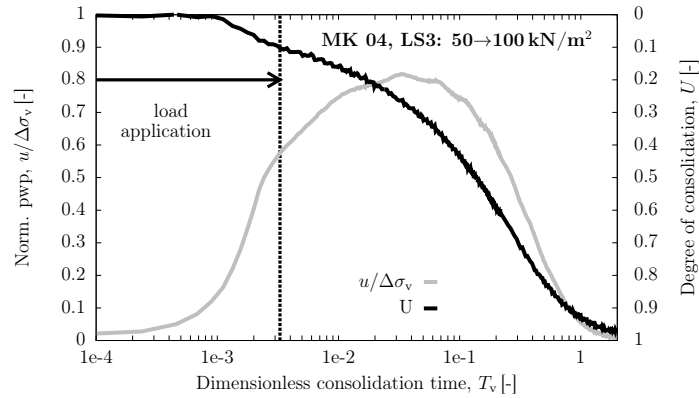


Figure 7.14: Development of pore water pressure with dimensionless consolidation time and increasing degree of consolidation.

According to Hanna et al. (2013) the degree of consolidation U_0 at the end of load application $t = t_0$ can be calculated by

$$U_0 = 1 - \frac{1}{T_0} \left[\sum_{m=0}^{\infty} \left(\frac{32}{(2m+1)^4 \cdot \pi^4} \right) (1 - e^{-\frac{\pi^2}{4} \cdot (2m+1)^2 \cdot T_0}) \right] \quad (7.9)$$

with $T_0 = \frac{c_v \cdot t_0}{H^2}$.

Simplifying for the present experiment $t_0 = 10$ s, $H = 0.02$ m – 0.015 m and $c_v = 1 \cdot 10^{-7} - 4 \cdot 10^{-6}$ m²/s (for kaolin clay) ranges of $T_0 = 0.0025 - 0.1778$ and $U_0 = 0.04 - 0.24$ for kaolin clay can be calculated. This range covers well the measured ranges for the loading paths in Fig. 7.13. For Onsøy clay assuming $c_v = 2 \cdot 10^{-8} - 3 \cdot 10^{-7}$ m²/s, $U_0 = 0.02 - 0.10$ for the reconstituted material can be calculated.

2. Imperfection in the measuring system

Another deviation of the experimental setup from Terzaghi's consolidation theory concerns the assumption, that all phases, i.e. the fluid and solid phase, are considered incompressible. In the experimental reality this is only up to a certain amount true. While the assumption of an incompressible solid phase can be regarded as valid, the fluid or water phase may show a certain compressibility. This compressibility is caused by two effects: (1) compressibility of the water pressure measuring system due to system flexibility and (2) compressibility of the pore water due to occluded air bubbles.

The system flexibility of the water pressure measuring system is a crucial point in the determination of pore water pressure. Thus, it was in the focus of scientific interest since the introduction of the first pore pressure measurement systems. Since then the relationship between volumetric deformability of the pressure measuring system C_{system}

and the soil matrix's compressibility C_m was analysed and the influence on the pore pressure measurement was studied (Whitman and Richardson, 1961; Gibson et al., 1963; Perloff et al., 1965; Northey and Thomas, 1965; Sonpal and Katti, 1973; Robinson, 1999).

According to Whitman and Richardson (1961) with increasing ratio C_{system}/C_m the maximum measured pore pressure becomes smaller and the delay of the pore pressure peak becomes larger. An increase in C_{system}/C_m can be caused either by a larger C_{system} or by a decrease of C_m . Usually, the system flexibility C_{system} can be assumed as constant. It depends mainly on the water volume inside the measuring system, its compressibility as well as on the expansibility of the material and applied pressure. To keep the system flexibility small, commonly, rigid material for the measuring device is used. To account for the compressibility of water in the measuring system, the pressure probe is placed as close to the sample as possible and de-aired water is used to guarantee for a gas-free liquid. In the case of the present study, all these requirements were fulfilled. The assumption of $C_{\text{system}}(t) = \text{const.}$, neglects the possibility that occluded air bubbles from the soil body could be pressed into the measuring system during compression. However, this assumption seems reasonable. Assuming a constant C_{system} a decrease in C_m with on-going compression, i.e. increasing c_v , following Whitman and Richardson (1961) would lead to a decrease in the maximum pore pressure and a retardation of the peak. This finding is in agreement with the data from the present study. Consequently, part of the effects found in pore measurement could also be attributed to the system flexibility. Albeit, due to the small compressibility of the measuring system C_{system} owing to the constructional design, this effect can be estimated to be rather small.

3. Imperfection in the soil sample

Terzaghi's basic theory assumes that both phases in the soil matrix, namely fluid and solid phase are incompressible ($C_f = C_s = 0$). For soils the assumption of $C_s = 0$ usually holds true, as clay minerals or sand grains are much stiffer compared to the soil matrix. For other porous material, e.g. concrete or rock, this may not be the case. The assumption of $C_f = 0$ for soils is of limited validity, when it comes to the questions of reduced soil saturation, e.g. in terms of occluded air bubbles in the pore water. In this case the water compressibility decreases significantly. Depending on the degree of saturation, the water compressibility can be calculated based on Boyle's gas law by

$$C_f = S \cdot C_{f,0} + \frac{(1 - S)}{p_0} \quad (7.10)$$

where C_f is the fluid or water compressibility, $C_{f,0} = 5 \cdot 10^{-10} \text{ m}^2/\text{N}$ is the compressibility of pure water, S is the degree of saturation and p_0 is the absolute pressure in the water.

From Eq. 7.10 it can be calculated that under atmospheric pressure ($p_0 = 100 \text{ kN/m}^2$) a reduction of the saturation by 1 % to $S = 0.99$, reduces the water compressibility by the factor $C_f/C_{f,0} = 200$. This shows how rapidly C_f decreases with decreasing saturation. Therefore, it can be argued that even a very small amount of gas in the water phase may justify the consideration of fluid compressibility in the framework of consolidation equations.

Assuming that $C_f \neq 0$, the so-called *hybrid model* introduced in Chapter 3.3.2 has to be applied for the calculation of the consolidation process. Due to the compressibility of water, the applied load σ_v is distributed between water phase (pore water pressure u) and soil matrix (effective stress σ'_v). The amount of load carried by the pore water and soil matrix respectively depends on the ratio of compressibilities C_f/C_m and the porosity of the matrix n . The ratio is expressed by the Skempton B coefficient (see Chapter 3.3). In case of compressible fluid and incompressible solid phase, B can be written as (compare Eq. 3.11)

$$B = \frac{1}{1 + n \cdot \frac{C_f}{C_m}} \quad (7.11)$$

With decreasing saturation, C_f increases while C_m is assumed to be constant. Hence, B decreases. Combining Eqs. 7.10 and 7.11 and introducing $n = \frac{e_0}{1+e_0}$, $C_m = 1/E_s$, B can be written as a function of S and E_s :

$$B = \frac{1}{1 + E_s \cdot \frac{e_0}{1+e_0} \cdot \left(S \cdot C_{f,0} + \frac{(1-S)}{p_0} \right)} \quad (7.12)$$

From Eq. 3.20 the pore water pressure and from Eq. 3.27 the consolidation settlements over consolidation time can be calculated accounting for $B \leq 1$. The influence of B on the dissipation of pore water pressure is shown in Fig. 7.15 using typical material characteristics derived experimentally for the two load steps $\Delta\sigma_v = 10 \rightarrow 100 \text{ kN/m}^2$ and $\Delta\sigma_v = 200 \rightarrow 400 \text{ kN/m}^2$. For constant permeability k and stiffness E_s , the initial pore water pressure at load application decreases with decreasing saturation. The influence of saturation on the maximum pore water pressure is more significant in the higher stress ranges, as with increasing stiffness E_s the ratio C_f/C_m is additionally increased.

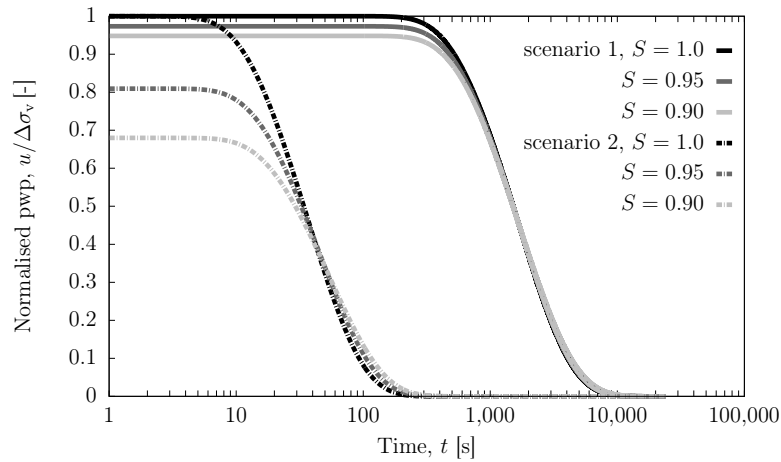


Figure 7.15: Pore water pressure dissipation with varying saturation for a kaolin clay sample (scenario 1: $p_0 = 10 \text{ kN/m}^2$, $k = 1 \cdot 10^{-8} \text{ m/s}$, $E_s = 100 \text{ kN/m}^2$, $h = 0.02 \text{ m}$; scenario 2: $p_0 = 400 \text{ kN/m}^2$, $k = 5 \cdot 10^{-9} \text{ m/s}$, $E_s = 5000 \text{ kN/m}^2$, $h = 0.015 \text{ m}$).

For the given scenarios, a reduction in the maximum pore water pressure up to approx. 40 % is computed. However, the underlying saturation $S = 0.9$ is very low, as calibration experiments have shown that for the present experiments the saturation can be assumed to be $S \geq 97\%$. Nevertheless, even a small reduction of maximum 2-3 % may result in a recognisable decrease in maximum pore water pressure. Thus, this effect can be stated to participate in the pore pressure dissipation behaviour measured in the present study.

The analytical solution presented in Fig. 7.15 does not show any time delay of the maximum pore water pressure with decreasing saturation S . However, it can be assumed that with increasing water compressibility a time delay due to slower load transmitting would occur.

7.3 Comparison to analytical solution

Figure 7.16 compares the measured consolidation settlements in terms of degree of consolidation and pore water pressure dissipation for different load steps (LS) of an exemplary test sample on kaolin clay to the analytical solution based on the hybrid model (see Chapter 3.3.2). The material parameters used within the analytical solution were derived based on the experimental data are given in Table 7.2. While the permeability in analytical solution AS1 was derived based on $c_{v,RA}$ and E_s , the permeability in the analytical solution AS2 was computed using $c_{v,Cas}$ and E_s .

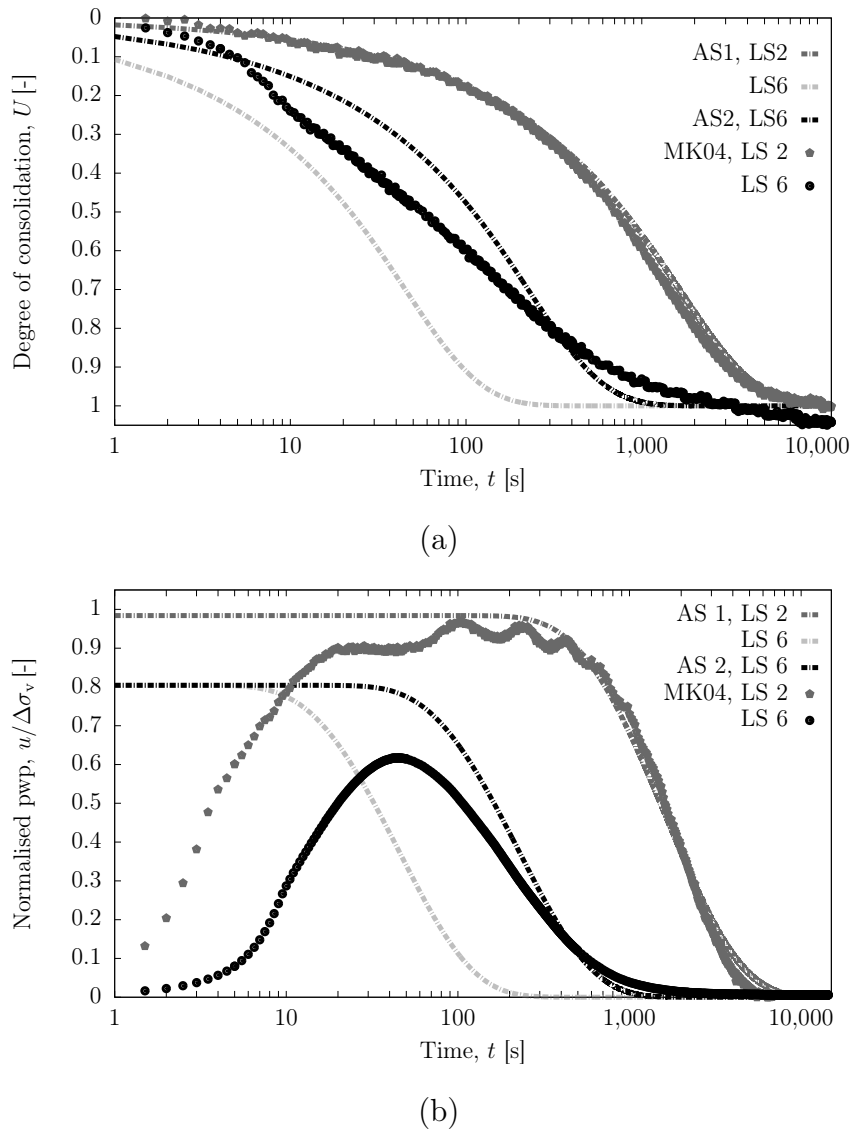


Figure 7.16: (a) Degree of consolidation and (b) pore water pressure dissipation - comparison between experimental data (test MK04) and analytical solution using the hybrid model.

From the comparison between experimental data and analytical solution it can be concluded, that generally, the hybrid model is able to fit the experimental data. This particularly holds true for the early loading steps at lower effective stress. The analytical solution based on the parameters derived from the experimental study, fit very well regarding the degree of consolidation and the pore water pressure. Only, the initial increase of pore water pressure due to gradual load application cannot be captured by the analytical solution.

Table 7.2: Parameters for computing of monotonic consolidation with analytical solution using the hybrid model.

	AS 1		AS 2
	LS 1	LS 2	LS 2
Applied vertical stress, σ_v [kN/m ²]	10 \rightarrow 20	200 \rightarrow 400	200 \rightarrow 400
Sample height, h [m]	0.02	0.015	0.015
Initial void ratio, e_0 [-]	1.5	0.95	0.95
Stiffness, E_s [kN/m ²]	100	5000	5000
Permeability, k [m/s]	1e-8	5e-9	1e-9
Degree of saturation, S [-]	0.97	0.97	0.97

For higher load steps, the analytical solution (AS 2) using the permeability k calculated from $c_{v,Cas}$ fits the experimental data much better than the analytical solution (AS 1) using k calculated from $c_{v,RA}$. $c_{v,RA}$ is computed from the earlier part of the consolidation curve, where in the experiments consolidation occurs faster. When fitted based on this part of the experimental curve, the analytical solution reproduces a faster consolidation behaviour and cannot account for the later retardation in the consolidation process observed in the experiment. The analytical solution using the permeability calculated based on $c_{v,Cas}$ fits the general consolidation process better for higher load steps. However, it predicts a slightly retarded consolidation at the beginning and a slightly accelerated consolidation at the end.

Neither of the analytical solutions based on the hybrid model is able to reproduce the secondary compression observed in the experiments, which is more dominant in the higher than in the lower stress state (compare Chapter 7.1.6).

7.4 Development of radial stress

The radial stress measured by strain gauges in the experiment is the mean total radial stress over the sample height, which is the sum of the radial stress transferred by the soil matrix σ'_{rad} and the radial stress transferred by the pore water pressure u .

$$\sigma_{rad} = \underbrace{\sigma'_v \cdot K_0}_{\sigma'_{rad}} + u \quad (7.13)$$

At the end of each load step, the radial stress equals the effective radial stress $\sigma_{\text{rad}}(t \rightarrow \infty) = \sigma'_{\text{rad}} = K_0 \cdot \sigma'_v$ as all pore pressure has been dissipated and the load is carried solely by the soil matrix. However, at the beginning of a load step, the part of the total stress carried by the soil matrix is equal to the effective stress applied in the prior load step, while the rest is carried by the pore water: $\sigma_{\text{rad},i}(t = 0) = \sigma'_{v,i-1} \cdot K_0 + (\sigma_v - \sigma'_{v,i-1})$.

Following Eq. 7.13 the effective radial stress can be calculated as follows:

$$\sigma'_{\text{rad}} = \sigma_{\text{rad}} - u \quad (7.14)$$

The radial stress measured in the experiment is an integral mean value over the sample height, while the measured pore water pressure is a local value at the bottom of the sample. Therefore, the mean radial, effective stress must be calculated from the mean pore water pressure u_{mean} , which by the assumption of parabolic excess pore pressure distribution over sample height can be taken as $u_{\text{mean}} = 2/3 u_{\text{bottom}}$. The mean radial, effective stress is thus given by

$$\sigma'_{\text{rad,mean}} = \sigma_{\text{rad,mean}} - 2/3 u_{\text{bottom}} \quad (7.15)$$

Figure 7.17 shows the development of total and effective radial stress with increasing consolidation time for the kaolin clay. As illustrated for a single load step in Fig. 7.18a, the total radial stress increases with applied loading $\Delta\sigma_v$. During consolidation the total radial stress decreases due to the load transfer from water (isotropic) to the soil matrix ($K_0 < 1$). Caused by the retardation in pore water pressure built up, the radial effective stress curve shows an increase and decrease before reaching the equilibrium state. In the unloading load steps first a sudden decrease in the total radial stress can be observed, which is due to the negative pore water pressures arising. When the load is transferred to the soil matrix the radial stress increases again.

The development of radial stress during consolidation is in accordance with studies in literature. In Gareau et al. (2006) a similar radial stress development over consolidation time based on experiments in an adapted oedometer cell incorporating radial stress measurement on kaolin and Pot Clay (see Fig. 7.18c) is shown.

After dissipation of the pore water pressure at the end of each load step, $\sigma'_{\text{rad}} = \sigma_{\text{rad}}$ (see Fig. 7.18c). From the ratio $\Delta\sigma'_{\text{rad}}/\Delta\sigma_v$ or $\sigma'_{\text{rad}}/\sigma'_v$ respectively, the coefficient of earth pressure at rest K_0 can be calculated. For kaolin clay K_0 can be determined from the ex-

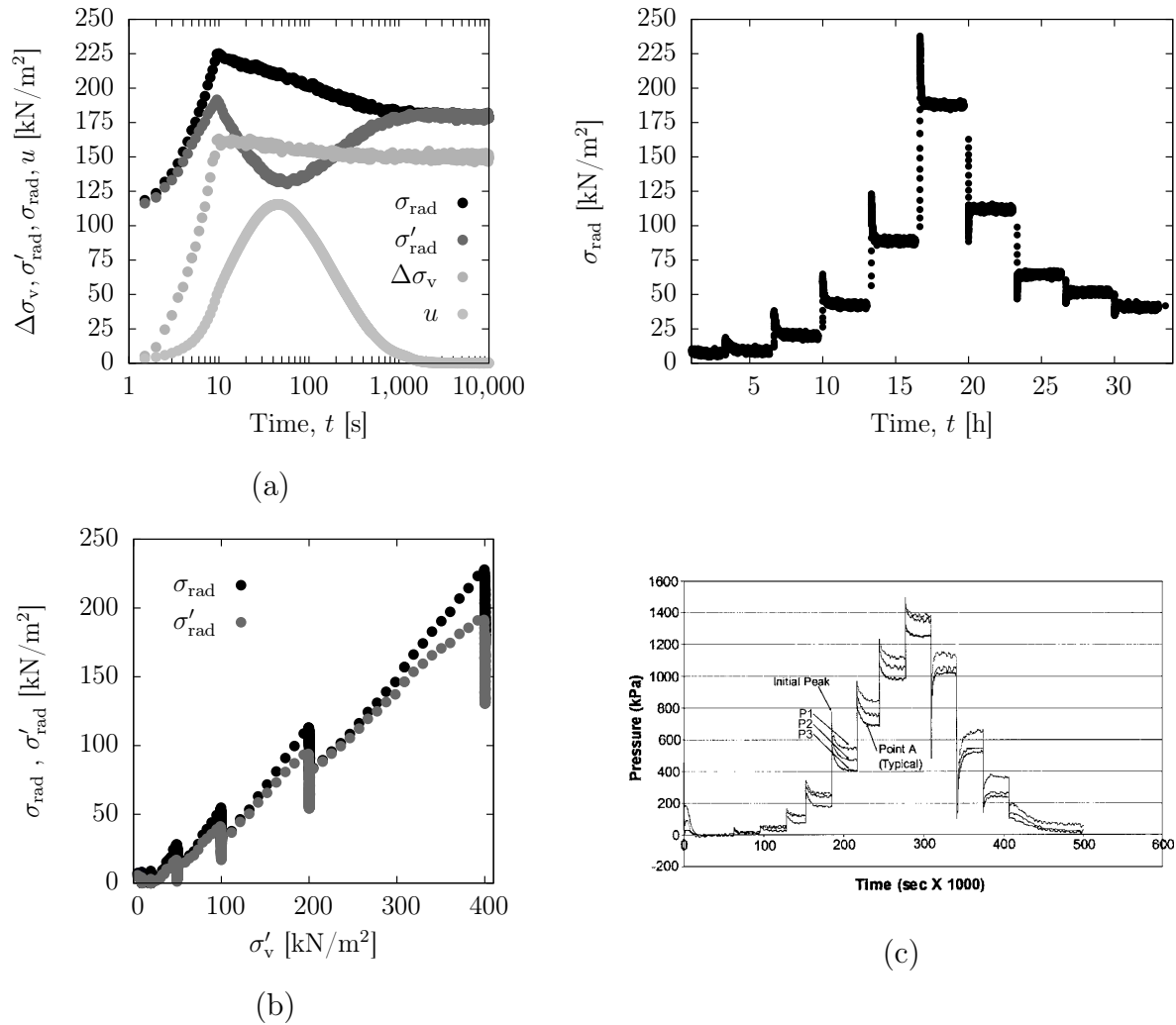


Figure 7.17: Development of radial stress from consolidation of kaolin clay: (a) Radial stress versus consolidation time in a single load-step 100 → 200 kN/m², (b) radial stress versus effective stress (c) radial stress versus consolidation time - comparison to Gareau et al. (2006).

perimental data to range between 0.4 and 0.5. Accounting for the friction, this lies within the lower range given in literature (see Chapter 2.2.9). In the lower stress range a strong variation is observed for the determined K_0 values. It can be concluded that a reliable determination of K_0 is limited to the higher stress range. During unloading the K_0 value increases slightly. Accounting for the friction in vertical stress due to oedometer friction, a correction may be applied to the K_0 value, resulting in a 10-15 % higher K_0 value. The same holds true for the K_0 values computed for Onsøy clay. With approximately 0.48, the K_0 value is slightly smaller than the value of 0.55 reported by Lunne et al. (2003).

The reconstituted Onsøy clay exhibits a much smaller K_0 . Further investigations on this effect should be accomplished, but are beyond the scope of this work.

7.5 Summary

The consolidation behaviour of kaolin and natural and reconstituted Onsøy clay under monotonic loading was studied. From the experimental data the general compression behaviour, development of consolidation settlements and pore water pressure dissipation as well as radial stress development and the secondary compression behaviour were analysed.

In an experimental series of 3 direct loading tests (10-110 kN/m²), 2 loading-unloading and 2 unloading-reloading tests the compression behaviour of kaolin was investigated. The compression and recompression indices were calculated from the compression curve to be $C_c = 0.30$ and $C_{ur} = 0.066$, which is in accordance with compression indices for kaolinite clays given in literature. From a test series on natural and reconstituted Onsøy clay the compression indices were determined to be $C_c = 0.40$ and $C_{ur} = 0.045$. The natural clay material exhibits the typical behaviour of a structured soil, also reflected by the position of its compression line to SCL and ICL in the $I_v - \sigma'$ plot according to Burland (1990). The yield stress of natural Onsøy clay was found to be approx. $\sigma'_y = 70$ kN/m², which is in accordance with the characterisation by Lunne et al. (2003).

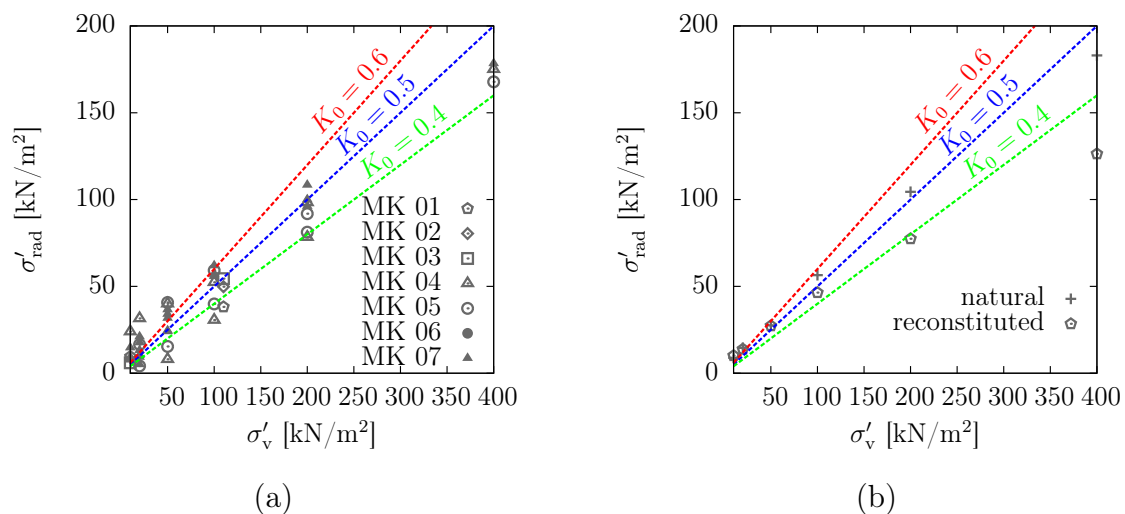


Figure 7.18: Radial effective stress versus vertical effective stress with respect to K_0 for (a) kaolin clay and (b) Onsøy clay.

The stress reduction between applied vertical pressure at the top of the oedometer device and measured vertical pressure underneath the sample referred to as friction, was analysed regarding its amount and origin. It was shown, that the friction for loading up to 400 kN/m² amounts up to 15 % in loading and up to 20 % in unloading stress paths. By a careful analysis it was attributed to three effects: (a) frictional contact in the oedometer cell between oedometer ring and sealing O-rings, (b) frictional contact between soil material and oedometer ring and (c) arching effects due to a change in the soil fabric during consolidation. The measured amount of friction is in accordance with the approach by Taylor (1942), presuming a friction of 10-12%. The additional friction can be attributed to the friction in the oedometer cell.

From the analysis of time-dependent deformation, the rate of consolidation and its development with increasing compression was analysed for the two clays. It was shown, that for both clays the rate of consolidation increases with increasing vertical, effective stress. Therefore, it could be concluded, referring to Karunaratne et al. (2001), that both clays, kaolin and Onsøy clay, are governed by their mechanical rather than their physico-chemical processes during consolidation. The coefficient of consolidation was computed from the time-settlement curves using the two common methods after Casagrande and Fadum (1940) and Robinson and Allam (1996). While the Robinson method uses the earlier part of the time-settlement curve, the Casagrande method considers the later part. Consequently, the Robinson method gives larger values (denoted as $c_{v,RA}$) as it nearly neglects the influence of secondary compression, which is more relevant for the kaolin clay in higher stress ranges. The $c_{v,RA}$ for kaolin clay was calculated to range between $1 \cdot 10^{-7} - 5 \cdot 10^{-6}$ m²/s in loading paths from 10 to 400 kN/m². In unloading paths of the same range of c_v was found to be higher for the same reference stress due to plastic deformation and higher stiffness. From the c_v - σ'_v -relationship for Onsøy clay the destructuration of natural clay can be observed. This process is reflected in a high c_v prior to yielding ($c_{v,RA} = 4 \cdot 10^{-5}$ m²/s) followed by a sudden drop to $c_{v,RA} = 1 \cdot 10^{-7}$ m²/s after reaching the yield stress. The reconstituted Onsøy clay was found to exhibit a c_v - σ'_v -relationship similar to the kaolin clay.

From the experimental data the stiffness E_s was computed to range between $E_s(\sigma'_v = 10 \text{ kN/m}^2) = 100 \text{ kPa}$ to $E_s(\sigma'_v = 400 \text{ kN/m}^2) = 5 \text{ MPa}$ for kaolin in loading paths. During unloading a much higher stiffness of $E_s(\sigma'_v = 200 \text{ kN/m}^2) = 100 \text{ MPa}$ and $E_s(\sigma'_v = 10 \text{ kN/m}^2) = 4 \text{ MPa}$ was found. At a reference stress $\sigma'_{v,ref} = 100 \text{ kN/m}^2$ for the kaolin clay a stiffness of $E_s^{ref} = 1.6/30 \text{ MPa}$ in compression/unloading was found. The reconstituted Onsøy clay shows a similar stiffness development as the kaolin clay with

$E_s^{ref} = 1.15/60$ MPa. Again, for natural Onsøy clay, the material behaviour before and after yielding has to be distinguished, as due to the structure stiffness is higher prior to yielding, while it assimilates to the behaviour of the reconstituted material after yielding.

The permeability k [m/s] was calculated from the derived E_s and c_v values for both clays. It was found to range between $k = 1 \cdot 10^{-8} - 1 \cdot 10^{-9}$ m²/s for kaolin and $k = 1 \cdot 10^{-7} - 1 \cdot 10^{-10}$ m²/s for Onsøy clay, depending on the void ratio and for Onsøy clay on the present soil fabric. A good fit of the void ratio-permeability relationship for both materials could be derived based on an exponential approach and the cluster model by Olsen (1962).

The pore water pressure dissipation was analysed as the second indicator for the consolidation progress. It was shown, that the experimental curves deviate from Terzaghi's solution in two main points: (1) the maximum pore water pressure measured in the experiment is smaller than the applied vertical effective stress in the load step, (2) the maximum pore pressure is not present instantaneously after load application but is retarded in time. From a detailed analysis, it could be shown, that the amount of maximum pore water pressure as well as the retardation depend on the consolidation ratio characterised by the consolidation coefficient c_v . As the reason for this behaviour three differences in the experiment from assumptions in Terzaghi's basic theory were illuminated. First of all, the load application in the experiment happens not instantaneously, but gradually within 10-15 s. A comparison to an analytical solution by Hanna et al. (2013) accounting for ramp loading in consolidation theory confirmed this. Secondly, imperfections in the measuring system due to system flexibility of the pressure measuring system were discussed. Thirdly, a deviation of experiment from Terzaghi's basic theory regarding the soil material, namely the compressibility of the water phase was found to be one of the reasons for the effects in pore pressure measurement. By using the hybrid model, the basic Terzaghi theory can be adapted accounting for the including of air bubbles in the pore water system. The influence of the degree of saturation on the maximum pore pressure was studied.

A comparison between the analytical solution using the hybrid model and the experimental data revealed, that this model is well suitable to reproduce the overall consolidation behaviour found in the experiments. Limitations concern the reproduction of changing rate of consolidation in higher stress states as well as the modelling of secondary compression. It was shown, that for higher stress state the analytical solution using permeability calculated based on Casagrande's method fits much better than the one using the permeability calculated based on c_v from the early-stage-log-t method.

Besides the basic consolidation behaviour, the development of radial stresses was analysed from the strain gauge measurements. It was shown, that the effective radial stress within

one load step increases with increasing degree of consolidation. In the end of each load step the coefficient of earth pressure at rest K_0 can be calculated from the $\sigma'_{\text{rad}}/\sigma'_v$ -ratio. For kaolin clay K_0 was found to be approximately 0.5, for Onsøy clay it was computed in the range of 0.48. Both values are slightly smaller than values suggested in literature, which may be corrected with respect to the higher friction in the present oedometer cell.

The secondary compression behaviour was analysed in terms of C_α and C_α/C_c -ratio. Kaolin clay with C_α lower than 0.01 shows a less pronounced creep behaviour compared to Onsøy clay with $C_\alpha = 0.15$.

8 Experimental study on cyclic consolidation

Chapter 8 covers the experimental analysis of the consolidation behaviour of fine-grained soils under cyclic loading. An experimental study on kaolin and Onsøy clay under varying material and loading conditions has been performed in the presented oedometer device. Results focusing on the development of consolidation compression as well as on the pore pressure dissipation are presented within this chapter. A comparison of soil characteristics, e.g. coefficient of consolidation, stiffness and permeability, derived from the cyclic tests to the findings from monotonic loading tests is drawn, in order to quantify the differences in monotonic and cyclic consolidation behaviour. Based on the identified material parameters, a comparison between the experimental results and the analytical solution presented in Chapter 4 reveals the limitations of the assumptions forming the basis of the mathematical model. To overcome these limitations numerical models using different constitutive approaches are introduced and studied regarding their ability to reproduce the effects observed in the experimental study.

8.1 Introduction

To analyse the cyclic consolidation process of fine grained soils an experimental series of oedometer tests on kaolin clay according to the experimental programme given in Chapter 6 has been carried out. The tests on kaolin clay were performed with varying initial and loading conditions in order to study the influence of material characteristics and loading conditions on the consolidation behaviour. A detailed survey of the chosen boundary and testing conditions is given Chapter 6.2.

To study the influence of clay structure on the consolidation behaviour, additionally, six oedometer tests on marine Onsøy clay under cyclic loading are evaluated. Here, the focus is set on the analysis of the influence of the applied load amplitude on the consolidation

characteristics. To do so, the load amplitude was chosen with reference to the yield stress. While one load amplitude was set to 50 kPa and hence chosen to be smaller than the yield stress, the other two amplitudes were set to be 100 kPa and 200 kPa exceeding the yield stress. The effect of the load amplitude on destructuration and thus on the consolidation process is analysed in terms of time-dependent deformation and pore water dissipation.

Parts of the following study have been published in Müthing et al. (2014), Müthing et al. (2015), Müthing et al. (2016a) and Müthing et al. (2017).

8.2 Friction

The vertical stress applied to the clay sample is reduced due to friction. As discussed for the oedometer tests under monotonic loading, the friction is caused by contact between clay material and oedometer ring as well within the oedometer cell sealing system (details see Chapter 7.1.2).

Figure 8.1a displays the development of vertical stress applied at the top σ_v^t of the oedometer system and vertical stress measured beneath the sample σ_v^b during the cyclic load application. The friction F is calculated according to Eq. 7.3 as the difference between σ_v^t and σ_v^b .

While the friction during loading F increases with consolidation progress from about 2 to 10%, the friction during unloading F_{ur} remains constant at approx. 8-10 % (see Fig. 8.1b). From this it can be concluded, that most of the friction in unloading results from

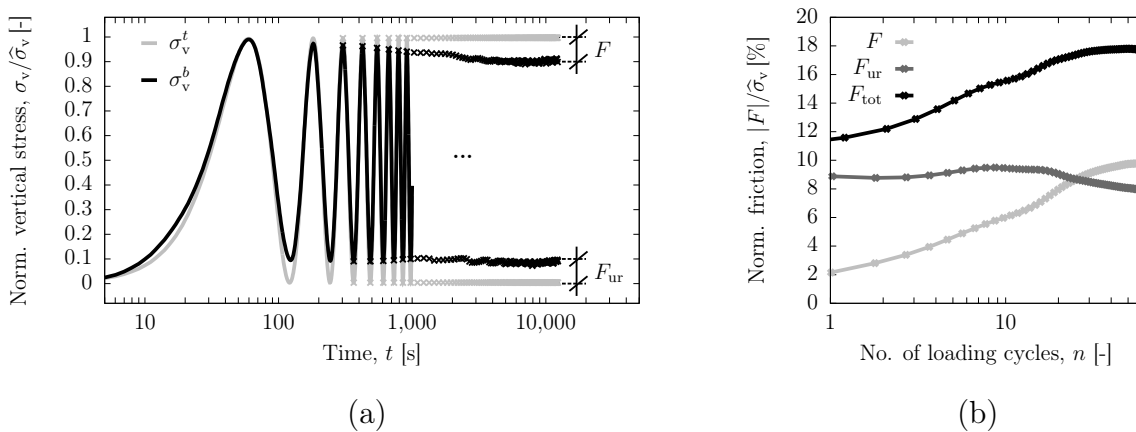


Figure 8.1: Development of friction in the cyclic oedometer tests: (a) vertical stress versus time, (b) friction versus number of loading cycle. (test CK08: $d = 120$ s, $\hat{\sigma}_v = 100$ kN/m²)

friction caused by the sealing system of the oedometer device, while the friction in loading partly may be attributed to the friction between sample and ring.

As it becomes obvious from Fig. 8.1, the friction in cyclic oedometer experiments has two effects on the loading characteristic. First of all, like as in the monotonic loading test, it reduces the final vertical effective stress applied at the end of each loading / unloading phase.

$$\text{Loading: } \sigma_v^b = \sigma_v^t - F \quad (8.1)$$

$$\text{Unloading: } \sigma_v^b = \sigma_v^t - F_{ur} \quad (8.2)$$

Secondly, it reduces the applied loading amplitude by

$$\Delta\sigma_v = \Delta\sigma_v - F_{tot} = \Delta\sigma_v - (F + F_{ur}) \quad (8.3)$$

where F_{tot} is the sum of friction during compression and unloading phase approaching 15-18 % in this experiment. The mean effective stress in the stationary state is not effected by friction.

For some aspects of the present study it is essential to perform the evaluation based on the load amplitude taking into account the reduction of load amplitude due to friction. For these cases, the load amplitude reduced by the measured friction in each loading cycle n is defined by

$$\widehat{\sigma}_{v,F}(n) = \sigma_{v,max}^b(n) - \sigma_{v,min}^b(n) \quad (8.4)$$

assuming that the frictional reduction is caused mainly by the contact between oedometer ring and cell sealing o-ring, neglecting the amount of friction due to ring - sample contact.

8.3 Cyclic deformation behaviour

8.3.1 General

Figure 8.2a shows the typical one-dimensional deformation behaviour of soft, fine-grained soils under haversine, cyclic loading and oedometric conditions in terms of the void ratio-time relationship.

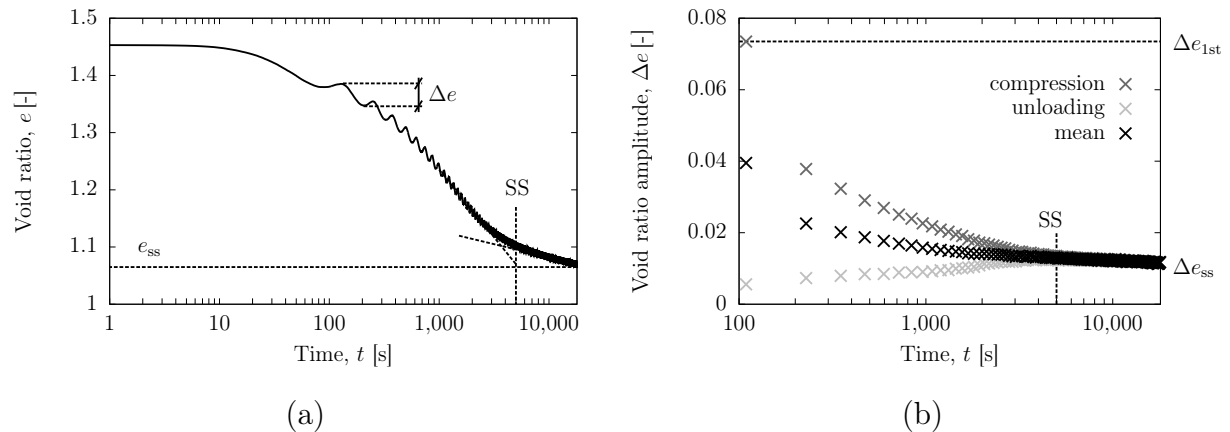


Figure 8.2: Deformation behaviour of kaolin clay under haversine loading: (a) void ratio versus time, (b) void ratio amplitude versus time. (test CK08: $d = 120$ s, $\hat{\sigma}_v = 100$ kN/m²)

The mean deformation under cyclic loading exhibits the typical s-shape of a consolidation curve. It is superposed by a cyclic deformation of variable amplitude. The increment of deformation accumulation is significantly decreasing from larger values in the first cycles to smaller ones approaching the end of primary consolidation, see Fig. 8.2b.

After a finite number of loading cycles or a distinct consolidation time respectively, a quasi stationary state is reached. It is referred to as *stationary state (SS)* in the following. The location of the beginning of the stationary state on $e - \log(t)$ -curve is equivalent to location of the EOP on $e - \log(t)$ -curve in a monotonic loading test. Generally, the stationary state is identified by the following characteristics, which will be analysed in detail in the following chapter:

- The accumulation of the deformation increment has reached its minimum. ($\Delta e \rightarrow \min.$)
- The increment of deformation is constant and identical in compression and unloading. ($\Delta e_{\text{comp.}} = \Delta e_{\text{recomp.}} = \text{const.}$)
- The mean pore water pressure is zero. ($u_{\text{mean}} = 0$)
- The increment of pore water pressure is constant and identical in compression and unloading. ($\Delta u_{\text{comp.}} = \Delta u_{\text{recomp.}} = \text{const.}$)

The number of cycles required for accomplishment of stationary state is material and load dependent and characterised by the coefficient of consolidation c_v of the mean deformation.

Generally, the time-dependent consolidation curve is identified by three characteristics: (1) the final mean deformation, in terms of void ratio in the stationary state e_{ss} , (2) the

rate of mean deformation characterized by the consolidation coefficient, c_v and (3) the deformation amplitude in terms of void ratio amplitude Δe and its development. While the final void ratio e_{ss} and the consolidation coefficient c_v are unique values calculated from the mean deformation of the cyclic consolidation process, the deformation amplitude Δe varies with consolidation progress. It can be identified by the final value after reaching stationary state Δe_{ss} and the *dissipation factor of deformation* η_e , which is defined as the ratio between the deformation amplitude in stationary state Δe_{ss} and the initial deformation amplitude in the first loading cycle Δe_{1st} .

$$\eta_e = \frac{\Delta e_{ss}}{\Delta e_{1st}} \quad (8.5)$$

The deformation in cyclic consolidation experiments is found to be shifted with respect to the applied loading by a phase shift ψ_e . A detailed analysis of this effect can be found in the subsequent chapter. In the following sections, the deformation characteristics e_{ss} , c_v and $\Delta e(T_v)$ identified by Δe_{ss} and η_e are analysed in more detail. Thereby, the influence of material and loading characteristics is demonstrated and the comparison to the equivalent measures from monotonic loading tests are drawn.

The deformation behaviour in terms of the three characteristics, e_{ss} , c_v and Δe , is significantly influenced by the loading characteristics, load period d and load amplitude $\hat{\sigma}_v$ (see Fig. 8.3). Therefore, in this study both loading characteristics were varied in order to analyse their effect on the consolidation behaviour.

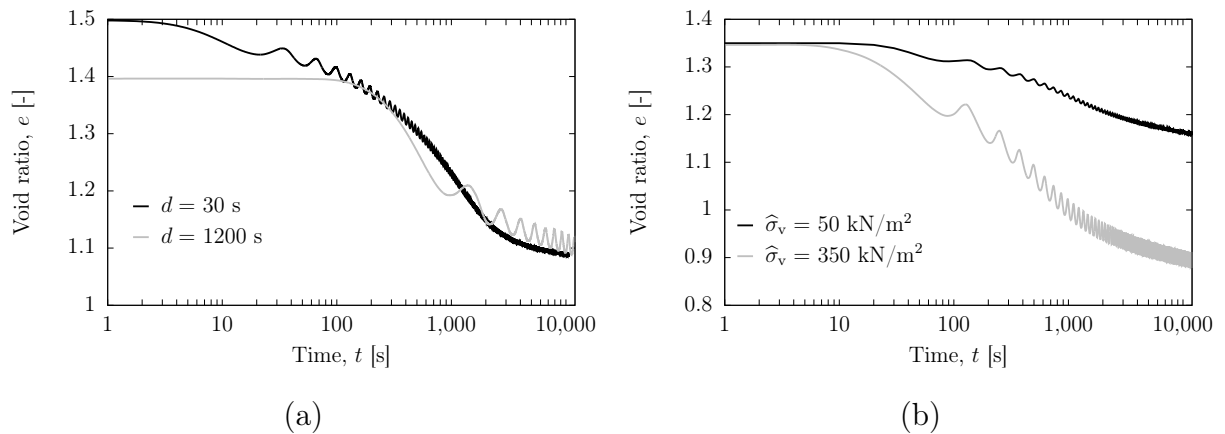


Figure 8.3: Deformation behaviour of kaolin clay under haversine loading: (a) influence of load period d , (b) influence of load amplitude $\hat{\sigma}_v$ (tests CK13,19,11,14).

8.3.2 Final mean deformation e_{ss}

The deformation in terms of the final void ratio e_{ss} reached under cyclic loading is a function of the vertical effective stress and thus, of the applied load amplitude. Figure 8.4 compares the void ratio-effective stress relationship determined from the step-wise monotonic tests to the e_{ss} derived from cyclic tests under different load amplitudes. Thereby, it has to be considered, that the effective stress in the stationary state of the cyclic tests is not constant. Like as the pore water pressure (compare Fig. 4.4), it varies over the sample height and time. Therefore, the load amplitude $\hat{\sigma}_v$ gives an idea of the effective stress range, but does not equal the mean effective stress in the sample.

Figure 8.4 shows, that under cyclic and monotonic loading the deformation follows nearly the same compression index C_c . In case of kaolin clay it was determined to be $C_c = 0.30$ from the present experimental data. For reconstituted Onsøy clay $C_c = 0.40$ was computed.

The compression in terms of the final void ratio e_{ss} in cyclic loading tests under a load amplitude $\hat{\sigma}_v$ on average is found to be in the range of the corresponding monotonic test under σ'_v . Thus, it can be stated, that in a cyclic test nearly the same degree of consolidation is reached as in the monotonic test of the same load amplitude. This is in accordance with the finding by Kono, Ochiai, Omine and Tsukamoto (1995) and Kono, Ochiai and Yasufuku (1995). The minor difference in final void ratio may be attributed to fluctuating pore water pressure in the stationary state, reducing the mean effective stress in the sample, as well as to the higher friction in the cyclic tests. A rate effect due to the lower strain rate in cyclic tests cannot be asserted.

Like as in the monotonic tests, the compression of reconstituted clay significantly exceeds the compression of natural clay at equivalent vertical stress. This corresponds to the compression under monotonic loading. It can be concluded that destructuration occurs similarly under monotonic and cyclic loading within the limits of loading rate applied for the present study. An effect of the non-monotonic loading on the yield stress cannot be identified. Testing with amplitudes in the direct vicinity of the yield stress could analyse this in more detail. However, this is beyond the scope of this work.

While the final compression is dependent on the load amplitude, the load period has only a minor effect on the final void ratio e_{ss} (see Fig.8.5).

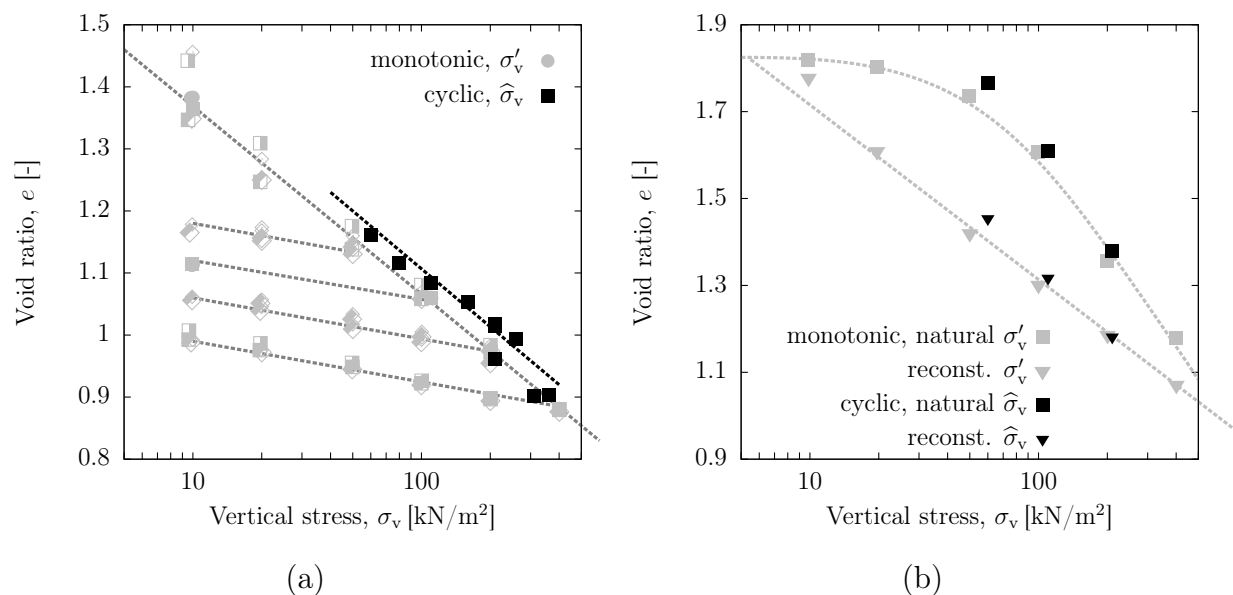


Figure 8.4: Compression behaviour of (a) kaolin clay and (b) natural and reconstituted Onsøy clay under cyclic loading ($d = 120$ s).

8.3.3 Rate of consolidation

As demonstrated in Chapter 7.2 for gradual load application, the rate of consolidation depends on the rate of load application. With decreasing loading rate, the rate of consolidation decreases correspondingly (Sivakugan et al., 2014). In the cyclic loading tests this effect can be observed from the consolidation behaviour in the first loading cycle. Figure 8.6 shows, that with increasing load period for a constant load amplitude the consolidation rate in the first loading cycle decreases. The same effect is valid during unloading. The mean degree of consolidation reached within one loading cycle is independent of the loading rate and thus, of the load period. Figure 8.7 demonstrates this from tests on kaolin under varying load period. Due to the load reversal and alternating compression and unloading phases, consolidation under cyclic loading exhibits a lower rate than under monotonic loading of the same vertical effective stress.

Figure 8.7b illustrates from test data on kaolin clay, that the consolidation rate under cyclic loading, as known from monotonic loading tests, also depends on the magnitude of the applied vertical effective stress. This particularly holds true for structured clays. Figure 8.8 shows the normalised time-dependent settlements under cyclic loading of Onsøy clay. The reconstituted samples all show a similar time-dependent compression behaviour. As in the cyclic loading process, the effective stress increases slower compared to the monotonic load application, the difference in loading amplitude is not as significant as

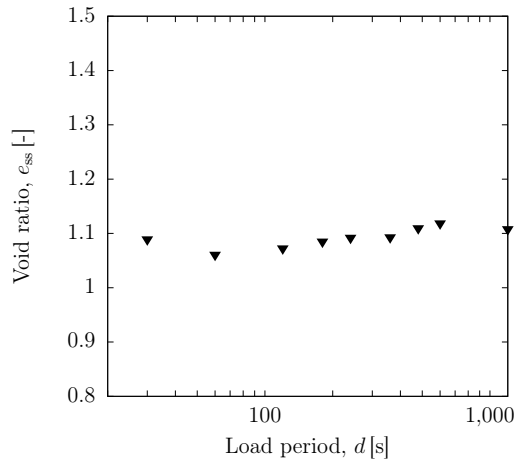


Figure 8.5: Influence of load period on the compression of kaolin under cyclic loading, tested at $\hat{\sigma}_v=100 \text{ kN/m}^2$.

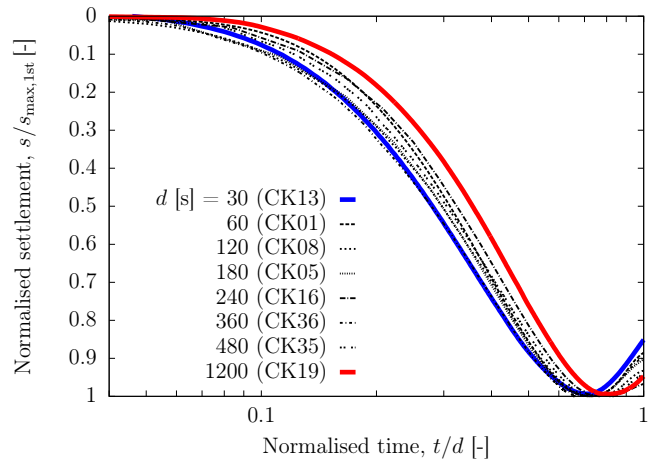
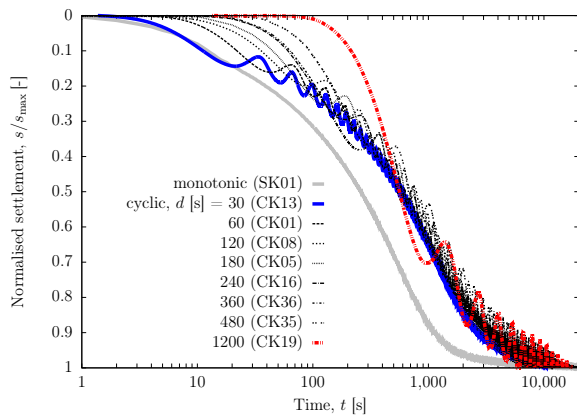
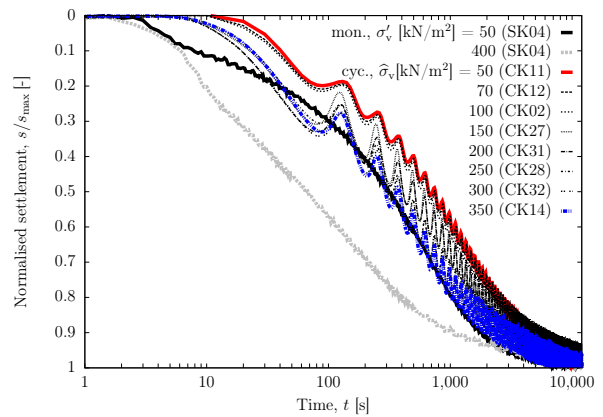


Figure 8.6: Normalised time-dependent settlements in the first loading cycle of kaolin clay ($\hat{\sigma}_v=100 \text{ kN/m}^2$).



(a)



(b)

Figure 8.7: Normalised time-dependent settlements versus time - comparison to monotonic loading tests for varying (a) load period and (b) load amplitude from cyclic loading tests on kaolin clay.

in the monotonic experiments. In contrast, the time-dependent compression behaviour of the natural clay significantly depends on the applied load amplitude. Loaded with an amplitude below yield stress, the clay exhibits much faster consolidation than the natural samples loaded with an amplitude above yield stress. This corresponds to the findings for consolidation under monotonic loading and is reflected in the development of c_v .

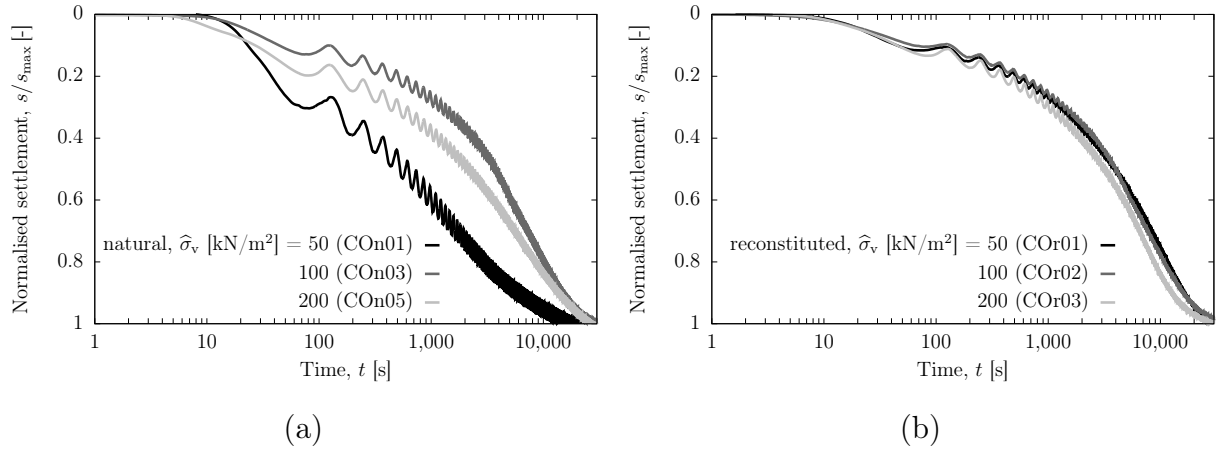


Figure 8.8: Normalised time-dependent settlements of (a) natural and (b) reconstituted Onsøy clay under cyclic loading with varying load amplitude $\hat{\sigma}_v$.

Coefficient of consolidation c_v

The consolidation coefficient c_v is a measure for the consolidation rate. It is given as a constant in Terzaghi's theory, assuming stiffness and permeability not to change during consolidation progress. As shown before, this does not hold true for larger load steps in the monotonic loading tests. Under cyclic loading the validity is further limited due to the load reversal in each cycle. However, the c_v value determined from the mean deformation in each cycle is a good measure to identify the rate of the consolidation process and to analyse its dependency on the loading characteristics.

Figure 8.9 summarizes the c_v computed from the experimental series in comparison to the c_v derived from monotonic loading tests. The c_v values computed by the early-stage-log-t method ($c_{v,RA}$) are higher than the c_v values determined by the classical Casagrande method ($c_{v,Cas}$), which is in accordance with the findings from monotonic loading tests. The load amplitude is found to have no influence on $c_{v,50}$ (see Fig. 8.9a). In contrast, $c_{v,RA}$ slightly decreases with increasing load period. The difference amounts a factor of 5 in lower period ranges to a factor of 1.5 for higher period duration. As $c_{v,RA}$ is computed based on the early part of the time-settlement curve, the faster consolidation in the first cycles for shorter load period is reflected in the c_v value. This effect decreases with increasing load period, as at higher load period a higher degree of consolidation is reached within the first cycle. The consolidation rate in the first cycle equals the overall consolidation rate. As the c_v from cyclic loading tests is used to identify the mean consolidation rate, in the following mainly $c_{v,Cas}$ is considered.

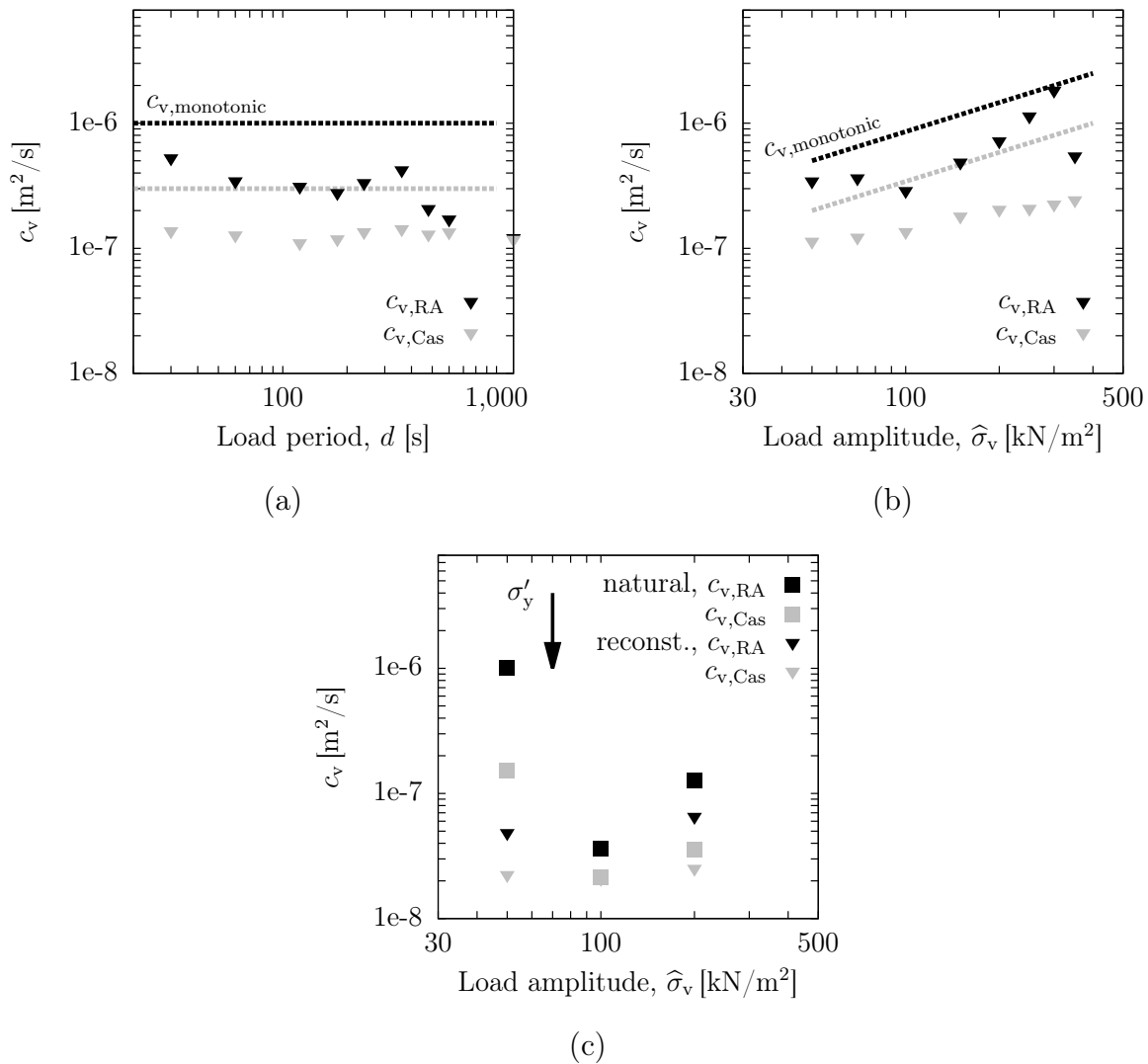


Figure 8.9: c_v versus (a) load period, tested at $\hat{\sigma}_v=100$ kN/m², and (b) load amplitude, tested at $d=120$ s, from cyclic consolidation tests on kaolin clay and (c) on Onsøy clay.

For reconstituted clays c_v increases with increasing load amplitude. Compared to development in monotonic loading tests, yet, the increase is of minor magnitude. For kaolin clay, c_v is found to increase from $1 \cdot 10^{-7}$ m²/s at $\hat{\sigma}_v=50$ kN/m² to approximately $2 \cdot 10^{-7}$ m²/s at $\hat{\sigma}_v=300$ kN/m², while in the same stress range the c_v under monotonic loading quintuples. Reconstituted Onsøy clay exhibits an almost constant c_v of $2 \cdot 10^{-8}$ m²/s for $\hat{\sigma}_v=50$ -200 kN/m², increasing only by a factor of 1.3.

The destructuration behaviour of the structured clay is clearly reflected in the computed consolidation coefficient. For $\hat{\sigma}_v < \sigma'_y$ a high c_v of $2 \cdot 10^{-7}$ m²/s is found. When $\hat{\sigma}_v$ exceeds the yield stress, c_v suddenly drops to $c_v = 1 \cdot 10^{-8}$ m²/s at $\hat{\sigma}_v=100$ kN/m². In this state the consolidation rate of natural, but already destructured clay equals the consolidation

rate of reconstituted material. For higher effective stress a subsequent increase in c_v can be observed. This behaviour is in accordance with the findings from monotonic loading tests.

The mean consolidation under cyclic loading, characterised by the final mean void ratio e_{ss} and the consolidation coefficient of mean deformation c_v , is found within the tested loading range to depend only on the applied load amplitude $\hat{\sigma}_v$. The load period is found to have only a minor influence, which lies within the range of measurement accuracy.

8.3.4 Amplitude of deformation Δe

In cyclic consolidation the mean deformation following the typical s-shape of a consolidation curve, is superposed by a cyclic deformation of variable amplitude Δe . As shown in Fig. 8.2 the deformation increment during loading Δe is decreasing, while the deformation increment during unloading Δe_{ur} is increasing with progressing consolidation. Compression and unloading increment converge to an equal mean value Δe_{ss} in the stationary state. As in one loading phase the compression is always larger than the deformation in unloading, the mean deformation increment Δe_{mean} decreases with consolidation progress towards Δe_{ss} .

In contrast to the characteristics of the mean consolidation behaviour (e_{ss} and c_v), the deformation increment Δe depends on both, load amplitude $\hat{\sigma}_v$ and load period d . This holds true for the initial deformation increment in the first loading cycle Δe_{1st} as well as the final deformation increment in the stationary state Δe_{ss} (see Fig. 8.10).

A larger load period or a larger load amplitude cause a larger deformation increment Δe . The deformation increments result from the consolidation deformation allowed in one loading cycle. Consequently, with a longer loading phase (larger load period) or a higher vertical effective stress (larger load amplitude) a larger deformation is procured within one cycle.

For kaolin clay a change in load period from 30 s to 1200 s is found to cause approximately the same change in final deformation increment Δe_{ss} than a change in load amplitude from 50 kN/m² to 350 kN/m². Namely, Δe_{ss} varies by a factor of 2 from 0.0075 to 0.018. Due to its generally higher stiffness, the deformation amplitude measured from cyclic tests on reconstituted Onsøy clay is smaller, ranging from $\Delta e_{ss} = 0.0015$ to $\Delta e_{ss} = 0.01$. This is approximately half of the value calculated for kaolin at the same stress state and corresponds to the stiffness ratio between the two clays derived from monotonic loading

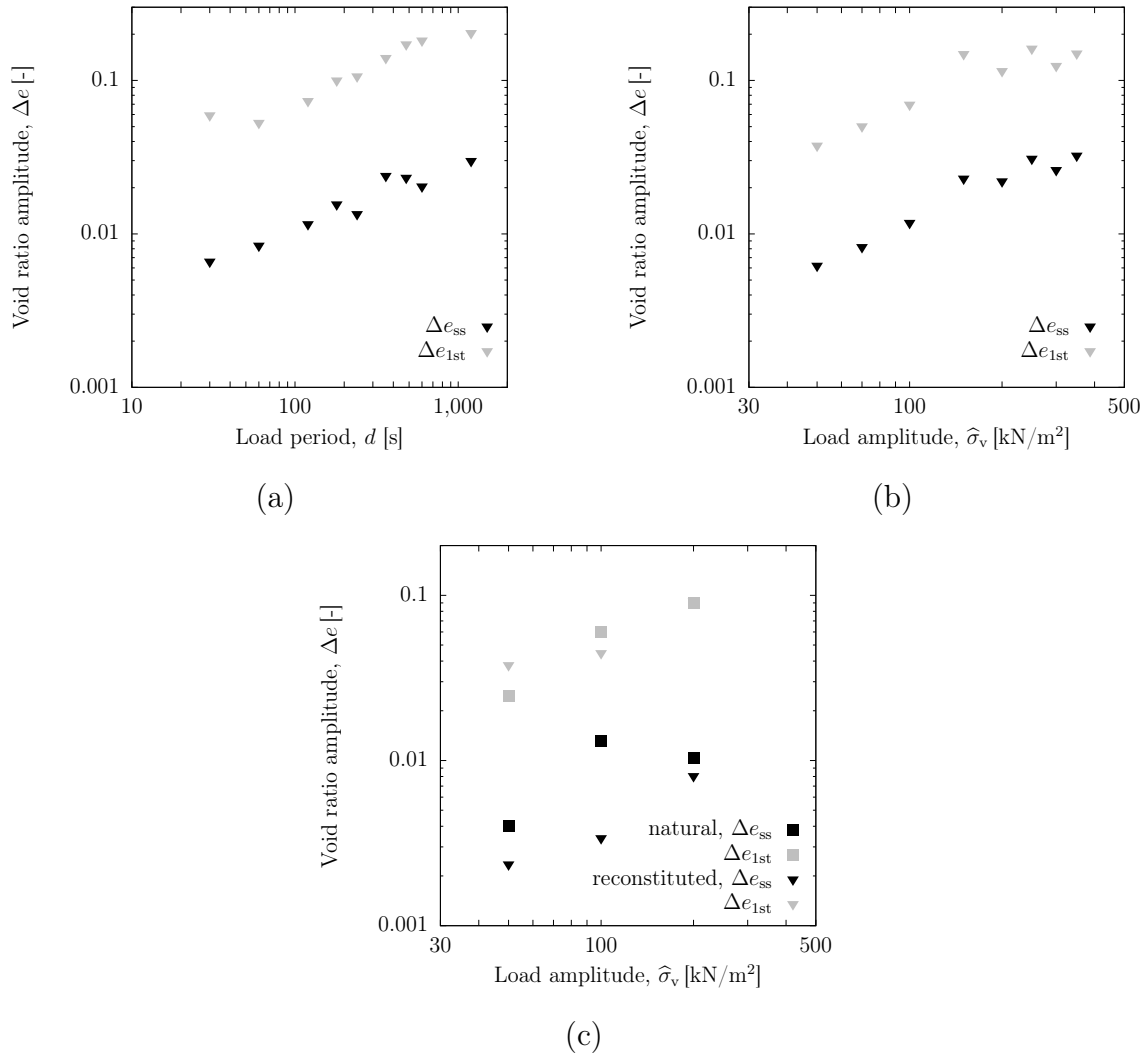


Figure 8.10: Dependency of final void ratio amplitude Δe_{ss} on (a) load period ($\hat{\sigma}_v=100$ kN/m²) and (b) load amplitude ($d=120$ s) from cyclic consolidation tests on kaolin clay and (c) Onsøy clay.

tests (see Chapter 7.1.5). Natural Onsøy clay exhibits a similar behaviour compared to the reconstituted clay with a slightly higher Δe_{ss} due to its stiffer fabric.

The other characteristic identifying the cyclic deformation behaviour during cyclic consolidation is the dissipation factor of deformation η_e , defined previously as the ratio between Δe_{ss} and Δe_{1st} . Figure 8.11 illustrates the dependency of η_e on the loading characteristics, load period and amplitude. The dissipation factor of deformation η_e is computed to be in the order of 0.15 for kaolin clay and 0.08 for reconstituted Onsøy clay. It is found to be independent of d , but to increase slightly with increasing $\hat{\sigma}_v$. Natural Onsøy

clay shows a decrease in η_e with larger load amplitude, which might be attributed to the destructuration process occurring mostly in the first loading cycles.

8.3.5 Development of equivalent stiffness \bar{E}_s

To compute the stiffness, the change in effective stress corresponding to a change in vertical strain is required. As discussed before, in the cyclic tests the vertical effective stress is not constant, but varies over sample height and time. Thus, the mean effective stress is unknown. Due to this fact, an equivalent stiffness \bar{E}_s , computed based on the load amplitude $\hat{\sigma}_v$, is considered in the following.

As illustrated before, the compression behaviour under cyclic loading is characterised by two deformation characteristics. In terms of vertical strain, these are the final deformation $\varepsilon_{v,ss}$ and the deformation amplitude in each loading cycle $\Delta\varepsilon_v$ (see Fig. 8.12a). Following this concept, two values for the equivalent stiffness can be calculated.

1. The equivalent stiffness \bar{E}_s computed from the final mean deformation $\varepsilon_{v,ss}$, given by

$$\bar{E}_s = \frac{\hat{\sigma}_v}{\varepsilon_{v,ss}} \quad (8.6)$$

\bar{E}_s is a mean value, accounting for the soil's compressibility during the overall consolidation process.

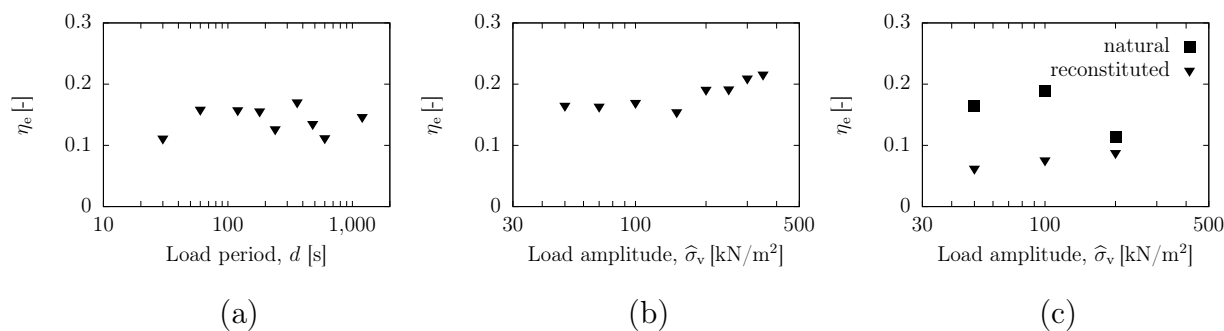


Figure 8.11: Dependency of η_e on (a) load period, tested at $\hat{\sigma}_v=100$ kN/m², and (b) load amplitude, tested $d=120$ s, from cyclic consolidation tests on kaolin clay and (c) Onsøy clay.

2. The equivalent stiffness $\bar{E}_{s,n}$ computed from the deformation $\Delta\varepsilon_{v,n}$ in each loading cycle n , given by

$$\bar{E}_{s,n} = \frac{\hat{\sigma}_v}{\Delta\varepsilon_{v,n}} \quad (8.7)$$

Fig. 8.12b illustrates the development of $\bar{E}_{s,n}$ over the number of loading cycles from a test on kaolin clay. $\bar{E}_{s,n}$ is computed from strain in compression and unloading of each loading cycle. The equivalent stiffness in unloading is always larger than in compression. After reaching the stationary state (SS), the equivalent stiffness in compression in unloading are of equal magnitude. This value is referred to as $\bar{E}_{s,ss}$, the equivalent stiffness in the stationary state. As in this state, the strain in compression in unloading are of the same size, this stiffness can be regarded as the quasi-elastic, unloading-reloading stiffness.

Figure 8.13 presents the equivalent stiffness computed from cyclic strain measurements for kaolin and Onsøy clay. The equivalent stiffness is calculated to be $\bar{E}_s^{ref} = 700$ kPa for kaolin and $\bar{E}_s^{ref} = 800$ kPa for Onsøy clay at a reference amplitude of $\hat{\sigma}_v^{ref} = 100$ kN/m². For natural Onsøy clay the equivalent stiffness for load amplitudes less than the yield stress is higher, analogue to the development of stiffness under monotonic loading. The equivalent stiffness is found to be dependent on the magnitude of the load amplitude and almost independent of the load period. Compared to the stiffness under monotonic loading, the increase in equivalent stiffness with increasing vertical stress is less pronounced. This must be attributed to the stress path magnitude. While in monotonic loading, stiff-

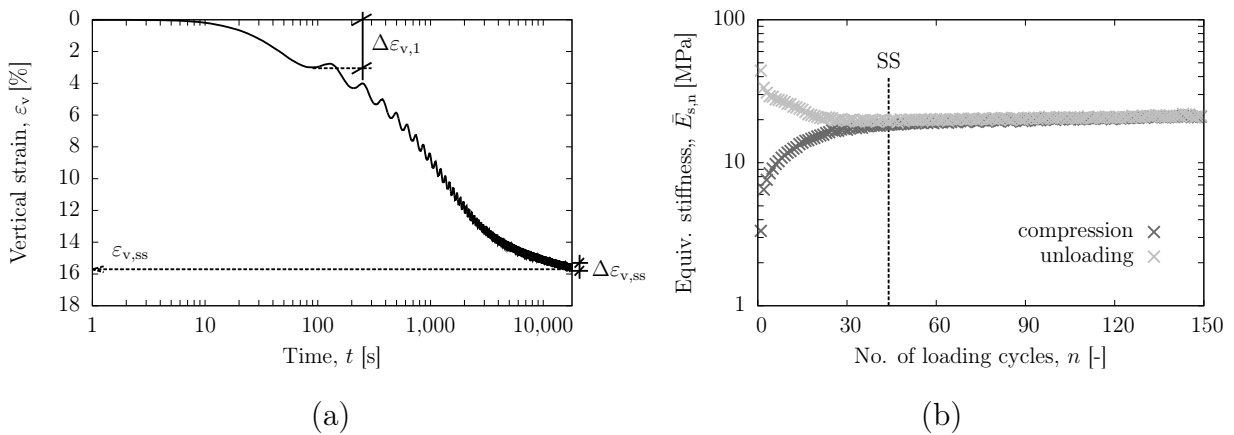


Figure 8.12: (a) Development ε_v over time during cyclic consolidation of kaolin clay, (b) development of $\bar{E}_{s,n}$ over number of loading cycles n (test CK08: $d = 120$ s, $\hat{\sigma}_v = 100$ kN/m²).

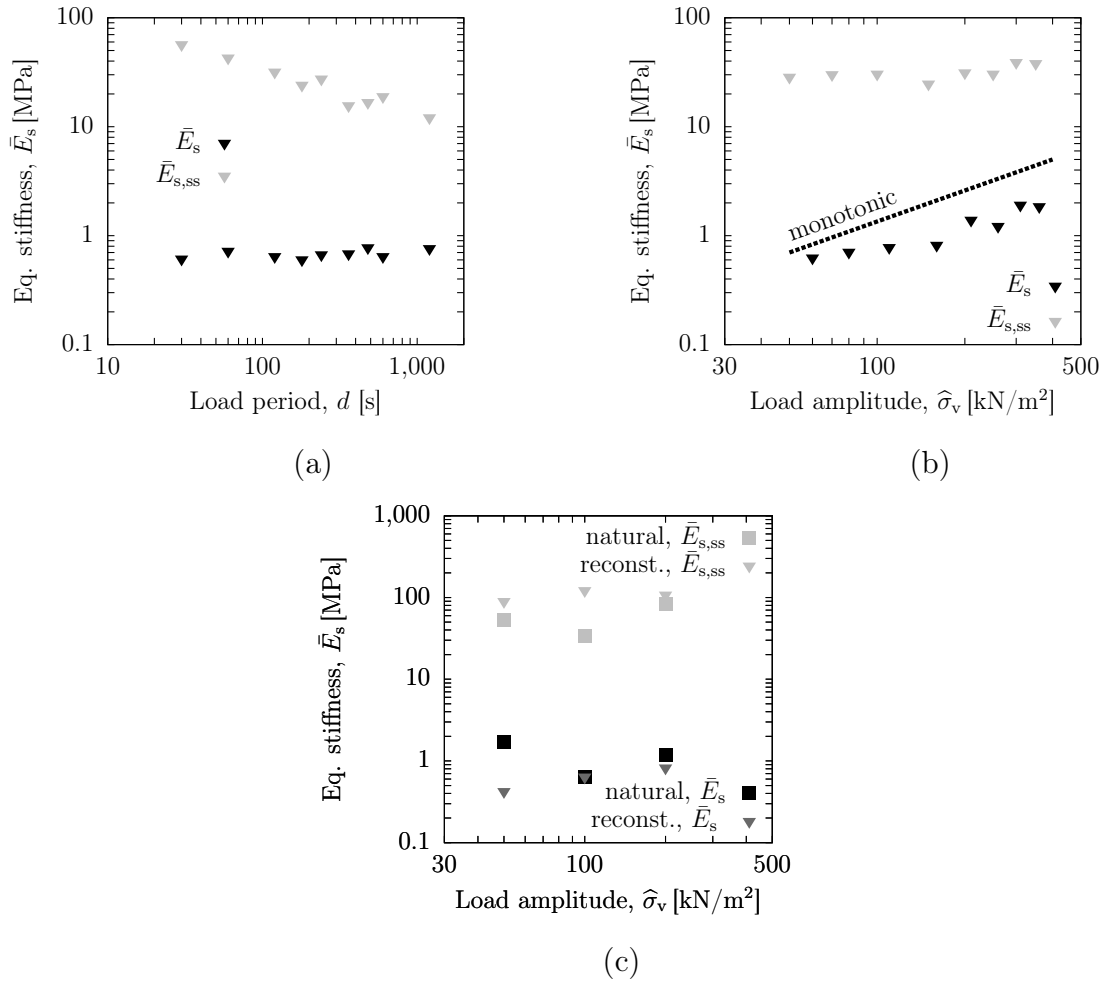


Figure 8.13: Equivalent stiffness \bar{E}_s versus (a) load period, tested at $\hat{\sigma}_v=100$ kN/m², (b) load amplitude, tested at $d=120$ s, from cyclic consolidation tests on kaolin clay and (c) Onsøy clay.

ness e.g. at $\sigma'_v = 200$ kN/m² is calculated from the $\sigma'_v = 100 \rightarrow 200$ kN/m² stress path, the equivalent stiffness in cyclic loading is calculated from the $\sigma_v = 10 \rightarrow 210$ kN/m² stress path.

The equivalent stiffness in the stationary state $\bar{E}_{s,ss}$ is found to depend on both loading characteristics, load period and load amplitude. With larger load amplitude $\bar{E}_{s,ss}$ is found to increase. With larger load period it decreases. Within the chosen variation range the dependency on the load period is more obvious than on the amplitude. While $\bar{E}_{s,ss}$ doubles in the variation range of $\hat{\sigma}_v = 50 - 350$ kN/m², it decreases by a factor of 5 in the tested variation range of $d = 30 - 1200$ s. For a reference amplitude of $\hat{\sigma}_v = 100$ kN/m² and a reference load period of $d = 120$ s, $\bar{E}_{s,ss}^{ref}$ is determined to approximately equal $\bar{E}_{s,ss}^{ref} = 30$ MPa for kaolin and $\bar{E}_{s,ss}^{ref} = 70$ MPa for Onsøy clay.

8.3.6 Permeability from cyclic c_v and equivalent stiffness

Analogue to the monotonic loading tests, the equivalent permeability in cyclic consolidation test can be computed from c_v and \bar{E}_s . Figure 8.14 presents the permeabilities calculated for kaolin and Onsøy clay. As k is computed from c_v and \bar{E}_s it is independent of the load period and can be plotted as only dependent on the final void ratio e_{ss} , which is again only dependent on the applied vertical effective stress. Compared to the values derived from monotonic loading tests, the permeability from cyclic loading tests is 2-4 times smaller. This results mathematically from the smaller c_v in cyclic loading tests and the following retardation in consolidation due to the repeated load reversal. Consequently it can be stated, that the determination of the permeability based on c_v from cyclic consolidation tests in this manner is not very accurate. However, as permeability accuracy is often given in terms of "power of ten", it is still a reasonable measure.

8.3.7 Deformation in the stationary state

As described above and demonstrated in Fig. 8.2, in the stationary state still small deformations occur. The rate of deformation in this state can be characterised analogue to the creep behaviour in a monotonic loading test by the coefficient \bar{C}_α , which is the secant modulus of the $e - \log(t)$ -curve in the stationary state.

$$\bar{C}_\alpha = -\frac{\Delta e}{\Delta(\log t)} \quad (8.8)$$

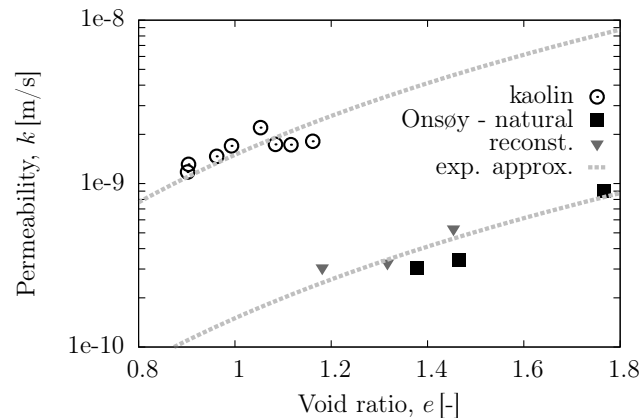


Figure 8.14: Void-ratio dependent permeability k computed from cyclic consolidation tests for kaolin and Onsøy clay.

\bar{C}_α was computed from the $e - \log(t)$ relationship in the cyclic consolidation test, using the mean void ratio of each loading cycle. The results are presented in \bar{C}_α versus d and \bar{C}_α versus $\hat{\sigma}_v$ plots in Fig. 8.15.

\bar{C}_α is found to be larger for higher load period and higher load amplitude. Compared to the behaviour of secondary compression under monotonic loading, both clays under cyclic loading exhibit a more pronounced deformation in the stationary state. This is particularly distinct for kaolin clay. Under monotonic loading C_α was found to be smaller than 0.01. In the cyclic tests it ranges between 0.02 and 0.03. The more pronounced deformation of kaolin clay in the stationary state of cyclic loading compared to its deformation in the secondary compression range, can be attributed to the non-constant effective stress in stationary state. After reaching the stationary state in the cyclic loading tests the effective stress still changes. This provokes a further settlements and a more pronounced re-arrangement of the clay particles. To proof this effect, structural analysis e.g. by ESEM analysis would be required, which are beyond of the scope of this work.

8.4 Cyclic pore water pressure dissipation

Figure 8.16 illustrates the dissipation of excess pore water pressure u during consolidation under cyclic loading of kaolin clay. The pore water pressure is measured locally at the bottom of the sample, which is the largest distance to the drainage and loading boundary. Within one loading cycle the pore water pressure increases with the increasing load to

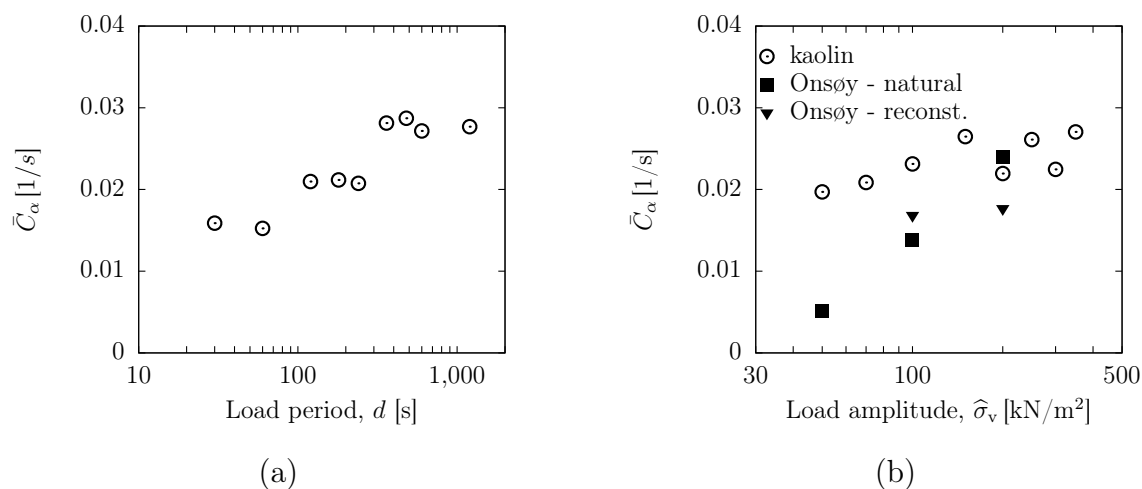


Figure 8.15: \bar{C}_α from cyclic loading tests on kaolin and Onsøy clay - dependency on (a) load period (b) load amplitude.

a maximum u_{\max} . During unloading the pore water pressure again decreases to a minimum u_{\min} . With consolidation progress the maximum and minimum pore water pressure decrease. The pore water pressures u_{\max} , u_{\min} as well as the mean pore water pressure, $u_{\text{mean}} = (u_{\max} + u_{\min})/2$, follow the typical s-shape of a pore water pressure dissipation curve.

The time, where the mean pore water pressure has almost completely dissipated, equals the time where the accumulation of the deformation increment has reached its minimum and the increment of deformation is constant and identical in compression and unloading. It is referred to as the stationary state. In the stationary state, the mean pore water pressure equals 0 ($u_{\text{mean}} = 0$) and is superposed by a cyclic pore water pressures of a constant amplitude Δu_{ss} .

The difference between maximum and minimum pore water pressure reached within one cycle is referred to as pore water pressure amplitude Δu . It is found to decrease from a higher value in the first loading cycle $\Delta u_{1\text{st}}$ to a smaller, but constant value in the stationary state Δu_{ss} (see Fig. 8.16a). The ratio characterising the amplitude reduction is referred to as *dissipation factor* η_u .

$$\eta_u = \frac{\Delta u_{\text{ss}}}{\Delta u_{1\text{st}}} \quad (8.9)$$

The dissipation of pore water pressure in cyclic oedometer tests analogue to the compression behaviour is identified by three characteristics: (1) the maximum pore water pressure

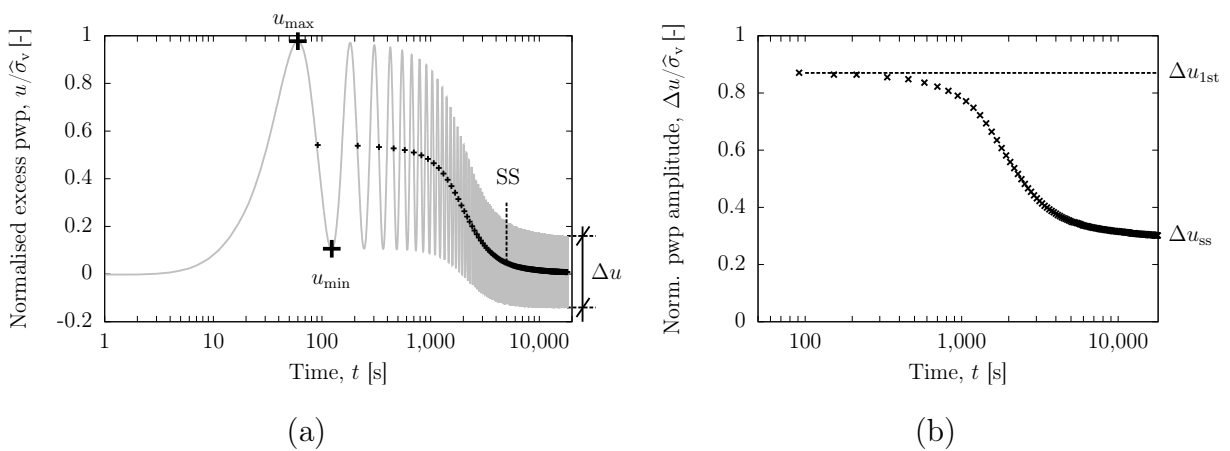


Figure 8.16: Pore water dissipation of kaolin clay under haversine loading: (a) normalised excess pore water pressure versus time, (b) normalised pore water pressure amplitude versus time (test CK08: $d = 120$ s, $\hat{\sigma}_v = 100$ kN/m²).

u_{\max} reached within the first loading cycles, (2) the rate of pore water pressure dissipation, characterised by the time, where almost all pore pressure has dissipated defined as t_{ss} and (3) the pore water pressure amplitude Δu and its development, characterised by Δu_{ss} and η_u .

As described for the compression curve, the pore water pressure and vertical stress curve are staggered in time by a phase shift ψ_u . More details on the phase shift and its development during consolidation progress will be given in Chapter 9.

Figure 8.17 shows, that the pore water pressure dissipation in terms of its three characteristics, u_{\max} , t_{ss} and Δu , is significantly influenced by the loading characteristics, load period d and load amplitude $\hat{\sigma}_v$. Therefore, in this study, the influence of both loading characteristics on the pore water pressure dissipation is analysed.

8.4.1 Maximum pore water pressure and rate of pore water pressure dissipation

Figure 8.18 shows the pore water dissipation during cyclic loading tests in comparison to the pore water pressure curve from a direct monotonic loading test in the same range of vertical effective stress ($\sigma'_v = 10 \rightarrow 110 \text{ kN/m}^2$). It can be seen, that the same maximum pore water pressure is reached. Due to the faster consolidation progress, the EOP in the monotonic loading test is reached earlier than the SS in the cyclic loading test.

The maximum pore water pressure is found to range between 94 and 98 % of the applied vertical load, except for the natural Onsøy clay, where u_{\max} amounts 70 to 80 % (see Fig.

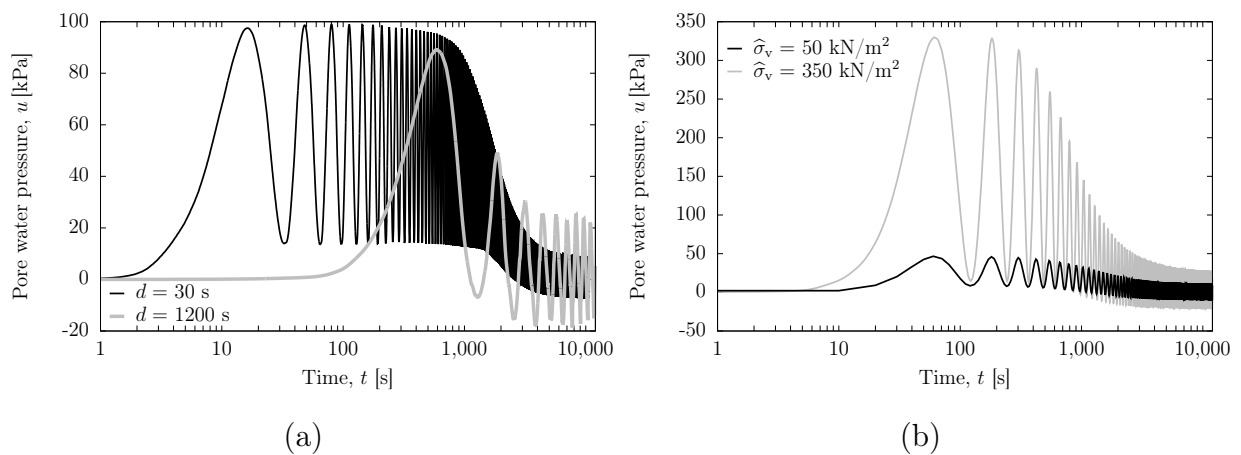


Figure 8.17: Pore water pressure dissipation of kaolin clay under haversine loading: (a) influence of load period d , (b) influence of load amplitude $\hat{\sigma}_v$ (tests CK13,19,11,14).

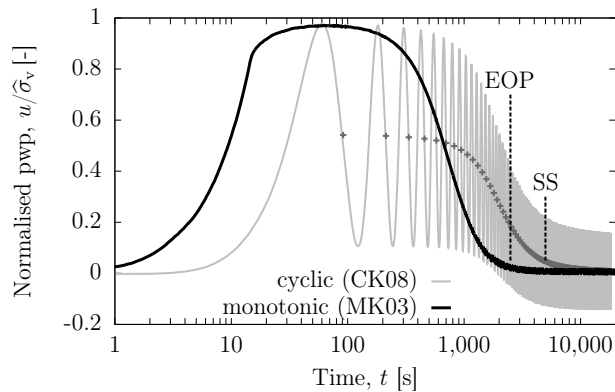


Figure 8.18: Pore water dissipation curves from monotonic and cyclic oedometer test.

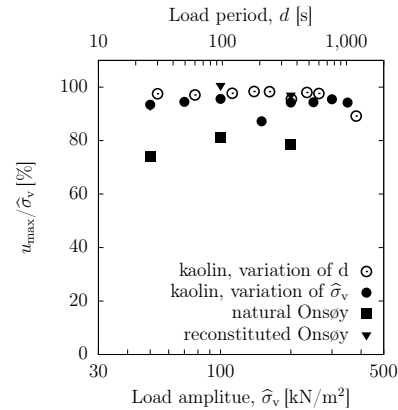


Figure 8.19: Maximum pore water pressure versus loading characteristics.

8.19). The lower pore water pressure reached for the natural clay may be attributed to the imperfection, that in the initial state this material exhibits a slightly lower degree of saturation. Within the tested range of load period and load amplitude variation, no effect of the loading characteristics on the maximum pore water pressure is found. Thence, also no dependency of the maximum pore water pressure on c_v can be described. This is different from the stepwise monotonic test, where the c_v is shown to have a significant influence on the time and magnitude of maximum pore water pressure. It can be concluded, that the differences in consolidation rate of the first loading cycle is not pronounced enough to have a major influence on the pore water pressure magnitude.

The time, at which the stationary state is reached, depends on c_v or stiffness and permeability respectively. Therewith, it is influenced by the inherent material characteristics as well as by the load amplitude rather than by the load period, as illustrated before.

The difference in pore water pressure dissipation rate becomes most obvious from a comparison between natural and reconstituted clay tested with a load amplitude below yield stress. Figure 8.20 compares the normalised time-dependent dissipation of pore water pressures for the two tests with a load amplitude of 50 kN/m^2 .

A significantly faster decay of mean pore water pressure is observed for the natural than for the reconstituted clay. Analogue to the monotonic loading, the bonding in the soil structure of the natural clay causes a higher stiffness of the material and thus a must faster consolidation. The effect is even more pronounced in the cyclic testing as here, due to the alternating loading the effective stress increases slower and thus seems to have a less distinct effect on the destructuration.

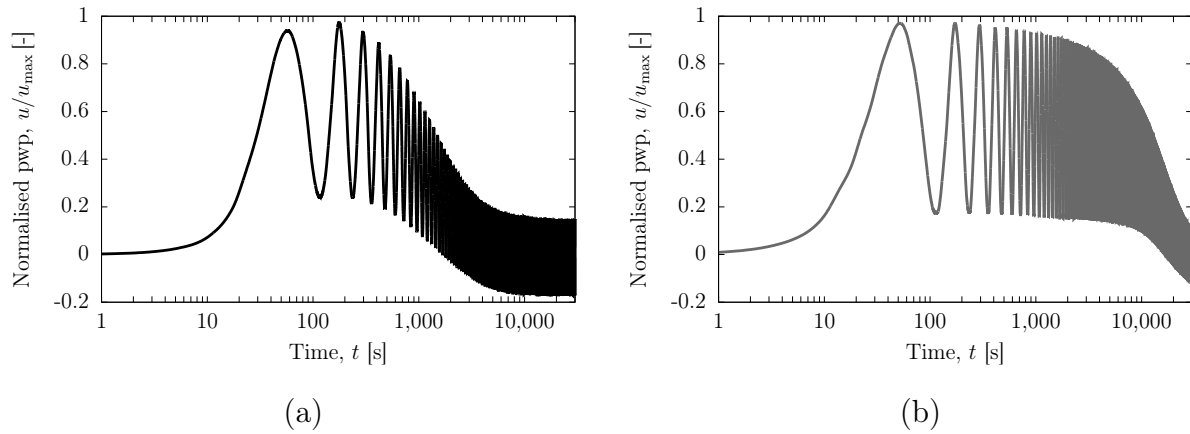


Figure 8.20: Pore water dissipation of natural and reconstituted Onsøy clay under cyclic loading with an amplitude of $\hat{\sigma}_v = 50 \text{ kN/m}^2 \leq \sigma'_y$.

8.4.2 Pore pressure amplitude Δu

The pore water pressure amplitude Δu is calculated as the difference between maximum and minimum pore water pressure in a loading cycle.

$$\Delta u_i = u_{\max,i} - u_{\min,i} \quad (8.10)$$

As shown in Fig. 8.19b, the pore water pressure amplitude decreases significantly during the consolidation progress from Δu_{1st} to Δu_{ss} . Due to the change in stiffness during the consolidation process, the rate of consolidation increases with increasing degree of consolidation. Thus, at the same loading time, a larger deformation and smaller pore water amplitude are measured. The magnitude of decrease from Δu_{1st} to Δu_{ss} , given by the factor η_u , depends on the loading and material characteristics. Fig. 8.21 displays the effect of loading characteristics on the pore pressure amplitude. Here, all values of pore water pressure amplitude are normalised by the applied loading amplitude corrected regarding friction. As the pore water pressure measurement is very sensitive, a generalised consideration of friction as performed before is not possible.

In the tested loading range the initial pore water pressure amplitude u_{1st} for all tests and both clay materials lies slightly below 1. For very high load periods $d \geq 480 \text{ s}$ an increase of u_{1st} up to $1.1 \cdot \hat{\sigma}_{F,1st}$ can be observed. The final pore water pressure amplitude decreases with increasing load amplitude. A clear trend for the dependency of the pore water pressure amplitude on the load period is difficult to identify as the measurement is subjected to variations. However, it is presumed that analogue to the dependency on

the load amplitude, with increasing T_0 and thus increasing d , Δu_{ss} decreases. A more pronounced decrease from $\Delta u_{ss} = 0.4$ to $\Delta u_{ss} = 0.2$ is observed within the tested range of load amplitude.

The reduction from $\Delta u_{1st} \approx 1$ to $\Delta u_{ss} = 0.2 - 0.4$ and its dependency on the loading characteristics is reflected in the η_u versus load period and load amplitude plots given in Fig. 8.22. The dissipation factor η_u decreases with increasing load period d and load amplitude $\hat{\sigma}_v$. The change in the dissipation factor is much more significant for increasing load amplitude than for increasing load period.

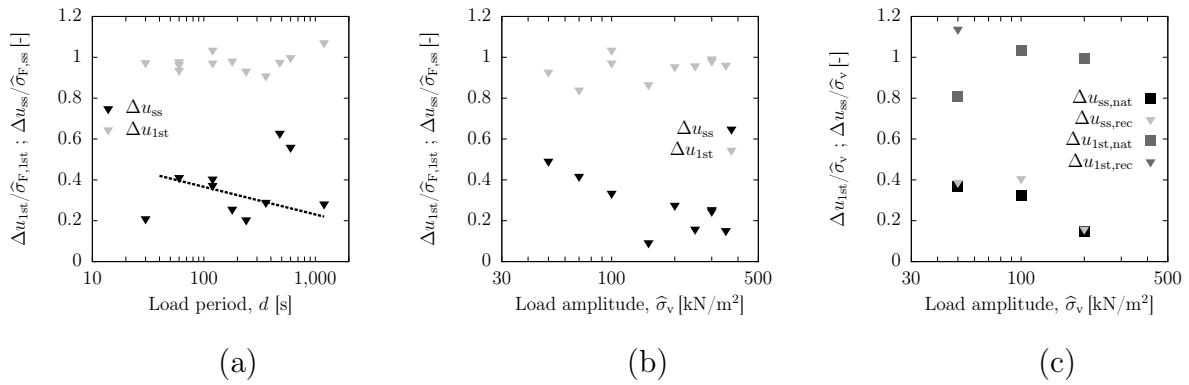


Figure 8.21: Pore water pressure amplitude Δu versus (a) load period, tested at $\hat{\sigma}_v=100$ kN/m² and (b) load amplitude, tested at $d=120$ s from cyclic consolidation tests on kaolin clay and (c) Onsøy clay.

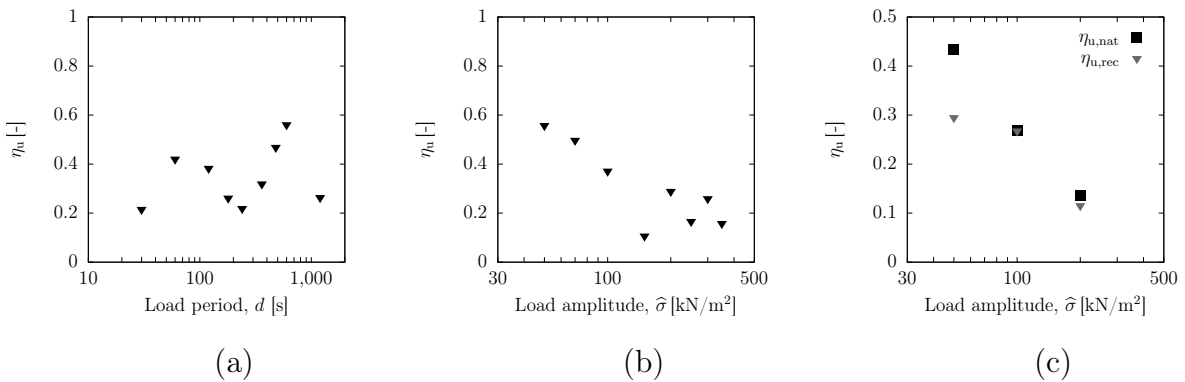


Figure 8.22: Dissipation factor η_u versus (a) load period, tested at $\hat{\sigma}_v=100$ kN/m² and (b) load amplitude, tested at $d=120$ s from cyclic consolidation tests on kaolin clay and (c) Onsøy clay.

8.5 Cyclic stress-strain behaviour

A useful way to display the development of deformation and pore water pressure is in terms of the stress - strain and the pore water pressure - strain relationship. Figure 8.23a and 8.23b give these two diagrams for kaolin clay. By principle of effective stress, from vertical total stress and pore water pressure measurement, the development of vertical effective stress at the bottom of the sample can be computed (see Fig. 8.23c). Here, the cyclic increase in vertical effective stress from 0.2 (resulting from the pre-consolidation phase) to almost 1 can be observed.

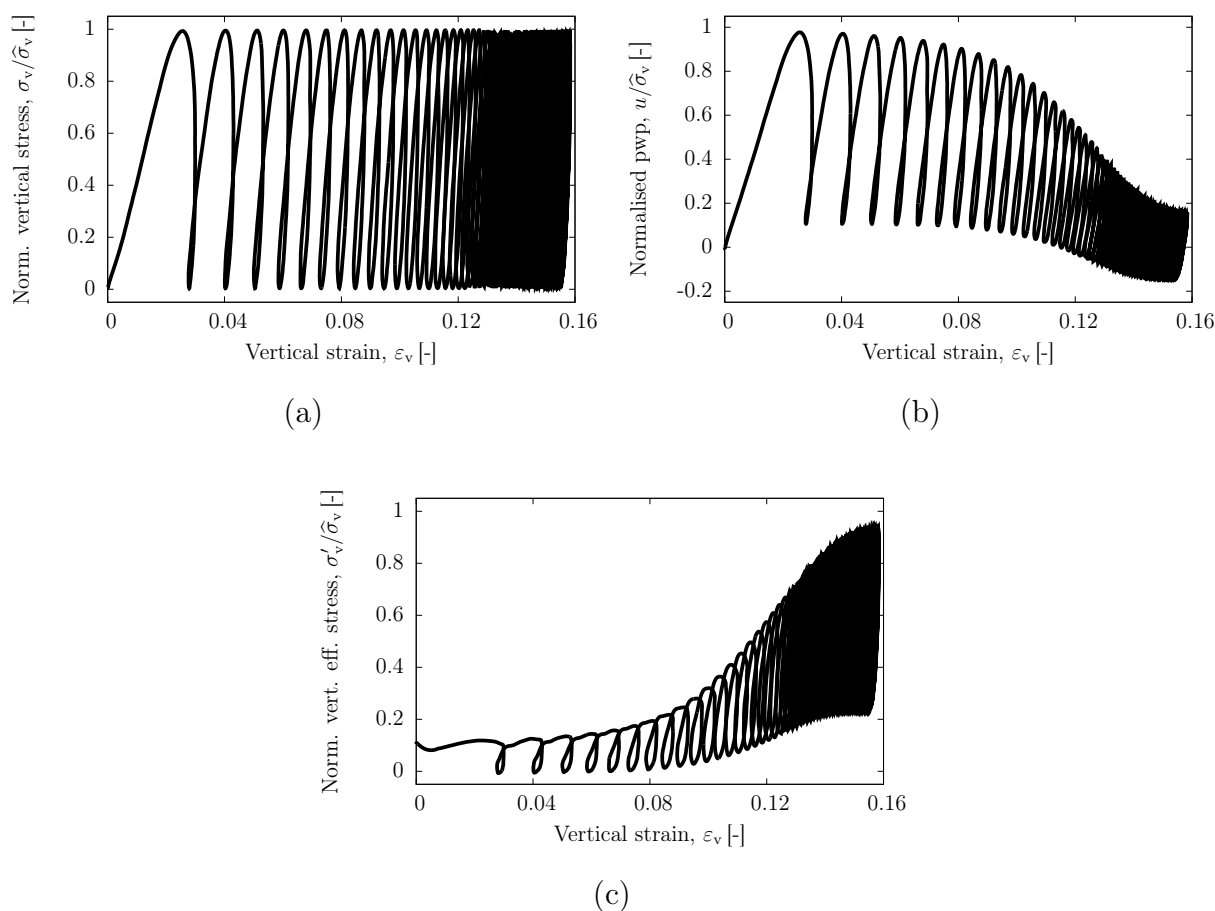


Figure 8.23: (a) Total stress, (b) pore water pressure and (c) effective stress versus strain diagram for cyclic consolidation of kaolin clay (test CK08: $d = 120$ s, $\hat{\sigma}_v = 100$ kN/m²).

8.6 Comparison to analytical solution

As demonstrated in Chapter 4 analytical solutions for the cyclic consolidation processes under haversine loading are available. However, these solutions are largely simplified models based on linear-elasticity and other simplifications. To analyse whether and how these models can still be used to reproduce the cyclic consolidation behaviour observed in the experiments, is studied in the following.

The material and loading parameters used within the analytical solution are given in Table 8.1. The linear analytical solution presented in Chapter 4 is based on the assumption of constant material parameters within each consolidation increment. Thus, S , k and E_s and consequently the consolidation parameters, i.e. c_v and T_0 , are considered as constants. As shown previously in this Chapter, this does not hold true for larger consolidation increments as usually encountered in oedometer testing. Therefore, for the comparison between experimental results and analytical solution different analytical scenarios (AS_{10} – AS_{400}) are considered.

Table 8.1: Computing parameters and consolidation characteristics derived from the analytical solution for consolidation under haversine cyclic loading.

	AS_{10}	AS_{100}	$AS_{100,ur}$	AS_{400}
Reference stress, σ'_v [kN/m ²]	10	100		400
Sample height, h [m]	0.02	0.018		0.015
Void ratio, e_0 [-]	1.5	1.07		0.95
Stiffness, E_s [kN/m ²]	100	1600	30,000	8500
Permeability, k [m/s]	1e-8	6e-9		3e-9
Consolid. coefficient c_v [m ²]	1e-7	1e-6	2e-5	2.5e-6
Load period, d [s]	30, 120, 1200	30, 120, 1200	120	120
Dimls. loading time, T_0 [-]	0.0075, 0.03, 0.3	0.09, 0.37, 3.7	6.7	1.36
Degree of saturation, S [-]	1.0	1.0	1.0	1.0
$u_{\text{mean,1st}}/\hat{\sigma}_v$ [kN/m ²]	0.5, 0.5, 0.54	0.5, 0.55, 0.22	0.08	0.49
$\Delta u_{ss}/\hat{\sigma}_v$ [-]	1.0, 1.0, 1.08	1.0, 1.1, 0.72	0.44	1.08
t_{EOP} [s]	4100	350	5	84
s_{ss} [-]	0.01	$5.63 \cdot 10^{-4}$	$3 \cdot 10^{-5}$	$3.5 \cdot 10^{-4}$
Δs_{norm} [10^{-3}]	0.04, 0.07, 0.22	0.12, 0.24, 0.83	0.933	0.51

All material and loading parameters used for the computing of the different scenarios are chosen with respect to different reference stresses, namely 10, 100, 400 kN/m². For these reference stresses the material parameters are derived based on the experimental data from monotonic and cyclic loading tests, cf. Table 7.2. For the reference stress $\sigma'_v = 100$ [kN/m²] two different scenarios are created. While AS_{100} is based on the equivalent stiffness \bar{E}_s , $AS_{100,ur}$ applies the equivalent stiffness $\bar{E}_{s,ss}$, derived from the stationary state deformation amplitude in cyclic loading tests.

Figures 8.24 and 8.25 compare the experimental results from an exemplary oedometer tests on kaolin clay under cyclic loading (CK08, $\hat{\sigma}_v = 100$ kN/m², $d=120$ s) to the results of the corresponding analytical solutions.

The comparison of the mean consolidation deformation reveals, that with the analytical solution $AS_{10,120s}$ the normalised settlement curve can be reproduced rather well. The same holds true for the mean pore water pressure and thus, the time of SS. Thus, it can be stated, that the rate of consolidation described by c_v is adequately reproduced by an analytical solution based on material parameters characterising the initial state of the soil (here: $AS_{10,120s}$).

The initial pore water pressure dissipation and the settlement behaviour in the first cycles (up to $t \approx 1500$ s) are in good agreement with the analytical solution $AS_{10,120s}$ as well. A comparison between u_{max} in the experiment (see Fig. 8.25) and $u_{mean,1st} = 0.5u_{max,1st}$ from the analytical solution (see Table 8.1) shows, that the analytical solution $AS_{10,120s}$ based on the initial material parameters is also able to reproduce this consolidation characteristic.

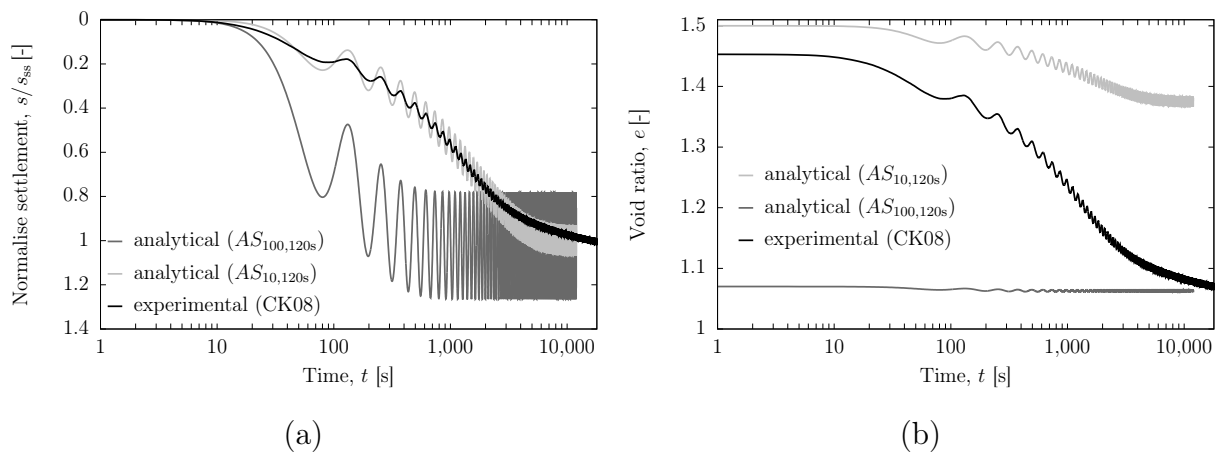


Figure 8.24: Consolidation deformation of kaolin clay under cyclic loading - comparison between experiment and analytical solution.

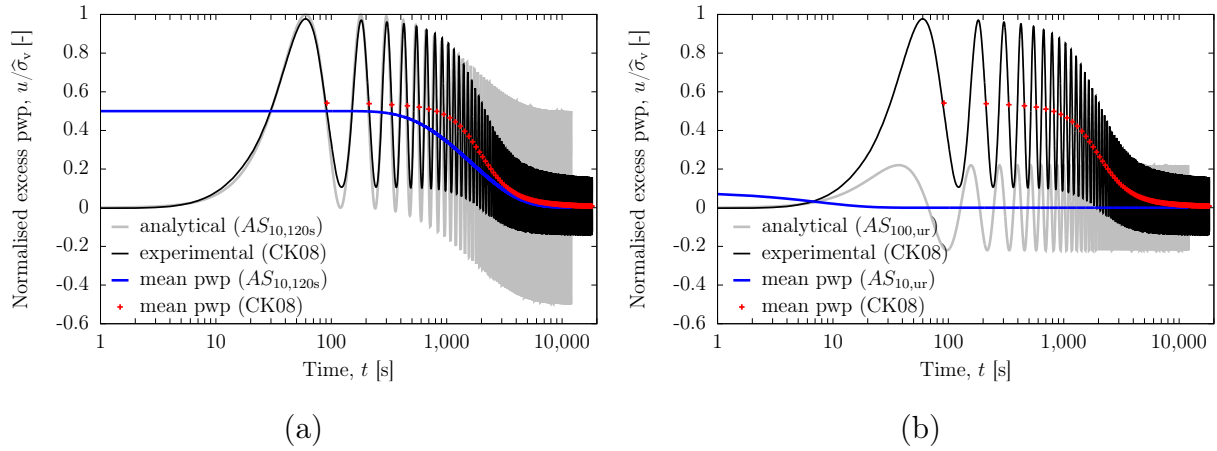


Figure 8.25: Pore water pressure dissipation of kaolin clay during consolidation under cyclic loading - comparison between experiment and analytical solution.

The slightly lower u_{\max} in the experiments must be attributed to the friction and can thus not be predicted by any of the suggested analytical solutions.

The comparison of the $e - \log(t)$ -curves exhibits, that the final void ratio in $AS_{10,120s}$ is much too small compared to the experimental data, which indicates that the stiffness in the analytical solution, $E_s = 100$ kPa, is still too high. In contrast, the final void ratio of $AS_{100,120s}$ fits the experimental data better, due to its reduced starting void ratio. The pore water pressure and deformation amplitude in stationary state are much too high in $AS_{10,120s}$ compared to the experimental data. It becomes obvious, that the consolidation behaviour in stationary state is more adequately reproduced by an analytical solution based on material parameters characterising the final state of the soil (here: $AS_{100,120s}$ or $AS_{100,120s,ur}$).

Due to the linearity of the mathematical model, the reduction in pore pressure amplitude (η_u) and deformation amplitude (η_e), as observed in the experiment, are not modelled by any of the analytical solutions.

To analyse, whether the effect of loading characteristics (load amplitude $\hat{\sigma}_v$ and load period d), on the consolidation characteristics described in the experimental study are equivalent in the analytical solution, Fig. 8.26, Fig. 8.27 and Fig. 8.28 compare experimental and analytical trends. The data points for the void ratio amplitude of the analytical solution are computed based on s_{norm} and the mean void ratio change between the reference stress levels according to Eq. 4.22. The coloured ranges in Fig. 8.26 and Fig. 8.27 mark the range of T_0 covered by the analytical solution (compare coloured numbers in Table 7.2). While the cross marks the analytical solution AS_{10} , the circle identifies the analytical

solution AS_{400} . The green colour refers to tests with a load period of $d = 30$ s, the red colour to tests with $d = 120$ s and the blue colour to $d = 1200$ s.

Figure 8.26 shows the comparison between results for pore water pressure amplitude Δu from analytical solution and experimental study. For all analytical solutions AS_{10} with material parameters based on the initial material state, the dimensionless loading time $T_0 \leq 0.3$. Therefore, all solutions show an initial pore water pressure amplitude $\Delta u_{1st}/\hat{\sigma}_v \approx 1$. Accounting for measurement accuracy and imperfections due to minor saturation deficiency in the system (see Chapter 7.2), $\Delta u_{1st}/\hat{\sigma}_v$ found in the experiments ranges between 0.9 and 1.0. Thus, it is in good accordance with the analytical solution AS_{10} .

With increasing reference stress level, T_0 becomes larger due to the higher c_v (see Fig. 8.26a). However, only for $AS_{100,120s,ur}$ and $AS_{10,1200s}$ T_0 becomes large enough to reach the range, where $\Delta u_{1st}/\hat{\sigma}_v \leq 1$. Consequently, to reproduce the reduced pore water pressure amp-

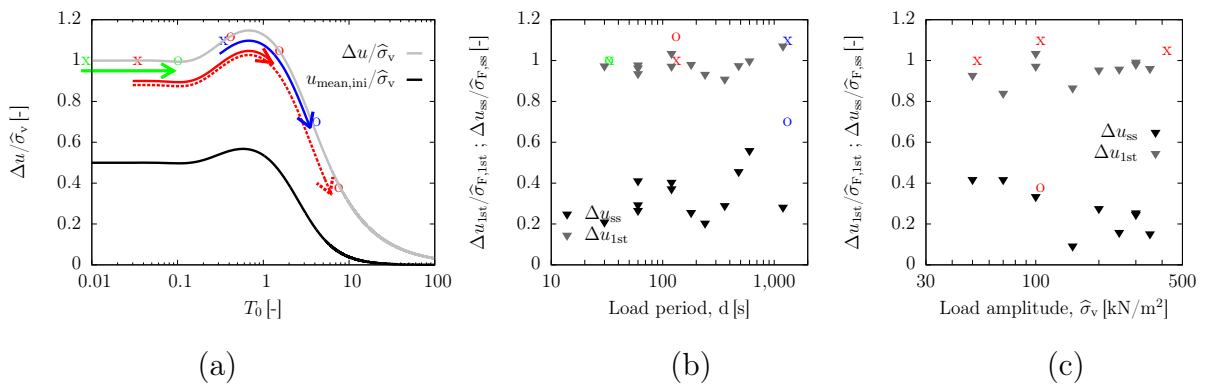


Figure 8.26: Development of pore water pressure amplitude Δu - comparison between results from (a) analytical solution and (b),(c) experiment.

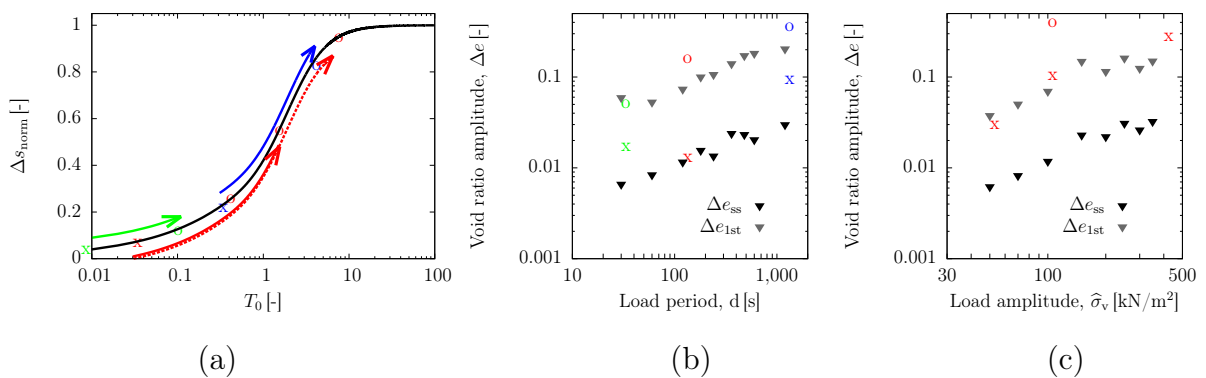


Figure 8.27: Development of deformation amplitude Δe - comparison between results from (a) analytical solution and (b),(c) experiment.

litude in stationary state, an increased stiffness based on $\bar{E}_{s,ss}$ as introduced in $AS_{100,120s,ur}$ must be applied to fit the experimental data, as demonstrated in Fig.8.26c.

Figure 8.28a summarises the comparison between experimental and analytical Δu . Here, for the experimental data T_0 is computed based on the c_v derived from the cyclic, experimental analysis. It can be seen, that the analytical solution fits very well the $\Delta u_{1st}/\hat{\sigma}_v$ found in the experimental study. In the experimental study T_0 increases with consolidation progress. Therefore, the experimental data plotted over $T_{0,initial}$ does not fit the analytical solution. However, shifted by a factor of 100, the trend of experimental data would be captured by the analytical solution, Thus, it can be concluded that T_0 increases by a factor of 100 due to the increase in stiffness and decrease in sample height.

Like as the final void ratio, also the void ratio amplitude can be reproduced better by an analytical solution based on final material parameters. This is confirmed by Fig. 8.27, where the solutions AS_{100} and AS_{400} are shown to fit the initial void ratio amplitude Δe_{1st} measured in the experiment. The increase in Δe with increasing load period and amplitude is also confirmed by the analytical solution as Δs_{norm} increases with increasing T_0 (see Fig. 8.28b). In the analytical solution the deformation is calculated by Δs_{norm} times $\frac{\hat{\sigma}_v}{2E_s}$ (compare Eq. 4.20). Therefore, with increasing stiffness the deformation amplitude decreases, which corresponds to the findings from the experimental study.

Concluding, it can be stated that due to the assumption of constant consolidation parameters ($c_v = const.$ and $E_s = const.$), the analytical solutions are not able to fit the overall cyclic consolidation process. The initial consolidation behaviour is well repro-

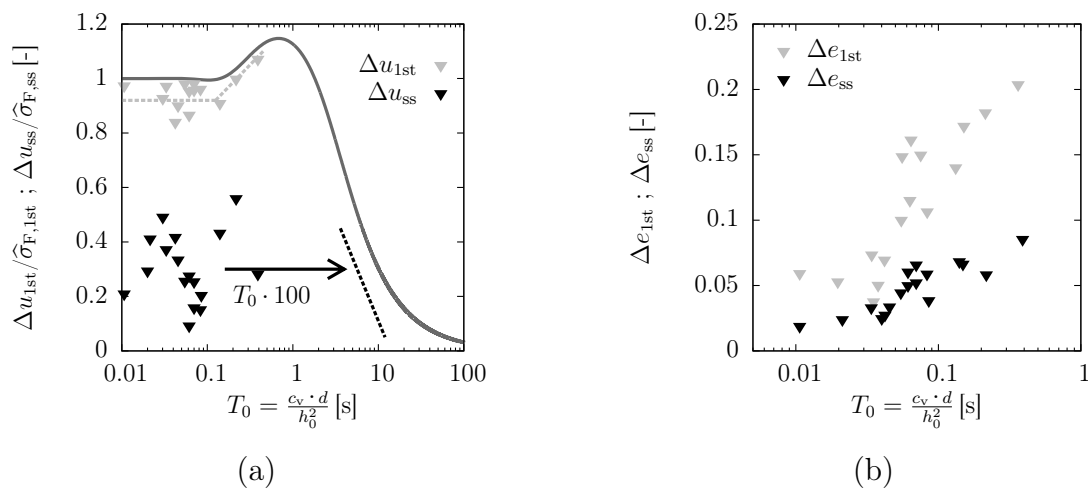


Figure 8.28: Development of (a) pore water pressure and (b) deformation amplitude with increasing T_0 - comparison between experiment and analytical solution.

duced by an analytical solution using material parameters derived at the initial material state. However, this solution is not able to reproduce the stationary state and deformation characteristics. To fit the material behaviour in the stationary state, an analytical solution using material parameters derived on the final or stationary-state material state is much more suitable, as this solution accounts for the increase in E_s and c_v with increasing vertical effective stress. Alternatively, a more complex analytical solution accounting for the change in E_s and c_v with increasing compression would be required.

8.7 Numerical modelling

As illustrated above, the linear elastic assumptions incorporated in the analytical solutions by Verruijt (2014) and Razouki and Schanz (2011); Razouki et al. (2013); Müthing et al. (2016b) do not allow for a holistic reproduction of the cyclic consolidation process, as with constant E_s , k and c_v only either the initial or the stationary state consolidation phase can be reproduced. As an analytical solution adapting c_v with respect to the changing effective stress and/or void ratio under cyclic loading is not available, a practical method to approach this problem is by numerical analysis, namely by Finite Element Modelling of the boundary value problem.

Therefore, in Müthing et al. (2016b) and Barciaga et al. (2017) studies have been published, analysing the numerical modelling of the cyclic consolidation process by use of different constitutive models. In Müthing et al. (2016b) an analytical solution derived for the cyclic consolidation problem with and without rest period is verified by comparison to a linear elastic FE analysis. In Barciaga et al. (2017) a numerical analysis to model the experimental data on natural Onsøy clay, presented in Müthing et al. (2017), is performed. Here, different constitutive models of a hierarchical model family are compared in order to analyse the influence of different model features (e.g. anisotropy and destructuration) on the cyclic consolidation response. These studies are introduced in the following.

8.7.1 Verification of the analytical solution by linear-elastic FEA

To verify the analytical solution given in Eq. 4.5 a numerical model introduced in Razouki et al. (2013) is used in Müthing et al. (2016b). The numerical solution is obtained using the FE software PLAXIS (Brinkgreve et al., 2010). The simplified numerical model consists of a soil bar ($h = 1\text{ m}$, $b = 0.1\text{ m}$) with a fixed and impermeable bottom (at $z/h = 0$) and impermeable sides, which are fixed in horizontal direction. The cyclic loading of

haversine type is applied at the top (at $z/h = 1$) of the soil bar, which is permeable. The material is considered to be linear elastic with $E = 100$ kPa and $\nu = 0$, so that $c_v \approx 1.0$ and $T_v \approx t$. To avoid a singular system of equations, a finite stiffness is assigned to the water. 20 triangular 6-node elements with quadratic interpolation of displacements and pore pressure form the FE mesh.

Figure 8.29 compares the normalised excess pore water pressure over sample height at different loading cycles from the linear-elastic, numerical solution and the analytical solution. It can be seen that both solutions are nearly the same. Further comparisons regarding the development of effective stress and the effect of a rest period on the development of pore water pressure and settlements, which can be found in detail in Müthing et al. (2016b), reveal that both solutions coincide perfectly for pore water pressure modelling.

However, as in the linear-elastic FEA also E_s , k and c_v are constant values, this numerical model has the same restrictions as the analytical solution regarding the comparison towards the experimental data. Therefore, numerical modelling using more sophisticated numerical models is needed to reproduce the effects observed in the experimental study.

8.7.2 Numerical analysis using hierarchical, constitutive models

In order to analyse which degree of sophistication of the constitutive model is required to reproduce the effects observed in the experimental study, a numerical analysis comparing different models of a hierarchical, constitutive model family is presented in Barciaga

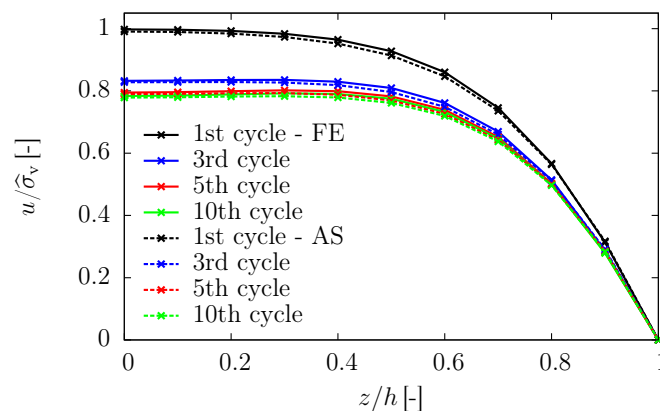


Figure 8.29: Pore water pressure over sample height for different loading cycles (at time of maximum loading) from the numerical simulation and analytical solution, according to (Müthing et al., 2016b).

et al. (2017). In particular, an adequate hierarchical constitutive soil model based on the bounding surface plasticity (BSP) concept is employed to investigate the influence of the constitutive model on the numerical simulation of the consolidation behaviour of natural Onsøy clay under cyclic loading. The hierarchical structure of the constitutive model enables the investigation of the influence of a particular model features, as e.g. inherent and the stress-induced anisotropy, structure and destructuration, by activation/deactivation of the associated constitutive parameters.

Boundary and initial conditions

The FE analysis is performed using the finite element software PLAXIS 3D. In there, the consolidation process is solved according to Biot's theory (Biot, 1941). The geometry (cylindrical sample with $d = 0.07$ m, $h = 0.02$ m) as well as the mechanical and hydraulic boundary conditions are chosen in accordance with the experimental setup. For further details on the numerical model see Barciaga et al. (2017).

Constitutive model

For the numerical analysis a hierarchical model is used. The model in its simplest form is based on the elastoplastic concept of critical state soil mechanics using the Modified Cam-Clay (MCC) approach incorporating isotropic hardening and softening. The introduction of rotational hardening allows to capture anisotropy. Moreover, an extension to model structure/destructuration is included. The most sophisticated model uses the bounding surface plasticity (BSP) concept to deal with complex loading paths. By adaptations of the corresponding constitutive parameters the most sophisticated model can be reproduced to the simplest model (details see Barciaga et al. (2017) and compare Table 8.2). Thereby, namely the following four constitutive models are derived:

- MCC → isotropic hardening and softening
- SANICLAY → additional anisotropy
- SANICLAY D → additional destructuration
- SANICLAY D + BSP → additional bounding surface plasticity

The constitutive parameters of the model were calibrated using test data under oedometric and triaxial loading conditions as well as drained and undrained hydraulic conditions. For the calibration, numerical simulations of these tests were performed. Details can be

found in Barciaga et al. (2017). Table 8.2 gives an overview of the constitutive parameters derived from the calibration and used within the numerical analysis.

Results

Figure 8.30 and 8.31 show the normalised excess pore-water pressure and settlements displayed over the number of loading cycles from the numerical modelling of the cyclic consolidation process using different constitutive models. To allow for a better comparison, the pore water pressure curves are normalised with the load amplitude $\hat{\sigma}_v$, while the settlement curves are normalised with the values derived from the SANICLAY D model.

From the numerical results of pore water pressure it can be seen, that all numerical models are able to reproduce the reduction in pore water pressure amplitude with increasing degree of consolidation as found in the experimental analysis (compare Fig. 8.32). However, the numerical models still underestimate the reduction in the excess pore-water pressure amplitude ($\Delta u_{ss}/\hat{\sigma}_v \approx 0.2$). Moreover, they predict a faster dissipation of the mean pore

Table 8.2: Constitutive parameters for natural Onsøy clay (Barciaga et al., 2017).

		MCC	SANICLAY	SANICLAY D	SANICLAY BSP+D
Critical state soil mechanics MCC	κ	0.024	0.024	0.024	0.024
	ν	0.2	0.2	0.2	0.2
	λ	0.185	0.185	0.185	0.185
	M_c	1.43	1.43	1.43	1.43
	M_e	0.83	0.83	0.83	0.83
	N	1.0	1.0	1.0	1.0
Anisotropy Rotational hardening	α_0	0	0.3	0.3	0.3
	c	0	10	10	10
	x_α	-	12.2	12.2	12.2
Structure Destructuration	S_{i0}	1	1	5	5
	k_i	-	-	0.7	0.7
	A	-	-	0.5	0.5
BSP	s_{eln}	100	100	100	1
	h_0	10,000	10,000	10,000	100
	a_{dam}	0	0	0	1

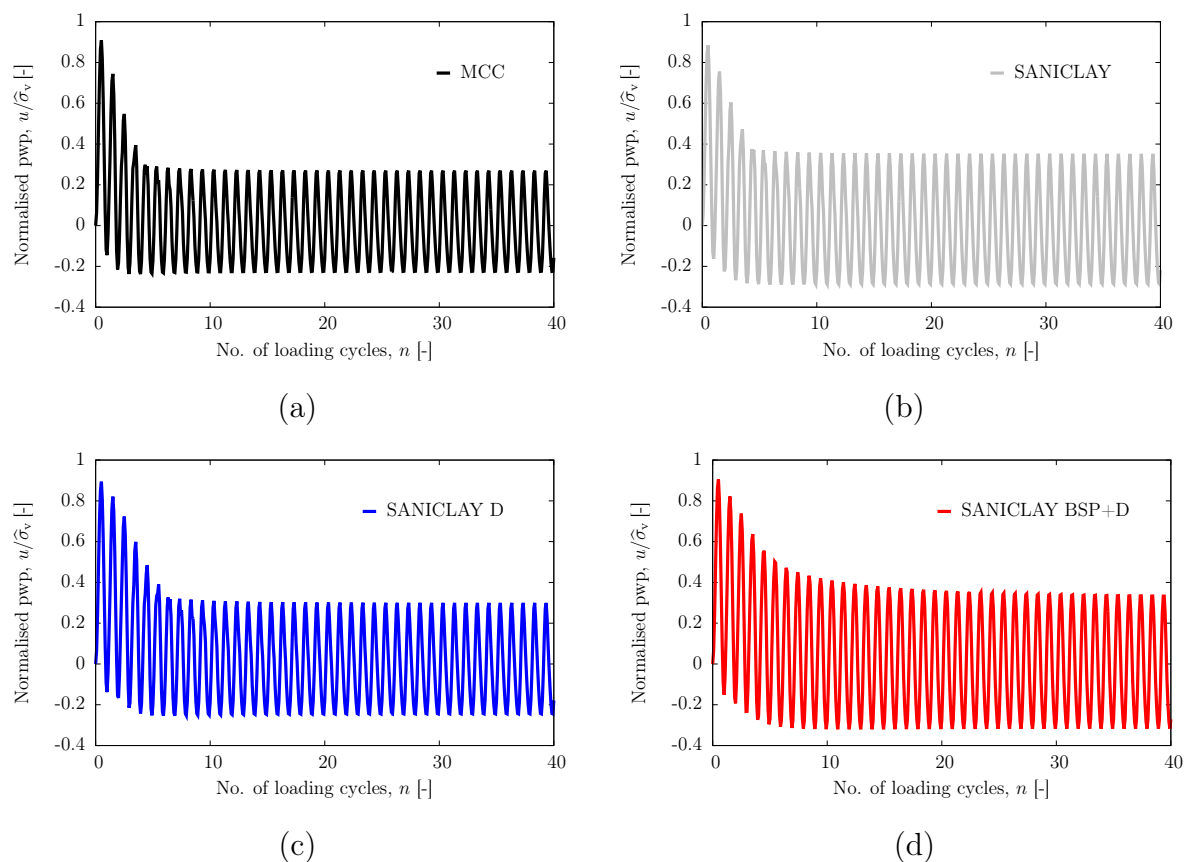


Figure 8.30: Development of the normalised excess pore-water pressure over the number of loading cycles from the numerical simulation of oedometer tests under cyclic loading on natural Onsøy clay ($\hat{\sigma}_v = 200 \text{ kN/m}^2$, $d = 120 \text{ s}$) - using different constitutive models: (a) MCC, (b) SANICLAY, (c) SANICLAY D, (d) SANICLAY BSP+D Barciaga et al. (2017).

water pressure compared to the experimental results. Namely, after the first 5-10 cycles the mean pore water pressure equals 0. This effect can be ascribed to a too high c_v in the numerical analyses. However, it can be observed that the models accounting for destructuration show a slightly slower consolidation behaviour and thus fit the experimental data slightly better.

The comparison of the deformation behaviour shows that the normalised settlements are most pronounced for the simulations employing the constitutive models with destructuration (SANICLAY D and SANICLAY BSP+D). Due to the fast pore water pressure dissipation predicted in all numerical analyses, also the settlements for all models occur earlier compared to the experimental results. While SANICLAY D gives results for the maximum settlements, which are close to those from the experiment, the less complex models underestimate the corresponding maximum experimental values.

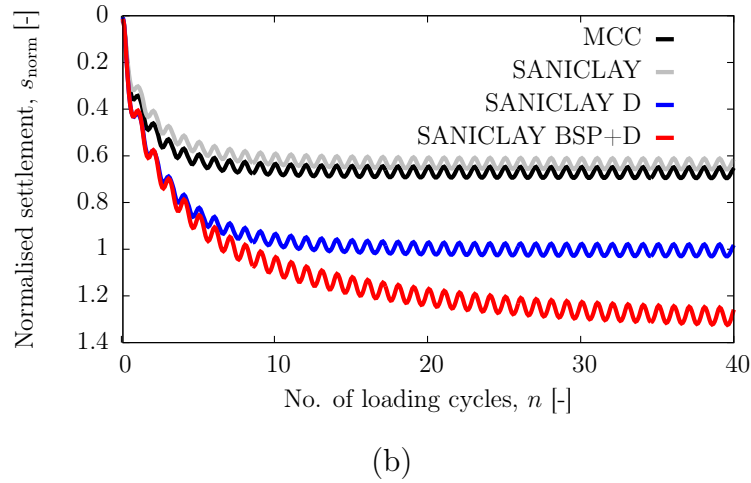


Figure 8.31: Development of the normalised settlement over the number of loading cycles from the numerical simulation of oedometer tests under cyclic loading on natural Onsøy clay using different constitutive models ($\hat{\sigma}_v = 200 \text{ kN/m}^2$, $d=120 \text{ s}$) (Barciaga et al., 2017).

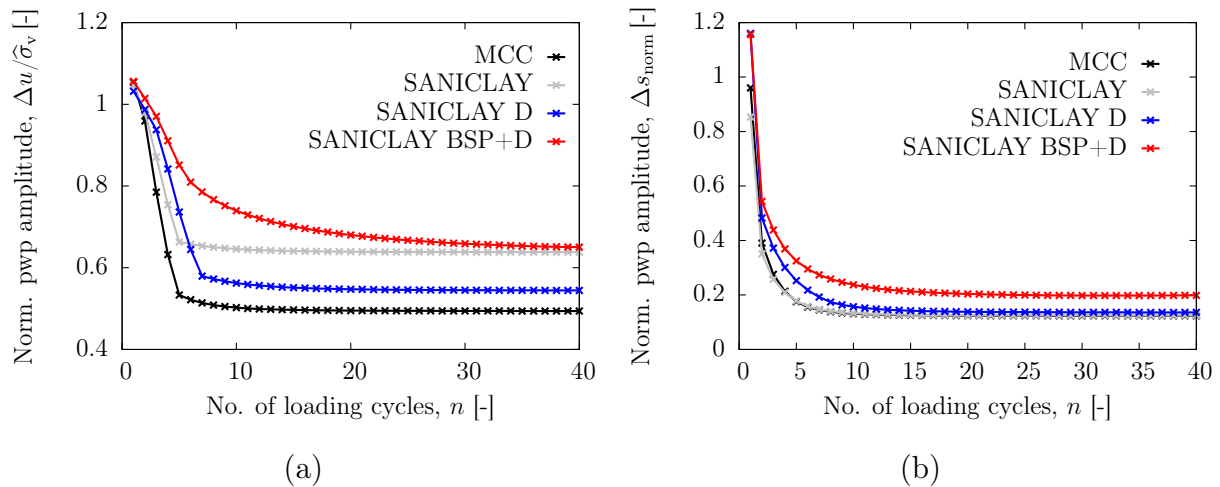


Figure 8.32: Development of (a) pore water pressure amplitude and (b) deformation amplitude over the number of loading cycles from the numerical simulation of oedometer tests under cyclic loading on natural Onsøy clay using different constitutive models ($\hat{\sigma}_v = 200 \text{ kN/m}^2$, $d=120 \text{ s}$).

Correspondingly, due to the accumulation of the plastic strains during cyclic loading the BSP+D model overestimates the final settlements observed in the experiments. All models are able to reproduce the decrease in settlement amplitude with time (compare Fig. 8.32).

8.7.3 Conclusions

From the comparison of the numerical analysis based on different constitutive approaches it can be seen, that linear elasticity is not able to reproduce the consolidation behaviour of fine-grained soils under cyclic loading. However, with more sophisticated models, adapting the stiffness E_s and thus c_v with respect to the effective stress and/or void ratio, a better reproduction of the effects measured experimentally can be reached from a qualitative point of view. For instance, the reduction of pore pressure and deformation amplitude with increasing degree of consolidation can be simulated. To model the behaviour of structured clay, models accounting for the destructuration process are better suitable than models of lower complexity. For an even better fit of the experimental data by numerical models, a global sensitivity analysis would be useful. Thereby, the most relevant parameters could be identified so that, particular focus could be set on the identification of these parameters. Moreover, the effect of models accounting for the viscosity, as e.g. Fuentes et al. (2017), should be studied in future work.

8.8 Development of radial stress

Figure 8.33a exemplarily presents the development of total radial stress σ_{rad} with consolidation progress from oedometer tests on kaolin clay under cyclic loading. It can be seen that with ongoing time, the maximum radial stress as well as the radial stress amplitude decrease.

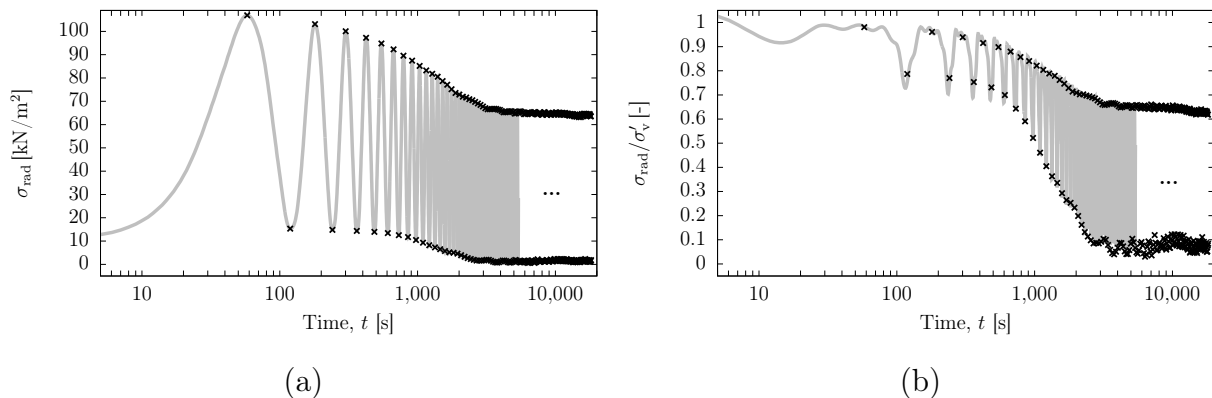


Figure 8.33: Development of (a) radial stress σ_{rad} and (b) normalised radial stress $\sigma_{\text{rad}}/\sigma'_v$ during cyclic consolidation. (test CK08: $d = 120$ s, $\hat{\sigma}_v = 100$ kN/m²)

As explained in Chapter 7.4 at the beginning the applied stress is completely carried by the pore water. In the first loading cycle, hence, σ_{rad} equals the applied vertical stress amplitude $\hat{\sigma}_v$, due to the isotropic stress distribution in water (see Fig. 8.33b). During the consolidation process, gradually the load is transferred from the pore water to the soil matrix. Thus, the radial stress decreases. After reaching the stationary state the applied loading is carried by the soil skeleton. Consequently, the radial stress σ_{rad} equals K_0 -times the applied loading.

However, as in cyclic consolidation experiments the normalised vertical effective stress in stationary state is not constant, but varies over time (see Fig. 8.23c) and the sample height, a further analysis of the development of K_0 is complex and beyond of the scope of this work. However, a more detailed study of the development of K_0 during consolidation is recommended. It could be supported by the analysis of fabric changes e.g. by means of ESEM investigations.

8.9 Summary and discussion

The consolidation behaviour of the two clays, Spergau kaolin and Onsøy clay, under cyclic loading was studied experimentally in a series of oedometer tests under variation of the loading characteristics, load period and load amplitude, and boundary conditions. Thereby, the cyclic development of deformations and pore water pressure dissipation were analysed.

The cyclic time-dependent deformation behaviour of soft clay under cyclic loading was found to follow the typical s-shape of a consolidation curve, superposed by a cyclic deformation of variable amplitude. After a finite number of cycles or a distinct consolidation time, a quasi stationary state is reached, in which the incremental deformation during compression and unloading becomes identical and only minor additional deformation is detected. This state is referred to as 'stationary state (SS)'. The deformation or final void ratio reached in the stationary state was found to be nearly identical to the deformation or void ratio reached in monotonic loading tests of equivalent applied vertical effective stress. However, the time to reach the EOP in the monotonic loading tests was found to differ from the time to reach SS in the cyclic loading tests. It was shown, that due to the load reversal in cyclic loading tests, the consolidation occurs slower, which is reflected in a lower c_v value computed from the mean time-settlement curve. The load period was found to have an insignificant influence on the final void ratio.

Generally, the cyclic deformation behaviour can be characterised by the development of the mean deformation, identified by final mean deformation e_{ss} and the rate of consolidation c_v , and the development of the cyclic deformation amplitude, identified by the deformation amplitude Δe and its reduction factor η_e . These characteristics were studied in detail regarding their dependency on the loading and material characteristics.

The rate of consolidation was found to change during the cyclic consolidation process due to the change in stiffness and permeability with increasing effective stress state and decreasing void ratio. In the first loading cycle the rate of consolidation was shown to depend on the loading rate and thus on the applied load period. In contrast, the overall consolidation rate computed from the mean cyclic deformation was shown to be independent of the load period but dependent on the load amplitude. This becomes particularly obvious from tests on natural, structured clay. However, as the overall consolidation rate is smaller, the effective stress increases slower compared to the monotonic loading tests and thus, the difference in consolidation rate between smaller and larger load amplitudes is not as significant as in the monotonic loading tests. The c_v values computed from the mean cyclic deformation curves reflect the described behaviour, being slightly smaller compared to the values from monotonic loading tests of equivalent vertical stress.

The amplitude of deformation Δe in the compression phase reduces with increasing, cyclic consolidation progress, while the amplitude of deformation in the unloading phase increases. In the stationary state, the deformation amplitude in compression and unloading are of the same magnitude. This deformation amplitude in stationary state is found to be dependent on both loading characteristics, load period and amplitude. With larger load period and larger load amplitude, the deformation amplitude in stationary state increases.

From the mean deformation the equivalent stiffness \bar{E}_s , characterising the overall, cyclic consolidation deformation, was computed. The reference stiffness for kaolin clay was found to be $\bar{E}_s^{ref} = 700 \text{ kPa}$ ($\hat{\sigma}^{ref} = 100 \text{ kN/m}^2$). The reference stiffness for reconstituted Onsøy clay was computed to be $\bar{E}_s^{ref} = 800 \text{ kPa}$ ($\hat{\sigma}^{ref} = 100 \text{ kN/m}^2$). Differences in \bar{E}_s compared to the stiffness computed from monotonic loading tests, result from the stress path used for the calculation of the stiffness. From the deformation amplitude in stationary state, the equivalent incremental stiffness in the stationary state $\bar{E}_{s,ss}$ was computed to be $\bar{E}_{s,ss}^{ref} = 30 \text{ MPa}$ for kaolin clay and $\bar{E}_{s,ss}^{ref} = 70 \text{ MPa}$ for the Onsøy clay. The equivalent stiffness in the stationary state $\bar{E}_{s,ss}$ was found to be significantly higher than the equivalent stiffness \bar{E}_s . From equivalent stiffness and c_v , values for the permeability were computed.

Analogue to the concept of secondary compression in the monotonic loading tests, the deformation rate in the stationary state under cyclic loading was evaluated in terms of \bar{C}_α , computed from the $e_{\text{mean}} - \log(t)$ -curves of the two clays.

In the experimental study, besides the deformation behaviour, the pore water pressure dissipation was studied. By measurement of the pore water pressure at the bottom of the sample important information on the consolidation behaviour can be gained. Generally, the pore water pressure dissipation curve like the deformation curve can be subdivided into the mean pore water pressure following the typical s-shape form and the cyclic pore water pressure characterised by changing amplitude Δu . The mean pore water pressure curve is characterised by the mean or maximum pore water pressure reached within the first loading cycle and the time where the mean pore water pressure has dissipated. It was found from the experimental results, that the maximum pore water pressure in the first cycle nearly equals the applied load amplitude for most tests and that the time of mean pore water dissipation equals the time of beginning of stationary state derived from the deformation curve. The pore water pressure amplitude Δu was found to decrease with increasing degree of consolidation. While Δu in the first cycle nearly equals the applied stress amplitude $\hat{\sigma}_v$ for all loading configurations, the pore water pressure in stationary state Δu_{ss} depends on the loading characteristics. Namely, with increasing load period and load amplitude, Δu_{ss} decreases, as with longer loading time and higher effective stress more pore water pressure can be dissipated in one loading cycle. This finding corresponds to the analysis of the deformation amplitude in stationary state.

To compare the experimental results to the prediction of the analytical solution, four parameter sets were derived based on the experimental findings from monotonic and cyclic loading tests for the analytical solution accounting for different material states at different vertical effective stress. Therefore, parameter sets to describe the initial material state at $\sigma'_v = 10 \text{ kN/m}^2$, the final material state at $\sigma'_v = 100 \text{ kN/m}^2$ and $\sigma'_v = 400 \text{ kN/m}^2$ were derived. Additionally, a parameter set characterising the final material state at $\sigma'_v = 100 \text{ kN/m}^2$ was derived accounting for the increased equivalent stiffness in stationary state. The comparison between analytical and experimental results revealed, that the analytical solution is generally able to qualitatively reproduce the findings of the experimental consolidation study in terms of deformation and pore water pressure dissipation behaviour. However, it was found that, due to the assumption of constant consolidation parameters ($E_s = \text{const.}$, $k = \text{const.}$ and $c_v = \text{const.}$), the analytical solutions are not able to fit the holistic cyclic consolidation process, but, that different states during the cyclic consolidation process must be modelled by analytical solutions

using different parameter sets. While, the mean pore water pressure dissipation and deformation can be captured by an analytical solution based on the initial material state, to reproduce the pore pressure and deformation amplitude in stationary state an analytical solution based on the final material state is required.

In order to model the holistic consolidation process mathematically, numerical modelling was employed and compared to the experiment findings. The numerical modelling was performed using the FE software PLAXIS. Thereby, different constitutive models, accounting for the variation in c_v and E_s , were used to analyse their ability to reproduce the experimental findings. The comparison of the numerical analysis based on different constitutive approaches revealed, that linear elasticity is not able to reproduce the consolidation behaviour of fine-grained soils under cyclic loading. However, with more sophisticated models, adapting the stiffness E_s and thus c_v with respect to the effective stress and/or void ratio, a better reproduction of the effects measured experimentally can be achieved. To model the behaviour of structured clay, models accounting for the destructuration process were found to better suit the experimental results than models of lower complexity.

9 Phase shift in cyclic consolidation

In the cyclic consolidation process a transient phase shift between the vertical loading and the pore water pressure and deformation arises. This phase shift and its ability to derive consolidation characteristics of the soil are evaluated in the following chapter. Therefore, first of all an analytical solution for the phase shift is derived based on the consolidation equations presented in Chapter 4. A short literature review summarises relevant publications on the phenomenon of phase shift in cyclic loading processes in the framework of consolidation analysis and other fields of physics. Furthermore, the experimental oedometer tests are used to deduce the phase shift between the pore water pressure and the vertical applied load as well as the dependency on the phase shift on the material and loading characteristics. The results from the experimental analysis are compared to the analytical solution. Hence, a method to derive the material-dependent consolidation characteristics, c_v , k , from the measurement of the phase shift is suggested.

9.1 Introduction

As demonstrated in Chapter 4 since mid of the last century the cyclic consolidation behaviour of fine-grained soils has been studied on the basis of mathematical (mainly analytical) approaches as well as in a few experimental studies. However, only a very limited number of studies discusses the effect of an arising phase shift during cyclic consolidation between vertical stress and pore water pressure and deformation. Nevertheless, from other fields of physics it is known, that the phase shift in conduction phenomena can be used to derive material characteristics as for instance the conduction coefficient. Therefore, in the following chapter the phase shift in the cyclic consolidation process is evaluated analytically as well as experimentally. From the findings a method to derive the material's consolidation characteristics, namely, the consolidation coefficient c_v and the hydraulic permeability k , is derived.

9.2 Analytical solution from consolidation equation

The analytical solution presented in Chapter 4.2 allows for a mathematical description of the development of deformation and pore water pressure during cyclic consolidation and thus, enables to derive the mathematical formulation of the phase shift.

In the framework of the 113th European Study Group with Industry in Sofia, the analytical solution for the phase shift between pore water pressure and applied loading during consolidation under haversine loading, was derived in cooperation with a group of mathematicians from Sofia. The analytical solution was compared to a numerical approximation of the problem. The results are published in Iliev et al. (2015).

According to Iliev et al. (2015), the phase shift ψ_u between applied vertical stress σ and the pore water pressure u in stationary state for the boundary value problem according to Razouki et al. (2013) (fixed, undrained boundary at $z = h$, drained boundary at $z = 0$) is given by

$$\psi_{u,ss} = \arctan \left[\frac{e^{\frac{-z}{\sqrt{d \cdot c_v/\pi}}} \cdot \sin \left(\frac{-z}{\sqrt{d \cdot c_v/\pi}} \right)}{1 - e^{\frac{-z}{\sqrt{d \cdot c_v/\pi}}} \cdot \cos \left(\frac{-z}{\sqrt{d \cdot c_v/\pi}} \right)} \right] \quad (9.1)$$

Introducing the $T_0 = \frac{c_v \cdot d}{h^2}$ as the dimensionless loading time $\psi_{u,ss}$ at the undrained boundary ($z = h$) can be written as

$$\psi_{u,ss} = \arctan \left[\frac{e^{\frac{-1}{\sqrt{T_0/\pi}}} \cdot \sin \left(\frac{-1}{\sqrt{T_0/\pi}} \right)}{1 - e^{\frac{-1}{\sqrt{T_0/\pi}}} \cdot \cos \left(\frac{-1}{\sqrt{T_0/\pi}} \right)} \right] \quad (9.2)$$

From Eq. 9.2 it can be seen that in the analytical solution, the phase shift only depends on T_0 and thus on c_v , d and h . Figure 9.1 shows the development of $\psi_{u,ss}$ with T_0 .

In Barends (2006) and Barends (2011) an analysis of the phase shift under mechanical and hydraulic cyclic loading can be found, which is equivalent to the phase shift derived based on the Verruijt solution in Chapter 4.2.

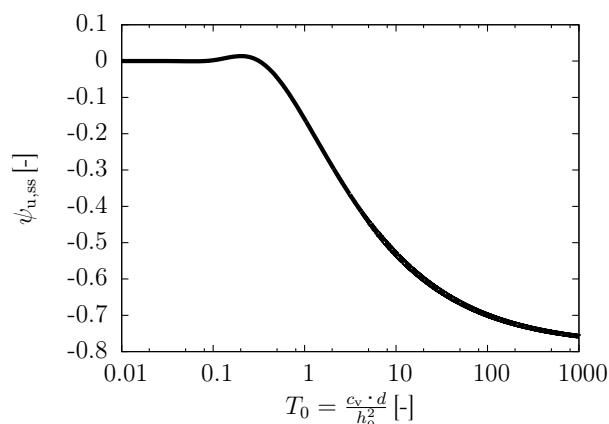


Figure 9.1: Phase shift between applied vertical stress σ and the pore water pressure u in stationary state, $\psi_{u,ss}$, versus dimensionless loading time T_0 .

However, as long as the analytical solutions are based on a linearised description of the material characteristics (i.e. in the case of consolidation: assuming $E_s = \text{const.}$, $k = \text{const.}$ and $c_v = \text{const.}$), as shown in the previous chapter, the quantitative validity to model the material behaviour measured experimentally is limited.

A description of the phase shift in experimental analysis to the author's knowledge can only be found in Vuez et al. (2000), where unfortunately, no detailed analysis of the phase shift and its dependency on soil and loading characteristics is given.

9.3 State of the art - Phase shift in conduction phenomena

Analogue to the problem of consolidation in soil mechanics, other physical problems in related fields of physics can be solved using identical mathematical concepts. For instance problems dealing with temperature propagation, diffusion processes and electric conduction or magnetic migration in porous media can be solved based on the same partial differential equations as the hydraulic problem of consolidation. Inversely, solutions derived for these physical problems can be transferred to derive new solutions in the framework of consolidation analysis. In this manner, existing solutions for the temperature propagation used to derive the thermal conductivity of a porous material can be used to derive the hydraulic permeability from fluid flow analysis during consolidation. The basic equations for this kind of mathematical problems and an overview of equivalent conduction phenomena can be found in Carslaw and Jaeger (1959) and Mitchell (1991).

Recent studies from related fields of physics using the phase shift in equivalent conduction phenomena are illustrated in the following. In the field of biomechanics, by analysing the stress deformation and fluid pressure in bone specimens under cyclic loading, the strain-derived interstitial fluid flow in lacuno-canalicular porosity is investigated. The lacuno-canalicular porosity is presumed to influence the prime mover for bone remodelling and is thus relevant in the framework of cancer research (Kameo et al., 2008, 2009; Ling et al., 2009; Kameo et al., 2010, 2011; Kameo and Adachi, 2012; Guth et al., 2014). In the field of rock mechanics, Renner and Messar (2006), Song and Renner (2006) and Song and Renner (2007) introduce a method to determine the hydraulic permeability of fractured rock by the analysis of oscillatory fluid flow. Mimouni et al. (2015) use cyclic interference analysis to determine the thermal diffusivity of the subsoil. In the field of material science, Guth et al. (2014) use the phase shift between strain and temperature to analyse MAR-M247 LC under thermo-mechanical fatigue loading.

9.4 Experimental analysis

From the experimental analysis, the phase shift between applied vertical loading and pore water pressure and deformation, in terms of void ratio, measurement was computed. In the following the evolution of the phase shift with consolidation progress as well as its dependency on the loading characteristics, load amplitude $\hat{\sigma}_v$ and load period d , and dimensionless loading time T_0 is evaluated,

9.4.1 Phase shift of deformation $\bar{\psi}_e$

In the cyclic consolidation process, the compression deformation in one loading cycle continues longer than the increase in loading. This means, that the compression continues during the time of early unloading, as illustrated in Fig. 9.2a.

After load reversal the compression continues as long as the vertical stress applied is larger than the effective stress present in the sample. The same holds true for the unloading phase. Due to this, the vertical stress and deformation curve are staggered by a phase shift $\bar{\psi}_e$ [s], which is calculated as the difference between time at local minimum void ratio $t(e_{\min})$ and time at maximum applied load $t(\sigma_{v,\max})$.

$$\bar{\psi}_e = t(\sigma_{v,\max}) - t(e_{\min}) \quad (9.3)$$

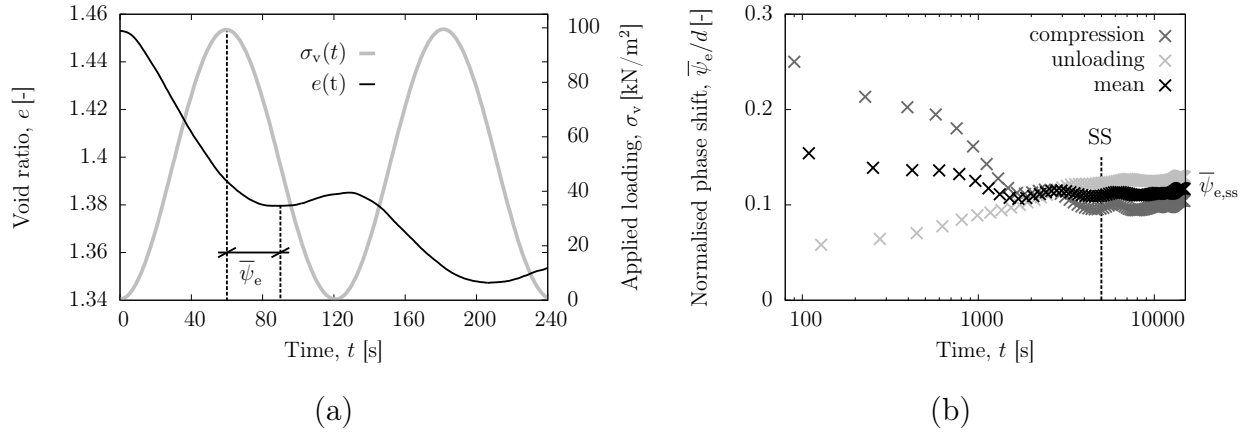


Figure 9.2: Deformation behaviour of kaolin clay under haversine loading: (a) void ratio versus time, (b) void ratio amplitude versus time. (test CK08: $d = 120$ s, $\hat{\sigma}_v = 100$ kN/m²)

Following, the development of effective stress, this phase shift $\bar{\psi}_e(t)$ decreases with increasing degree of consolidation (see Fig. 9.2b). The development of the phase shift can be identified by $\eta_{\bar{\psi}_e}$, which is defined as the ratio between the phase shift in stationary state and first cycle:

$$\eta_{\bar{\psi}_e} = \frac{\bar{\psi}_{e,ss}}{\bar{\psi}_{e,1st}} \quad (9.4)$$

Figure 9.3 demonstrates the dependency of the deformation phase shift in stationary state $\bar{\psi}_{e,ss}$, computed from the $e - \log(t)$ -curves, on the loading characteristics, load period d , load amplitude $\hat{\sigma}_v$ and the normalised loading time T_0 . Here, the phase shift in stationary state at maximum compression and unloading is illustrated. It can be observed, that $\bar{\psi}_{e,ss}$ increases for larger load period and slightly decreases for larger load amplitude. However, in the tested loading range, $\bar{\psi}_{e,ss}$ is more significantly influenced by the load period d than by the load amplitude $\hat{\sigma}_v$. As $\hat{\sigma}_v$ in the tested range has a smaller influence on T_0 , the $\bar{\psi}_{e,ss}$ - T_0 diagram still shows a unique relationship. The deformation phase shift in unloading is found to be slightly larger than the in compression.

9.4.2 Phase shift of pore water pressure $\bar{\psi}_u$

As analysed for the compression curve, also the pore water pressure is staggered in time with respect to the applied loading. The difference between time at maximum, local pore

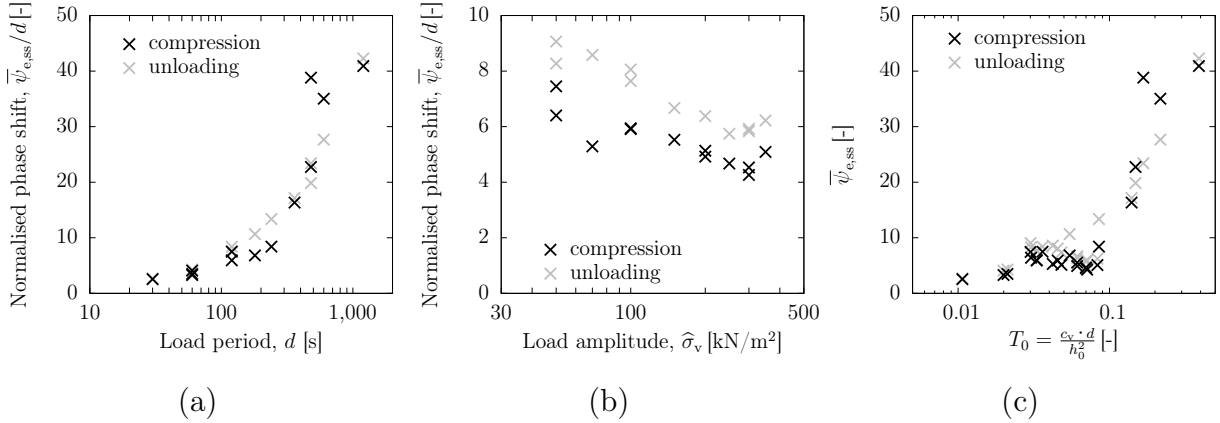


Figure 9.3: Deformation phase shift in stationary state $\bar{\psi}_{e,ss}$ versus (a) load period, tested at $\hat{\sigma}_v=100$ kN/m², (b) load amplitude, tested at $d=120$ s, (c) normalised loading time T_0 , from cyclic consolidation tests on kaolin clay.

water pressure $t(u_{\max})$ and time at maximum applied load $t(\sigma_{v,\max})$, is referred to as the pore pressure phase shift $\bar{\psi}_u$ [s].

Figure 9.4a illustrates the pore pressure phase shift $\bar{\psi}_u$ with respect to the applied loading function for the cyclic consolidation process. In contrast to the phase shift of the compression curve, $\bar{\psi}_u$ increases in magnitude with the consolidation progress from a value close to 0 to a constant value in stationary state $\bar{\psi}_{u,ss}$ as illustrated in Fig. 9.4b.

$$\bar{\psi}_u = t(\sigma_{v,\max}) - t(u_{\max}) \quad (9.5)$$

Figure 9.5 illustrates the dependency of the pore pressure phase shift in stationary state $\bar{\psi}_{u,ss}$ on the loading characteristics, load period d and load amplitude $\hat{\sigma}_v$, as well as on the normalised loading time T_0 . The phase shift is analysed in compression and unloading of each cycle.

In the tested loading range, $\bar{\psi}_{u,ss}$ is more significantly influenced by the load period d than by the load amplitude $\hat{\sigma}_v$. This is due to that fact, that the load period d has a stronger influence on T_0 than the load amplitude $\hat{\sigma}_v$, which influences T_0 only by changing c_v . The phase shift in compression and unloading for the lower range of load period ($d \leq 200$ s) is similar, while the values deviate for higher load period.

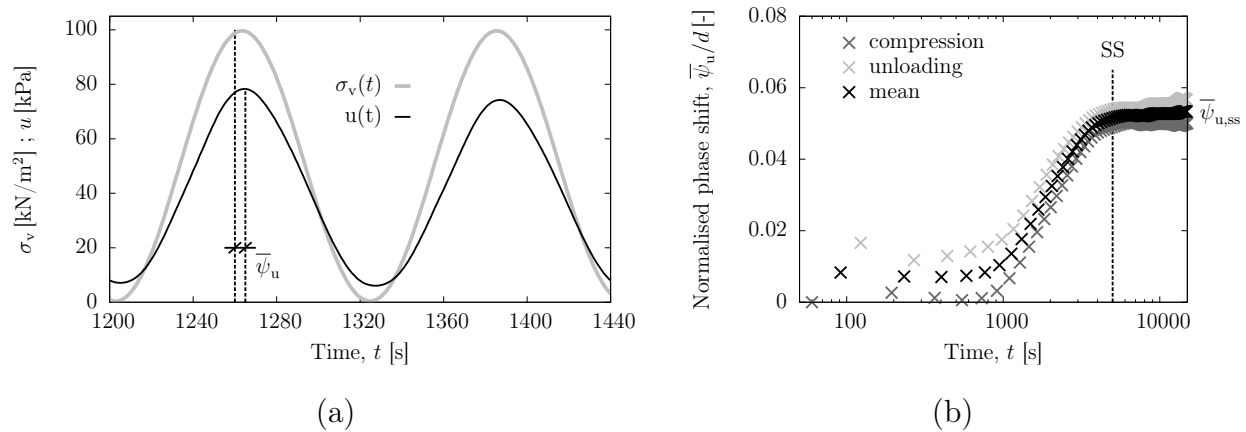


Figure 9.4: Deformation behaviour of kaolin clay under haversine loading: (a) void ratio over time, (b) void ratio amplitude over time

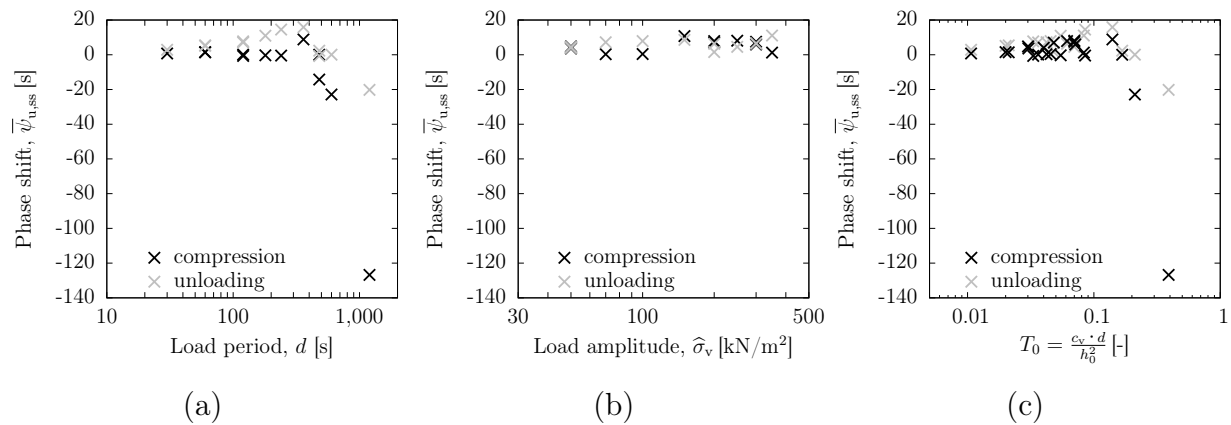


Figure 9.5: Pore water pressure phase shift in stationary state $\bar{\psi}_{u,ss}$ versus (a) load period, tested at $\hat{\sigma}_v=100 \text{ kN/m}^2$, (b) load amplitude, tested at $d=120 \text{ s}$, (c) normalised loading time T_0 , from cyclic consolidation tests on kaolin clay.

9.4.3 Comparison to analytical solution

Figure 9.6 compares the findings for the relationship between the phase shift and T_0 from experimental analysis and analytical solution.

It can be observed that the findings from experimental and analytical analysis qualitatively show the same behaviour. For smaller values of T_0 , $\psi_{u,ss}$ and $\bar{\psi}_{u,ss}$ are found to be approximately constant. After reaching a threshold value the phase shift decreases and becomes negative.

From a quantitative point of view some differences are present. First of all, in the analytical solution for values of $T_0 \leq 0.1$ $\psi_{u,ss}$ equals 0. In the experimental study also for smaller values of T_0 a positive phase shift is measured. Furthermore, the threshold value

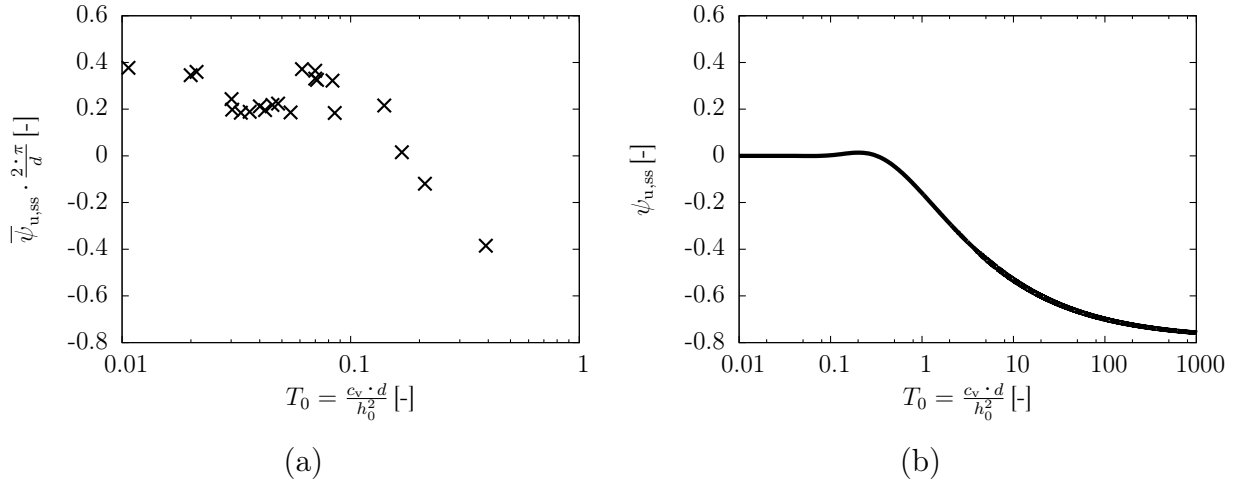


Figure 9.6: Pore water pressure phase shift - comparison between (a) experimental results $\bar{\psi}_{u,ss}$ and (b) analytical solution $\psi_{u,ss}$.

of T_0 , after which the phase shift becomes negative, is found to be much smaller in the experimental study than in the analytical solution. This corresponds to the finding, that in the experimental analysis the decrease in phase shift with increasing T_0 after reaching $T_{0,thres}$ occurs much faster. For $T_0 = 0.4$ in the experimental analysis $\bar{\psi}_{u,ss} = 0.4$, while in the analytical solution this value is reached for $T_0 \geq 2$. Both effects can be explained by the fact, that the T_0 value used for the present experimental analysis is computed based on the mean c_v value. As the stiffness in the stationary state increases significantly, it can be presumed that also c_v is significantly higher. Thus, T_0 for the experimental results will be underestimated. This corresponds to the findings from the comparison between experimental analysis and analytical solution for deformation and pore water pressure amplitude in the stationary state (see Chapter 8.6).

An analytical solution for the deformation phase shift at the moment is not available in literature. For the further study of the phase shift and the validation of the testing concept described in the following, however, it would be of great benefit and thus, should be derived in further studies.

9.5 Testing concept: from phase shift to material characteristics

9.5.1 Motivation

The precise knowledge of a soils' consolidation coefficient and its permeability is of significant importance in a multitude of geotechnical applications. This particularly holds true when fine-grained, low permeable soils are considered. To name just a few applications, c_v and k are mandatory parameters for the settlement prognoses, the stability and flow analysis of excavation walls, retaining walls and dam constructions, for the analysis of sealing systems in geoenvironmental applications (construction of landfill), the modelling of pollutant dispersal in the subsoil as well as for the dimensioning and evaluation of drinking water plants and geothermal or reservoir systems.

While the consolidation coefficient is commonly derived from step-wise oedometer tests, common procedures and standardised methods to determine the permeability of a soil are either based on flow tests using Darcy's law or on the evaluation of the consolidation behaviour under monotonic loading from oedometer or CRS/CG tests (see Chapter 2.3). As discussed in Chapter 2.3 for low permeable soils the methods to determine the hydraulic permeability based on flow measurement are extensively time consuming and susceptible to measuring inaccuracy due to the small flow rate and small volume of flowing pore liquid per time. On the other hand, the determination of hydraulic permeability based on the evaluation of the consolidation behaviour under monotonic loading is criticised as inaccurate due to the linearisation of the underlying consolidation theory (compare Tavenas et al. (1983)).

A method to determine the consolidation coefficient and hydraulic permeability based on the semi-empirical evaluation of the phase shift from cyclic consolidation tests is a promising approach as for low permeable soils it is many times faster than any flow experiment and additionally accounts for the non-linearities in the consolidation process.

Figure 9.7 exemplarily shows the development of the phase shift $\bar{\psi}_u$ from cyclic consolidation tests on Spergau kaolin clay and Querenburg silt, a local silt material from Bochum. Under identical loading conditions in terms of load period and load amplitude, the two soils develop a significantly different phase shift. The difference in the phase shift in the stationary state $\bar{\psi}_{u,ss}$ can be used to identify the soil's consolidation coefficient and thus, its permeability.

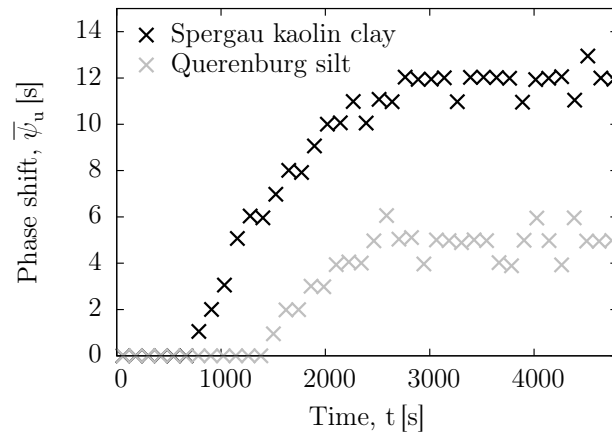


Figure 9.7: Concept of deriving consolidation parameters from the of phase shift between applied vertical stress σ and the pore water pressure u in stationary state of cyclic consolidation by semi-analytical fit.

9.5.2 Suggested concept and validation strategy

In order to identify c_v and k from the measurement of the phase shift a unique, semi-empirical relationship between $\bar{\psi}_{u,ss}$ and T_0 is required. Therefore, the analytical solution needs to be adapted to account for the non-linearities in the experimental measurement of the consolidation process. Thereby, a fitting function $\bar{\psi}_{u,ss}(T_0)$ is created. The invert of the adapted function $T_0(\bar{\psi}_{u,ss})$, allows for the back-calculation of T_0 from $\bar{\psi}_{u,ss}$.

With the given mathematical expression, $T_0(\bar{\psi}_{u,ss})$, the consolidation coefficient and hydraulic permeability can be computed based on the measured phase shift by the following calculation steps, illustrated in Fig. 9.8.

1. Back-calculate T_0 from the measured phase shift by use of the fitting function $T_0(\bar{\psi}_{u,ss})$.
2. Compute $c_v = \frac{T_0 \cdot h^2}{d}$, by use of the load period d and sample height h .
3. Derive the equivalent stiffness \bar{E}_s from the measured deformation.
4. Compute the hydraulic permeability as $k = \frac{c_v \cdot \gamma_w}{E_s}$.

This methodic concept to derive the hydraulic permeability from the measured phase shift in cyclic consolidation has been registered for patent approval as a German patent (DE 10 2015 114 864 A1 2017.03.09) with the title "Verfahren zur Messung der hydraulischen Permeabilität von feinkörnigen und gemischtkörnigen Böden geringer Durchlässigkeit und Sonde zur Durchführung des Verfahrens". The patent verification is currently in progress (status: June 2017).

For the validation of the suggested method and to provide the *proof of concept* for the general validity of the testing concept, the following validation steps have to be accomplished:

1. Identify a universal relationship between ψ and T_0 :

To identify a unique function $T_0(\bar{\psi}_{u,ss})$ first of all more data points are required using soils of significantly varying stiffness and permeability. Thereby, particular focus should be set on the range of $T_0 \geq 0.1$, where $\bar{\psi}_{u,ss}$ varies stronger (area II, Fig. 9.8), which can be accomplished by using higher load periods d . For the case that this function gives multiple possible solutions for $T_0(\bar{\psi}_{u,ss})$, criteria for the identification of T_0 have to be stated.

2. Verification of the method by comparison to conventional permeability tests:

To verify the method the results have to be proven correct by comparison to permeability values of the same materials derived by standard permeability tests. If necessary, further adaption of the semi-empirical equation has to be introduced, based on the empirical relationship derived.

Due to the required conventional permeability tests, the validation of the method is rather time-consuming. The *proof of concept* for the general validity of the testing concept is therefore, in the focus of the continuative, further phase II study and beyond of the scope of this work.

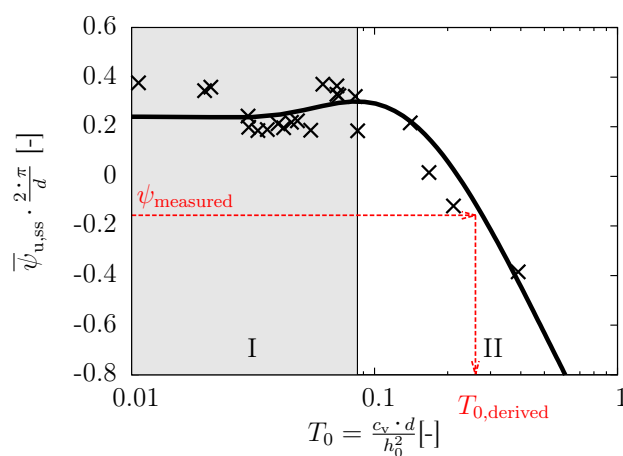


Figure 9.8: Concept of deriving consolidation parameters from the of phase shift between applied vertical stress σ and the pore water pressure u in stationary state of cyclic consolidation by semi-analytical fit.

9.6 Summary

The transient phase shift between the vertical stress and the pore water pressure in the cyclic consolidation process was studied in this chapter. Based on the consolidation equations an analytical solution for the phase shift in stationary state $\psi_{u,ss}$ was derived. Introducing the dimensionless loading time $T_0 = \frac{c_v \cdot d}{h^2}$ the derived equation for $\psi_{u,ss}$ could be shown to depend on T_0 only. In a literature review relevant research on the phase shift in consolidation studies and in the investigation of conduction phenomena in related fields of physics was examined. The phase shift between applied vertical loading and measured pore water pressure $\bar{\psi}_u$ and deformation $\bar{\psi}_e$ from cyclic oedometer testing was evaluated. It was shown, that the loading characteristics have a significant influence on the phase shift in stationary state. In the tested loading range, the phase shift in the stationary state $\bar{\psi}_{u,ss}$ was found to depend more significantly on the load period d than on the load amplitude $\hat{\sigma}_v$, as the load period d has a stronger influence on T_0 . The comparison between experimental results and analytical solution revealed that the relationship between phase shift and T_0 qualitatively shows the same trends. However, quantitative differences due to the presumed underestimation of T_0 from the experiments were found. Analogue to methods from related fields of physics, a concept to derive the soil's consolidation parameters c_v and k from the measured phase shift in cyclic consolidation was motivated and introduced. The concept registered for German patent approval is based on the back-calculation of T_0 from the measured value of $\bar{\psi}_{u,ss}$ by a semi-empirical/semi-analytical approach. A strategy for the validation of the introduced method was illustrated aiming at the *proof of concept* for the general validity of the testing concept to be accomplished in a phase II study of this work.

10 Summary and conclusions

In the present thesis, the consolidation behaviour of fine-grained soils under cyclic loading was experimentally investigated by advanced oedometer tests on Spergau kaolin clay and Onsøy clay. A modified oedometer device was designed and constructed in the framework of this study allowing for the measurement of pore water pressure, radial stress and friction. The influence of material characteristics and loading conditions on the stress and strain state and the time-dependent development of settlements and pore water pressure dissipation was assessed from the experimental testing data. The effect of phase shift in conduction phenomena was analysed for the cyclic consolidation process. Based on the experimental evaluation of the measured phase shift between the vertical effective stress and the pore water pressure, a concept to derive the material characteristics, consolidation coefficient c_v and hydraulic permeability k , was suggested. Analytical solutions for the one-dimensional consolidation process under cyclic loading were derived and used to validate the experimental findings. By comparison of the experimental results to mathematical solutions of the boundary value problem (analytical solutions and numerical modelling), the limitations of the mathematical models incorporating constitutive linearisations was evaluated and the necessity of different, constitutive non-linearities to reproduce the experimental results was assessed.

10.1 Conclusions

From the present study the following main conclusions can be drawn.

The consolidation behaviour of clays is strongly dependent on the effective stress state of the soil. For both clays investigated in the present study, the rate of consolidation characterised by the consolidation coefficient c_v increases with increasing vertical, effective stress σ'_v . Referring to Karunaratne et al. (2001) it could be concluded, that both clays, Spergau kaolin and Onsøy clay, are governed by their mechanical rather than their physico-chemical processes during consolidation. In unloading paths of the same stress range in

monotonic loading tests, c_v was found to be much higher for the same reference stress due to plastic deformation and the resulting higher stiffness. The presence of an inherent soil structure has a significant influence on the c_v - σ'_v -relationship. The present bonding of the clay prior to yielding procures a high stiffness and high c_v . The destructureation occurring after reaching the yield stress causes a strong decrease in stiffness, which results in a sudden drop in the c_v - σ'_v -curve.

The pore water pressure measured during monotonic loading tests deviates from Terzaghi's solution of the consolidation problem in two main points: (1) the maximum pore water pressure measured in the experiment is smaller than the applied vertical effective stress in the load step, (2) the maximum pore pressure is not present instantaneously after load application, but is retarded in time. The amount of the maximum pore water pressure as well as the retardation depend on the consolidation ratio characterised by the consolidation coefficient c_v . Three reasons were identified. First, the load application in the experiment happens not instantaneously, but gradually. Second, imperfections in the measuring system due to system flexibility of the pressure measuring system may occur. Third, the compressibility of the water phase or the ratio between compressibility of water phase and compressibility of the soil matrix is not considered in Terzaghi's theory. By using the hybrid model ($C_s = 0, C_f \neq 0$) this effect can be accounted for.

The K_0 value computed from vertical effective stress and radial stress depends on the present effective stress state in the sample. After load reversal a finite amount of radial stress (residual radial stress) stays imprinted in the sample, resulting in a higher K_0 for over-consolidated states. This finding is in accordance with analyses by Mayne and Kulhawy (1982).

The time-dependent mean deformation and pore water pressure of soft clay during consolidation under stress-controlled cyclic loading follow the typical s-shape of a consolidation curve known from monotonic loading tests. They are superposed by a cyclic deformation and pore water pressure of variable amplitude. After a finite number of cycles or a distinct consolidation time, a quasi stationary state is reached, in which the incremental deformation during loading and unloading becomes identical, so that the accumulation of the deformation increment reaches a minimum and the mean pore water pressure has dissipated to zero. This state is referred to as 'stationary state'.

The final void ratio reached in the stationary state of a cyclic consolidation test is identical to the deformation or void ratio reached in a monotonic loading test of equivalent vertical effective stress. However, the time required to reach the stationary state is larger than the time to EOP in monotonic loading tests. Due to the load reversal in cyclic loading tests,

the consolidation occurs slower, which is reflected in a lower c_v value computed from the mean time-settlement curve. The load period has no significant influence on the final void ratio.

The rate of consolidation changes during the cyclic consolidation process due to the change in stiffness and permeability with increasing effective stress. While the consolidation rate in the first loading cycle depends on the loading rate and thus on the applied load period, the overall consolidation rate computed from the mean cyclic deformation is only dependent on the load amplitude but not on the load period.

The deformation amplitude, given in terms of the void ratio amplitude Δe , in the compression phase and the pore water pressure amplitude Δu decrease with cyclic consolidation progress. In the stationary state, the deformation amplitude as well as the pore water pressure amplitude depend on both loading characteristics, load period and amplitude. With larger load period or larger load amplitude, the deformation amplitude in stationary state increases, while the pore pressure amplitude decreases.

The general consolidation process under cyclic loading can be qualitatively reproduced by the analytical solution for consolidation under cyclic loading based on the Terzaghi theory. However, due to the assumption of linear elasticity and constant consolidation parameters ($E_s = \text{const.}$, $k = \text{const.}$ and $c_v = \text{const.}$), the analytical solutions are not able to fit the holistic cyclic consolidation process. Different states during the cyclic consolidation process (initial and stationary state) must be modelled by analytical solutions using different parameter sets. While, the mean pore water pressure dissipation and deformation can be captured by an analytical solution based on the initial material state, to reproduce the pore pressure and deformation amplitude in stationary state an analytical solution based on the final material state is required. With more sophisticated constitutive models, which adapt E_s and c_v with respect to the effective stress and/or void ratio, a better reproduction of the effects measured experimentally can be achieved. To model the behaviour of structured clay, models accounting for the destructuration process better suit the experimental results than models of lower complexity.

The phase shift between the vertical stress and the pore water pressure in the stationary state $\psi_{u,ss}$ of the cyclic consolidation process is a function of the dimensionless loading time $T_0 = \frac{c_v \cdot d}{h^2}$. The experimental function qualitatively follows the same trend as the $\psi_{u,ss}-T_0$ function found from the analytical solution derived. Analogue to methods from related fields of physics, the phase shift in stationary state $\psi_{u,ss}$ can be used to derive the soil's consolidation parameters c_v and k . This concept of material parameter derivation

is based on the back-calculation of T_0 from measured value of $\bar{\psi}_{u,ss}$ by a semi-empirical / semi-analytical approach and was registered for German patent approval.

10.2 Recommendations for further studies

From the findings and conclusions the following open questions and recommendations for further studies are given.

In order to accomplish the *proof of concept* for the general validity of the testing concept to derive the soil's consolidation parameters c_v and k from the measured phase shift in stationary state $\bar{\psi}_{u,ss}$, the pursued phase II study of this work is supposed to follow the strategy for the validation of the method suggested in Chapter 9.5.2. Additionally, cyclic loading tests with changing frequencies could be investigated regarding their ability to derive more information on the material characteristics within one test. Moreover, the analytical solution for the deformation phase shift should be derived and used for the concept validation.

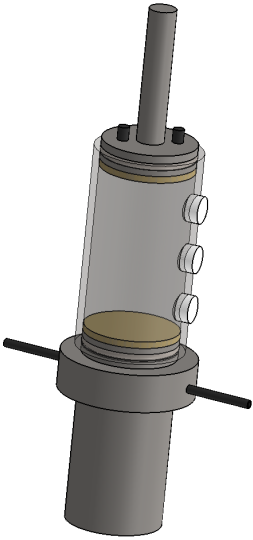
The pore water pressure distribution over the sample height during cyclic loading tests should be investigated experimentally. The knowledge of the pore pressure at different positions would enable the experimental determination of the effective stress distribution. This would allow for a more comprehensive analysis of the deformation and pore pressure dissipation behaviour. The measurement of pore water pressure at different positions over the sample height could be accomplished either by large scale tests, increasing the sample size, or by adapting the oedometer ring of the present device, applying miniature pore pressure sensors (see Fig. 10.1).

A microstructural analysis following the progress of consolidation by means of cryo BIB-SEM investigations, would procure an insight into the hydro-mechanical processes taking place on the micro-structural level during consolidation. From a comparison of macroscopic and micro-structural findings a better understanding on the hydro-mechanical coupling and changes in soil structure could be gained.

Further investigations on the development of K_0 during consolidation are recommended. A quantitative analysis of the development of the radial stress and K_0 with increasing degree of consolidation and depending on the stress state and over-consolidation state could be accomplished. Combined with a microstructural analysis e.g. by ESEM investigations would procure a better understanding of the changing stress distribution with changes in the soil structure.



(a.)



(b.)

Figure 10.1: Prospect facilities for measuring the pore water pressure distribution over the sample height: (a) large scale oedometer tests, (b) adaption of the existing oedometer cell according to Schudy (2015).

Bibliography

- Abbaspour, M. (2014), 'An investigation of consolidation process under triangular cyclic loading by numerical and experimental analysis', *Electronic Journal of Geotechnical Engineering* **19 F**, 1403–1417.
- Abbott, M. B. (1960), 'One-Dimensional Consolidation of Multi-Layered Soils', *Géotechnique* **10**(4), 151–165.
- Abdelhamid, M. S. and Krizek, R. J. (1976), 'At-rest lateral earth pressure of a consolidating clay.', *J. Geotech. Enging Div., ASCE* **102**(GT7), 721–738.
- Abousleiman, Y., Cheng, A. D., Cui, L., Detournay, E. and Roegiers, J. C. (1996), 'Mandel's problem revisited', *Geotechnique* **46**(2), 187–195.
- Abuel-Naga, H. M. and Pender, M. J. (2012), 'Modified Terzaghi consolidation curves with effective stress-dependent coefficient of consolidation', *Géotechnique Letters* **2**(2), 43–48.
- Achari, G., Joshi, R. C., Bentley, L. R. and Chatterji, S. (1999), 'Prediction of the hydraulic conductivity of clays using the electric double layer theory', *Canadian Geotechnical Journal* **36**(5), 783–792.
- Al-Zoubi, M. S. (2015), 'Consolidation analysis by the extended taylor method (ETM)', *Jordan Journal of Civil Engineering* **9**(1), 71–83.
- Alpan, I. (1967), 'The empirical evaluation of the coefficient K_0 and K_{OR} ', *Soil and Foundations* **7**(1), 31–40.
- ASTM D 5084-00 (2002), *Standard Test Methods for Measurement of Hydraulic Conductivity of Saturated Porous Materials Using a Flexible Wall Permeameter*.
- ASTM D4318-10e1 (2010), *Standard Test Methods for Liquid Limit, Plastic Limit, and Plasticity Index of Soils*.

- ASTM D4943-08 (2008), *Standard Test Method for Shrinkage Factors of Soils by the Wax Method*.
- ASTM D854-14 (2014), *Standard Test Methods for Specific Gravity of Soil Solids by Water Pycnometer*.
- Ausilio, E. and Conte, E. (2005), Remarks on consolidation in unsaturated soils from experimental results, *in* T. Schanz, ed., 'Unsaturated Soils: Experimental Studies: Proceedings of the International Conference "From Experimental Evidence towards Numerical Modeling of Unsaturated Soils," Weimar, Germany, September 18–19, 2003 Volume I', Springer Berlin Heidelberg, Berlin, Heidelberg, pp. 373–382.
- Baille, W. (2014), *Hydro-Mechanical Behaviour of Clays - Significance of Mineralogy*, Dissertation, Ruhr-Universität Bochum.
- Baligh, M. and Levandoux, J. (1978), 'Consolidation Theory for Cyclic Loading', *Journal of Geotechnical Engineering Division* **GT4**, 415–431.
- Barciaga, T., Müthing, N., Datcheva, M. and Schanz, T. (2017), Cyclic Response of Natural Onsoy Clay, *in* T. Triantafyllidis, ed., 'Holistic Simulation of Geotechnical Installation Processes, Theoretical Results and Applications - Lecture Notes in Applied and Computational Mechanics', Vol. 82, pp. 275–296.
- Bard, E. (1993), *Methode d'analyse des lois de comportement des soils*, Phd thesis, Ecole Centrale de Paris.
- Barden, L. (1965), 'Consolidation of Compacted and Unsaturated Clays', *Géotechnique* **15**(3), 267–286.
- Barends, F. B. J. (1992), *Theory of consolidation*, Lecture notes, TU Delft.
- Barends, F. B. J. (2006), Transient wave induced pore pressures in a stratified seabed, *in* 'Proceedings Third International Conference on Scour and Erosion November 1 - 3, 2006 Amsterdam, The Netherlands', pp. 1–8.
- Barends, F. B. J. (2011), *Introduction to Soft Soil Geotechnique*, IOS Press BV.
- Barksdale, R. (1971), 'Compressive stress pulse times in flexible pavements for use in dynamic testing', *Highway Research Record* **345**(4), 32–44.
- Bauer, E. (1992), *Zum mechanischen Verhalten granularer Stoffe unter vorwiegend ödometrischer Beanspruchung*, Dissertation, Universität Fridericiana, Karlsruhe.

- Been, K. and Sills, G. C. (1981), 'Self-weight consolidation of soft soils: an experimental and theoretical study', *Géotechnique* **31**(4), 519–535.
- Bellotti, R., Formigoni, G. and Jamiolkowski, M. (1975), Remarks on the effect of over-consolidation on the coefficient of earth pressure at rest., *in* 'Proc.1st Baltic CSMFE, Vol.2', Gdansk, pp. 59–71.
- Bergaya, F. and Lagaly, G. (2013), *Handbook of clay science, Volume 1*, Elsevier Ltd.
- Bergmann, J. (2005), *Manual: Rietveld Analysis Program, BGMN*, 4th, revis edn.
- Berre, T. and Iversen, K. (1972), 'Oedometer tests with different specimen heights on a clay exhibiting large secondary compression', *Geotechnique* **22**(1), 53–70.
- Biot, M. (1941), 'General theory of three-dimensional consolidation', *Journal of Applied Physics* **12**(2), 155–164.
- Biot, M. (1955), 'Theory of Elasticity and Consolidation for a Porous Anisotropic Solid', *Journal of Applied Physics* **26**(2), 182–185.
- Biot, M. (1956), 'General Solutions of the Equations of Elasticity and Consolidation for a Porous Material', *Journal of Applied Mechanics* **23**, 91–96.
- Biot, M. and Willis, D. (1957), 'The elastic coefficients of the theory of consolidation', *Journal of Applied Mechanics* **24**, 594–601.
- Bishop, A., Webb, D. and Skinner, A. E. (1965), Triaxial tests on soil at elevated cell pressures, *in* 'Proc. 6 th Int. Conf. on Soil Mech. and Found. Eng., Toronto, Vol.1', pp. 170–174.
- Bjerrum, L. (1954), 'Geotechnical Properties of Norwegian Marine Clays', *Géotechnique* **4**(2), 49–69.
- Bjerrum, L. (1967), 'Engineering Geology of Norwegian Normally-Consolidated Marine Clays as Related to Settlements of Buildings', *Géotechnique* **17**(2), 83–118.
- Bouckovalas, G. D., Andrianopoulos, K. I. and Papadimitriou, A. G. (2003), 'A critical state interpretation for the cyclic liquefaction resistance of silty sands', *Soil Dynamics and Earthquake Engineering* **23**(2), 115–125.
- Boudali, M. (1995), Comportement tridimensionnel et visqueux des argiles naturelles, PhD thesis, Université Laval.

- Brinkgreve, R., Swolfs, W. and Engin, E. (2010), *PLAXIS 2D 2010. User Manual*, Plaxis bv.
- Brooker, E. W. and Ireland, H. O. (1965), 'Earth Pressures at Rest Related to Stress History', *Canadian Geotechnical Journal* **2**(1), 1–15.
- Brown, S. F., Lashine, A. K. F. and Hyde, A. F. L. (1975), 'Repeated load triaxial testing of a silty clay', *Géotechnique* **25**(1), 95–114.
- Buisman, A. S. (1936), Results of long duration settlement tests., in 'Proc. 1st Int. Conf. Soil Mech. Fdn Engng', Cambridge, pp. 103–197.
- Burland, J. (1990), 'Compressibility and shear strength of natural clays', *Géotechnique* **40**(3), 329–378.
- Burland, J. B. and Roscoe, K. H. (1969), 'Local Strains and Pore Pressures in a Normally Consolidated Clay Layer During One-Dimensional Consolidation', *Géotechnique* **19**(3), 335–356.
- Cai, Y. Q., Geng, X. Y. and Xu, C. J. (2007), 'Solution of one-dimensional finite-strain consolidation of soil with variable compressibility under cyclic loadings', *Computers and Geotechnics* **34**(1), 31–40.
- Carman, P. C. (1956), 'Flow of gases through porous media.'.
- Carslaw, H. and Jaeger, J. (1959), *Conduction of heat In solids*, Oxford at the Clarendon Press.
- Casagrande, A. and Fadum, R. (1940), 'Notes on Soil Testing for Engineering Purposes', *Harvard Soil Mechanics, Series No. 8, Cambridge, Mass* .
- Castro, G. (1975), 'Liquefaction and cyclic mobility of saturated sands', *Journal of the Geotechnical Engineering Division* **100**(GT6), 551–569.
- Chandler, R., de Freitas, M. and Marino, P. (2004), Geotechnical Characterisation of Soils and Rocks: a Geological Perspective, in 'Advances in geotechnical engineering: The Skempton conference', London, pp. 67–102.
- Chandler, R. J. and Cotecchia, F. (2000), 'A general framework for the mechanical behaviour of clays', *Géotechnique* **50**(4), 431–447.
- Chen, G. J. (2002), 'Analysis of pumping in multilayered and poroelastic half space', *Computers and Geotechnics* **30**(1), 1–26.

- Conte, E. (2004), 'Consolidation analysis for unsaturated soils', *Canadian Geotechnical Journal* **41**(4), 599–612.
- Conte, E. and Troncone, A. (2006), 'One-dimensional consolidation under general time-dependent loading', *Canadian Geotechnical Journal* **43**(11), 1107–1116.
- Cryer, C. (1963), 'A comparison of the three-dimensional theories of Biot and Terzaghi', *The Quarterly Journal of Mechanics and Applied Mathematics* **16**(4), 401–412.
- Darcy, H. (1856), 'Les fontaines publiques de la ville de Dijon', *Recherche* p. 647.
- Das, B. M. (2010), *Principles of Geotechnical Engineering*, Vol. Seventh Ed, Cengage Learning.
- Davis, E. H. and Poulos, H. G. (1972), 'Rate of settlement under two- and three-dimensional conditions', *Géotechnique* **22**(1), 95–114.
- Davis, E. H. and Raymond, G. (1965), 'A non-linear theory of consolidation', *Géotechnique* **15**(2), 161–173.
- de Boer, R. (2000), *Theory of Porous Media*, Springer Berlin Heidelberg, Berlin, Heidelberg.
- de Boer, R. (2005), *The Engineer and the Scandal*, Springer Berlin Heidelberg, Berlin, Heidelberg.
- de Boer, R., Schiffman, R. L. and Gibson, R. E. (1996), 'The origins of the theory of consolidation: the Terzaghi—Fillunger dispute', *Géotechnique* **46**(2), 175–186.
- De Josselin de Jong, G. and Verruijt, A. (1965), 'Primary and Secondary Consolidation of a Spherical Clay Sample'.
- De Leeuw, E. (1964), 'Consolidatie en drie dimensies'.
- De Leeuw, E. (1965), 'The Theory of Three-dimensional Consolidation Applied to Cylindrical Bodies'.
- Desbois, G., Urai, J., Hemes, S., Brassinnes, S., De Craen, M. and Sillen, X. (2014), 'Nanometre-scale pore fluid distribution and drying damage in preserved clay cores from Belgian clay formations inferred by BIB-cryo-SEM', *Engineering Geology* **179**(September), 117–131.

- Diamond, S. (1970), 'Pore Size Distributions in Clays', *Clays and Clay Minerals* **18**(1), 7–23.
- DIN EN ISO 11260 (2011), *Bodenbeschaffenheit - Bestimmung der effektiven Kationenaustauschkapazität und der Basensättigung unter Verwendung von Bariumchloridlösung.*
- DIN EN ISO 18130-1 (1989), *Baugrund – Untersuchung von Bodenproben – Bestimmung des Wasserdruchlässigkeitsbeiwert - Teil 1: Laborversuche.*
- DIN EN ISO 22475-1 (2007), *Geotechnische Erkundung und Untersuchung – Probenentnahmeverfahren und Grundwassermessungen – Teil 1: Technische Grundlagen der Ausführung (ISO 22475-1:2006); Deutsche Fassung EN ISO 22475-1:2006.*
- DIN EN ISO 23470 (2011), *Bodenbeschaffenheit - Bestimmung der effektiven Kationenaustauschkapazität (KAK) und der austauschbaren Kationen mit Hexammin-cobalt-trichlorid-Lösung.*
- DIN ISO/TS 17892-6 (Vornorm) (2005), *Geotechnische Erkundung und Untersuchung - Laborversuche an Bodenproben - Teil 6: Fallkegelversuch (ISO/TS 17892-6:2004).*
- DIN:18122-1 (1997), *Baugrund – Untersuchung von Bodenproben – Zustandsgrenzen (Konsistenzgrenzen) - Teil 1: Bestimmung der Fließ- und Ausrollgrenze.*
- DIN:18122-2 (2000), *Baugrund – Untersuchung von Bodenproben – Zustandsgrenzen (Konsistenzgrenzen) - Teil 1: Bestimmung der Schrumpfgrenze.*
- DIN:18123 (1996), *Baugrund – Untersuchung von Bodenproben – Bestimmung der Korngrößenverteilung.*
- DIN:18135 (2012), *Baugrund – Untersuchung von Bodenproben – Eindimensionaler Kompressionsversuch.*
- DIN:18196 (2006), *Erd- und Grundbau – Bodenklassifikation für bautechnische Zwecke.*
- Drnevich, P., Tidfors, M. and Sällfors, G. (1989), 'Temperature Effect on Preconsolidation Pressure', *Geotechnical Testing Journal* **12**(1), 93.
- Dyvik, R., Lacasse, S. and Martin, R. (1985), Coefficient of lateral stress from oedometer cell, *in* 'Norwegian Geotechnical Institute, Publication Nr. 163'.
- Elgohary, M. M. (1973), Consolidation of Soils Under Cyclic Loading, M.sc. thesis, McMaster University Hamilton.

- Eriksson, L. (1989), Temperature effects on consolidation properties of sulphide clays., *in* ‘Proceedings of the twelfth international conference on soil mechanics and foundation engineering.’, pp. 2087–2090.
- Favaretti, M. and Soranzo, M. (1995), A simplified consolidation theory in cyclic loading conditions, *in* ‘Proceedings of the International Symposium on Compression and Consolidation of Clayey Soils’, Hiroshima, pp. 405–409.
- Fillunger, P. (1935), ‘Das Delesse’sche Gesetz’, *Monatshefte für Mathematik* **42**(1), 87–96.
- Fredlund, D. G. and Hasan, J. U. (1979), ‘One-dimensional consolidation theory: unsaturated soils’, *Canadian Geotechnical Journal* **16**(3), 521–531.
- Fuentes, W., Tafili, M. and Triantafyllidis, T. (2017), ‘An isa-plasticity-based model for viscous and non-viscous clays’, *Acta Geotechnica* .
URL: <http://dx.doi.org/10.1007/s11440-017-0548-y>
- Fujiwara, H., Yamanouchi, T., Yasuhara, K. and Ue, S. (1985), ‘Consolidation of alluvial clay under repeated loading’, *Soils and Foundations* **25**(3), 19–30.
- Gao, Y., Wang, Y. H. and Chow, J. K. (2017), ‘Application of Film-Like Sensors for K₀ and Pore Water Pressure Measurement in Clay During 1D Consolidation’, *Geotechnical Testing Journal* **40**(1).
- Gareau, L., Molenkamp, F. and Sharma, J. (2006), ‘An Improved Oedometer Apparatus to Measure Lateral Stress During Testing’, *Geotechnical Testing Journal* **29**(3).
- Geng, X., Xu, C. and Cai, Y. (2006), ‘Non-linear consolidation analysis of soil with variable compressibility and permeability under cyclic loadings’, *International Journal for Numerical and Analytical Methods in Geomechanics* **30**(8), 803–821.
- Gibson, R. (1989), ‘On cryer’s problem with large displacements’, *International Journal for Num. and Anal. Methods in Geomechanics* **13**(June 1988), 251–262.
- Gibson, R. E. (1963), ‘An Analysis of System Flexibility and its Effect on Time-Lag in Pore-Water Pressure Measurements’, *Géotechnique* **13**, 1–11.
- Gibson, R. E., England, G. L. and Hussey, M. J. L. (1967), ‘The Theory of One-Dimensional Consolidation of Saturated Clays’, *Géotechnique* **17**(3), 261–273.

- Gibson, R. E., Knight, K. and Taylor, P. W. (1963), A critical experiment to examine theories of three-dimensional consolidation, *in* 'Proc. European Conf. Soil Mech. Found. Eng., Wiesbaden', Vol. 1, pp. 69–76.
- Gibson, R. E. and Sills, G. C. (1975), 'Settlement of a strip load on a non-homogeneous or orthotropic incompressible elastic half-space', *The Quarterly, Journal of Mechanics and Applied Mathematics* **28**(2), 233–243.
- Gibson, R., Schiffman, R. and Pu, S. (1970), 'Plane strain and axially symmetric consolidation of a clay layer on a smooth impervious base', *The Quarterly Journal of Mechanics and Applied Mathematics* **XXIII**, 13–15.
- Graham, J., Crooks, J. H. a. and Bell, a. L. (1983), 'Time effects on the stress-strain behaviour of natural soft clays', *Géotechnique* **33**(3), 327–340.
- Graham, J., Tanaka, N., Crilly, T. and Alfaro, M. (2001), 'Modified Cam-Clay modelling of temperature effects in clays', *Canadian Geotechnical Journal* **38**, 3608–3621.
- Grim, R. (1968), *Clay Mineralogy*, 2nd editio edn, McGraw-Hill Book Company.
- Guth, S., Doll, S. and Lang, K.-H. (2014), 'Lifetime, Cyclic Deformation and Damage Behaviour of MAR-M247 LC under Thermo-Mechanical Fatigue Loading with 0, 180, -90 and +90 deg. Phase Shift between Strain and Temperature', *Procedia Engineering* **74**, 269–272.
- Haase, H. and Schanz, T. (2016), 'Compressibility and saturated hydraulic permeability of clay-polymer composites — experimental and theoretical analysis', *Applied Clay Science* **130**, 62–75.
- Hamilton, J. J. and Crawford, C. B. (1960), Improved Determination of Preconsolidation Pressure of a Sensitive Clay, *in* 'Papers on Soils 1959 Meetings', ASTM International, 100 Barr Harbor Drive, PO Box C700, West Conshohocken, PA 19428-2959, pp. 254–254–18.
- Hanna, D., Sivakugan, N. and Lovisa, J. (2013), 'Simple Approach to Consolidation Due to Constant Rate Loading in Clays', *International Journal of Geomechanics* **13**(2), 193–196.
- Hardin, B. O. and Black, W. L. (1969), 'Closure to: Vibration modulus of normally consolidated clays', *J. Journal of Soil Mechanics and Foundation Division, ASCE*, **95**(6), 1531–1537.

- Head, K. (1998), *Manual of Soil Laboratory Testing - Volume III*, John Wiley & Sons, Inc.
- Heinrich, G. (1938), 'Wissenschaftliche Grundlagen der Theorie der Setzung von Tonschichten', *Wasserkraft und Wasserwirtschaft* **33**, 5–10.
- Heinrich, G. and Desoyer, K. (1961), 'Theorie dreidimensionaler Setzungsvorgänge in Tonschichten', *Ingenieur-Archiv* **30**, 225–253.
- Hendron, A. J. (1963), The Behaviour of Sand in One Dimensional Compression, PhD thesis, University of Illinois.
- Holtz, R. D. and Jamiolkowski, M. B. (1985), 'Discussion on: Time Dependence of Lateral Earth Pressure', *Journal of Geotechnical Engineering* **111**(10), 1239–1242.
- Hsu, T.-W. and Liu, H.-J. (2013), 'Consolidation for Radial Drainage under Time-Dependent Loading', *Journal of Geotechnical & Geoenvironmental Engineering* **139**(12), 2096–2103.
- Hsu, T.-W. and Lu, S.-C. (2006), 'Behavior of One-Dimensional Consolidation under Time-Dependent Loading', *Journal of Engineering Mechanics* **132**(4), 457–462.
- Huang, Y. (1993), *Pavement Analysis and Design*, Prentice -Hall, Inc. Englewood Cliffs, New Jersey.
- Iliev, P., Stoykov, S., Markovi, B., Datcheva, M., Yovkov, L., Liolios, K., Menseidov, C., Müthing, N. and Barciaga, T. (2015), Rigorous and Approximated Solutions of the Consolidation Problem for a Soil Layer with Finite Thickness under Cyclic Mechanical Loading, in '113-th European Study Group with Industry (ESGI'113)', Sofia, Bulgaria, pp. 73–83.
- Jaky, J. (1944), 'The coefficient of earth pressure at rest.', *Journal of the Society of Hungarian Architects and Engineers* **78**(22), 355–358.
- Jaky, J. (1948), Pressure in silos., in 'Proc., 2nd Int. Conf. on Soil Mechanics and Foundation Engineering', pp. 103–107.
- Janbu, N. (1963), Soil compressibility as determined by oedometer and triaxial tests, in 'Proceedings European Conference on Soil Mechanics and Foundation Engineering', pp. 19–25.

- Kameo, Y. and Adachi, T. (2012), ‘Poroelastic analysis of interstitial fluid flow in trabecula under cyclic loading’, *Journal of Biomechanics* **45**(1).
- Kameo, Y., Adachi, T. and Hojo, M. (2008), ‘Transient response of fluid pressure in a poroelastic material under uniaxial cyclic loading’, *Journal of the Mechanics and Physics of Solids* **56**(5), 1794–1805.
- Kameo, Y., Adachi, T. and Hojo, M. (2009), ‘Fluid pressure response in poroelastic materials subjected to cyclic loading’, *Journal of the Mechanics and Physics of Solids* **57**(11), 1815–1827.
- Kameo, Y., Adachi, T. and Hojo, M. (2011), ‘Effects of loading frequency on the functional adaptation of trabeculae predicted by bone remodeling simulation’, *Journal of the Mechanical Behavior of Biomedical Materials* **4**(6), 900–908.
- Kameo, Y., Adachi, T., Sato, N. and Hojo, M. (2010), ‘Estimation of bone permeability considering the morphology of lacuno-canalicular porosity’, *Journal of the Mechanical Behavior of Biomedical Materials* **3**(3), 240–248.
- Karunaratne, G. P., Chew, S. H., Lee, S. L. and Sinha, A. (2001), ‘Bentonite:Kaolinite Clay Liner’, *Geosynthetics International* **8**(2), 113–133.
- Kaufhold, S., Dohrmann, R., Ufer, K. and Meyer, F. (2002), ‘Comparison of methods for the quantification of montmorillonite in bentonites’, *Applied Clay Science* **22**(3), 145–151.
- Kaufhold, S., Ufer, K., Halisch, M. and Dohrmann, R. (2016), Internal Report on Onsoy clay, Technical report.
- Kavazanjian, E., J. and Mitchell, J. K. (1984), ‘Time Dependence of Lateral Earth Pressure’, *Journal of Geotechnical Engineering* **110**(4), 530–533.
- KELLER (2007), ‘Data sheet: Piezoresistive oeM Pressure transducers, Series 9’.
- Keshian, B., Ladd, C. C. and Olson, R. E. (1977), Sedimentation-consolidation behavior of phosphatic clay, *in* ‘Geotechnical Practice for Disposal of Solid Waste Materials, ASCE Specialty Conference’, pp. 188–209.
- Kjellman, W. and Jakobsen, B. (1955), Some Relations between Stress and Strain in Coarse Grained Cohesionless Materials, *in* ‘Proc. Royal Swedish Geotechnical Inst., No. 9.’.

- Klaver, J., Hemes, S., Houben, M., Desbois, G., Radi, Z. and Urai, J. (2015), 'The connectivity of pore space in mudstones: insights from high pressure Wood's Metal Injection, BIB-SEM imaging and Mercury Intrusion Porosimetry.', *Geofluids* **15**(4), 577–591.
- Kolymbas, D. and Bauer, E. (1993), 'Soft Oedometer—A New Testing Device and Its Application for the Calibration of Hypoplastic Constitutive Laws', *Geotechnical Testing Journal* **16**(2), 263–270.
- Komoronik, A. and Zeiteln, J. (1965), An Apparatus for Mesuring Lateral Soil Swelling Pressure in the Laboratory, *in* 'Proc. 6th ICSMFE, Vol.1.'
- Kono, T., Ochiai, H., Omine, K. and Tsukamoto, Y. (1995), Consolidation behavior of clay under cyclic loading, *in* 'Proceedings of the International Symposium on Compression and Consolidation of Clayey Soils', pp. 111–116.
- Kono, T., Ochiai, H. and Yasufuku, N. (1995), Estimation of Change in the Void Ratio of Clay under Cyclic Loading (in Japanese language), Technical report.
- Kono, T., Ochiai, H., Yasufuku, N. and Umezaki, T. (1995), Design and Development of an Inter-connected Consolidation Apparatus for Cyclic Loading (in Japanese), Technical report.
- Koppejan, A. W. (1948), A formula combining the Terzaghi load compression relationship and the Buisman secular time effect., *in* 'Proc. 2nd Int. Conf. Soil Mech. Fdn Engne', Rotterdam, pp. 32–37.
- Kozeny, J. (1927), 'Über kapillare Leitung des Wassers im Boden', *Akad. Wiss. Wien* **136**, 271–306.
- Kulhawy, F. H. and Mayne, P. W. (1990), 'Manual on Estimating Soil Properties for Foundation Design'.
- Kumamoto, N. and Yoshikuni, H. (1982), 'A Key to Solution of the Irrotational Consolidation and its Application to Cylindrical Clay', *Soils And Foundations* **21**(2), 35–46.
- Ladd, C. C., Foott, R., Ishihara, K., Schlosser, F. and Poulos, H. (1977), Stress-Deformation and Strength Characteristics, *in* 'Report of IX ICSMFE 1977', Tokyo.
- Lade, P. V. and De Boer, R. (1997), 'The concept of effective stress for soil, concrete and rock', *Géotechnique* **47**(1), 61–78.
- Lambe, T. W. and Whitman, R. V. (1969), 'Soil Mechanics'.

- Lee, I. S. (2008), Computational Techniques for Efficient Solution of Discretized Biot's Theory for Fluid Flow in Deformable Porous Media, PhD thesis, Virginia Polytechnic Institute and State University.
- Lefebvre, G. and Poulin, C. (1979), 'A new method of sampling in sensitive clay', *Canadian Geotechnical Journal* **16**(1), 226–233.
- Leonards, G. and Girault, P. (1961), A study of the one-dimensional consolidation test, in 'Proceedings of the 5th International Conference of Soil Mechanics and Foundational Engineering', Vol. 1, pp. 213–218.
- Leroueil, S. (2006), 'The isotache approach . Where are we 50 years after its development by Professor Šuklje ? (2006 Prof . Šuklje ' s Memorial Lecture)', *13th Danube-European Conference on Geotechnical Engineering* pp. 13–46.
- Leroueil, S., Tavenas, F. and Locat, J. (1985), 'Discussion: Correlations between index tests and the properties of remoulded clays', *Géotechnique* **35**(2), 223–229.
- Leroueil, S. and Vaughan, P. R. (1990), 'The general and congruent effects of structure in natural soils and weak rocks', *Géotechnique* **40**(3), 467–488.
- Lieske, W. (2015), Compression behaviour of a natural and remoulded clay, Master's thesis, Ruhr-Universität Bochum.
- Ling, H. I., Ling, E. and Wang, J.-P. (2009), 'Stress Deformation and Fluid Pressure of Bone Specimens under Cyclic Loading', *Journal of Engineering Mechanics* **135**(5), 375–381.
- Liu, J. C. and Griffiths, D. V. (2015), 'A general solution for 1D consolidation induced by depth- and time-dependent changes in stress', *Géotechnique* **65**(1), 66–72.
- Lovisa, J., Read, W. and Sivakugan, N. (2012), 'Calculating c_v based on non-uniform initial excess pore pressure', *Géotechnique* **62**(8), 741–748.
- Lovisa, J. and Sivakugan, N. (2015), 'Tall Oedometer Testing: Method to Account for Wall Friction', *International Journal of Geomechanics* **15**(2), 04014045.
- Lowe, J., Jonas, E. and Obrcian, V. (1969), 'Controlled Gradient Consolidation Test', *Journal of the Soil Mechanics and Foundations Division* **95**(1), 77–98.

- Lunne, T., Berre, T., Andersen, K. H., Strandvik, S. and Sjursen, M. (2007), 'Effects of sample disturbance and consolidation procedures on measured shear strength of soft marine Norwegian clays', *Canadian Geotechnical Journal* **44**(1), 726–750.
- Lunne, T., Long, M. and Forsberg, C. (2003), Characterisation and engineering properties of Onsøy clay, *in* T. Tan, ed., 'Characterisation and Engineering Properties of Natural Soils, Volume 1', A.A. Balkema Publishers, pp. 395–427.
- Major, J. (2000), 'Gravity-driven consolidation of granular slurries—implications for debris-flow deposition and deposit characteristics', *Journal of Sedimentary Research* **I**, 64–83.
- Mandel, J. (1953), 'Consolidation des sols (étude mathématique)', *Géotechnique* **3**(7), 287–299.
- Marques, M. E. S., Leroueil, S. and de Almeida, M. d. S. S. (2004), 'Viscous behaviour of St-Roch-de-l'Achigan clay, Quebec', *Canadian Geotechnical Journal* **41**(1), 25–38.
- Mayne, P. W. and Kulhawy, F. H. (1982), 'Ko - OCR relationship in soil', *Journal of the Geotechnical Engineering Division, ASCE* **108**(6), 851–872.
- Mckinley, J. and Sivakumar, V. (2009), 'Coefficient of consolidation by plotting velocity against displacement', *Géotechnique* **59**(6), 553–557.
- Meier, L. and Kahr, G. (1999), 'Determination of the cation exchange capacity (cec) of clay minerals using the complexes of copper(ii) ion with triethylenetetramine and tetraethylenepentamine', *Clays and Clay Minerals* **47**(3), 386–388.
- Mesri, G. and Castro, A. (1987), 'C α /C c Concept and K 0 During Secondary Compression', *Journal of Geotechnical Engineering* **113**(3), 230–247.
- Mesri, G. and Godlewski, P. M. (1977), 'Time and stress compressibility interrelationships', *J. Geotech. Enging Div., ASCE* **103**(GT5), 417–430.
- Mesri, G. and Olson, R. E. (1971), 'Mechanisms controlling the permeability of clays', *Clays and Clay Minerals* **19**(3), 151–158.
- Miao, L., Wang, F. and Wang, X. (2010), 'One Dimensional Consolidation of Double-Layered Foundation with Multi-Level Load', *Marine Georesources & Geotechnology* **28**(1), 1–24.
- Mikasa, M. (1965), 'The consolidation of soft clay - a new consolidation theory and its application', *Japan Society of Civil Engineering* pp. 21–26.

- Mimouni, T., Lei, L. and Laloui, L. (2015), 'Estimating soil thermal diffusivity with interference analyses', *Acta Geotechnica* **10**(2), 197–208.
- Mitchell, J. (1956), The fabric of natural clays and its relation to engineering properties, *in* 'Proceedings of the Highway Research Board', pp. 693–713.
- Mitchell, J. K. (1991), 'Conduction phenomena: from theory to geotechnical practice', *Géotechnique* **41**(3), 299–340.
- Mitchell, J. K., Baxter, C. and Soga, K. (1997), Time effects on the stress - deformation behaviour of soils, *in* 'Proceedings of Professor Sakuro Murayama Memorial Symposium', Kyoto University, April 12, 1997, pp. 1–64.
- Mitchell, J. K. and Soga, K. (2005), *Fundamentals of Soil Behavior*, John Wiley and Sons.
- Mohamad, R. and Dobry, R. (1987), 'Undrained monotonic and cyclic triaxial strength of sand', *Journal of Geotechnical Engineering* **112**(10), 941–958.
- Morris, P. H. (2002), 'Analytical solutions of linear finite-strain one-dimensional consolidation', *Journal of Geot. and Geoenv. Engineering* **128**(4), 319–326.
- Muhs, H. and Kany, M. (1954), 'Einfluss von Fehlerquellen beim Kompressionsversuch', *Fortschritte und Forschungen im Bauwesen* **Heft 17**.
- Muir Wood, D. (2016), 'Analysis of consolidation with constant rate of displacement', *Canadian Geotechnical Journal* **53**(5), 740–752.
- Müthing, N., Barciaga, T. and Schanz, T. (2016a), On the Use of Isotropic Hardening Plasticity to Model Cyclic Consolidation of Fine Grained Soils, *in* T. Triantafyllidis, ed., 'Lecture Notes in Applied and Computational Mechanics', Springer International Publishing, pp. 131–147.
- Müthing, N., Barciaga, T. and Schanz, T. (2017), Cyclic Response of Natural Onsøy Clay, *in* 'Lecture Notes in Applied and Computational Mechanics', Vol. 82, Springer International Publishing, pp. 257–274.
- Müthing, N., Razouki, S. S., Datcheva, M. and Schanz, T. (2016b), 'Rigorous solution for 1-D consolidation of a clay layer under haversine cyclic loading with rest period', *SpringerPlus* **5**(1), 1987.

- Müthing, N., Röchter, L., Datcheva, M. and Schanz, T. (2014), Cyclic consolidation of soft soils, *in* 'Aktuelle Forschung in der Bodenmechanik 2013', Springer Berlin Heidelberg, Berlin, Heidelberg, pp. 77–87.
- Müthing, N., Schanz, T. and Datcheva, M. (2015), 'On the influence of loading frequency on the pore-water dissipation behavior during cyclic consolidation of soft soils', *Computer Methods and Recent Advances in Geomechanics - Proceedings of the 14th Int. Conference of International Association for Computer Methods and Recent Advances in Geomechanics, IACMAG 2014* pp. 441–445.
- Narasimhan, T. N. and Witherspoon, P. A. (1977), 'Numerical Model for Saturated-Unsaturated Flow in Deformable Porous Media - I. Theory', *Water resources research* **13**(3), 657–664.
- Ni, J., Indraratna, B., Geng, X.-Y., Carter, J. P. and Rujikiatkamjorn, C. (2013), 'Radial consolidation of soft soil under cyclic loads', *Computers and Geotechnics* **50**, 1–5.
- Niemunis, A., Wichtmann, T. and Triantafyllidis, T. (2005), 'A high-cycle accumulation model for sand', *Computers and Geotechnics* **32**(4), 245–263.
- Northey, R. and Thomas, R. (1965), Consolidation test pore pressures, *in* 'Proceedings of the 6th international conference on soil mechanics and foundation engineering, Montreal, Vol. 1', pp. 323–327.
- Ohde, J. (1939), 'Zur Theorie der Druckverteilung im Baugrund.', *Der Bauingenieur.* **20**, 451–459.
- Olsen, H. (1962), Hydraulic flow through saturated clays, *in* 'Proceedings of the 9th National Conference on Clays and Clay Minerals', Pergamon Press, pp. 131–160.
- Olson, R. E. (1977), 'Consolidation Under Time-Dependent Loading', *Journal of the Geotechnical Engineering Division* **103**(1), 55–60.
- Olson, R. E. (1986), State-of-the-art: Consolidation testing, *in* 'Consolidation of Soils: Testing and Evaluation', American Society for Testing and Materials, Philadelphia, PA, pp. 7–70.
- Pandian, N., Knodel, P., Sridharan, A. and Kumar, K. (1992), 'A New Method for the Determination of Coefficient of Consolidation', *Geotechnical Testing Journal* **15**(1), 74.
- Paria, G. (1958), 'Axisymmetric consolidation for a porous elastic material containing a fluid'.

- Paul, M. and Sahu, R. B. (2012), 'One dimensional consolidation under cyclic loading', *International Journal of Geotechnical Engineering* **6**(3), 395–401.
- Paul, M., Sahu, R. and Biswas, S. (2010), One Dimensional Consolidation of Soft Cohesive Soils Under Cyclic Loading, in 'Indian Geotechnical Conference – 2010', pp. 317–320.
- Perloff, W., Nair, K. and Smith, J. (1965), Effect of measuring system on pore water pressures in the consolidation test, in 'Proceedings of the 6th International Conference on Soil Mechanics and Foundation Engineering', pp. 338–341.
- Peron, H., Hueckel, T. and Laloui, L. (2007), 'An Improved Volume Measurement for Determining Soil Water Retention Curves', *Geotechnical Testing Journal* **30**(1), 1–8.
- Pollmann, N. and Steeb, H. (2014), Consolidation of a poroelastic sphere: Numerical investigations of Cryer's problem, in 'Proceedings in Applied Mathematics and Mechanics', pp. 505–506.
- Porhoseini, R., Barkhordari, K. and Abbaspour, M. (2014), 'An Experimental Study on One-Dimensional Consolidation of Clay under Cyclic Loading', *Geodynamics Research International Bulletin (GRIB)* **2**(3), 10–19.
- Qin, A.-f., Chen, G.-j., Tan, Y.-w. and Sun, D.-a. (2008), 'Analytical solution to one-dimensional consolidation in unsaturated soils', *Applied Mathematics and Mechanics* **29**(10), 1329–1340.
- Rahal, M. A. and Vuez, A. R. (1998), 'Analysis of Settlement and Pore Pressure Induced by Cyclic Loading of Silos', *Journal of Geot. and Geoenv. Eng.* **124**(12), 1208–1210.
- Rahardjo, H. and Fredlund, D. G. (1995), 'Experimental verification of the theory of consolidation for unsaturated soils', *Canadian Geotechnical Journal* **32**(5), 749–766.
- Razouki, S. S., Bonnier, P., Datcheva, M. and Schanz, T. (2013), 'Analytical solution for 1D consolidation under haversine cyclic loading', *International Journal for Numerical and Analytical Methods in Geomechanics* **37**(14), 2367–2372.
- Razouki, S. S. and Schanz, T. (2011), 'One-dimensional consolidation under haversine repeated loading with rest period', *Acta Geotechnica* **6**(1), 13–20.
- Renner, J. and Messar, M. (2006), 'Periodic pumping tests', *Geophysical Journal International* **167**(1), 479–493.

- Robertson, P. K. and Wride, C. E. (1998), 'Evaluating cyclic liquefaction potential using the cone penetration test', *Canadian Geotechnical Journal* **35**, 442–459.
- Robinson, R. (1999), 'Consolidation analysis with pore water pressure measurements', *Géotechnique* **49**(1), 127–132.
- Robinson, R. G. and Allam, M. M. (1996), 'Determination of coefficient of consolidation from early stage of log t plot', *Geotechnical Testing Journal* **19**(3), 316–320.
- Robinson, R. G. and Allam, M. M. (1998), 'Effect of clay mineralogy on coefficient of consolidation', *Clays and Clay Minerals* **46**(5), 596–600.
- Roma, J. R. (1976), Geotechnical properties of Florida phosphatic clays., Phd thesis, Massachusetts Institute of Technology.
- Rosenqvist, I. T. (1953), 'Considerations on the sensitivity of Norwegian quick clays', *Géotechnique* **3**(5), 195–200.
- Rowe, P. (1957), $C = 0$ hypothesis for normally loaded clays at equilibrium., in 'Proc. 4th Int. Conf. on Soil Mech.', London, pp. 189–192.
- Rowe, P. W. and Barden, L. (1966), 'A New Consolidation Cell', *Géotechnique* **16**(2), 162–170.
- Sakai, A., Samang, L. and Miura, N. (2003), 'Partially-Drained Cyclic Behavior and Its Application to the Settlement of a Low Embankment Road on Silty-Clay.', *Soils and Foundations* **43**(1), 33–46.
- Samarasighe, A. M., Huang, Y. H. and Drnevich, V. P. (1982), 'Permeability and Consolidation of Normally Consolidated Soils', *Journal of Geotechnical Engineering* **108**(GT6), 835–850.
- Schanz, T. (1998), Zur Modellierung des mechanischen Verhaltens von Reibungsmaterialien, Habilitationsschrift, Universität Stuttgart.
- Schiffman, R. L. (1958), 'Consolidation of soil under time-dependent loading and varying permeability', *Proceedings of the Thirty-Seventh Annual Meeting of the Highway Research Board* pp. 584–617.
- Schmatz, J., Berg, S., Urai, J. and Ott, H. (2015), 'Nano-scale imaging of pore-scale fluid-fluid-solid contacts in sandstone', *Geophysical Research Letters* .

- Schmatz, J., Urai, J., Desbois, G., Berg, S. and Ott, H. (2015), Cryogenic Broad Ion Beam milling (BIB) and Scanning Electron Microscopy (SEM) to image pore morphology and fluid contacts in hydrocarbon reservoir rocks, *in* 'Acta Stereologica, Proceedings of the 14th International Congress for Stereology and Image Analysis', Liège (Belgium).
- Schmertmann, J. H. (1983), 'A Simple Question About Consolidation', *Journal of Geotechnical Engineering* **109**(1), 119–122.
- Schmidt, B. (1966), 'Discussion on Earth Pressures at Rest Related to Stress History', *Canadian Geotechnical Journal* **3**(4), 239–242.
- Schmidt, B. (1983), 'Discussion of 'Ko-OCR relationships in soil' by Mayne and Kulhawy (1982)', *Journal of the Geotechnical Engineering Division* **109**(6), 866–867.
- Schofield, A. N. and Wroth, P. (1968), *Critical state soil mechanics*, McGraw-Hill Book Company.
- Schudy, R. (2015), Personal communication: Sketch of oedometer ring adaption applying miniature pore pressure sensors, Technical report.
- Seneviratne, N., Fahey, M., Newson, T. and Fujiyasu, Y. (1996), 'Numerical modelling of consolidation and evaporation of slurried mine tailings', *International Journal for Numerical and Analytical Methods in Geomechanics* **20**(9), 647–671.
- Senneset, K. (1989), A new oedometer with splitted ring for the measurement of lateral stress, *in* 'Proceedings of the 12th Intern. Conf. on Soil Mech. and Found. Eng., Rio de Janeiro, 1/29', pp. 115–118.
- Shackelford, C. D., Benson, C. H., Katsumi, T., Edil, T. B. and Lin, L. (2000), 'Evaluating the hydraulic conductivity of GCLs permeated with non-standard liquids', *Geotextiles and Geomembranes* **18**(2-4), 133–161.
- Sherif, M. A., Ishtbashi, I. and Ryden, D. E. (1974), Coefficient of Lateral Earth Pressure At Rest in Cohesionless Soils, *in* 'Soil Engineering Research Report No. 10, University of Washington, Seattle.'
- Sivakugan, N., Lovisa, J., Ameratunga, J. and Das, B. M. (2014), 'Consolidation settlement due to ramp loading', *International Journal of Geotechnical Engineering* **8**(2), 191–196.
- Sivaram, B. and Swamee, A. (1977), 'A Computational Method for Consolidation Coefficient', *Soils and Foundations* **17**(2), 48–52.

- Sivrikaya, O. and Togrol, E. (2006), 'Measurement of side friction between specimen and consolidation ring with newly designed oedometer cell', *Geotechnical Testing Journal* **29**(1), 87–94.
- Skempton, A. (1944), 'Notes on the compressibility of clays.', *Quarterly Journal of the Geological Society* **100**, 119.
- Skempton, A. (1953), The Colloidal " Activity " of Clays, in 'Proc. 3rd Int. Conf. Soil Mech., Zürich', pp. 57–61.
- Skempton, A. W. (1954), 'The Pore-Pressure Coefficients A and B', *Géotechnique* **4**(4), 143–147.
- Skempton, A. W. (1969), 'The consolidation of clays by gravitational compaction', *Quarterly Journal of the Geological Society* **125**(1-4), 373–411.
- Smith, R. E. and Wahls, H. E. (1969), 'Consolidation under Constant Rates of Strain', *Journal of the Soil Mechanics and Foundations Division* **95**(2), 519–540.
- Soga, K. and Mitchell, J. K. (1996), 'Rate-dependent deformation of structured natural clays', *Geotechnical Special Publication No. 61, American Society of Civil Engineers*, pp. 243–257.
- Song, I. and Renner, J. (2006), 'Linear pressurization method for determining hydraulic permeability and specific storage of a rock sample', *Geophysical Journal International* **164**(3), 685–696.
- Song, I. and Renner, J. (2007), 'Analysis of oscillatory fluid flow through rock samples', *Geophysical Journal International* **170**(1), 195–204.
- Sonpal, R. and Katti, R. (1973), Consolidation - an analysis with pore pressure measurements, in 'Proceedings of the 8th international conference on soil mechanics and foundation engineering', Moscow, pp. 385–388.
- Soumaya, B. and Kempfert, H. G. (2010), 'Verformungsverhalten weicher Böden im spannungsgesteuerten Kompressionsversuch', *Bautechnik* **87**(2), 73–80.
- Sridharan, A. (1971), 'Pore size distribution studies', *Journal of the Soil Mechanics and Foundations Division ASCE* **97**(SM5), 771–787.

- Sridharan, A. (2002), Engineering behaviour of clays: Influence of mineralogy, *in* C. Di Maio, T. Hueckel and B. Loret, eds, 'Proceedings of the Workshop on Chemo-Mechanical Coupling in Clays: From Nano-scale to Engineering Applications', A.A. Balkema Publishers, pp. 3–28.
- Sridharan, A. and Prakash, K. (1985), 'Improved Rectangular Hyperbola Method for Determination of Coefficient of Consolidation.', *Geotechnical Testing Journal* **8**(1), 37–40.
- Sridharan, A. and Prakash, K. (1993), ' δ -t/ δ Method for the Determination of Coefficient of Consolidation', *Geotechnical Testing Journal* **16**(1), 131–134.
- Sridharan, A. and Prakash, K. (2003), 'Self Weight Consolidation: Compressibility Behavior of Segregated and Homogeneous Finegrained Sediments', *Marine Georesources & Geotechnology* **21**(2), 73–80.
- Suklje, L. (1957), The analysis of the consolidation process by the isotache method., *in* 'Proceedings of the 4th International Conference on Soil Mechanics and Foundation Engineering', London, pp. 200–206.
- Tavenas, F., P., J., Leblond, P. and Leroueil, S. (1983), 'The Permeability of natural soft clays. Part1: Methods of Laboratory measurement', *Canadian Geotechnical Journal* **20**, 644–659.
- Taylor, D. W. (1942), *Research on Consolidation of Clays*, Massachusetts Institute of Technology. Dept. of Civil and Sanitary Engineering., Publication 82.
- Taylor, D. W. (1948), *Fundamentals of soil mechanics*, John Wiley & Sons, Inc.
- Taylor, D. W. and Merchant, W. (1940), 'A Theory of Clay Consolidation Accounting for Secondary Compression', *Journal of Mathematics and Physics* **19**(1-4), 167–185.
- Terzaghi, K. (1923), 'Die Berechnung der Durchlässigkeitsziffer des Tones aus dem Verlauf der hydrodynamischen Spannungserscheinungen', *Sitzungsberichte der Akademie der Wissenschaften in Wien, Mathematisch-Naturwissenschaftliche Klasse, Abteilung IIa* **132**, 125–138.
- Terzaghi, K. (1925), *Erdbaumechanik auf bodenphysikalischer Grundlage*, F. Deuticke.
- Terzaghi, K. (1943), *Theoretical Soil Mechanics*, John Wiley & Sons, Inc., Hoboken, NJ, USA.

- Terzaghi, K. (1944), 'End and means in soil mechanics', *Engineering Journal* **27**.
- Ting, C. M. R., Sills, G. C. and Wijeyesekara, D. C. (1994), 'Development of KO in soft soils', *Géotechnique* **44**(1), 101–109.
- Toorman, E. a. (1999), 'Sedimentation and self-weight consolidation: constitutive equations and numerical modelling', *Géotechnique* **49**(6), 709–726.
- Toufigh, M. M. and Ouria, A. (2008), 'Application of Mapping and Superimposing Rule for Solution of Parabolic PDE in Porous Medium under Cyclic Loading', *International Journal of Civil, Environmental, Structural, Construction and Architectural Engineering* **2**(5), 1039–1044.
- Toufigh, M. M. and Ouria, A. (2009), 'Consolidation of inelastic clays under rectangular cyclic loading', *Soil Dynamics and Earthquake Engineering* **29**(2), 356–363.
- van Olphen, H. (1977), *An introduction to clay colloid chemistry*, 2nd edn, John Wiley & Sons, New York London Sydney Toronto.
- Verruijt, A. (1969), Elastic storage of aquifers, in 'Flow through porous media', pp. 331–376.
- Verruijt, A. (2010a), *An Introduction to Soil Dynamics*, Springer Netherlands, Dordrecht.
- Verruijt, A. (2010b), *Poroelastodynamics*, Delft University of Technology, The Netherlands.
- Verruijt, A. (2014), *Theory and problems of poroelasticity*.
- Vuez, A. R., Lanos, C. and Rahal, A. (2000), Soil Compaction by Cyclic Loading: Ins and Outs, in D. Kolymbas and W. Fellin, eds, 'Compaction of Soils, Granulates and Powders: International Workshop on Compaction of Soils, Granulates and Powders: Innsbruck, 28-29 February 2000 (Advances in Geotechnical Engineering and Tunneling)', Innsbruck, pp. 175–185.
- Watabe, Y., Udaka, K., Nakatani, Y. and Leroueil, S. (2012), 'Long-term consolidation behavior interpreted with isotache concept for worldwide clays', *Soils and Foundations* **52**(3), 449–464.
- Whitman, R. and Richardson, A. (1961), Time-lags in pore pressure measurements, in 'Proc. 5th ICSMFE 1', pp. 407–411.

- Wichtmann, T. (2005), Explicit accumulation model for non-cohesive soils under cyclic loading, PhD thesis, Institut für Grundbau und Bodenmechanik, Ruhr-Universität Bochum.
- Wichtmann, T. (2016), Soil behaviour under cyclic loading - experimental observations, constitutive description and applications, Habilitationsschrift, Institut für Bodenmechanik und Felsmechanik am Karlsruher Institut für Technologie (KIT).
- Wichtmann, T., Andersen, K. H., Sjørusen, M. a. and Berre, T. (2013), ‘Cyclic tests on high-quality undisturbed block samples of soft marine’, *Canadian Geotechnical Journal* **50**(4), 400–412.
- Wichtmann, T. and Triantafyllidis, T. (2016a), ‘An experimental database for the development, calibration and verification of constitutive models for sand with focus to cyclic loading: part I -tests with monotonic loading and stress cycles’, *Acta Geotechnica* **11**(4), 739–761.
- Wichtmann, T. and Triantafyllidis, T. (2016b), ‘An experimental database for the development, calibration and verification of constitutive models for sand with focus to cyclic loading: part II - tests with strain cycles and combined loading’, *Acta Geotechnica* **11**(4), 763–774.
- Wilson, N. E. and Elgohary, M. M. (1974), ‘Consolidation of Soils Under Cyclic Loading’, *Canadian Geotechnical Journal* **11**(3), 420–423.
- Wissa, A. . E. . Z., Christian, J. T., Davis, E. . H. and Heiberg, S. . (1971), ‘Consolidation at Constant Rate of Strain’, *Journal of the Soil Mechanics and Foundations Division* **97**(SM10), 1393–1413.
- Wissa, A. E., Fuleihan, N. F. and Ingra, T. S. (1983), Consolidation behavior of phosphatic clays, Technical report, Florida Institute of Phosphatic Research, Research Project FIPR 80-02-002., Technical report.
- Xiao-Yun, G., Da-Neng, X. and Wei, D. (1995), A computing model based on cyclic consolidation tests, *in* ‘Proceedings of the Fifth Int. Symposium on Land Subsidence’, The Hague, pp. 295–303.
- Xie, K.-H., Huang, D.-Z., Wang, Y.-L. and Deng, Y.-B. (2014), ‘Analytical Theory for One-Dimensional Consolidation of Soil Induced by Time-Dependent Pumping and Loading’, *Marine Georesources & Geotechnology* **32**(4), 328–350.

- Xie, K.-H., Qi, T. and Dong, Y.-q. (2006), ‘Nonlinear analytical solution for one-dimensional consolidation of soft soil under cyclic loading’, *Journal of Zhejiang University-SCIENCE A* **7**(8), 1358–1364.
- Xie, K. H., Xie, X. Y. and Gao, X. (1999), ‘Theory of one dimensional consolidation of two-layered soil with partially drained boundaries’, *Computers and Geotechnics* **24**(4), 265–278.
- Xie, K.-H., Xie, X.-Y. and Li, X.-B. (2008), ‘Analytical theory for one-dimensional consolidation of clayey soils exhibiting rheological characteristics under time-dependent loading’, *International Journal for Numerical and Analytical Methods in Geomechanics* **32**(14), 1833–1855.
- Xu, L., Yuan-qiang, C. and Shi-ming, W. (2002), ‘Study on one-dimensional consolidation of saturated soil with semi-pervious boundaries and under cyclic loading’, *Journal of Zhejiang University-SCIENCE A* **3**(5), 513–519.
- Yao, D. T. C., de Oliveira-Filho, W. L., Cai, X. C. and Znidarcic, D. (2002), ‘Numerical solution for consolidation and desiccation of soft soils’, *International Journal for Numerical and Analytical Methods in Geomechanics* **26**(2), 139–161.
- Yasuhara, K., Konami, T., Hyodo, M. and Hirao, K. (1991), Earthquake-Induced Settlement in Soft Grounds, in ‘International Conferences on Recent Advances in Geotechnical Earthquake Engineering and Soil Dynamics.’, pp. 365–370.
- Yazdani, H. and Toufigh, M. M. (2012), ‘Nonlinear consolidation of soft clays subjected to cyclic loading-Part I: theory’, *Geomechanics and Engineering* **4**(4), 229–241.
- Zhang, X. and Briaud, J.-L. (2006), Mandel-Cryer Effect in Unsaturated Soils, Vol. 189, p. 174.
- Zhu, G. and Yin, J.-H. (1998), ‘Consolidation of soil under depth-dependent ramp load’, *Canadian Geotechnical Journal* **35**(2), 344–350.
- Zhuang, Y.-c. and Xie, K.-H. (2005), ‘Study on one-dimensional consolidation of soil under cyclic loading and with varied compressibility’, *Journal of Zhejiang University-Science A* **6**(2), 141–147.
- Zimmerer, M. M. (2011), Identifikation konstitutiver Parameter von weichen feinkörnigen Böden, Beitrag zum Konsolidationsverhalten von Ton, Dissertation, Bauhaus-Universität Weimar.

**Schriftenreihe des Lehrstuhls für Grundbau, Boden- und Felsmechanik der
Ruhr-Universität Bochum**

Herausgeber: H.L. Jessberger

- 1 (1979) **Hans Ludwig Jessberger**
Grundbau und Bodenmechanik an der Ruhr-Universität Bochum
- 2 (1978) **Joachim Klein**
Nichtlineares Kriechen von künstlich gefrorenem Emschermergel
- 3 (1979) **Heinz-Joachim Gödecke**
Die Dynamische Intensivverdichtung wenig wasserdurchlässiger Böden
- 4 (1979) **Poul V. Lade**
Three Dimensional Stress-Strain Behaviour and Modeling of Soils
- 5 (1979) **Roland Pusch**
Creep of soils
- 6 (1979) **Norbert Diekmann**
Zeitabhängiges, nichtlineares Spannungs-Verformungsverhalten von gefrorenem Schluff unter triaxialer Belastung
- 7 (1979) **Rudolf Dörr**
Zeitabhängiges Setzungsverhalten von Gründungen in Schnee, Firn und Eis der Antarktis am Beispiel der deutschen Georg-von-Neumayer- und Filchner-Station
- 8 (1984) **Ulrich Güttler**
Beurteilung des Steifigkeits- und Nachverdichtungsverhaltens von ungebundenen Mineralstoffen
- 9 (1986) **Peter Jordan**
Einfluss der Belastungsfrequenz und der partiellen Entwässerungsmöglichkeiten auf die Verflüssigung von Feinsand
- 10 (1986) **Eugen Makowski**
Modellierung der künstlichen Bodenvereisung im grundwasserdurchströmten Untergrund mit der Methode der finiten Elemente
- 11 (1986) **Reinhard A. Beine**
Verdichtungswirkung der Fallmasse auf Lastausbreitung in nichtbindigem Boden bei der Dynamischen Intensivverdichtung
- 12 (1986) **Wolfgang Ebel**
Einfluss des Spannungspfades auf das Spannungs-Verformungsverhalten von gefrorenem Schluff im Hinblick auf die Berechnung von Gefrierschächten
- 13 (1987) **Uwe Stoffers**
Berechnungen und Zentrifugen-Modellversuche zur Verformungsabhängigkeit der Ausbaubeanspruchung von Tunnelausbauten in Lockergestein
- 14 (1988) **Gerhard Thiel**
Steifigkeit und Dämpfung von wassergesättigtem Feinsand unter Erdbebenbelastung

- 15 (1991) **Mahmud Thaher**
Tragverhalten von Pfahl-Platten-Gründungen im bindigen Baugrund,
Berechnungsmodelle und Zentrifugen-Modellversuche
- 16 (1992) **Rainer Scherbeck**
Geotechnisches Verhalten mineralischer Deponieabdichtungsschichten
bei ungleichförmiger Verformungswirkung
- 17 (1992) **Martin M. Bizialiele**
Torsional Cyclic Loading Response of a Single Pile in Sand
- 18 (1993) **Michael Kotthaus**
Zum Tragverhalten von horizontal belasteten Pfahlreihen aus langen Pfählen in Sand
- 19 (1993) **Ulrich Mann**
Stofftransport durch mineralische Deponieabdichtungen:
Versuchsmethodik und Berechnungsverfahren
- 20 (1992) **Festschrift anlässlich des 60. Geburtstages von Prof. Dr.-Ing. H. L. Jessberger**
20 Jahre Grundbau und Bodenmechanik an der Ruhr-Universität Bochum
- 21 (1993) **Stephan Demmert**
Analyse des Emissionsverhaltens einer Kombinationsabdichtung im Rahmen der
Risikobetrachtung von Abfalldeponien
- 22 (1994) **Diethard König**
Beanspruchung von Tunnel- und Schachtausbauten in kohäsionslosem Lockergestein
unter Berücksichtigung der Verformung im Boden
- 23 (1995) **Thomas Neteler**
Bewertungsmodell für die nutzungsbezogene Auswahl von Verfahren zur Altlastensanierung
- 24 (1995) **Ralph Kockel**
Scherfestigkeit von Mischabfall im Hinblick auf die Standsicherheit von Deponien
- 25 (1996) **Jan Laue**
Zur Setzung von Flachfundamenten auf Sand unter wiederholten Lastereignissen
- 26 (1996) **Gunnar Heibroek**
Zur Rissbildung durch Austrocknung in mineralischen Abdichtungsschichten
an der Basis von Deponien
- 27 (1996) **Thomas Siemer**
Zentrifugen-Modellversuche zur dynamischen Wechselwirkung zwischen Bauwerken
und Baugrund infolge stoßartiger Belastung
- 28 (1996) **Viswanadham V. S. Bhamidipati**
Geosynthetic Reinforced Mineral Sealing Layers of Landfills
- 29 (1997) **Frank Trappmann**
Abschätzung von technischem Risiko und Energiebedarf bei Sanierungsmaßnahmen
für Altlasten
- 30 (1997) **André Schürmann**
Zum Erddruck auf unverankerte flexible Verbauwände
- 31 (1997) **Jessberger, H. L. (Herausgeber)**
Environment Geotechnics, Report of ISSMGE Technical Committee TC 5 on
Environmental Geotechnics

Herausgeber: Th. Triantafyllidis

- 32 (2000) **Triantafyllidis, Th. (Herausgeber)**
Boden unter fast zyklischer Belastung: Erfahrung und Forschungsergebnisse (Workshop)
- 33 (2002) **Christof Gehle**
Bruch- und Scherverhalten von Gesteinstrennflächen mit dazwischenliegenden Materialbrücken
- 34 (2003) **Andrzej Niemunis**
Extended hypoplastic models for soils
- 35 (2004) **Christiane Hof**
Über das Verpressankertragverhalten unter kalklösendem Kohlensäureangriff
- 36 (2004) **René Schäfer**
Einfluss der Herstellungsmethode auf das Verformungsverhalten von Schlitzwänden
in weichen bindigen Böden
- 37 (2005) **Henning Wolf**
Zur Scherfugenbänderung granularer Materialien unter Extensionsbeanspruchung
- 38 (2005) **Torsten Wichtmann**
Explicit accumulation model for non-cohesive soils under cyclic loading
- 39 (2008) **Christoph M. Loreck**
Die Entwicklung des Frischbetondruckes bei der Herstellung von Schlitzwänden
- 40 (2008) **Igor Arsic**
Über die Bettung von Rohrleitungen in Flüssigböden
- 41 (2009) **Anna Arwanitaki**
Über das Kontaktverhalten zwischen einer Zweiphasenschlitzwand und nichtbindigen Böden

Herausgeber: T. Schanz

- 42 (2009) **Yvonne Lins**
Hydro-Mechanical Properties of Partially Saturated Sand
- 43 (2010) **Tom Schanz (Herausgeber)**
Geotechnische Herausforderungen beim Umbau des Emscher-Systems
Beiträge zum RuhrGeo Tag 2010
- 44 (2010) **Jamal Alabdullah**
Testing Unsaturated Soil for Plane Strain Conditions: A New Double-Wall Biaxial Device
- 45 (2011) **Lars Röchter**
Systeme paralleler Scherbänder unter Extension im ebenen Verformungszustand
- 46 (2011) **Yasir Al-Badran**
Volumetric Yielding Behavior of Unsaturated Fine-Grained Soils
- 47 (2011) **Usque ad finem**
Selected research papers
- 48 (2012) **Muhammad Ibrar Khan**
Hydraulic Conductivity of Moderate and Highly Dense Expansive Clays
- 49 (2014) **Long Nguyen-Tuan**
Coupled Thermo-Hydro-Mechanical Analysis: Experimental and Back Analysis
- 50 (2014) **Tom Schanz (Herausgeber)**
Ende des Steinkohlenbergbaus im Ruhrrevier: Realität und Perspektiven für die Geotechnik
Beiträge zum RuhrGeo Tag 2014
- 51 (2014) **Usque ad finem**
Selected research papers
- 52 (2014) **Houman Soleimani Fard**
Study on the Hydro-Mechanical Behavior of Fiber Reinforced Fine Grained Soils,
with Application to the Preservation of Historical Monuments
- 53 (2014) **Wiebke Baille**
Hydro-Mechanical Behaviour of Clays - Significance of Mineralogy
- 54 (2014) **Qasim Abdulkarem Jassim Al-Obaidi**
Hydro-Mechanical Behavior of Collapsible Soils
- 55 (2015) **Veselin Zarev**
Model Identification for the Adaption of Numerical Simulation Models -
Application to Mechanized Shield Tunneling
- 56 (2015) **Meisam Goudarzy**
Micro and Macro Mechanical Assessment of Small and Intermediate Strain
Properties of Granular Material
- 57 (2016) **Oliver Detert**
Analyse einer selbstregulierenden interaktiven Membrangründung für Schüttkörper
auf geringtragfähigen Böden
- 58 (2016) **Yang Yang**
Analyses of Heat Transfer and Temperature-induced Behaviour in Geotechnics

- 59 (2017) **Alborz Pourzargar**
Application of suction stress concept to partially saturated compacted soils
- 60 (2017) **Hanna Haase**
Multiscale Analysis of Clay-Polymer Composites for Geoenvironmental Applications
- 61 (2017) **Kavan Khaledi**
Constitutive modeling of rock salt with application to energy storage caverns
- 62 (2017) **Nina Silvia Müthing**
On the consolidation behaviour of fine-grained soils under cyclic loading

Lebenslauf

Persönliche Daten

Name Nina Silvia Müthing
Geburtsdatum/-ort 14. Februar 1987 in Essen
Email Nina.Muething@RUB.de



Berufliche Erfahrungen

05/2010 – 12/2017 **Wissenschaftliche Mitarbeiterin am**
02/2016 – 12/2017 Lehrstuhl für Grundbau, Boden- und Felsmechanik, Ruhr-Universität Bochum
08/2011 – 02/2016 Lehrstuhl für Grundbau, Boden- und Felsmechanik, Ruhr-Universität Bochum
und Lehrstuhl Baugrund-Grundbau, TU Dortmund (Forschungskooperation)
08/2010 – 08/2011 Institut für Strukturmechanik, Bauhaus-Universität Weimar
05/2010 – 07/2010 Lehrstuhl für Grundbau, Boden- und Felsmechanik, Ruhr-Universität Bochum

03/2006 – 09/2009 **Studentische Hilfskraft am**
Lehrstuhl für Grundbau, Boden- und Felsmechanik, Ruhr-Universität Bochum

07/2005 - 10/2005 **Praktikum** bei Brückner Grundbau GmbH, Essen

Schulausbildung und Studium

09/2017 **Promotion zum Doktor-Ingenieur (Dr.-Ing.)** an der Ruhr-Universität Bochum
Titel der Dissertation: *On the consolidation behaviour of fine-grained soils under cyclic loading*
Erstgutachter: Prof. Dr.-Ing. habil. Tom Schanz, Ruhr-Universität Bochum
Datum der Promotionsprüfung: 25. September 2017

10/2005 – 03/2010 **Studium des Bauingenieurwesens** an der Ruhr-Universität Bochum
Abschluss: Diplom-Ingenieurin (Dipl.-Ing.)
Vertiefungsrichtung: Grundbau- und Tunnelbautechnik
Titel der Diplomarbeit: *Experimental and numerical slope stability analysis considering initial and hydraulic boundary conditions*

08/1997 - 06/2005 **B.M.V.-Schule** Essen, staatl. anerk. Mädchengymnasium
Abschluss: allgemeine Hochschulreife

